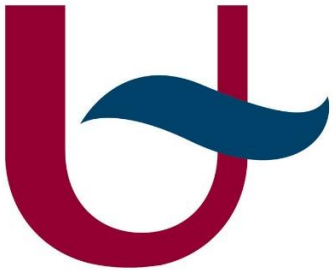

Faculteit Wetenschappen

Departement Fysica

TOWARD FAST AND DOSE EFFICIENT ELECTRON TOMOGRAPHY

NAAR SNELLE EN DOSIS-EFFICIËNTE ELEKTRONENTOMOGRAFIE

Proefschrift voorgelegd tot het behalen van de graad van
Doctor in de Wetenschappen: Fysica
aan de Universiteit Antwerpen, te verdedigen door:

Hans Vanrompay

Promotor
Prof. Dr. Sara Bals

Antwerpen, 2020

The candidate was financially supported by the Research Foundation Flanders (FWO).

De kandidaat werd financieel gesteund door het Fonds voor Wetenschappelijk Onderzoek Vlaanderen (FWO).

Doctoral Committee

Chairman
Prof. Dr. Floris Wuyts, University of Antwerp – Belgium

Promotor
Prof. Dr. Sara Bals, University of Antwerp – Belgium

Members

Prof. Dr. Pierre Van Mechelen, University of Antwerp – Belgium

Prof. Dr. Johan Verbeeck, University of Antwerp – Belgium

Prof. Dr. Sammy Verbruggen, University of Antwerp – Belgium

Prof. Dr. Joost Batenburg, Leiden University – The Netherlands

Dr. Hugo Perez-Garza, DENSsolutions – The Netherlands

Contact Information

Hans Vanrompay
University of Antwerp – Department of Physics
EMAT – Electron Microscopy for Materials Science
Groenenborgerlaan 171
B-2020 Antwerp
Belgium
Hans.Vanrompay@uantwerpen.be

Table of Contents

Summary

During the last decades, engineered nanoscale materials have become a common occurrence in available products and their functionalities are well spread across many topics such as catalysis, coatings, filtration, batteries, lubricants, cosmetics, medicine and electronics applications. The specific properties of nanosystems are very often sensitive to their three-dimensional (3D) structure. Therefore, for the development of nanomaterials geared towards specific applications there is an urgent need for fast and accurate 3D characterization tools. One indispensable tool to study nanomaterials is transmission electron microscopy (TEM). State- of- the- art TEM can reach a resolution of the order of 50 pm, but conventionally only results in two- dimensional (2D) projections of 3D objects. Therefore, "electron tomography" was developed as a technique to investigate the 3D structure of nanomaterials. The approach is based on the acquisition of multiple 2D TEM images along different tilt angles. Next, these images are aligned and used as an input for a mathematical reconstruction algorithm that enables one to obtain the 3D structure of the original object.

Although electron tomography yields very precise and local information on the 3D structure of nanoparticles, it is far from straightforward to obtain 3D information that can be considered as an averaged or statistically relevant result. This is a major drawback when trying to connect the properties of the nanoparticles to their 3D structure, which is crucial in order to obtain a general understanding concerning their structure- activity relations. Currently, such studies cannot be performed due to the fact that both the acquisition of the tilt series and the 3D reconstruction are very time consuming. Even under ideal conditions, approximately 1 hour is required to acquire all TEM images during a tomography experiment for a single nanoparticle. The offline alignment and 3D reconstruction further increase the total processing time to at least 2 hours. This is a drastic disadvantage of electron tomography in comparison to conventional 2D imaging by TEM.

Obviously, one of the emerging challenges in the field of electron tomography is to increase the throughput of 3D reconstructions of nanoparticles. At the same time, the quality of the reconstructions should still enable one to obtain reliable and quantitative results. Moreover, 3D studies of radiation sensitive materials are nowadays extremely challenging

since samples will degrade and deform when long acquisition times are required. Finally, if we would be able to perform 3D studies in quasi real- time, 3D in-situ microscopy will become possible. This would allow to directly observe the dynamical structure evolution and measure the relevant property changes, at the nanoscale under more realistic, environmental, conditions. For example, through the development of in-situ 3D electron tomography, we will be capable of understanding thermal instability mechanisms.

Here I will present novel techniques, aimed to reduce the run time of electron tomography experiments in order to enable high- throughput and quasi real- time characterization of nanostructures. Such high- throughput electron tomography experiments will yield statistically relevant 3D information concerning critical properties of nanomaterials. By developing acquisition methodologies that enable us to acquire a tomographic tilt series within several minutes, a plethora of applications will become possible such as in-situ tomography where morphology changes of nanosystems can be determined as a function of e.g. temperature. Fast acquisition methodologies will also decrease the electron dose and/or dose rate, therefore lowering the harmful influence of the electron beam. In addition, by optimizing the alignment and reconstruction processes, quasi real- time 3D imaging at the electron microscope will come within reach. In this manner, the efficiency and applicability of 3D studies will improve and allow the user to dynamically steer ongoing tomographic experiments.

This thesis is divided into three main parts, an introduction on the techniques used, a part on fast and dose efficient acquisition methodologies and finally a part on a more efficient reconstruction strategy. In more detail the layout is as follows:

Part I: Introduction

This part presents a literature overview that starts with a short introduction on nanoscience. In addition, the concepts of electron microscopy and tomography are introduced. The final chapter of this part covers original work that displays the capabilities of state-of-the-art electron tomography.

Chapter 1: Historical Perspective.

This chapter introduces the concept of nanoscience and presents the historical background that lead to the development of electron microscopy and tomography.

Chapter 2: Electron tomography: The Principles.
This chapter summarizes the theoretical foundations of electron tomography. It furthermore introduces several common reconstruction algorithms and the concepts on which they are based.

Chapter 3: Electron tomography in Practice.
This chapter presents the electron microscope and details important aspects concerning imaging modalities. The different steps necessary to perform a successful tomography experiment are listed.

Chapter 4: State-of-the-Art Electron Tomography for Material Sciences.
This chapter displays two experimental studies where tomography was successfully applied to unravel the complex structure-property relationships of different nanomaterials.

Part II: Accelerated Acquisition
This part presents original work where different acquisition strategies were developed in order to enhance the throughput capabilities and/or improve the dose efficiency of electron tomography experiments.

Chapter 5: Experimental Evaluation of Undersampling Schemes.
This chapter studies three different undersampling techniques, with as focus their mutual experimental comparison, capable of reducing the electron dose and/or acquisition time of an electron tomography experiment.

Chapter 6: Fast HAADF-STEM for High-Throughput Electron Tomography.
This chapter covers the development of a fast HAADF-STEM acquisition approach, aimed at investigating nanoparticles with an improved throughput and statistical relevance.

Chapter 7: Fast In-Situ Electron Tomography of Branched Au Nanoparticles.
This chapter presents an experimental study where the fast HAADF-STEM approach was combined with in-situ tomography to quantitatively investigate the thermal reshaping of branched Au nanoparticles.

Chapter 8: Improving the Accuracy of Fast Tomography.
This chapter introduces a neural network based filter and a hybrid acquisition strategy which can be used to improve the accuracy of fast HAADF-STEM tomography.

Part III: Accelerated Reconstruction
This part represents original work which enables efficient and real-time electron tomography experiments.

Chapter 9: Reconstruction of Arbitrary Slices for Real-Time Tomography.
This chapter proposes a new electron tomography strategy which improves the efficiency of the 3D characterization of nanomaterials by TEM. Furthermore, it enables explorative imaging and provides valuable 3D information to dynamically adjust the experimental parameters during an electron tomography experiment.

Samenvatting

In de afgelopen decennia komen materialen op nanoschaal steeds meer voor in dagdagelijkse producten. Bovendien worden hun eigenschappen steeds vaker gebruikt in verschillende toepassingsvelden zoals zoals katalyse, coatings, filtratie, batterijen, smeermiddelen, cosmetica, medicijnen en elektronische toepassingen. De specifieke eigenschappen van nanosystemen zijn vaak erg gevoelig aan hun driedimensionale (3D) structuur. Daarom is er bij de synthese van nanomaterialen, gericht op specifieke toepassingen, dringend behoefte aan snelle en nauwkeurige 3D karakteriseringsmethoden. Een onmisbaar instrument om nanomaterialen te onderzoeken is de transmissie-elektronenmicroscoop (TEM). Hoewel een geavanceerde TEM tegenwoordig een resolutie kan bereiken in de orde van 50 pm, resulteert het echter slechts in tweedimensionale (2D) projectiebeelden van 3D objecten. Daarom werd “elektronentomografie” ontwikkeld als een techniek om de 3D structuur van nanomaterialen te visualiseren. De aanpak is gebaseerd op de combinatie van meerdere 2D TEM projectiebeelden die verkregen werden langs verschillende tilthoeken. Deze projectiebeelden worden uitgelijnd ten op zichte van mekaar en gebruikt als invoer voor een wiskundig reconstructie algoritme waarmee men de 3D structuur van het oorspronkelijke object kan verkrijgen.

Ondanks de zeer nauwkeurige en lokale informatie die elektronentomografie oplevert over de 3D structuur van nanodeeltjes, is het verre van eenvoudig om 3D informatie te verkrijgen die beschouwd kan worden als een gemiddeld of statistisch relevant resultaat. Dit is een groot nadeel bij het koppelen van de eigenschappen van de nanodeeltjes aan hun 3D structuur, wat net cruciaal is om een algemeen inzicht te krijgen omtrent hun structuur-activiteit relaties. Dergelijke studies kunnen momenteel niet worden uitgevoerd op een eenvoudige wijze omdat zowel de opname van de tiltserie als de 3D reconstructie zeer tijdrovend is. Onder ideale omstandigheden is minstens 1 uur nodig om alle TEM projectiebeelden op te nemen. De hieropvolgende uitlijning en 3D reconstructie verhogen de totale verwerkingstijd verder tot minimaal 2 uur. Dit is een drastisch nadeel van elektrontomografie in vergelijking met conventionele 2D beeldvorming door TEM.

Een van de gote uitdagingen op het gebied van elektrontomografie is daarom net het vergroten van de doorvoer van het 3D onderzoek van nanodeeltjes. Tegelijkertijd moet de kwaliteit van de reconstructies voldoende betrouwbaar blijven zodat er kwantitatieve resultaten kunnen verkregen worden. Bovendien zijn 3D onderzoeken naar stralingsgevoelige materialen tegenwoordig enorm uitdagend, aangezien de nanomaterialen kunnen degraderen of vervormen wanneer er lange opnametijden gehanteerd worden. Als we tot slot de uitlijning en reconstructie in real time kunnen uitvoeren, wordt de directe observatie van dynamische veranderingen van nanomaterialen gedurende in-situ experimenten mogelijk. Hiermee kunnen we bijvoorbeeld mechanismen voor thermische instabiliteit van nanodeeltjes onderzoeken.

In deze thesis zal ik nieuwe technieken ontwikkelen, gericht op het verminderen van de duur van elektrontomografie experimenten, en zo een hoge doorvoer en real-time karakterisering van nanostructuren mogelijk te maken. Dergelijke elektronentomografie experimenten met hoge doorvoer zullen statistisch relevante 3D informatie opleveren over de belangrijke eigenschappen van nanomaterialen. Door nieuwe methodes voor de opname te ontwikkelen die ons in staat stellen om binnen enkele minuten een tomografische tiltserie op te nemen, zal een overvloed aan nieuwe onderzoeken mogelijk worden, waaronder real-time in-situ tomografie, waar morfologische veranderingen van nanosystemen kunnen worden onderzocht als een functie van b.v. temperatuur. Bovendien zullen dergelijke snelle opname methodes de elektronendosis en/of de stroom verlagen, waardoor de potentiële schadelijke invloed van de elektronenbundel wordt verlaagd. Ten slotte, zullen de uitlijnings- en reconstructieprocessen geoptimaliseerd worden om zo real-time 3D elektronenmicroscopie mogelijk te maken. Dit zal de efficiëntie van 3D onderzoeken drastisch verbeteren en staat de gebruiker toe het tomografische experiment dynamisch aan te sturen, terwijl het nog in uitvoering is.

Dit proefschrift is onderverdeeld in drie delen, een inleiding over de gebruikte technieken, een deel over snelle en dosisefficiënte opname methoden en ten slotte een deel over een efficiëntere reconstructiestrategie. Het proefschrift is in meer detail opgebouwd als volgt:

Deel I: Inleiding

Dit deel presenteert een literatuuroverzicht dat begint met een korte introductie over de nanowetenschap. Daarnaast worden de concepten elektronenmicroscopie en tomografie geïntroduceerd. Het laatste hoofdstuk van dit deel behandelt origineel werk dat de mogelijkheden van hedendaagse elektrontomografie presenteert.

Hoofdstuk 1: Historisch perspectief.

Dit hoofdstuk introduceert het concept van nanowetenschap en presenteert de historische achtergrond die geleid heeft tot de ontwikkeling van elektronenmicroscopie en tomografie.

Hoofdstuk 2: Elektrontomografie: de fundamenten.

Dit hoofdstuk vat de theoretische grondslagen van elektrontomografie samen. Verder introduceert het verschillende vaak gebruikte reconstructie algoritmen en hun achtergrond.

Hoofdstuk 3: Elektrontomografie in de praktijk.

Dit hoofdstuk presenteert de elektronenmicroscoop en beschrijft belangrijke aspecten met betrekking tot beeldvormingsmodaliteiten. Daarnaast worden de verschillende stappen, nodig voor het uitvoeren van een succesvol tomografisch experiment, opgesomd.

Hoofdstuk 4: Hedendaagse elektrontomografie voor materiaalwetenschappen.

Dit hoofdstuk toont twee experimentele studies waarin tomografie succesvol werd toegepast om de complexe structuur-eigenschaps relaties van verschillende nanodeeltjes te ontrafelen.

Deel II: Versnelde Acquisitie

Dit deel presenteert origineel werk waarbij verschillende opname strategieën werden ontwikkeld om de doorvoercapaciteit te versterken en/of de dosisefficiëntie van elektrontomografie experimenten te verbeteren.

Hoofdstuk 5: Experimentele evaluatie van onderbemonsteringsschema's.

Dir hoofdstuk bestudeert drie verschillende onderbemonsteringstechnieken, gefocust op een onderlinge experimentele vergelijking, die in staat zijn om de elektronendosis en/of acquisitietijd van een elektrontomografie experiment te verlagen.

Hoofdstuk 6: Versnelde HAADF-STEM voor hoge doorvoer elektronentomografie.
Dit hoofdstuk behandelt de ontwikkeling van een snelle HAADF-STEM opname methode, gericht op het onderzoeken van nanodeeltjes met een verbeterde doorvoer en statistische relevantie.

Hoofdstuk 7: Versnelde in-situ elektrontomografie van vertakte Au Nanodeeltjes.
Dit hoofdstuk presenteert een experimenteel onderzoek waarin de snelle HAADF-STEM benadering wordt gecombineerd met in-situ tomografie om de thermische stabiliteit van vertakte Au nanodeeltjes kwantitatief te onderzoeken**.**

Hoofdstuk 8: Verbetering van de nauwkeurigheid van snelle tomografie.
Dit hoofdstuk introduceert een neuraal netwerk geleerde filter en een hybride opname strategie die gehanteerd kunnen worden om de nauwkeurigheid van versnelde HAADF-STEM tomografie te verbeteren**.**

Deel III: Versnelde Reconstructie
Dit deel presenteert origineel werk dat efficieënte, real-time elektrontomografie-experimenten mogelijk maakt.

Hoofdstuk 9: Reconstructie van willekeurige snedes voor real-time tomografie.
In dit hoofdstuk wordt een nieuwe werkwijze voor elektronentomografie gepresenteerd die de efficiëntie van de 3D karakterisering van nanomaterialen door TEM sterk verbetert. Bovendien maakt het onderzoekende beeldvorming mogelijk en biedt het in real-time waardevolle 3D informatie zodat de experimentele parameters van het elektronentomografie experiment dynamisch kunnen worden aangepast.

List of Abbreviations

1D	One-Dimensional
2D	Two-Dimensional
3D	Three-Dimensional
ADF	Annular Dark Field
ART	Algebraic Reconstruction Technique
ASTRA	All Scale Tomographic Reconstruction Antwerp
BEM	Boundary Element Method
BF	Bright Field
CCD	Charged Coupled Device
CNN	Convolutional Neural Network
COM	Component Object Model
CPU	Central Processing Unit
CS	Compressive Sensing
CTAB	Cetyltrimethylammonium bromide
DART	Discrete Algebraic Reconstruction Technique
DF	Dark Field
EDXS	Energy Dispersive X-ray Spectroscopy
EM	Expectation Maximization
FBP	Filtered Back Projection
FEG	Field Emission Gun
FEM	Finite Element Modeling
FFT	Fast Fourier Transform
FIB	Focused Ion Beam
GPU	Graphics Processing Unit
HAADF	High Angle Annular Dark Field
I-US	Image-Undersampling
LFO	$LaFeO_3$
LSPR	Localized Surface Plasmon Resonances
MEMS	Microelectromechanical systems
MNPBEM	Boundary Element Method for Metallic Nanoparticles
MS-D	Mixed-Scale Dense

MSE	Mean Square Error
NIR	Near Infrared
NP	Nanoparticle
NR	Nanorod
NS	Nanostar
PXRD	powder X-ray diffraction
ReLU	Rectified Linear Unit
RMSE	Root Mean Square Error
R-US	Random-Undersampling
SEM	Scanning Electron Microscopy
SERS	Surface Enhanced Raman spectroscopy
SIRT	Simultaneous Iterative Reconstruction Technique
SSR	Sparse Sphere Reconstruction
STEM	Scanning Transmission Electron Microscopy
S-US	Structured-Undersampling
TEM	Transmission Electron Microscopy
T-US	Tilt-Undersampling
TV	Total Variation
TVM	Total Variation Minimization
UV	Ultraviolet
UV-vis	Ultraviolet-visible
VR-US	Virtual Random-Undersampling

PART I: INTRODUCTION

1. Historical Perspective

In the first chapter of this thesis, we sketch the historical perspective of the advent of nanoscience and the importance Transmission Electron Microscopy has played.

1.1 Nanoscience

One of the defining points in the history of nanoscience is the famous Feynman lecture, entitled "There is plenty of room at the bottom".(Richard P. Feynman, 1960) Feynman considered the potential of directly manipulating individual atoms as a powerful form of synthetic chemistry. Even more so, he concluded his lecture by challenging scientists to work at this small scale, a challenge that has been taken up within the field of "nanoscience". Nanoscience is the study of structures and materials for which at least one of their dimensions' ranges from 1 to approximately 100 nm. Nanoscience seeks to exploit the peculiar properties of nanomaterials which differ vastly from those of their bulk counterparts. Since the size of materials is scaled down, their surface-to-volume ratio drastically increases. The contribution of surface atoms therefore grows and surfaces start to dominate and control the properties of the nanomaterials. This leads to unique physical and chemical properties which differ greatly from those of the bulk materials, making them highly interesting for various applications.

While nanoscience is often perceived as something new, nanostructures have been beneficially used long before they were actively studied. A well-known example is the Lycurgus cup, a decorative Roman treasure from the 4th century. Surprisingly, when lit from outside, the cup looks green but when lit from inside, the cup appears red (**Figure 1.1**). This color change is attributed to dichroic light effects caused by gold-silver alloyed nanoparticles, dispersed throughout its structure. The alloyed nanoparticles have a plasmon resonance in the green-blue region of the visible spectrum. As a result, green-blue light is absorbed and diffused, whereas red light is transmitted.(Colomban, 2009; Freestone et al., 2008)

Figure 1.1*: The Lycurgus Cup in (a) reflected and (b) transmitted light. © The Trustees of the British Museum*

Not all progress in nanoscience or nanotechnology are the result of human activity. Indeed, evolution has had approximately a 3-billion-year head start when it comes to manipulating materials at the smallest scale. Geckos, for instance, have the ability to cling unto and detach from a variety of surfaces without any apparent effort. This ability follows from the presence of adhesive toe pads on their feet, which are composed of hierarchically structured hair-like adhesive surfaces or "setae". The setae, in turn, branch out in nanometer sized tips, or so-called "spatula" (**Figure 1.2**). The adhesive ability of the gecko arises, amongst others, from the van der Waals attraction force between their feet and the surface they climb. Although the van der Waals force is negligible at microscale, it is significant at the nanoscale. The millions of spatula on the gecko feet, produce a large cumulative adhesion force. Other factors potentially contributing to this strong adhesion force include contact electrification and capillary forces.(Niewiarowski et al., 2016) This extraordinary adhesive ability has inspired researchers to imitate the nanostructure of gecko toe pads in the design of climbing robots and improved tire grip.(S. Kim et al., 2008)

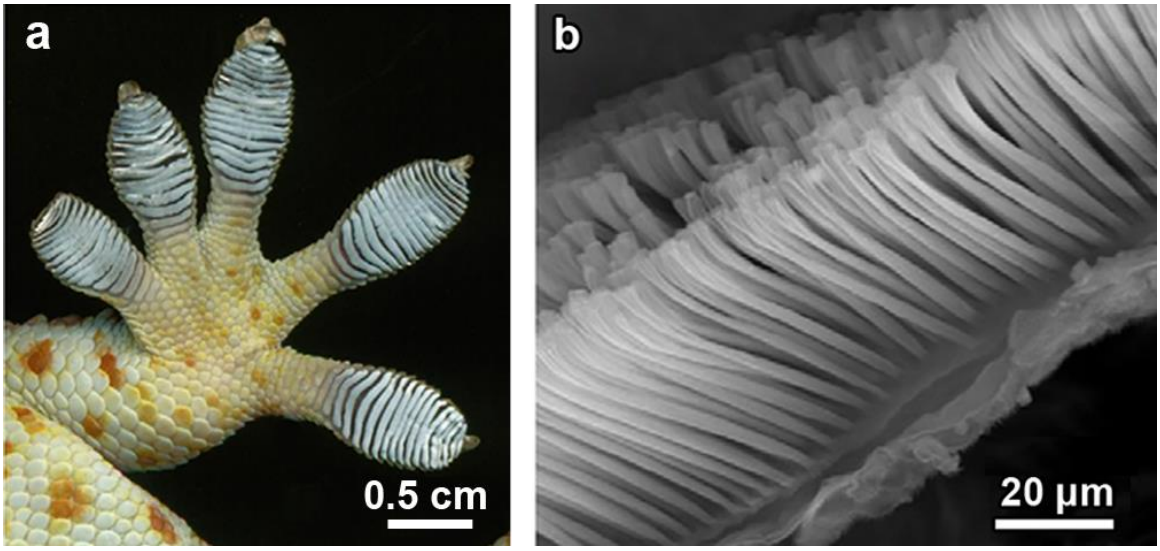

***Figure 1.2**: An overview of the hierarchical nature of the gecko adhesive system. (a) Lamellae on the gecko toe pads. (b) Branched setae on the gecko toe pads. (Image adapted from ref.(Niewiarowski et al., 2016))*

The unique properties occurring at the nanoscale have led to an increased interest in nanoscience and rapid developments in various fields of applications including chemistry, materials science, energy, medicine, electronics, food, etc.(Nasrollahzadeh et al., 2019) Although often unaware, the average person encounters nanotechnology on a daily basis. Indeed, silver nanoparticles are used as anti-bacterial in food packaging or in disinfectants.(Neethirajan & Jayas, 2011) Zinc and titanium nanoparticles act as the UV-protective elements in modern sunscreen.(Popov et al., 2005; Schulz et al., 2002) Electronic devices such as smartphones, benefit from nanotechnology as well, making them faster, smaller, more portable and able to manage and store larger amounts of information.(Shulaker et al., 2013, 2017) But perhaps most relevant, each living cell (of which an average human body contains approximately 30 trillion) is a remarkable example of nanoscience.

At the core of the progress that nanotechnology has made in the past century, lies the research dedicated to understanding the connection between the structure of the nanomaterials and their physical and chemical properties. Such comprehension is crucial for guiding the synthesis of novel nanomaterials with predefined properties in a rational and reproducible manner. The specific properties of nanomaterials are indeed strongly related to their 3D shape, size and composition. Therefore, in order to understand the nanomaterials their peculiar properties, a precise structural and chemical characterization is required. Commonly used techniques to characterize nanomaterials at the nanometer scale or below,

include powder X-ray diffraction (PXRD), scanning electron microscopy (SEM) and transmission electron microscopy (TEM).

PXRD measures the diffraction pattern of crystalline materials. Each material will produce a unique “finger print” depending on the structure of its crystal lattice. However, since X-rays only interact weakly with nanomaterials, they provide an average result from diffraction, instead of local structure information. This technique is therefore only suitable for periodic systems which is not always the case for nanomaterials.

A scanning electron microscope (SEM) is a type of electron microscope for which a focused beam of electrons is scanned across the surface of the nanomaterial. Because of the strong interaction between the electrons and the nanomaterials, various signals are generated that contain local information about the surface topography and chemical composition of the sample. However, this information only relates to the surface of the nanomaterial and therefore does not provide any insight into its internal structure.

Transmission Electron Microscopy (TEM) is a microscopy technique in which a beam of electrons is transmitted through the nanomaterial. The main benefit of TEM in comparison to PXRD is that TEM is able to retrieve local structural information of single nanoparticles with a 50 picometer resolution. Since the electron beam is transmitted through the nanomaterial, this information is, in comparison to SEM, not restricted to the surface of the nanomaterial. However, TEM only yields two-dimensional (2D) projections of a three-dimensional (3D) object. Therefore, TEM has been expanded to the third dimension through the use of electron tomography.

The aim of my thesis is to develop new TEM and tomography techniques to improve the efficiency of the characterization of nanomaterials. For the remainder of **Part I,** I will extensively discuss TEM imaging and tomography. To conclude, I will present two case studies wherein electron tomography was used to characterize two different nanomaterials.

1.2 Transmission Electron Microscopy

In 1873 Ernst Abbe postulated that the achievable resolution of optical microscopes was limited by the wavelength of the probing wave.(Ernst, 1874) Given the difficulty of creating glass lenses for high frequency photons, or UV light, it was believed for a long time that it would be impossible to obtain images with sub-micrometer resolution.

After de Broglie had formulated his famous wave-particle hypothesis in 1927(De Broglie, 1925, 1929) and Hans Busch had demonstrated that a magnetic field can deflect electrons(Busch, 1926), Knoll's research group realized the potential of using electrons as probing wave in a dedicated microscope. Since the wavelength of electrons is many orders of magnitude smaller than those of photons, spatial resolutions far beyond those achievable through optical microscopes became within reach. In 1932, Ernst Ruska and Max Knoll built the first TEM prototype at the University of Berlin.(Knoll & Ruska, 1932) In the following year, Ernst Ruska improved the original model and designed a TEM capable of producing images with a resolution exceeding that of optical light microscopy. The development of the electron microscope continued at Siemens, dedicated to imaging biological samples.(Borries & Ruska, 1933) For his contribution in the development of the electron microscope, Ernst Ruska was co-awarded the Nobel Prize in Physics in 1986.

In 1938, Manfred von Ardenne built the first Scanning Transmission Electron Microscopy (STEM) in Berlin for Siemens.(von Ardenne, 1938) It was not until the 1970's that the idea of STEM was further developed by Albert Crewe at the University of Chicago. After designing the first field emission gun and adding a high quality objective lens, Crewe was able to observe heavy atoms on a thin carbon layer with STEM for the first time.(Crewe et al., 1970) A continued effort in STEM technology allowed for samples to be imaged at Ångström resolution in the 1990s. The addition of aberration correctors in STEM further improved the resolution, enabling the visualization of individual atomic columns with an unprecedented resolution.(Haider et al., 1998)

1.3 Electron Tomography

The further development of (S)TEM enabled the retrieval of information of nano-sized objects down to the atomic scale.(Bals et al., 2012, 2016; Goris, Bals, et al., 2012; Van Aert et al., 2011) However, TEM only provides 2D projection images of 3D objects, therefore missing a wealth of information. The interpretation of a 3D structure based on only 2D projections can lead to an incomplete and unreliable understanding.(Bals et al., 2014; Midgley et al., 2007; Midgley & Weyland, 2003) It is therefore evident that retrieving the missing third dimension is essential to unravel the peculiar structure-property relationship. By combining the powerful imaging capacity of a TEM with the mathematical principles of computed tomography, TEM investigations can nowadays be extended to the third dimension.

The mathematical foundation behind computed tomography dates back to 1917 when the Austrian mathematician Radon described the "Radon transform".(Radon, 1917) He illustrated the potential of reconstructing an object from an infinite amount of projection images. Twenty years later, the Polish mathematician Kaczmarz developed a methodology to retrieve an approximate solution to a large system of linear algebraic equations, resulting in iterative tomography.(Kaczmarz, 1937a, 1993) In the late 1950's, Cormack established the theoretical base for a X-ray tomography scanner for 3D medical imaging.(Cormack, 1963) This work generated little interest until Hounsfield and colleagues adapted this idea and built the first CT scanner in 1971.(Hounsfield, 1973) For their independent efforts, Cormack and Hounsfield received the Nobel prize for Physiology in 1979.

It was only in 1968 that tomography was first combined with electron microscopy. Rosier and Klung determined the 3D structure of a symmetrical organic macromolecule, based on a single projection image.(De Rosier & Klug, 1968) Simultaneously, Hoppe demonstrated the ability to retrieve the 3D structure of an asymmetric system, given a sufficient number of projection images. Furthermore, he introduced the idea of acquiring a tilt series along a common tilt axis.(Hoppe et al., 1968) Independently, Hart demonstrated that by increasing the number of projection images, the quality of a tomographic reconstruction could be improved.(Hart, 1968)

In the past few decades, electron tomography has benefited from enormous technological developments in both instrumentation, computational power as well as novel reconstruction algorithms. The onset of electron tomography in materials sciences occurred at the start of the millennium when Koster et al. retrieved the 3D structure of a porous zeolite using bright field tomography(Koster et al., 2000) whereas Weyland and Midgley developed Z-contrast tomography.(Midgley & Weyland, 2003) In **Chapter 2,** the mathematical principles of tomography will be extensively covered.

PART I: INTRODUCTION

2. Electron Tomography: The Principles

In the second chapter we cover the mathematical principles of computed tomography and will introduce various reconstruction algorithms.

2.1 Tomography

The word tomography is derived from the Ancient Greek *tomos* and *graphō*, respectively meaning “slice” or “section” and “to write” or "to describe". Tomography refers to retrieving both the internal as well as external structure of an object, through the use of a specific type of penetrating wave. Nowadays, tomography is used in various branches of science, including materials science, biology, radiology, astrophysics and archeology, to name a few. The reason for its widespread popularity is that tomography is in principle a non-destructive technique. Hence, the method allows for investigation of the interior of specimens such as living objects, historic requisites or nanoparticles, without the necessity of physically cutting them open. In many cases, a source emits a probing wave (e.g. as electrons, X-rays or β-particles) which travels through the specimen and interacts with its interior. Afterwards, the propagated wave is collected by a dedicated detector. Since the propagating wave projects its interaction with a 3D object onto a 2D detector, the detected signals are typically referred to as “projections”. These projections thus contain 3D information and can therefore be used to retrieve the 3D morphology of the specimen through tomographic reconstruction algorithms.

2.2 Analytic Reconstruction Techniques

The mathematical framework of tomography was introduced in 1917 by Johan Radon.(Radon, 1917) The Radon transform R, illustrated in **Figure 2.1**, is an integral transformation over straight lines which confirms to taking a *n-1* dimensional projection of a *n* dimensional object. Consider an unknown 2D object, represented by the function f. The Radon transform $R(f)$ is then defined as:

$$R(f) = \int f ds \qquad [2.1]$$

with ds the unit vector along the projection direction. The set of projections is typically referred to as a sinogram or a tilt series.

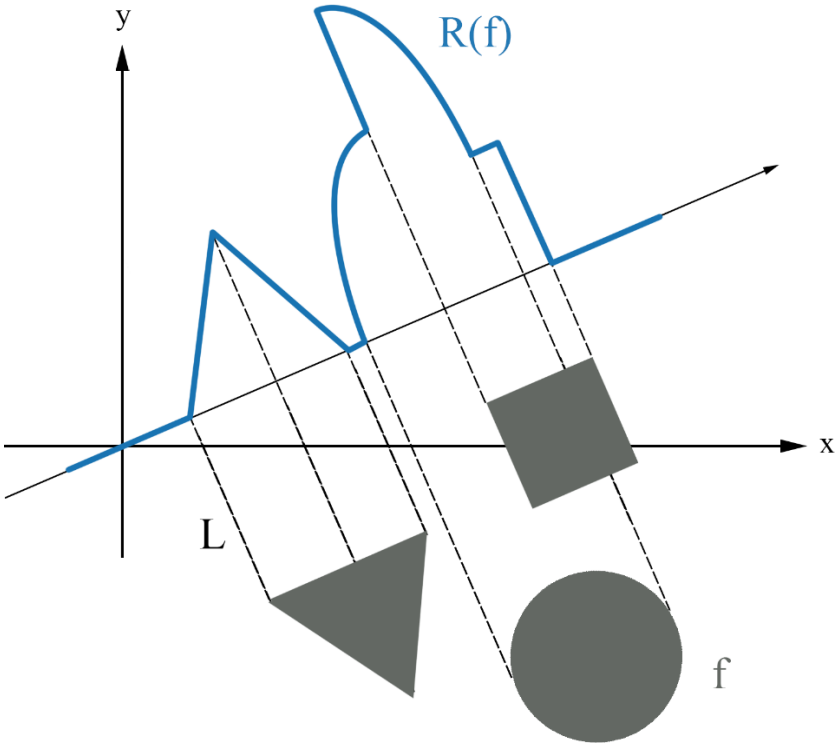

***Figure 2.1**: Illustration of the Radon transform $R(f)$ of a 2D function f along the straight lines L.*

In **Figure 2.2a-b** we respectively show the 2D Shepp-Logan phantom, and the sinogram obtained after the Radon transform. The sinogram has been built up by linking successive projection images. Hence, each column in the sinogram corresponds to a single one-dimensional (1D) projection of the 2D object.The most common analytical formula to recover an object from its projections is the inverse Radon transform, better known as the Filtered Back Projection (FBP). In **Figure 2.2c** the reconstruction obtained of the sinogram, with 0.5° tilt interval, using FBP is displayed. However, FBP is an integral transform and therefore requires ideally an infinite amount of noise-free projection images. For many practical applications it is either impossible or undesirable to acquire a large amount of "perfect" projection images. As a result, FBP only provides an approximation of the original object. In **Figure 2.2d** the FPB reconstruction of the sinogram with a 5° tilt interval is shown. Many so-called "streaking artefacts" are present, lowering the reconstruction accuracy. In addition, almost all information concerning the interfaces of the reconstructed object is lost.

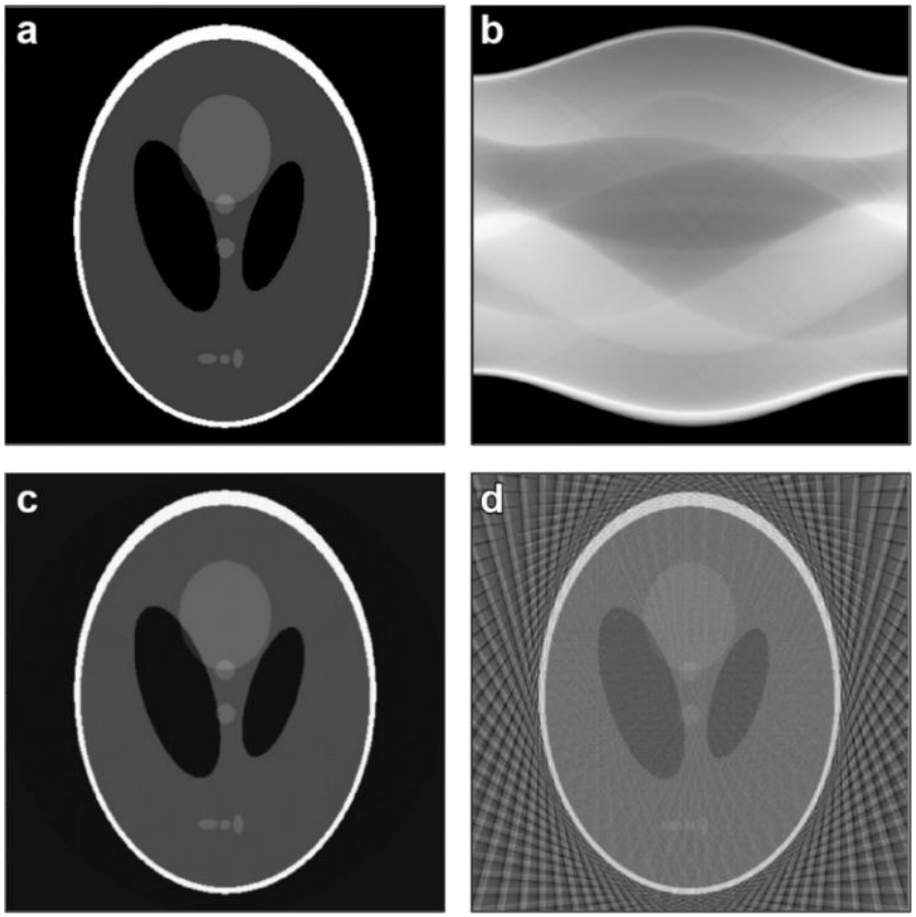

***Figure 2.2**: (a) Shepp-Logan phantom. (b) sinogram of (a) composed out of projections obtained from 0° to 180° with an 0.5° tilt interval. (c) inverse Radon transform of the sinogram displayed in (b). (d) inverse Radon transform of a subsampled sinogram with an angular range of 0° to 180° and a 5° tilt interval.*

2.2.1 Fourier Slice Theorem

By considering the reconstruction problem from an alternative representation in Fourier space, it is possible to understand the origin of these artefacts. According to the Fourier Slice Theorem, the Fourier transform of a projection is equivalent to a central slice, perpendicular to the projection direction, through the Fourier transform of the object (**Figure 2.3a-b**). In the case of a 2D object $f(x, y)$, it is straightforward to demonstrate this theorem. Without any loss of generality, the projection direction can be taken along the y-axis. The projection along the y-axis of the 2D function $f(x, y)$ is defined as:

$$p(x) = \int_{-\infty}^{\infty} f(x, y) dy. \qquad [2.2]$$

Its Fourier transform is therefore equal to:

$$F\big(p(x)\big) = p(u) = \int_{-\infty}^{\infty} p(x)e^{-2\pi i(xu)}dx$$
$$= \int_{-\infty}^{\infty}\int_{-\infty}^{\infty} f(x,y)e^{-2\pi i(xu)}dxdy. \qquad [2.3]$$

On the other hand, the Fourier transform of $f(x,y)$ is equivalent to:

$$F\big(f(x,y)\big) = f(u,v) = \int_{-\infty}^{\infty}\int_{-\infty}^{\infty} f(x,y)e^{-2\pi i(xu+yv)}dxdy. \qquad [2.4]$$

Hence, the central slice through the Fourier transform of the object, orthogonal to the projection direction (v = 0) equals to the Fourier transform of the measured projection image:

$$f(u,0) = \int_{-\infty}^{\infty}\int_{-\infty}^{\infty} f(x,y)e^{-2\pi i(xu)}dxdy. \qquad [2.5]$$

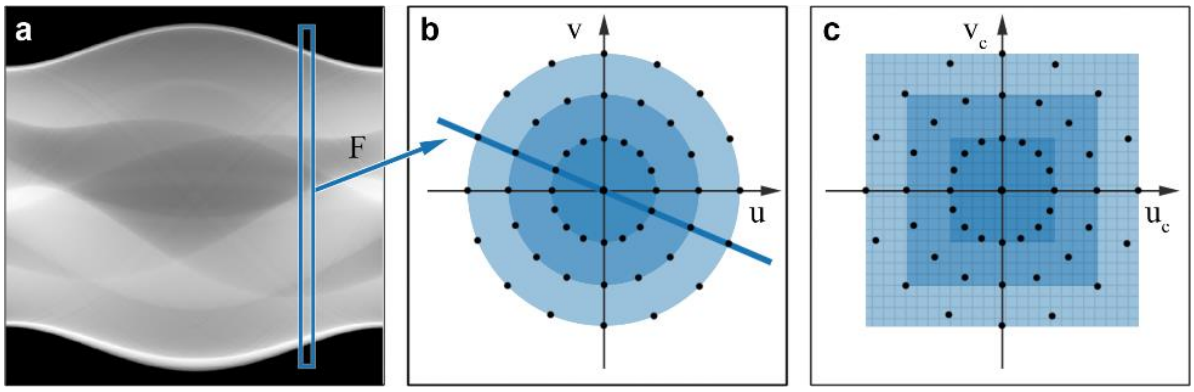

***Figure 2.3**: (a-b) Illustration of the Fourier slice theorem which states that Fourier transform of a projection at a certain angle of an object, corresponds to a central slice through the Fourier transform of that object. The polar sampling causes low frequencies to be oversampled, which is evident from the more closely packed dots near the center of the Fourier domain. (c) Illustration of the polar sampled dots on a Cartesian grid.*

While proven for a specific projection line, there is no loss of generality since the theorem also holds for rotated and shifted projection lines. The Fourier transform is namely rotation invariant and a translation only imposes an additional phase. By acquiring projections along different tilt angles, the Fourier representation of the unknown object can be sampled. However, the finite amount of projection images, lowers the number of sampled features, especially at the higher frequencies (**Figure 2.3b**). Such undersampling is difficult

to avoid experimentally for electron tomography experiments and introduces blurring into the reconstruction.

The inverse Radon transform or FBP corresponds to filtering the obtained projections with a so-called Ramp filter (**Figure 2.4, blue**), prior to projecting them back along their original direction. By convolving the reconstruction with a filter with a Fourier representation that has zero weight at the center and increases linearly increases towards the edge, the overestimation of the low frequencies is partly compensated and blurring is reduced. More advanced methods multiply the Ramp filter, for instance, with a Hamming- or Hann filter, such that the end result does not linearly increase until the edge, but tails off at high frequencies (**Figure 2.4, green and red)**. In this manner, they simultaneously compensate the overestimation of low frequencies and for the contribution of noise which stems from high frequencies. Selecting the most appropriate filter therefore depends on the trade-off between the signal-to-noise ratio and the desired spatial resolution.

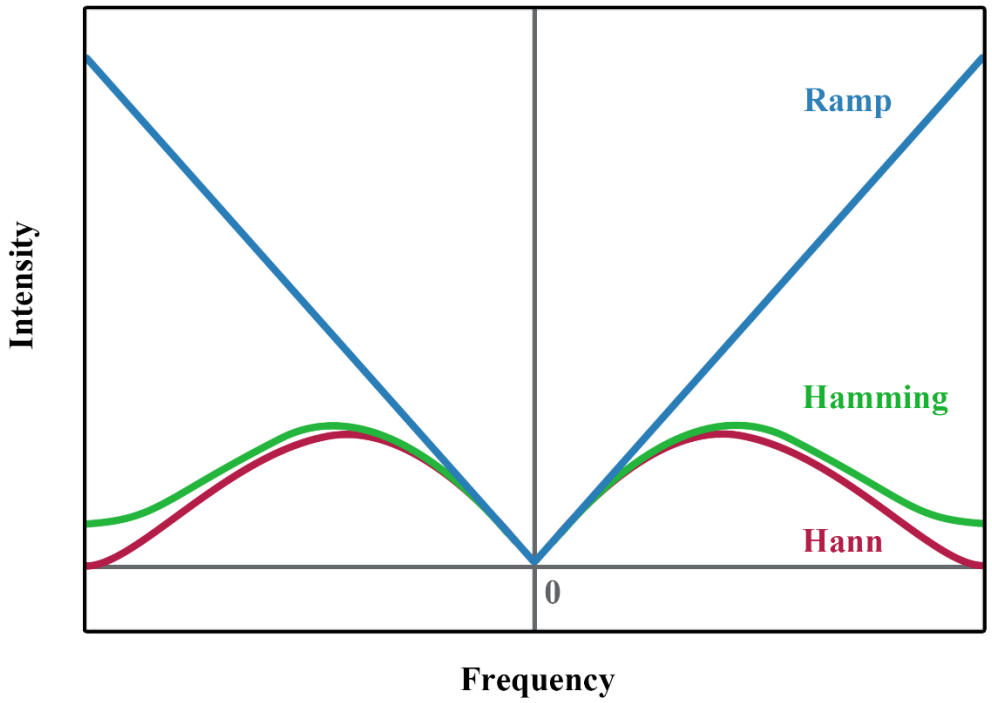

***Figure 2.4**: Frequency representation of the Ramp filter and the product between a Ramp and Hamming-, or Hann filter.*

Another way of retrieving the original object from its projections is based on the Fourier Slice theorem. Since each projection samples part of the object its Fourier space, the unknown object can be retrieved from the inverse Fourier transform of the sampled subspace.(Bracewell, 1956) However the sampling geometry complicates such

reconstruction methodologies (**Figure 2.3b-c**). Each projection correlates to a central line through the Fourier transform of the object. Therefore, all points in Fourier space are sampled on a polar grid. In order to obtain the reconstruction in a Cartesian basis and facilitate futher quantification, it is necessary to interpolate the radial points to points on a Cartesian grid. Unfortunately, artefacts might arise from such interpolation.(Smith et al., 1973) Various techniques have been proposed to improve the reconstruction obtained from the inverse Fourier transform. Although they often improve the image accuracy, they remain computationally very demanding.(Marone & Stampanoni, 2012; Y. Yang et al., 2017)

2.3 Algebraic Reconstruction Methods

In order to produce more accurate reconstructions in a computationally more efficient manner, algebraic reconstruction methods were developed. The main advantage of algebraic methods is their inherent ability of introducing prior information about the object or data acquisition during the reconstruction. Introducing such knowledge can lead to improved reconstructions and is non-trivial to do so for analytical methods.

The principle behind algebraic reconstruction techniques is rather straightforward. In general, they rely on two types of operations: a forward and back projection. An algebraic reconstruction method typically starts by retrieving an initial reconstruction by back projecting the experimental projection images, similar to FBP. Next, projection images that correspond to the initial reconstruction are simulated through forward projection. Ideally, the simulated projection images should be in perfect agreement with the acquired ones. However, the presence of noise, a limited amount of projections and other experimental restrictions will lead to discrepancies between both. This difference, often referred to as the "projection distance", can therefore be used to improve the initial reconstruction by iteratively repeating the described process until the projection distance is minimal and convergence is reached.(Heidari Mezerji et al., 2011) From a mathematical point of view, algebraic reconstruction methods can be seen as a discretization of the reconstruction problem into a set of linear equations:

$$Wx = p. \qquad [2.6]$$

All projection images are combined in a 1D array p and contain the measured projection intensities. The unknown object is represented as a 1D array x and each element w_{ij} of the matrix W represents the contribution of voxel i to the projection ray j. This contribution is

often defined as the normalized cross section between the ray and the unknown voxel as illustrated in **Figure 2.5**.

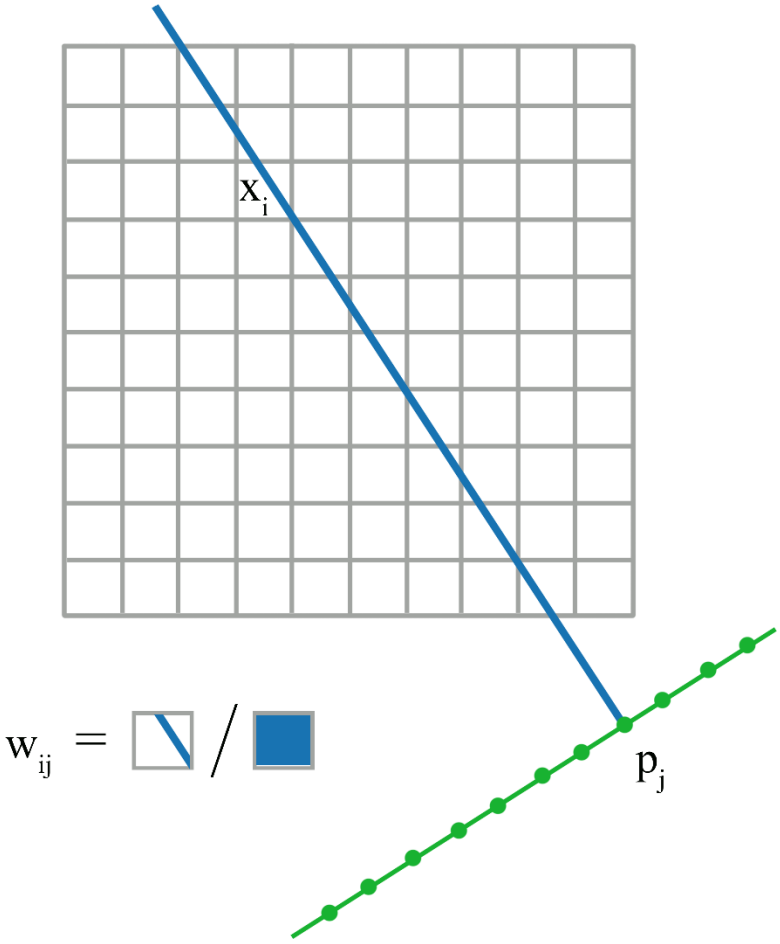

***Figure 2.5**: Scheme representing the discretization of the object to grid of unknowns and their relation to the measured projection values.*

The easiest way to solve this set of linear equations, would be multiplying **Equation 2.6** with the inverse of the projection matrix W. However, during a typical electron tomography experiment, only 51 projection images are acquired, evenly distributed between -75° and 75°. Consider that each projection image contributes 1024 x 1024 knowns to the set of linear equations, depending on the size of the projection image. In this case the unknown object consists out of 1024 x 1024 x 1024 unknowns, which is approximately 20 times larger than the amount of knowns. Since the number of unknowns far exceeds the number of knowns, the linear set of equations is underdetermined. Noise and artefacts further impede the reconstruction problem, resulting in an ill-posed inverse problem. Hence, instead of trying to find a direct inverse of the weighting matrix W, the reconstruction is computed by minimizing the norm of the projection distance $\|Wx - p\|$ in an iterative manner.

In 1970, Gordon, Bender and Herman proposed the use of the Kaczmarz method to minimize the projection distance and renamed the methodology to the Algebraic Reconstruction Technique (ART).(Gordon et al., 1970; Kaczmarz, 1937b) One year later, Gilbert suggested a modified approach which is widely known as the Simultaneous Iterative Reconstruction technique (SIRT). Whereas ART sequentially updates the reconstruction, projection image per projection image, SIRT utilizes all available projections to optimize the reconstruction at once.(Gilbert, 1972) Using all projection images to update the reconstruction, drastically improves the behavior of the reconstruction algorithm in case the projection images contain noise. For SIRT, the value of element x_j in the *kth* iterations is thus calculated as:

$$x_j^k = x_j^{k-1} + \frac{\sum_i \left[\frac{w_{ij}\left(p_i - \sum_h w_{ih} x_h^{k-1}\right)}{\sum_h w_{ih}} \right]}{\sum_i w_{ij}}. \qquad [2.7]$$

SIRT remains to date one of the most used reconstruction algorithms in the field of electron tomography. Since algebraic methods are based on a model of the data and therefore do not assume perfect data, they often result in higher quality reconstructions than their analytical counterparts when presented with a limited number of projections. Furthermore, the effect of noise on the reconstruction can be minimized by including prior knowledge or regularization during the iterative method. An example of a comparison between a SIRT and FBP reconstruction is presented in **Figure 2.6**, obtained from a simulated sinogram across the entire angular range with a 3° tilt interval. It is clear that the streaking artefacts present in the FBP reconstruction (**b**) are almost entirely gone in the SIRT reconstruction (**c**). In the bottom right corner, the Mean Squared Error (MSE) to the original phantom is indicated and is found to be significantly lower for SIRT. This result confirms that whenever there is a limited amount of projection images available, algebraic techniques can result in superior reconstructions in comparison to analytic methods, at the cost of a prolonged computational time. Fortunately, the emergence of GPUs and parallel computing have made it possible to efficiently implement the necessary forward and back projections such that the computational load remains limited. One example of an open source library containing such operations and various reconstruction algorithms is the ASTRA toolbox.(Palenstijn et al., 2016; van Aarle et al., 2015) Through the use of the ASTRA toolbox, one can compute a 1024 x 1024 x 1024 reconstruction within the order of minutes.

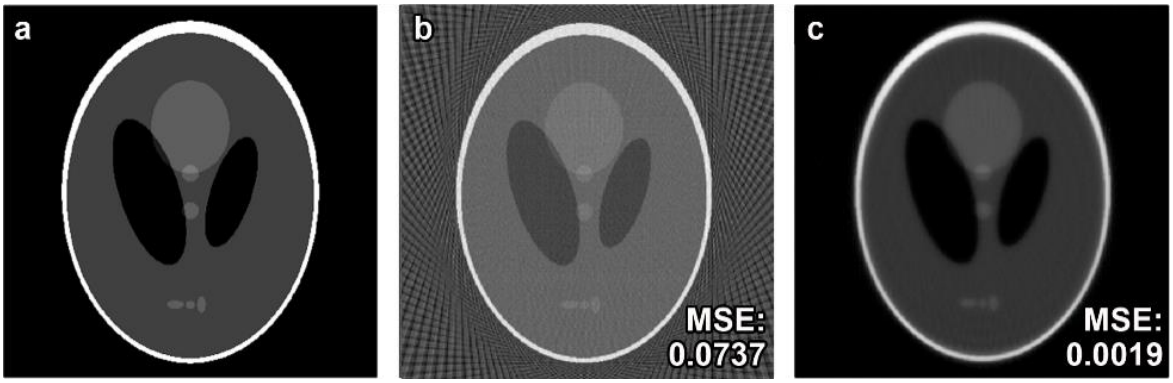

***Figure 2.6**: (a) Shepp-Logan phantom object. (b-c) FBP and SIRT reconstruction of the sinogram simulated across the entire angular range with a 3° tilt interval. The SIRT reconstruction was obtained after 100 iterations. The Mean Squared Error to the original phantom is indicated in the bottom right corner.*

2.4 Prior Knowledge

In many practical applications, physical limitations restrict the number and the quality of projection images that can be obtained. When the electrons interact with the sample during the acquisition, they can scatter (in)elastically and transfer energy.(Egerton et al., 2004) This may cause, amongst others, atomic displacement or ionization to occur within the sample, ultimately leading to specimen degradation. To prevent specimen damage, the amount of recorded projection images and the exposure time have to be restricted. This results in a limited amount of projection data, often with a relatively low signal-to-noise ratio. In addition, shadowing effects of the holder and/or grid confine the range of available tilt angles for standard electron tomography experiments. For a typical tomography holder, the specimen can only be tilted from -75° to 75°, resulting in the so-called "missing wedge", referring to a missing wedge of information in Fourier space (**Figure 2.7**). The lack of sampled frequencies within this wedge leads to blurring of the features of the object in the reconstruction, defined by those frequencies. Obviously, this decreases the quality of the reconstruction and hinders an accurate quantification.

Although practical solutions exist to this limited angle problem, they are far from generally applicable. One manner to reduce the missing wedge is by acquiring the projection images using two perpendicular tilt-axes.(Arslan et al., 2006; Mastronarde, 1997) This technique reduces the missing wedge to a missing pyramid. As a result, the artefacts in the reconstruction diminish and the quality of the reconstruction is enhanced. A drawback of this

method is that the acquisition of multiple tilt series results in a longer total exposure time, which is unwanted for radiation sensitive samples. The missing wedge can be even further reduced using on-axis tomography. This technique has the potential to completely eliminate the missing wedge, by acquiring a tilt series over the complete angular range.(Ke et al., 2010) For this technique, a dedicated needle-shaped specimen needs to be prepared using Focused Ion Beam (FIB) milling. The full on-axis tilt series results from merging two independent tilt series of ± 70° where the second series is tilted 120° along the same tilt axis, with respect to the first tilt series. Although this technique seems promising, it is often impossible to create a needle-shaped sample from the investigated material. Therefore, the number of on-axis tomography experiments remains limited up to date.

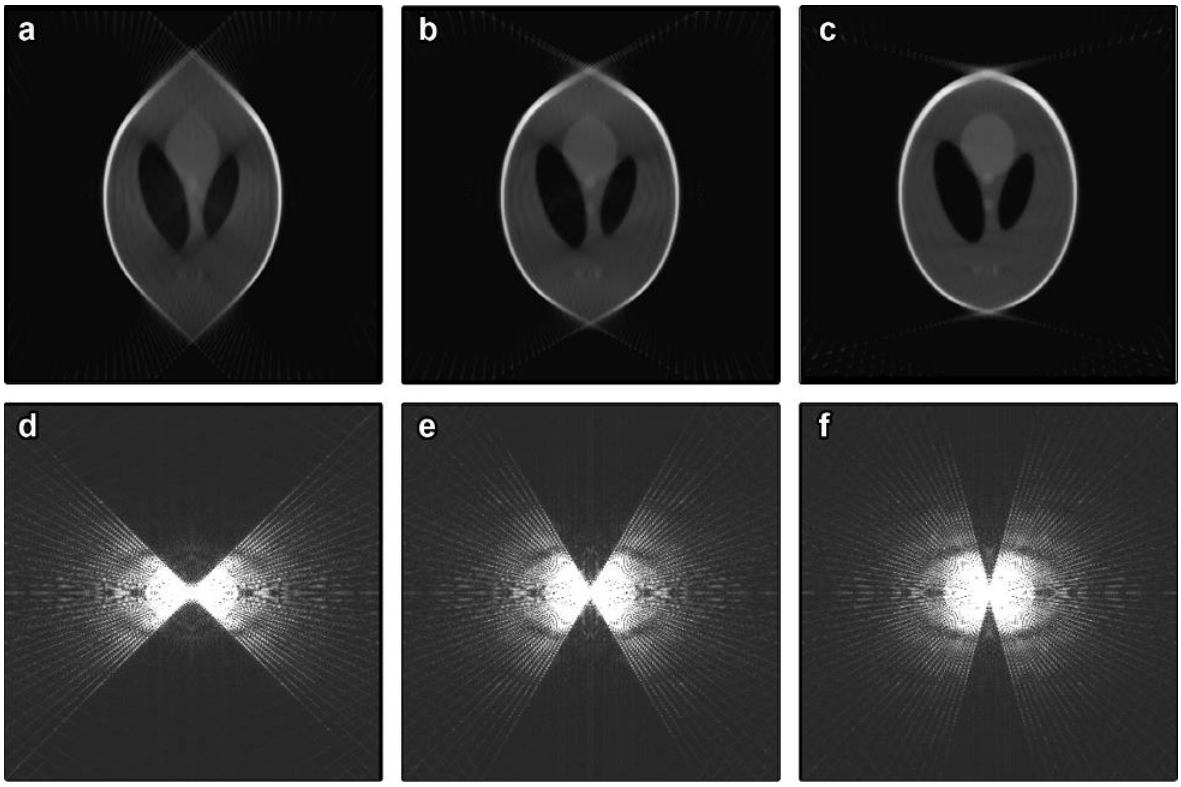

Figure 2.7*: (a-c) SIRT reconstructions of a sinogram of the Shepp-Logan phantom simulated for tilt ranges of respectively confined to -45° to 45°, -60° to 60° and -75° to 75°, all with a tilt interval equal to 3°. (d-f) Corresponding discrete Fourier transforms, displaying the extent of the missing wedge within each reconstruction. The larger this wedge, the more elongation artefacts can be observed in the reconstruction.*

A powerful approach to overcome the influence of the experimental limitations on the reconstruction quality consists out of incorporating prior knowledge within the reconstruction algorithm.The idea to include such knowledge with the aim to help solve the

inverse problem, was first proposed by Andrey Tikhonov in 1963.(Tikhonov, 1963) Although it might be impossible to find a unique solution to the set of equations described by the data discrepancy term $D(p,x)$, in this case the projection distance, he suggested to include a regularization term $R(x)$, to give preference to a certain solution. An approximate solution to the reconstruction problem can then be found as:

$$\hat{x} = \underset{x}{\operatorname{argmin}}\ D(p,x) + \mu R(x), \qquad [2.8]$$

with μ a weighting parameter that balances the relative importance between the data discrepancy term and the regularization term. In both terms, prior knowledge can now be included to facilitate the reconstruction problem. The data term can be altered with regard to the measured data (e.g. the expected noise model) while prior information about the object can be included into the regularization term.

2.4.1 Expectation Maximization

For (S)TEM imaging, data dependent Poisson noise is unavoidable. Such prior information about the noise model can be included into the data discrepancy term. If the projections p and by extension the unknown object x can be seen as random variables, then Bayes theorem (Bayes & Price, 1763; Laplace, 1812) can be applied:

$$\mathbb{P}(x|p) = \frac{\mathbb{P}(p|x)\mathbb{P}(x)}{\mathbb{P}(p)}. \qquad [2.9]$$

Here, $\mathbb{P}(x|p)$ describes the probability of x being the unknown object, given its projections p. $\mathbb{P}(p|x)$ is the a-priori probability and defines the probability of measuring the projection images p, given the object x. $\mathbb{P}(x)$ and $\mathbb{P}(p)$ describe the probability distributions for x and p respectively. An estimate to the object x can now be reconstructed by maximizing the a-posteriori probability:

$$\begin{aligned}\hat{x} &= \operatorname{argmax} \mathbb{P}(x|p) = \underset{x}{\operatorname{argmax}}\ \frac{\mathbb{P}(p|x)\mathbb{P}(x)}{\mathbb{P}(p)} \\ &= \underset{x}{\operatorname{argmax}}\ \mathbb{P}(p|x)\mathbb{P}(x). \end{aligned} \qquad [2.10]$$

Instead of maximizing the a-posteriori probability, the logarithm of the probability can be maximized instead:

$$\hat{x} = \underset{x}{\operatorname{argmax}}\big(\log\big(\mathbb{P}(x|p)\big)\big)$$

$$= \underset{x}{\operatorname{argmax}}\big(\log\big(\mathbb{P}(p|x)\big) + \log\big(\mathbb{P}(x)\big)\big). \qquad [2.11]$$

Notice the similarity to the reconstruction problem defined by **Equation 2.8**. Both a data discrepancy term $D(p,x) = -\log\big(\mathbb{P}(p|x)\big)$ as a regularization term $R(x) = -\log(\mathbb{P}(x))$ are present. Prior knowledge on the expected noise model can now efficiently be incorporated into the data discrepancy.

The basic Expectation Maximization (EM) algorithm is an iterative method than attempts to retrieve x by maximizing the log of the a-posteriori probability (**Equation 2.11**), without knowing x.(Moon, 1996) EM therefore alternates between performing an expectation (E) and a maximization (M) step. During the E-step, the expectation of the log-likelihood is evaluated for the current parameter estimate of x. In the subsequent M-step, the found expected log-likelihood is maximized by adjusting those parameters.

In **Figure 2.8** the outcome of 100 iterations of SIRT and 25 iterations of EM are compared for a tilt series simulated across the entire angular range with a 3° tilt interval. As displayed in **Figure 2.8a**, Poisson noise was added to the simulated tilt series. Again, the MSE in comparison to the original phantom is indicated in the bottom right corner. The inclusion of the noise model into the algorithm leads to an as accurate reconstruction, together with a 4 times faster convergence. Moreover, EM leads to smoother reconstructions where the influence of the noise is suppressed, facilitating further quantification.

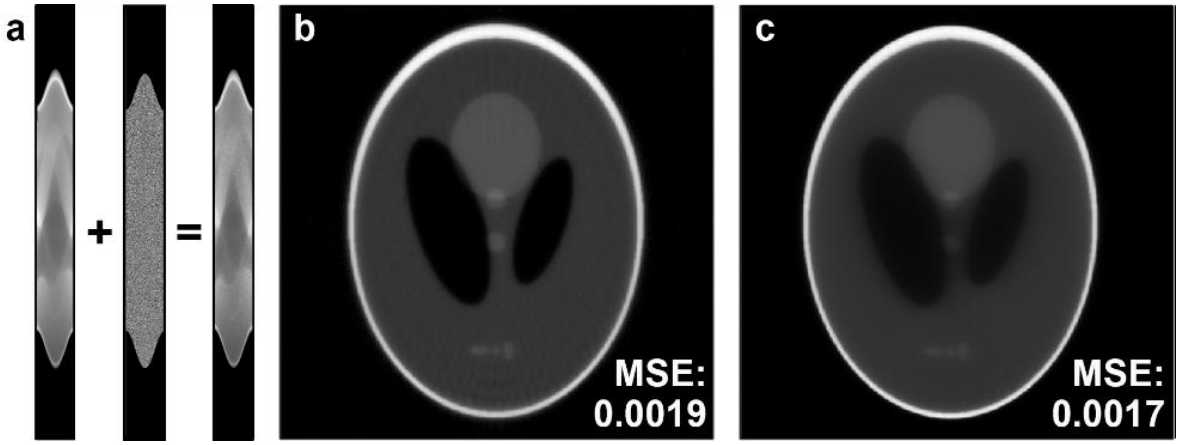

***Figure 2.8**: (a) Inclusion of data dependent Poisson noise. (b-c) SIRT and EM reconstruction utilizing respectively 100 iterations and 25 iterations. The Mean Squared Error of the reconstructions to the original phantom is indicated in the bottom right corner.*

2.4.2 Total Variation Minimization

Besides the data term, prior knowledge can be included in the regularization term as well. An often used method in the field of electron tomography which includes such regularization is the Total Variation Minimization (TVM) strategy.(Bals et al., 2014; Goris, Van den Broek, et al., 2012; Leary et al., 2013a) The idea behind TVM originates from the use of compressive sensing for signal de-noising. Donoho and co-workers were the first ones to propose the expansion of these principles to tomography and they demonstrated the possibility of obtaining high quality reconstructions of a phantom object, even with very few projection images.(Donoho, 2006; Lustig et al., 2007, 2008) TVM exploits prior knowledge concerning the sparsity of the investigated object. Although the object itself is often not sparse, its gradient image often is (**Figure 2.9a**). This sparsity assumption can be incorporated into the reconstruction problem, by introducing a regularization term equal to the norm of the discrete gradient of the object (∇x):

$$\hat{x} = \underset{x}{\operatorname{argmin}} \; \|Wx - p\|_{l_2} + \mu\|\nabla x\|_{l_1}. \qquad [2.11]$$

As a result, a solution to the ill-posed set of equations is obtained of which the total variation remains low and therefore favors sharp edges over gradual changes. TVM yields a significant reduction in reconstruction artefacts when the available projection data are limited or distorted, as illustrated in **Figure 2.9b-c**. On the other hand, the procedure is at least 20 times slower than other iterative techniques, depending on the size of the reconstructed object.

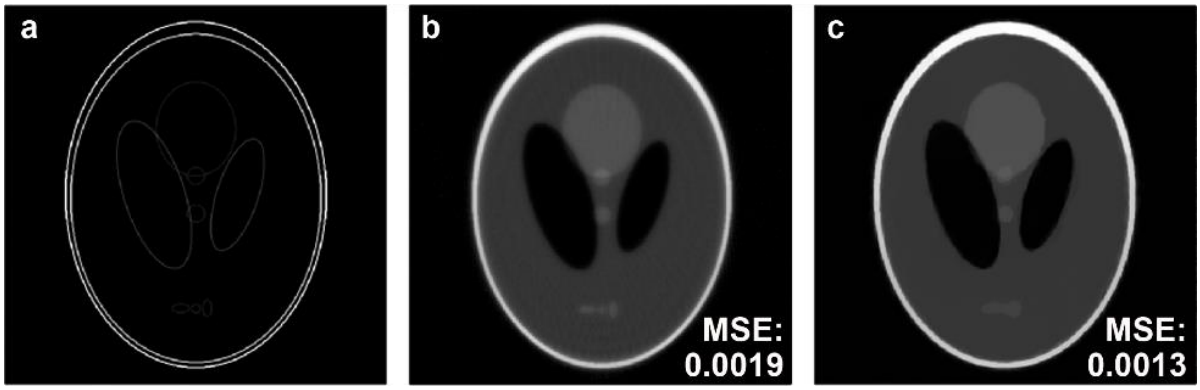

***Figure 2.9**: (a) Gradient magnitude of the Shepp-Logan phantom object. (b-c) SIRT and TVM reconstruction algorithm of the Poisson distorted sinogram, respectively utilizing 100 iterations. The Mean Squared Error to the original phantom is indicated in the bottom right corner for each reconstruction.*

2.5 Limitations and Challenges

In addition to EM and SIRT, there exists a broad range of different reconstruction algorithms, exploiting different kinds of prior knowledge. The Discrete Algebraic Reconstruction Technique (DART), for instance, uses prior knowledge on the discrete density of an object.(Batenburg et al., 2009; Batenburg & Sijbers, 2011). If the material consists out of homogeneous regions, separated by sharp interfaces, DART is able to produce accurate reconstructions for a limited amount of projection images. The Sparse Sphere Reconstruction (SSR), on the other hand, includes knowledge on the shape of the investigated nanomaterial to improve upon the reconstruction accuracy and can instantly derive quantitative information.(Zanaga, Bleichrodt, et al., 2016) Although these methods often lead to more accurate reconstructions, they drastically increase the computational cost as well. Consequently, it is not straightforward to obtain statistically relevant results and even impossible to obtain any real-time 3D information, which is a major drawback to electron tomography.

PART I: INTRODUCTION

3. Electron Tomography in Practice

In this chapter, we briefly summarize the working principles of the electron microscope and the imaging modes used in this thesis. In addition, we discuss the necessary steps of a practical electron tomography experiment.

3.1 The Electron Microscope

The image formation process in a TEM is very similar to that of an optical light microscope. The main difference is related to the use of electrons as the source of light and the associated replacement of glass lenses by electromagnetic coils. In a TEM, electrons are accelerated using high voltages and afterwards directed towards the specimen, in order to obtain images with a resolution higher than achievable in optical light microscopes.(Lipson et al., 1995) These electrons are emitted from a thermionic gun or a field emission gun (FEG). Afterwards they pass through a system of condenser lenses, to produce a beam with desired size, intensity and convergence. In TEM mode, a parallel coherent beam is formed, which illuminates the sample uniformly. In STEM mode however, the beam is focused into a fine probe, which is scanned across the specimen. An ideal lens system is expected to image a single point source as a point. Scherzer, however, demonstrated that for round symmetric electromagnetic lenses, spherical and chromatic aberrations are unavoidable.(Scherzer, 1936) Spherical aberrations cause rays, located far away from the optical axis of the spherical lens, to have a different focal point than rays with the same wavelength, close to the optical axis. Chromatic aberrations are observed when rays with distinct wavelengths, focus differently. All together, these aberrations contribute to blurring of the image.(Rose & Wan, 2005) Typically, a limiting aperture is placed behind the condenser lenses to reduce the spherical aberrations and define the beam convergence angle.

Once the desired electron beam is formed, it interacts with the specimen, which is placed in a dedicated specimen holder. This holder is located between the two pole pieces of the objective lens. The transmitted electrons are focused by the objective lens into a diffraction pattern in the back focal plane of the objective lens after which they recombine, yielding an enlarged image of the specimen in the objective lens its image plane. An objective aperture in the back focal plane can be used to select different spots of the diffraction pattern to enhance the contrast in the enlarged image. If the diffracted beam(s) is used for image formation, the imaging is referred to dark field (DF) imaging. The selection of the central, undiffracted beam results in bright field (BF) imaging. As will be discussed later, different contrast mechanisms contribute to the image formation of the different imaging modes. For both the condenser and objective lenses, stigmators are present that correct for astigmatism. Astigmatism occurs when the magnetic field in the lens is not symmetrical. Stigmators apply a correcting field to compensate for this asymmetry.

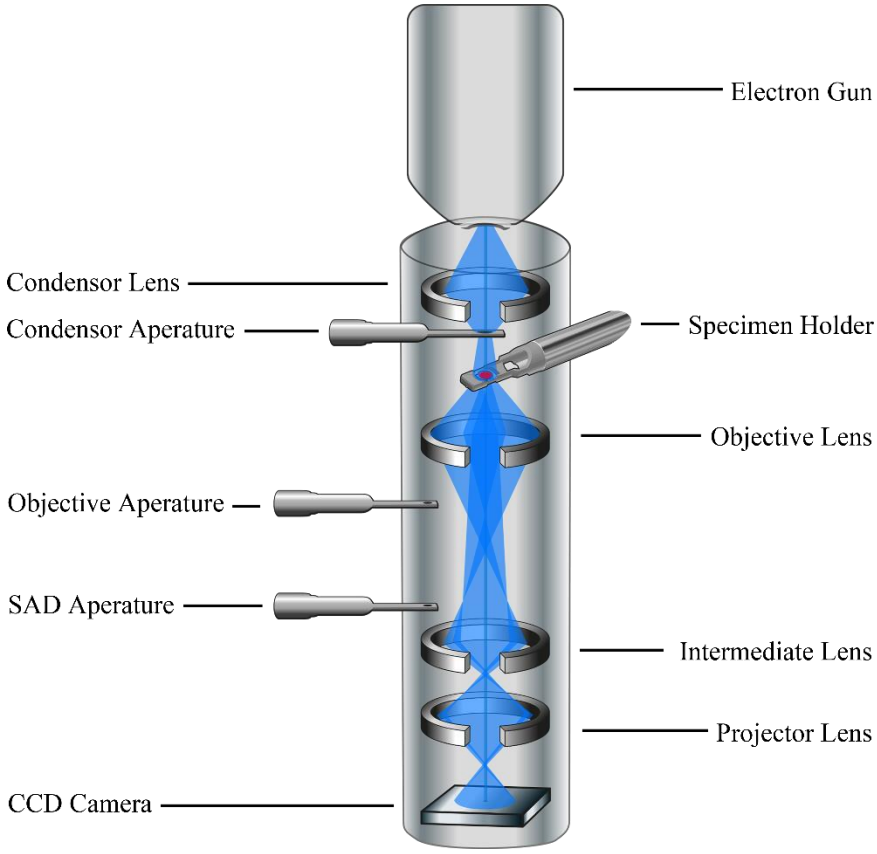

***Figure 3.1**: Illustration of the electron ray path for bright field electron microscopy.*

Below the objective lens, a system of intermediate and projector lenses creates a magnified image of either the sample in real space or the corresponding diffraction pattern in reciprocal space. This image can e.g. be visualized using a Charged Coupled Device (CCD). The complete buildup of a transmission electron microscope is presented in **Figure 3.1**. Since electrons are much lighter and smaller than air molecules, the possibility of unwanted scattering occurring in the TEM column is extremely high. Therefore, the entire TEM column is kept at high vacuum conditions (10^{-7} mbar) using a series of different vacuum pumps.

3.2 TEM Imaging

All contrast information in TEM images results from electron scattering and interaction with the illuminated sample. In order to understand all contrast formation mechanisms, it is important to keep the de Broglie's wave-particle dualism in mind. When considering electrons as particles, there is a probability that they will be influenced by the composing atoms of the specimen while they transverse through the sample. When interacting, they can scatter either elastically or inelastically, potentially yielding a wide

range of secondary signals (e.g. X-rays) that contain valuable information on the sample. When considering the wave nature of the electrons, coherent or incoherent diffraction can occur whenever the specimen has an ordered atomic structure. Coherent waves share their frequency and direction but can have a constant phase difference after specimen interaction. Incoherent diffracted waves, on the other hand, share no frequency, direction or phase relationship after interaction. Diffraction- or phase contrast arises from the interference between the coherent elastically scattered electrons and is often exploited to obtain high resolution TEM images. The incoherent elastically scattered, or Rutherford scattered, electrons give rise to amplitude contrast. Since Rutherford scattering is proportional to Z^n with Z the atomic number and $1.6 < n < 2$, the produced contrast is chemically sensitive. When the specimen has variations in mass, thickness or both, additional mass-thickness contrast arises as well, owing to the variation in amount of scattering within the specimen.

By choosing the imaging mode and detection modality or by inserting apertures, it is possible to gain control over the predominant contrast mechanism contributing to the image formation. By selectively allowing diffraction rays pass through the objective aperture in TEM mode either a BF- or DF TEM image can be formed. In scanning (S)TEM mode, an electron probe is scanned across the sample, generating a signal at each position of the beam. This signal is collected for each position using an annular detector. Depending on the convergence semi angle (θ_{conv}) and the inner and outer collection semi angles (θ_{in} and θ_{out}) of the detector, different contrast mechanisms dominate the image formation. The inner and outer collection semi angles can be changed by physically adapting the camera length of the annular detector (**Figure 3.2**).

By using a long camera length, an annular dark field (ADF) STEM image is formed by electrons which were scattered to low angles ($\theta_{in} \approx \theta_{conv}$). With the use of a short camera length, a high angle annular dark field (HAADF) STEM image is obtained by collecting the electrons scattered to higher angles ($\theta_{in} \approx 3\theta_{conv}$). For crystalline samples, it is preferential to operate in HAADF-STEM mode. In this mode, contrast contributions of diffracted beams are minimized and predominantly mass-thickness and Z contrast are present. This is particularly important for electron tomography for which the projection requirement states that the recorded intensities need to represent a sum or integral of a monotonic function of a property of the structure.(Midgley & Weyland, 2003) The various STEM imaging modes are illustrated in **Figure 3.2**.

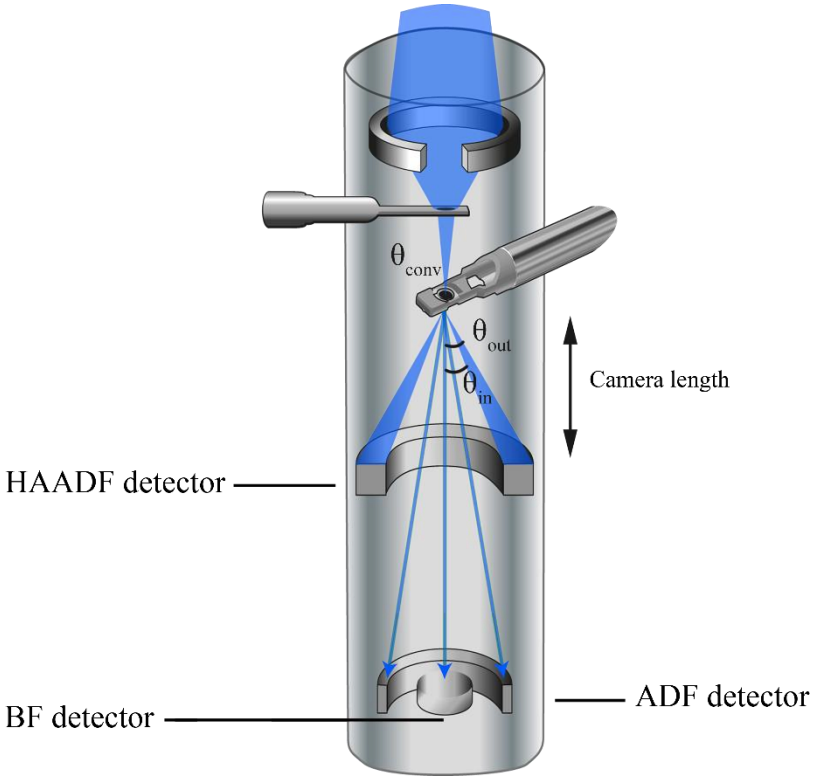

***Figure 3.2**: Schematic overview of the STEM-imaging detection set-up with the various annular detection modalities.*

3.3 Spectral Imaging

As mentioned above, the interaction between the high-energy electrons and the atoms of the investigated specimen may result in inelastic scattering whereby energy is transferred from the electrons to the sample. In order to revert back to the lower energy state, a range of secondary signals can be emitted by the specimen. When the colliding electron ejects an inner shell electron from the specimen, an outer shell electron will fill the created hole. The difference in energy between the higher and lower shell energy may be released in the form of an X-ray as illustrated in **Figure 3.3**. Since the energy of these X-rays are characteristic to the atomic structure of the emitting element, they can be used to analyze the elemental composition of the sample. In Energy Dispersive X-ray Spectroscopy (EDXS), these signals can be measured using a dedicated energy-dispersive spectrometer. In STEM-EDXS, the generated X-rays are recorded while scanning the electron probe across the specimen. This results in an elemental map of the investigated structure wherein each pixel contains a spectrum. Since the intensities of the recorded X-ray peaks scale with the sample thickness, they fulfil the projection requirement and can be used for tomography.

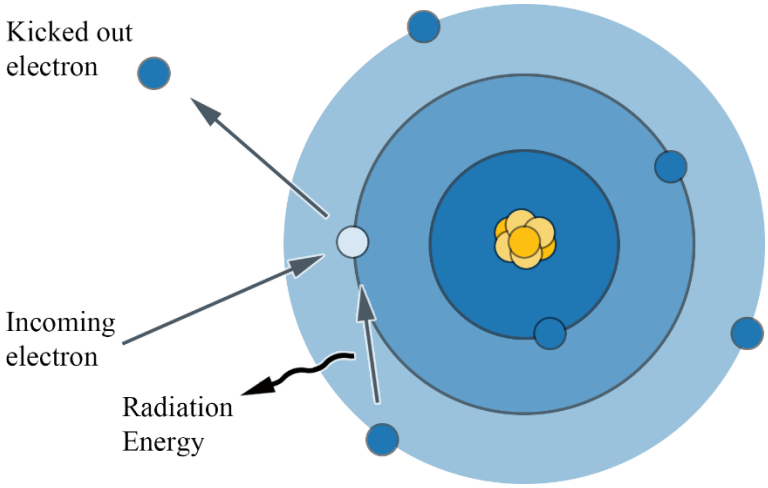

***Figure 3.3**: Principle of X-ray generation.*

3.4 Holder and Stages

Prior to the investigation, the sample is placed on a dedicated grid, conventionally made out of copper and coated with a thin layer of holey carbon. In case the sample is already dispersed in a liquid (e.g. colloidal solution of nanoparticles), it is simply drop casted on the grid. Powders have to be dissolved in a solvent (e.g. water or ethanol) prior to drop casting. Afterwards, the grid is secured onto the TEM holder and inserted into the goniometer through an air lock. The airlock ensures that the vacuum levels in the TEM remain low upon inserting the holder into the column. The TEM holder is inserted between the pole pieces of objective lens, to minimize lens aberrations and therefore maximize the spatial resolution. Since the stage design is inherent to the microscope manufacturer, the holders require a dedicated design. For Thermo Fisher Scientific TEM instruments, side entry holders are typically used (**Figure 3.4**).

TEM tomography holders have been specifically designed to achieve a maximal tilt range. In this work, a Fischione 2020 advanced tomography holder was used for all regular tomography experiments. The narrow tip and cut-out around the region of the sample, allow for a tilt interval ranging from -78° to 78°, which is a large improvement in comparison to the ± 30° tilt range of a standard Thermo Fisher Scientific CompuStage double tilt specimen holder. Despite such a dedicated holder, the tilt range remains restricted. This results from the limited space between the pole pieces of the objective lens and blockage of the electron beam by the grid and/or holder at high tilts. As a result, conventional electron tomography experiments always contain missing wedge artefacts (**Figure 2.7**).

***Figure 3.4**: Image of the Fischione 2020 advanced tomography holder, highlighting the dedicated clamping mechanism to limit shadowing. © Fischione Instruments.*

Conventional TEM is performed in high vacuum under static conditions, which does not suffice to observe the dynamic behavior of nanoparticles under more realistic conditions or when given external stimuli (i.e. heat). Therefore, in-situ TEM devices have been designed to act both as a sample carrier as well as a microscopic laboratory. In this thesis, the microelectromechanical systems (MEMS) based DENSsolutions wildfire system was used to perform temperature sensitive tomography experiments.(van Omme et al., 2018) The wildfire Nano-chip is presented in **Figure 3.5** and is inserted into a dedicated holder where it makes an Ohmic contact with four needles. A four-point measurement of the local resistance is performed during which two of these contacts induce Joule heating through the chip. The two remaining contacts determine the resistance in order to monitor the temperature. The wildfire Nano-chips are specially designed to ensure stability of the sample, homogeneity of the temperature across the chip, a short settling time and the ability to perform heating EDXS experiments at high temperatures (~1000 °C).

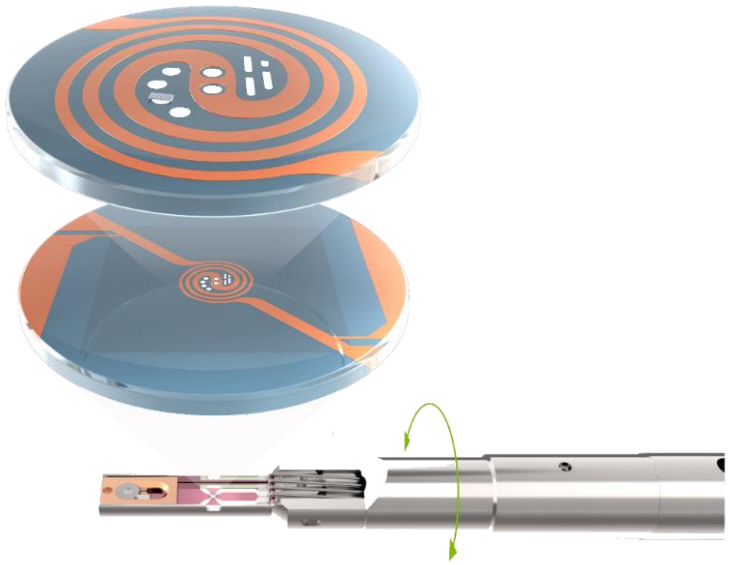

***Figure 3.5**: Illustration of MEMS based heating chip and the DENSsolutions wildfire tomography holder. © DENSsolutions.*

3.5 Electron Tomography in Practice

In order to obtain an accurate 3D reconstruction, it is essential to optimize all steps of the experiment, including acquisition, post-processing and reconstruction. This optimization therefore includes both experimental aspects (e.g. the choice of imaging mode) as well as computational factors (e.g. the used reconstruction algorithm). In the next section, I will describe the standard workflow of a HAADF-STEM tomography experiment.

3.5.1 Sample Preparation

A variety of preparation techniques exists for nanoparticle synthesis. Based on the synthesis method, they may be dispersed in liquid, in powder form or already deposited on a surface. If the nanoparticles are in powder form, the powder is often first dispersed in a liquid (e.g. water or ethanol). A drop of the dispersion is casted on a holey carbon coated TEM grid. Conventionally, grids are loaded into the tomography holder such that the mesh of the grid is rotated 45° relative to the holder axis as illustrated in **Figure 3.6**. Selecting a nanoparticle in the center of a mesh (black square, **Figure 3.6**), increases the highest achievable tilt before shadowing by the mesh borders occurs. For a successful electron tomography experiment, the degree of dilution is of paramount importance. An insufficiently diluted specimen leads to grids where particles start to overlap when tilted. On the other

hand, a sample that is overtly diluted, decreases the probability of finding a representative nanoparticle in the center of the mesh.

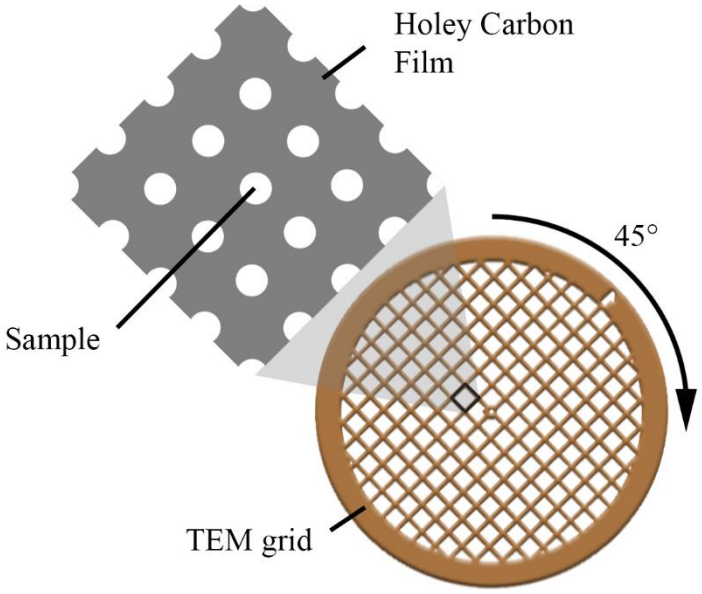

***Figure 3.6**: Depiction of the placement of the grid in the tomographic holder.*

3.5.2 Tilt Series Acquisition

After successfully drop casting the specimen onto the TEM grid and inserting it into the TEM column using a dedicated holder, several experimental parameters have to be optimally tuned to successfully acquire a tilt series. In order to ensure that the projection requirement is fulfilled, the detected intensities should be monotonically related to a property of the specimen. For STEM imaging, this is done by selecting a low camera length, thus a high inner collection semi angle ($\theta_{in} \approx 3\theta_{conv}$), to minimize the contribution of diffraction contrast. However, by increasing the inner collection semi angle, the total measured intensity simultaneously reduces and therefore a compromise has to be made. Next, the beam current has to be set by changing the beam spot size, inserting a C2 aperture or tuning the monochromator (if available). Higher currents provide an increased amount of scattering and therefore better signal, but may damage the sample during the process. Furthermore, it is important that the sensitivity and amplification of the detection system is correctly tuned through the brightness and contrast settings. This ensures that the measured intensities fall in the linear range of the detector. If not, saturation of the detector might occur, consequently violating the projection requirement. Finally, one needs to select the frame size and exposure time. A larger exposure time improves the signal-to-noise ratio, but again increases the risk

of specimen damage. Routinely, projection data in this thesis are acquired with a 1024 x 1024 frame size, 6 s frame time and a beam current corresponding to a measured screen current of 50 pA.

3.5.3 Image Alignment

During the reconstruction of the tomographic series, it is assumed that the particle does not shift over the course of the acquisition. Given an imperfect setting of the goniometer stage, relatively small shifts will occur when tilting the sample from one angle to the next. Therefore, the recorded projection images have to be registered prior to the reconstruction. A common manner to estimate the relative translation between two images is the use of correlation techniques.(Fitchard et al., 1998) The cross-correlation between two images is computed as the normalized product between the Fourier transform of one image and the complex conjugate of the Fourier transform of the second image. By locating the maximum in the cross-correlation, the relative shift between the images can be determined, as illustrated in **Figure 3.7**.

Cross-correlation is an efficient approach when both images were acquired with a small difference in tilt and are of sufficient quality. These conditions are not always valid and consequently, an inaccurate alignment might be obtained. Methods to overcome these limitations include amongst others, aligning images to the average of the prior projection images or including the alignment parameters as a part of the iterative reconstruction process.(Goris et al., 2015; Houben & Bar Sadan, 2011)

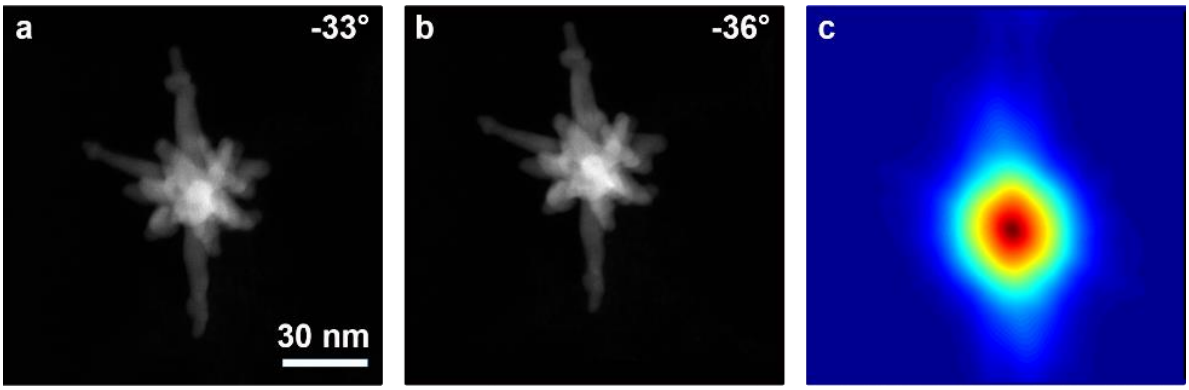

***Figure 3.7**: Cross-correlation image (c) of two successive projection images, (a) and (b), of a gold nanostar. The position of the maximum in the cross-correlation with respect to the middle (dark red) reveals the relative shift between both images.*

3.5.4 Tilt Axis Alignment

Most tomographic reconstruction algorithms rely on forward and back projections. Hence it is important that the computational tilt axis (blue line **Figure 3.8a**) is aligned to the experimental one. A possible discrepancy between both depends on the position of the particle of interest on the TEM grid. Also slight bending of the grid or holder might cause a deviation and result in a precession motion of the specimen instead of a pure tilt. Misalignment of the tilt axis will lead to streaking artefacts in the reconstruction, lowering the quality and hampering further quantification. These artefacts are illustrated in **Figure 3.8**. In **Figure 3.8a,** we display the averaged sinogram, after image alignment. The assumed tilt axis is indicated by the blue vertical line. When reconstructing a top (green, **Figure 3.8b**), central (red, **Figure 3.8c**) and bottom (yellow, **Figure 3.9d**) slice, streaking artefacts appear in the reconstruction. These artefacts can be minimized by translating and rotating the presumed, computational, tilt axis.

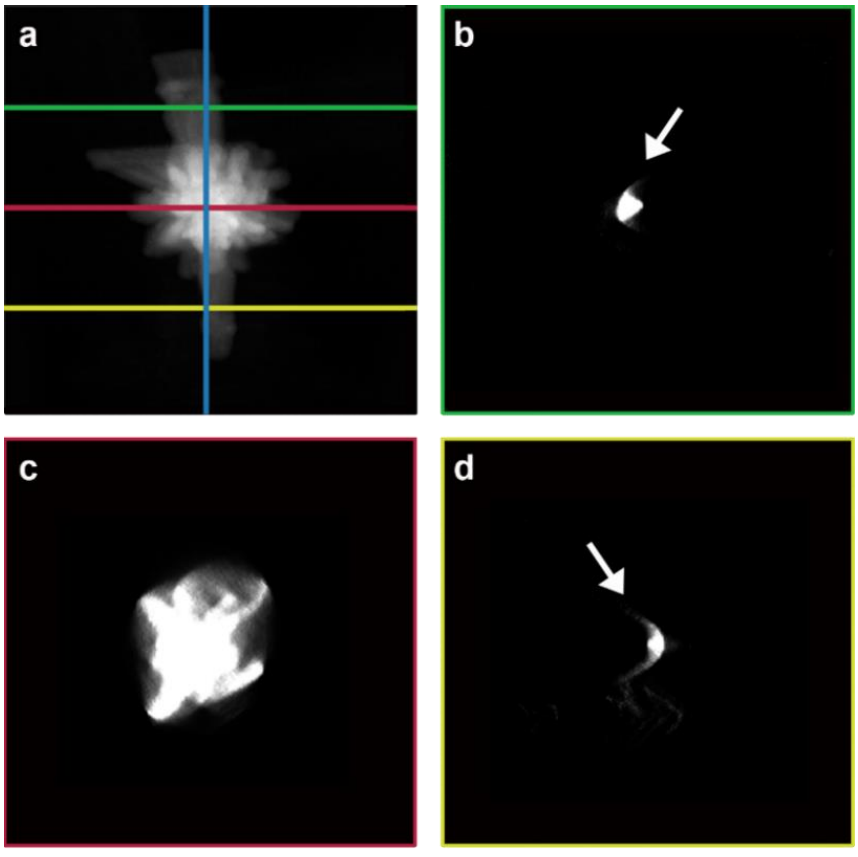

Figure 3.8*: (a) averaged sinogram after image alignment. The presumed, computational tilt axis is indicated by the blue vertical line. The location of the reconstructed slices is indicated in green, red and blue. (b-d) The respective reconstructed slices. The streaking artefacts, caused by the ill–chosen tilt axis, are indicated by the white arrows.*

3.5.5 Reconstruction

Once properly aligned, the tilt series serves as input for a reconstruction algorithm. In this thesis, the ASTRA-toolbox, a MATLAB and Python toolbox intended for tomography, was used to perform all reconstructions. The ASTRA toolbox is an open source project supported by the CWI in Amsterdam and VisionLab at the University of Antwerp, intended to develop one's own reconstruction algorithms.(Palenstijn et al., 2016; van Aarle et al., 2015) The main advantage of the ASTRA toolbox is that both the forward as well as back projection, essential to most reconstruction algorithms, are GPU-accelerated through CUDA. In this manner, reconstructions can be obtained in a fraction of the time required by their CPU supported counterparts.(Buurlage, Bisseling, et al., 2019; Palenstijn et al., 2011)

3.6 EDXS Tomography

The development of the novel "Super-X" detector geometry prompted the possibility of EDXS tomography.(Kawai et al., 2014; Schlossmacher et al., 2010) Until then, the specimen had to be tilted towards the X-ray detector in order to measure the X-rays. At other tilt angles, the holder would block the signal to the detector, therefore obscuring the elemental map. Only when using dedicated needle shaped samples, such shadowing effects could be avoided.(Lasagni et al., 2010; Lepinay et al., 2013) However, in the Super-X detection system, four X-ray detectors are symmetrically placed around the sample, effectively reducing the blocking of the detection system when tilting a regular tomographic holder.(Schlossmacher et al., 2010) Whereas the shadowing is minimized, the amount of detected X-rays for a nanoparticle is not entirely tilt angle independent. Hence without any correction, the projection requirement would still be violated.(Goris et al., 2014; Slater et al., 2014, 2016; Zanaga, Altantzis, Polavarapu, et al., 2016) Various methodologies exist to overcome this shadowing effect, including: selectively turning on and off different detectors of the Super-X system as function of the tilt angle, varying the acquisition duration at each tilt angle or normalizing the total signal for every map.(Burdet et al., 2016; Goris et al., 2014; Haberfehlner et al., 2014; Slater et al., 2014, 2016) Turning off any of the detectors during the acquisition is disadvantageous since the yield of X-rays is inherently low as is. Similarly, normalization will blow up the noise in certain projection images, hampering the 3D reconstruction. Varying the time of each projection image results in longer specimen exposure, thus an increased probability for beam damage to occur. In addition, a careful calibration of the amount of detected X-rays per tilt angle is necessary prior to the

acquisition. Recently Zanaga et al. proposed a synergetic approach in which the information of the HAADF-STEM projection images and quantified EDXS maps was combined to create chemically quantified projection images.(Zanaga, Altantzis, Polavarapu, et al., 2016) The proposed method effectively reduces the effect of the blockage of the X-ray signal, ensuring the that the projection requirement remains fulfilled. Such projection images can subsequently be aligned and used as an input for the 3D reconstruction. In the remainder of this work we will use this approach whenever EDXS-tomography is applied.

PART I: INTRODUCTION

4. State-of-the-Art Electron Tomography for Material Sciences

In this chapter, we discuss two different studies for which electron tomography was essential to unravel the nanoparticles their unique behaviour. First we will investigate the 3D structure of perovskite nanofibers using HAADF-STEM tomography in order to understand their increased detection sensitivity. In a second case study we will perform a compositional investigation using both EDXS and HAADF-STEM tomography to gain insight in the often used Turkevich synthesis method for obtaining Au-Ag alloy nanoparticles.

This chapter is based on:

Queraltó, A., Graf, D., Frohnhoven, R., Fischer, T., Vanrompay, H., Bals, S., Bartasyte, A., & Mathur, S. (2019). LaFeO3 Nanofibers for High Detection of Sulfur-Containing Gases. *ACS Sustainable Chemistry and Engineering*, *7*(6), 6023–6032. https://doi.org/10.1021/acssuschemeng.8b06132

Blommaerts, N., Vanrompay, H., Nuti, S., Lenaerts, S., Bals, S., & Verbruggen, S. W. (2019). Unraveling Structural Information of Turkevich Synthesized Plasmonic Gold–Silver Bimetallic Nanoparticles. *Small*, *15*(42), 1902791. https://doi.org/10.1002/smll.201902791

The synthesis of the $LaFeO_3$ sample was carried out at the Institute of Inorganic Chemistry, of the University of Cologne. The Au-Ag specimen was prepared at the sustainable energy, air and water technology (DuEL) laboratory at the University of Antwerp. The TEM characterization was carried out at the research group for electron microscopy of materials science (EMAT) at the University of Antwerp. I was responsible all TEM acquisition and analysis.

4.1 Structural Characterization

Development of reliable gas sensing devices with enhanced detection capabilities is vital for applications such as environmental monitoring, food inspection, and medical diagnostics.(Ding et al., 2010; Konstantynovski et al., 2018; Righettoni et al., 2015) Hazardous gases such as SO_2 and H_2S, originating from geothermal activity, combustion of fossil fuels in power plants or from sewers, are particularly important do detect since they pose a serious threat to human life and vegetation even at very low concentrations. Hence, the development of chemo specific and highly sensitive sensors is needed to address such issues.(Bari et al., 2015; Carn et al., 2016, 2017; Fioletov et al., 2016; Hansell & Oppenheimer, 2004; McLinden et al., 2016) In previous work, the use of semiconducting monometal oxides as gas sensors has been explored. Upon adsorption or desorption of gas molecules, the resistance of the semiconductor changes, providing sensitive detection capabilities. Perovskite oxides have been identified as promising semiconducting materials for sensor applications due to their excellent surface activities (e.g. high electrical conductivity and catalytic activity towards surface driven reduction/oxidation reactions).(Carpenter et al., 2013; Mathur et al., 2007; Maziarz et al., 2016; Pan et al., 2010; Von Hagen et al., 2014) Recent work investigated the gas sensing abilities of $LaFeO_3$ (LFO), a p-type semiconductor, and discovered its ability to accurately detect gasses such as CO, but only when present at high concentrations (i.e. 200 ppm and larger).(Bai et al., 2009; Fan et al., 2011) This sensing behaviour is caused by the adsorption, dissociation and ionization of oxygen species at the surface of the material, as illustrated in **Figure 4.1**. When the semiconductor is placed in ambient air, oxygen bonds to its surface. This accumulates a large number of holes in the valence band of the semiconductor, providing a pathway for conducting electrons. Upon interaction with a reducing gas such as SO_2 and H_2S, the ionabsorbed oxygen will bond to the reducing gas molecules. As a result, the electrons will be injected back into the material, recombining with the holes previously created, leading to an increase in resistance and therefore a measure for the concentration of reducing gas molecules.(H. J. Kim & Lee, 2014)

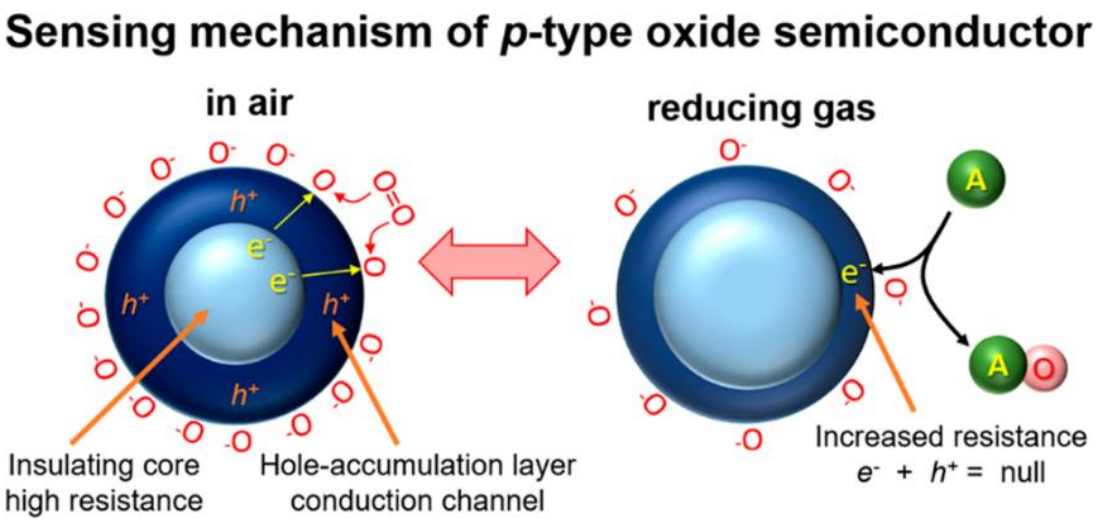

***Figure 4.1**: Schematic representation of the detection mechanism for p-type semiconducting oxides toward reducing analyte gases (image adapted from (Queraltó et al., 2019)).*

Various engineering strategies such as patterning have been investigated with the aim of creating optimized bulk gas sensor devices at a low cost.(Bialuschewski et al., 2018; Obradors et al., 2014; Pyeon et al., 2016, 2018; Queraltó et al., 2013) It is evident, that increasing the detection sensitivity of these gas sensors is of utmost importance. Nanomaterials are highly suitable for sensitive gas sensing devices due to their increased surface-to-volume ratio.(Gad et al., 2012; Giebelhaus et al., 2013; Hackner et al., 2011; Hernandez-Ramirez et al., 2009, 2011; Huber et al., 2017; Lehnen et al., 2014; Rumyantseva et al., 2018; F. Shao et al., 2013) Recently electrospinning has been explored as a potential cost-effective, high throughput nanostructuration strategy.(Choi et al., 2013; Ding & Si, 2011; Hwang et al., 2011) Electrospinning is able to create dense metal oxide nanofiber networks, as illustrated in **Figure 4.2**, with superior sensing capabilities of reducing toxic gasses down to 0.5 ppm.

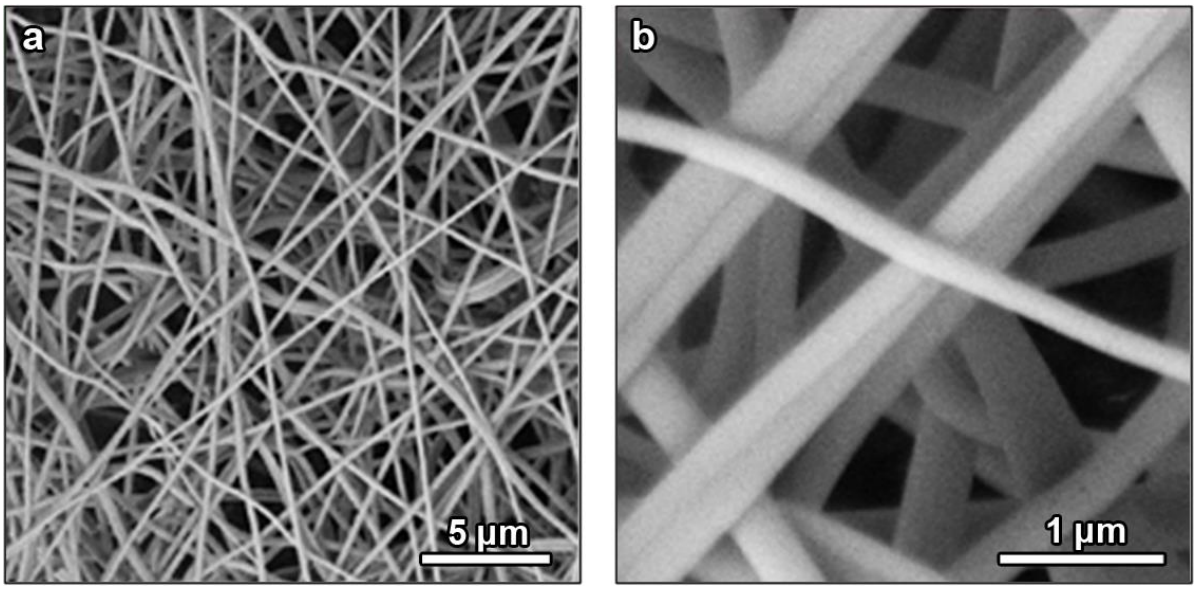

***Figure 4.2**: SEM images of as-prepared electrospun LFO wires, at various magnifications (Figure adapted from (Queraltó et al., 2019)).*

4.1.1 HAADF-STEM Analysis

In order to understand the increase in detection sensitivity, the LFO specimen was investigated using HAADF-STEM using the Thermo Fisher Tecnai Osiris microscope operated at 200 kV. In **Figure 4.3,** HAADF-STEM images of the LFO sample are presented. Elongated string-like structures were found with radii ranging from approximately 30 nm to 150 nm. Each string-like nanostructure appears to be composed out of smaller units, which interconnect with each other. Within each HAADF-STEM projection image, variations in gray level can be seen as well. The observed change in contrast can either be due to changes in thickness, density or composition. To elucidate whether the nanostring sample is porous or has for instance a varying chemical composition, HAADF-STEM tomography was applied. Tomography series were acquired of the nanostring sample along an angular range of ± 74° with a 3° increment. After the acquisition, the images were aligned with respect to each other using a cross-correlation procedure and the tilt axis was corrected. The outcome was used as an input for the ASTRA toolbox implementation of the EM algorithm. (Moon, 1996; Palenstijn et al., 2016; van Aarle et al., 2015)

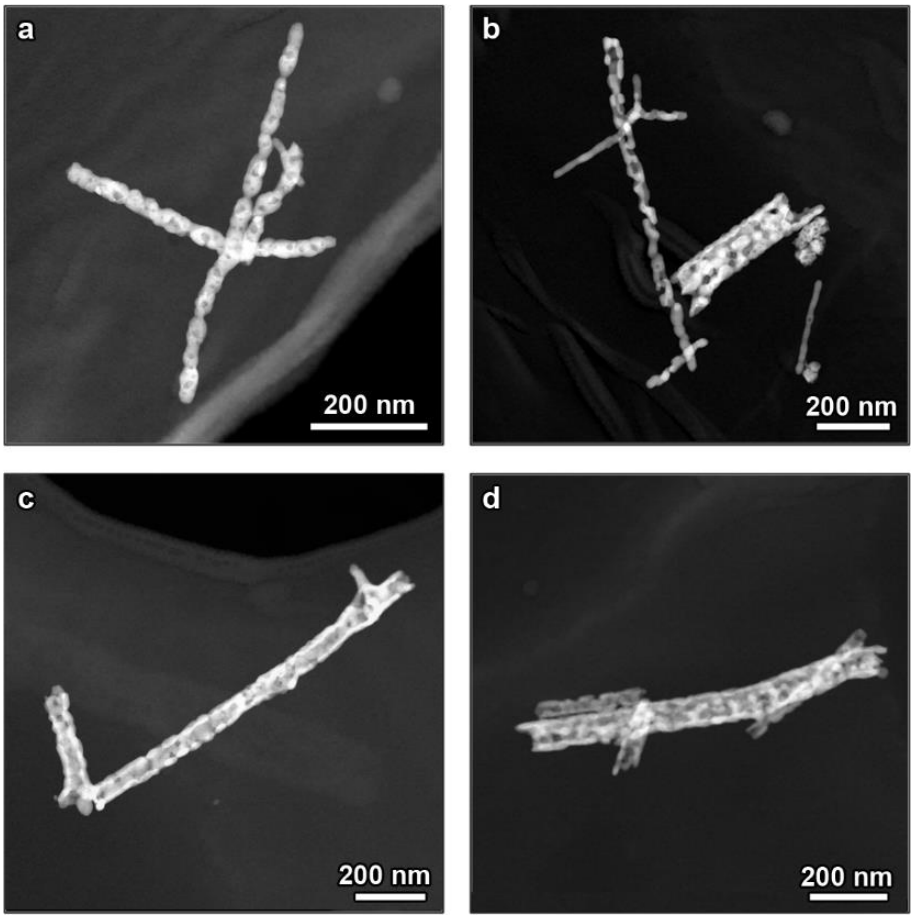

***Figure 4.3**: HAADF-STEM projection images of the investigated LFO specimen. Long string like structures were found with diameters ranging from 30 nm up to 150 nm.*

In **Figure 4.4,** a 3D rendering of the structure of the nanofiber is illustrated together with central orthoslices through the reconstruction. The orientation of the orthoslices is indicated in the top right corner. The orthoslices reveal that the nanostring is highly porous. This is in agreement with the HAADF-STEM projection images for which the center of the string showed a lower intensity than its edges. The porosity of these nanostrings drastically increases their surface-to-volume ratio. In addition, multiple interconnections between the interior and exterior (indicated by the green arrows) are present, making the interior surface easily accessible for the analyte gasses. Since the sensing capabilities of the LFO specimen rely on redox reactions occurring at the surface of the nanowires, the porosity contributes to the superior gas sensing performances of the electrospun LFO nanofibers. In combination with gas sensing measurements, we were able to explain the high detection capabilities of electrospun p-type semiconducting LFO nanofiber–based gas sensors towards reducing gases, which is of enormous importance for environmental monitoring and protection.(Queraltó et al., 2019)

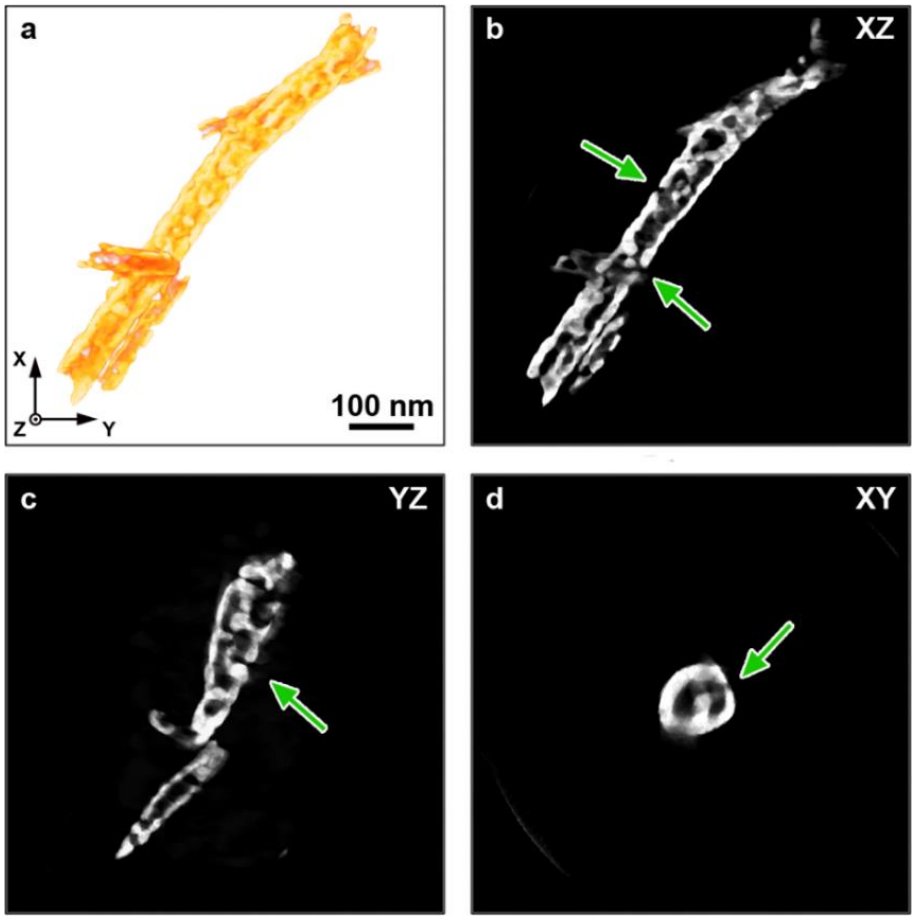

***Figure 4.4**: (a) 3D rendering of the reconstruction obtained from the tilt series of one LFO nanostructure with an angular range of ± 74° and a 3° tilt increment. (b-d) Orthoslices through the reconstruction, displaying the porosity of the nanostring. Green arrows indicate connections towards the exterior.*

4.2 Compositional Characterization

Besides structural information, HAADF-STEM tomography can provide compositional information as well. In this second case study, we demonstrate the application of HAADF-STEM and EDXS tomography for evaluating a well-known nanoparticle synthesis strategy.

Bimetallic nanoparticles are of specific interest because of their versatility for photo(catalytic) applications. Especially gold (Au) - silver (Ag) nanoparticles have been explored, because of the tunability of their optical surface plasmon resonance across the entire visible range of the electromagnetic spectrum.(Liz-Marzán, 2006; Verbruggen et al., 2014, 2016) The most widely used method to synthesize Au-Ag bimetallic nanoparticles is the Turkevich method.(Turkevich et al., 1953) While most studies report on the formation

of alloy nanoparticles using this method, other research indicates that the end product might be core-shell structures instead.(K. Kim et al., 2010; Link & Wang, 1999) The assumption of the formation of a full alloy is typically based on Ultra-Violet visible (UV-vis) absorption data, showing a single plasmon band.(Gonzalez et al., 2009; T. Li et al., 2010; Link & Wang, 1999; Mallin & Murphy, 2002; Sánchez-Ramírez et al., 2008; Uppal et al., 2011) Indeed, for core-shell structures, two separate plasmon bands are expected.(Gonzalez et al., 2009; Liao et al., 2018; Lu et al., 2013) Nevertheless, caution has to be taken, since a single plasmon band can also indicate the appearance of a core-shell structure with a sufficiently thick shell to eliminate the core contribution to the UV-vis absorption data.(Mie, 1908) Here, we aim to use different TEM techniques to accurately understand whether the universally applied Turkevich synthesis pathway results in $Au_{0.5}Ag_{0.5}$ alloy nanoparticles or core-shell morphologies instead. To do so, samples were taken at various time intervals during the synthesis and analyzed using EDXS and HAADF-STEM.

4.2.1 HAADF-STEM Analysis

Figure 4.5a displays HAADF-STEM overview images of the obtained nanoparticles after 30 min of synthesis. **Figures 4.5b-c** show single nanoparticles at higher magnification. Spherical nanoparticles were found with a size of 50 ± 9 nm. The advantage of using HAADF-STEM, is that the observed contrast can be correlated to the atomic number Z of the composing materials. Since there is a significant difference in Z number between Au (79) and Ag (47), high intensities hint towards areas containing an increased Au concentration. Darker areas, on the other hand, imply Ag rich regions. In contradiction to the expected alloy formation, the nanoparticles seemingly have formed a core-shell type of nanostructure. For Pd-Ag alloy nanoparticles it is known that silver has the tendency to segregate towards the surface of the particle.(Løvvik & Opalka, 2008) A similar behavior could explain the observed contrast difference between the inner and outer region of the $Au_{0.5}Ag_{0.5}$ nanoparticles. Nevertheless, 2D projections can be very misleading and the potential presence of remaining diffraction contrast further complicates any quantitative interpretations. To gain insight on the composition and formation process of the investigated nanoparticles, tomography series and EDXS maps were acquired for samples which were collected at several time intervals throughout the synthesis.

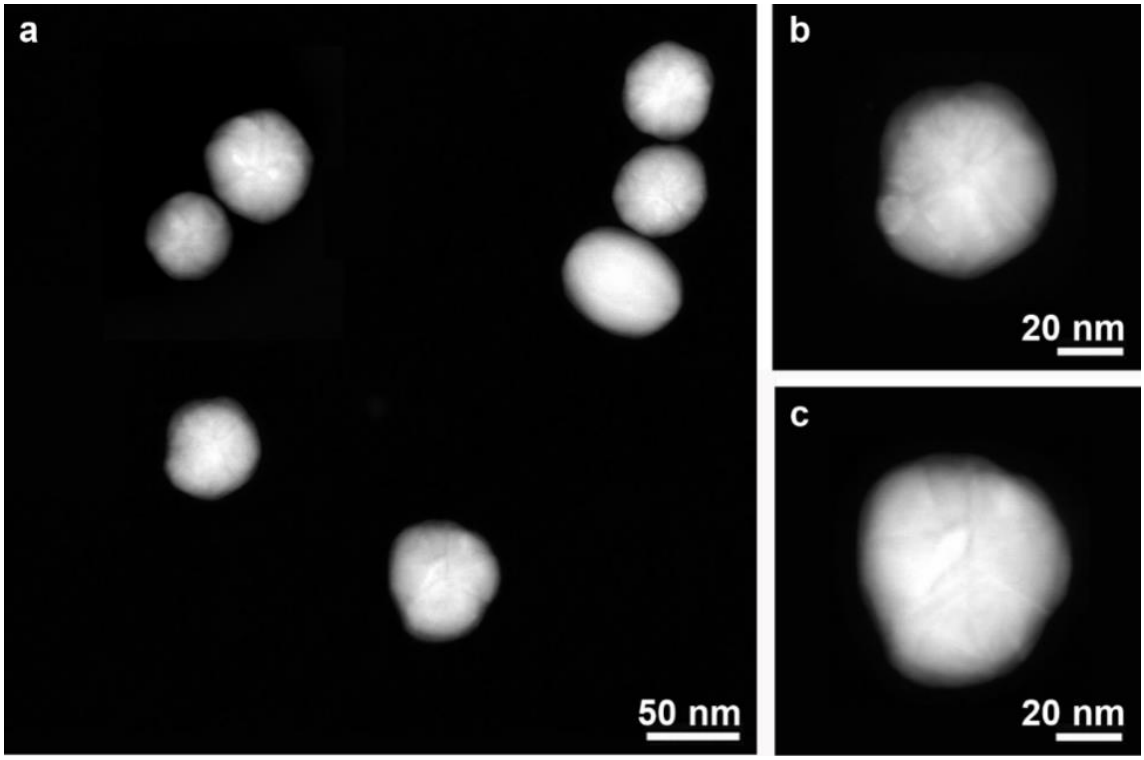

***Figure 4.5**. (a-c) HAADF-STEM images of spherical $Au_{0.5}Ag_{0.5}$ bimetallic nanoparticles with an average size around 50 nm.*

4.2.2 EDXS Analysis

EDXS maps were acquired for five different time steps (4, 7, 10, 13, 16 min). In the first column of **Figure 4.6,** HAADF-STEM projection images of different nanoparticles acquired after the different stages of synthesis are displayed. In the second and third column, the EDXS maps of the Au (red) and Ag (green) signal are shown. The last column displays the superposition of both maps. Comparing the combined EDXS maps for the different time steps indicates that although the nanoparticles seemingly form an alloy at the beginning of the synthesis, they steadily develop a silver-enriched shell across the surface of the nanoparticle. From **Figure 4.6c** it can be seen that even after one EDXS map, the Ag shell forms clusters along the surface of the nanoparticle. At later stages of the reaction, as the formation of the shell continued, this effect becomes less pronounced. This indicates that initially the alloy nanoparticle is more unstable under long electron beam exposure, making a quantitative 3D EDXS analysis of the earlier stages unfeasible.

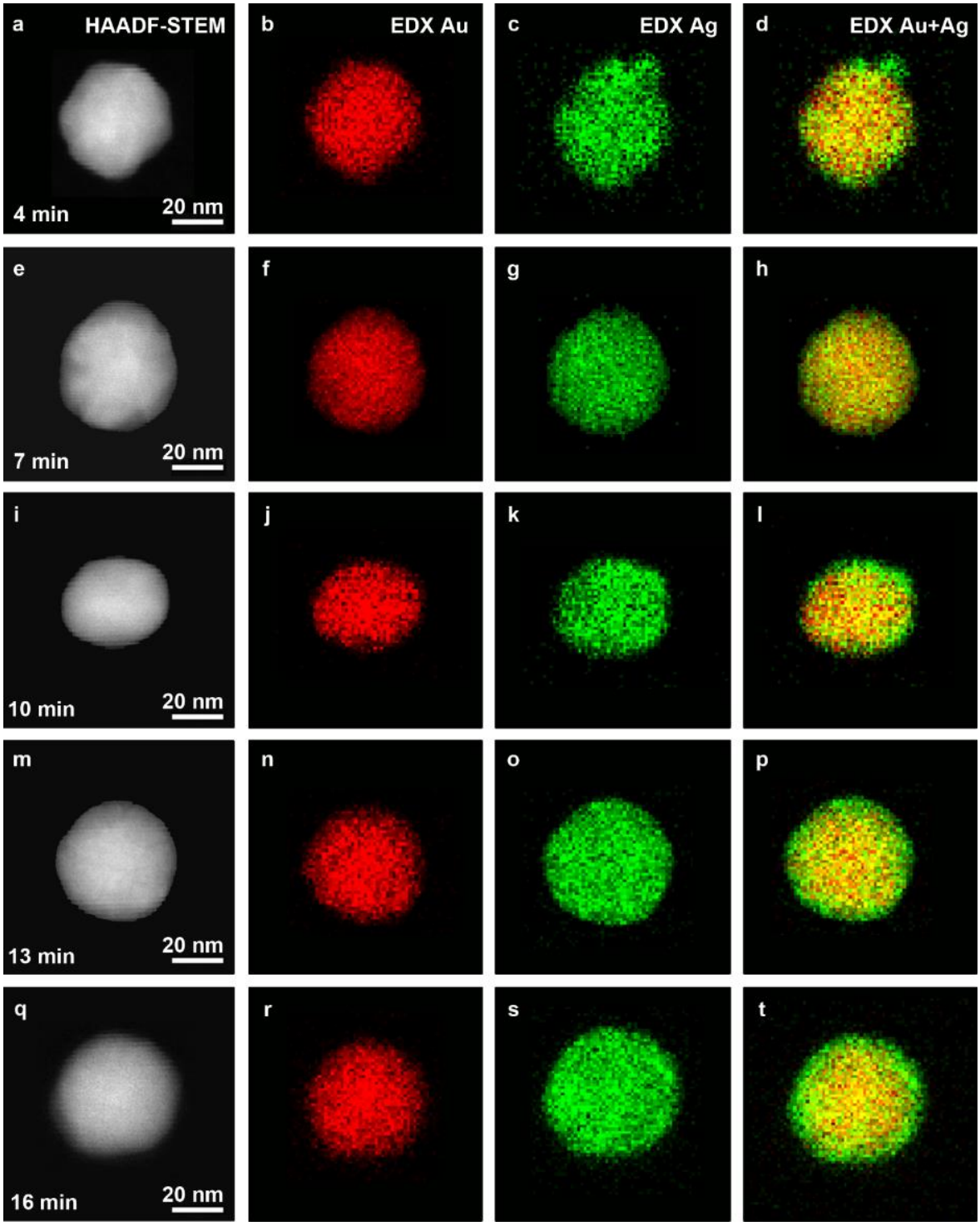

***Figure 4.6**: HAADF-STEM and net count EDXS maps of different nanoparticles sampled at intermediate times during the synthesis procedure.*

4.2.3 Tomography Analysis

Given the radiation sensitivity of the samples obtained at earlier stages of the synthesis, HAADF-STEM tomography, instead of EDXS tomography, was performed on all different stages of the synthesis procedure. The detection efficiency for HAADF-STEM imaging is far better than that of EDXS imaging. Therefore, a shorter acquisition time, equivalent to a lower electron dose, is required for each projection image. While HAADF-STEM tomography does not reveal any quantitative information concerning the chemical composition of the nanoparticle, it does offer a qualitative picture.

HAADF-STEM tilt series was acquired over a tilt range of ± 75° with a 3° increment at a Thermo Fisher Scientific Tecnai Osiris microscope operated at 200 kV. The probe convergence semi angle was equal to 16 mrad and inner and outer collection semi angles of respectively 80 and 240 mrad were used for the detection. After the acquisition, the images were aligned with respect to each other using cross-correlation. Reconstructions were calculated through the ASTRA toolbox implementation of the EM algorithm(Moon, 1996; Palenstijn et al., 2016; van Aarle et al., 2015). 3D renderings of the reconstruction and corresponding central orthoslices through the reconstruction are shown in **Figure 4.6**. By comparing different reaction stages, it becomes obvious that the particle starts as an alloy but gradually turns into a core-shell morphology. After 10 minutes of synthesis the first signs of a shell are visible in the HAADF-STEM reconstruction. As the synthesis continues, the shell further grows until it is almost 5 nm thick.

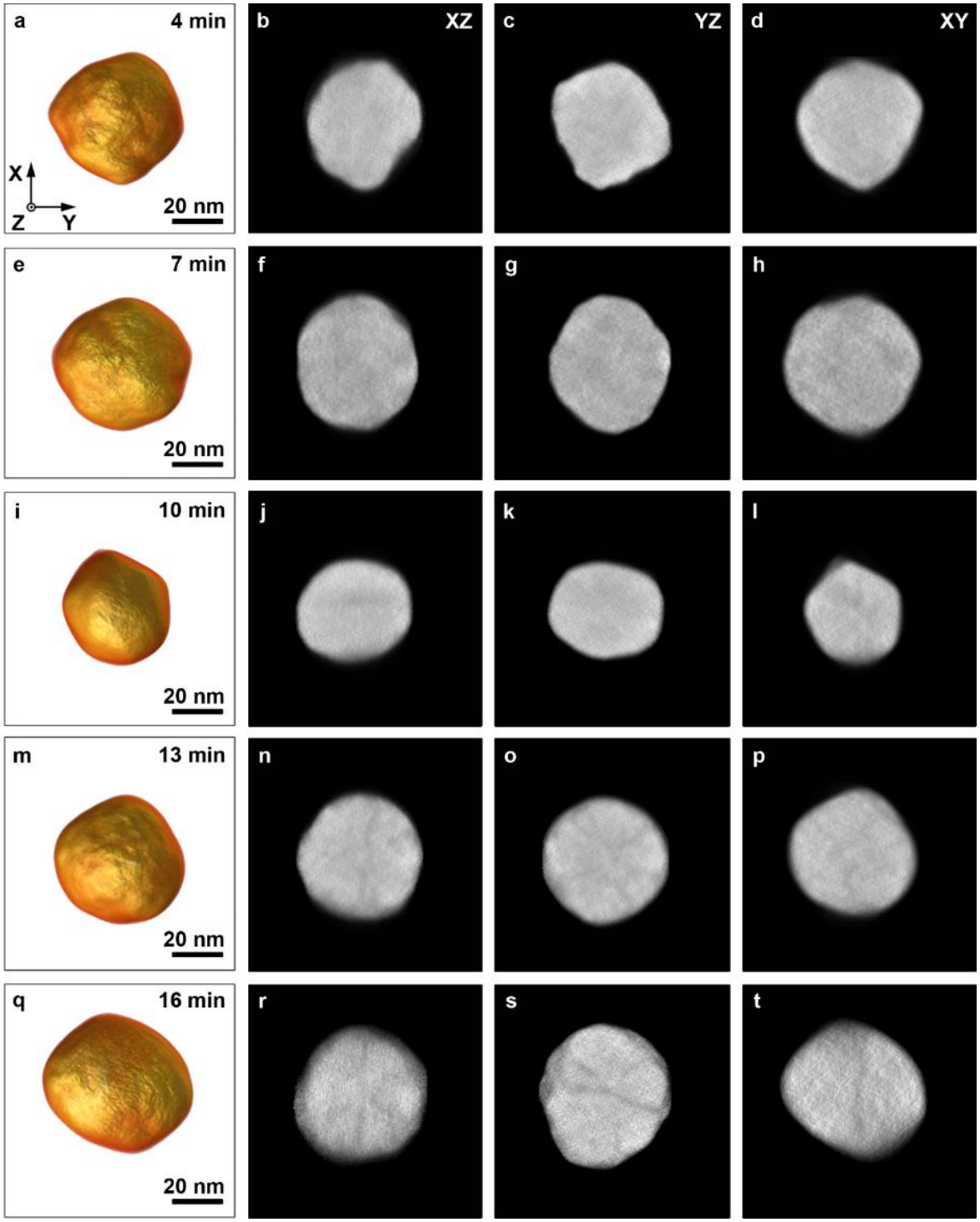

***Figure 4.6**: 3D rendering and central orthoslices from the HAADF-STEM tomography reconstructions of nanoparticles sampled at intermediate times during the synthesis procedure. The orientation of the orthoslices is indicated in the top right corners of the first row.*

Given the increased stability of the final state of the nanoparticle, EDXS tomography was performed on the 16 min sample using a synergistic combination of HAADF-STEM and EDXS tomography.(Zanaga, Altantzis, Polavarapu, et al., 2016; Zanaga, Altantzis, Sanctorum, et al., 2016) Each voxel of the final reconstruction contains a distribution of the different elements of the nanoparticle, in this case Au and Ag. In this manner, not only qualitative but also quantitative information concerning the 3D composition of the final state is retrieved. The EDXS tilt series were acquired on the Super-X detection system over an angular range of ± 70° with a tilt increment of 10°. In **Figure 4.7a**, a 3D rendering of the investigated particle is presented. The central orthoslice through the reconstruction (**Figure 4.7b**) reveals the core-shell morphology, represented by a large difference in gray value between their relative compositions. Orthoslices through the Au and Ag signal of the corresponding EDXS tomography reconstruction confirm that the core contains a higher amount of Au, whereas the shell primarily consists out of Ag. This is in agreement with the HAADF-STEM reconstructions for which the core consistently showed a higher intensity than the shell.

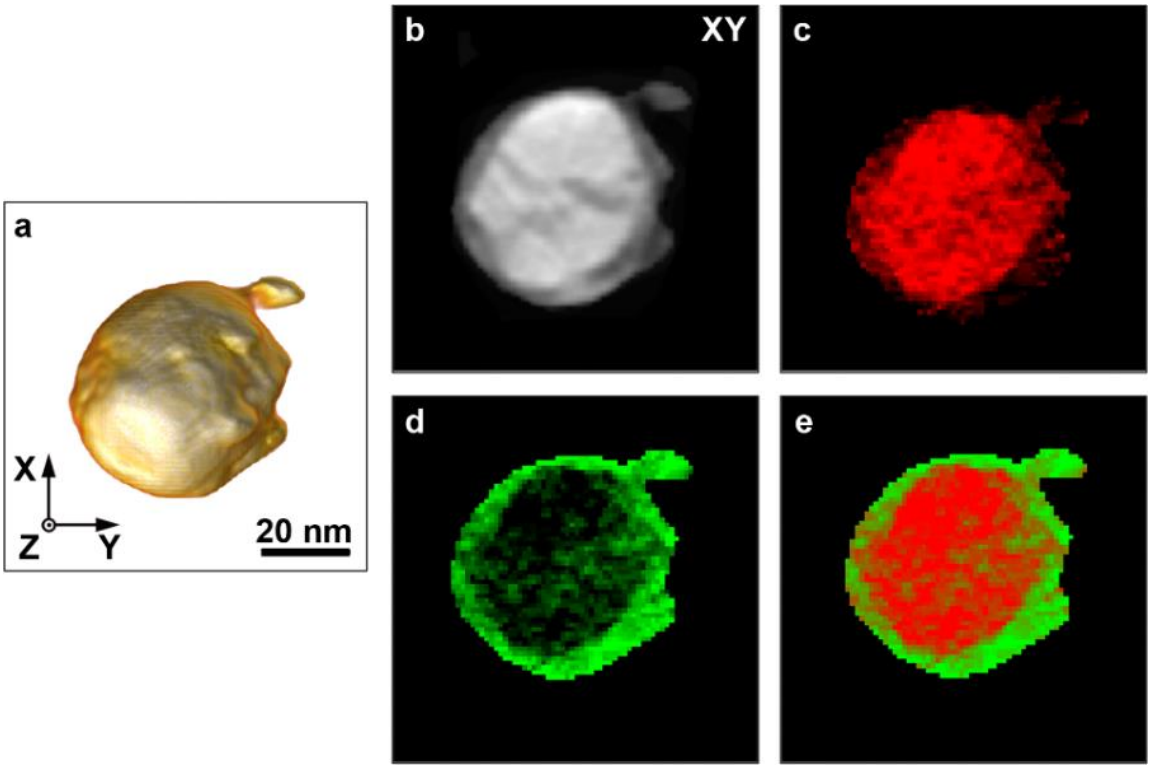

***Figure 4.7**: (a-b) 3D rendering and a central XY orthoslice of the HAADF-STEM tomographic reconstruction of a nanoparticle obtained after 16 min of synthesis. (c-d) Central XY orthoslices through the corresponding EDXS tomography of the Au and Ag signal. (e) Superposition of the Au and Ag signal.*

From the HAADF-STEM reconstruction, a mask was derived for both the core as the shell through histogram based segmentation. By multiplying these masks with the Au and Ag reconstructions, it is possible to separate the contributions of Au and Ag in each region. It was found that on average the core contains 82 ± 3% Au and 18 ± 2% Ag, whereas the shell approximately consists of 35 ± 4% Au and 65 ± 5% Ag. This is in agreement with the central line profile through the EDXS reconstruction presented in **Figure 4.8**. More importantly, the line profiles of the relative Au and Ag frequency steadily rise and decay. This indicates that there is no sharp boundary between the core and shell, but that the composition steadily changes along the radius of the nanoparticle.

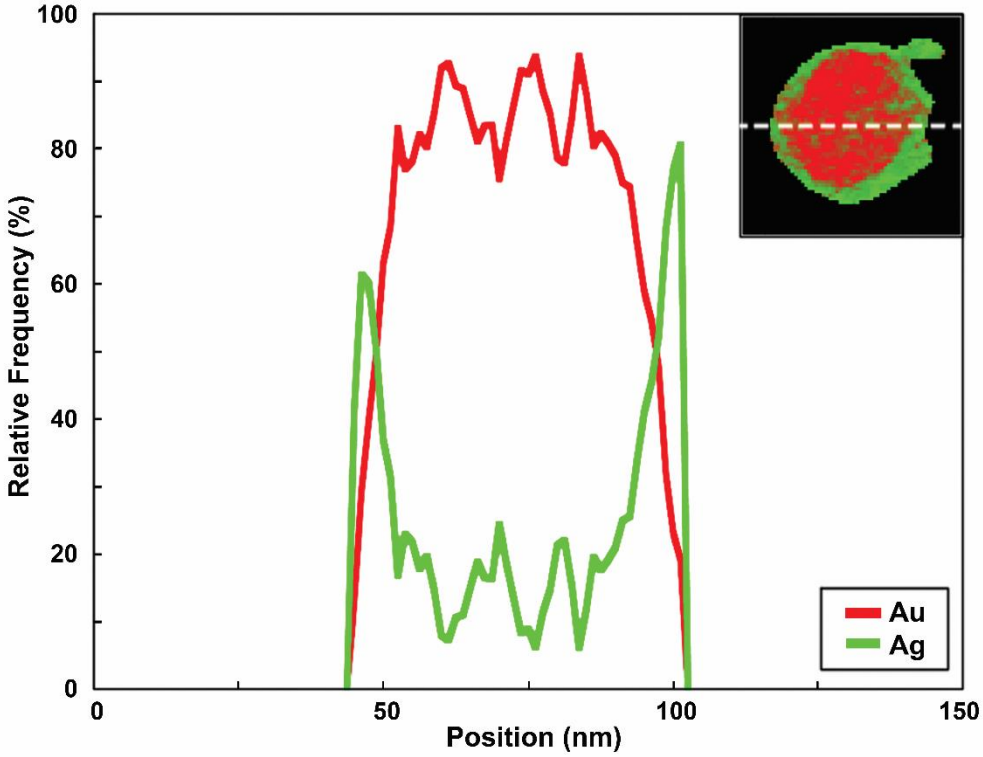

***Figure 4.8**: Central line profile through the XY orthoslice (as indicated in the inset).*

In combination with additional UV-vis experiments and Finite Element Modelling (FEM), we were able to proof that indeed core-shell type nanoparticles with a smooth transition in alloy composition, result in a single plasmon band for which the position and width almost perfectly coincides with the experimental data.(Blommaerts et al., 2019) We proof that the often used Turkevich synthesis method does not necessarily results in pure alloy nanoparticles but rather core-shell like structures are formed with a smoothly altering composition. We therefore demonstrate that UV-vis spectra alone do not suffice to determine the compositional distribution obtained after synthesis.

Objectives

Electron tomography experiments clearly provide very precise and local information on the 3D structure and composition of nanoparticles. However, a major drawback is the total run time that is required to obtain the necessary 2D projection images, to align them and to compute the final 3D reconstruction. Since easily 2 hours are required to study a single nanoparticle in 3D, it is far from straightforward to obtain information in 3D that can be considered as a statistically relevant result. This is clearly a limitation when trying to connect the properties of the nanoparticles to their 3D structure. For example, when studying the porosity or composition of a large number of respectively catalytic or plasmonic nanoparticles, it is crucial to obtain a general understanding of the connection between their structure and activity. Currently, such studies cannot be easily performed due to the fact that both the acquisition of the tilt series as well as the alignment and the 3D reconstruction are too time consuming.

Obviously, one of the emerging challenges in the field of electron tomography is to increase the throughput of 3D reconstructions of nanoparticles. At the same time, the quality of the reconstructions should still enable one to obtain reliable and quantitative results concerning parameters such as particle size and surface morphology. Moreover, 3D studies of radiation sensitive materials are nowadays extremely challenging since samples will degrade and deform when exposed to high electron doses. Finally, the extensive acquisition time for electron tomography together with the time consuming alignment and reconstruction steps, results in a very inefficient process. Ideally, one would be able to obtain fast feedback on the 3D structure of a nanoparticle under investigation such that additional or more detailed experiments can be performed using the same nanoparticle if necessary.

In this thesis I will go beyond state-of-the-art of electron tomography in order to overcome such limitations. My aim is to reduce the run time of electron tomography experiments in order to enable high-throughput and real-time characterization of nanostructures. As I studied crystalline samples, the main focus will be on improving the throughput of HAADF-STEM tomography experiments. To reach this goal, the acquisition, alignment and reconstruction need to be optimized.

Therefore, I aim to:

- Develop acquisition strategies that enable the recording of tomographic series within a few minutes. The reduction of the acquisition time will be accompanied by a decrease in electron dose, allowing new 3D experiments to be conducted.

- Propose new computational methods capable of processing the tilt series acquired using fast acquisition schemes. Such developments are necessary since the fast tilt series will typically yield a lower signal-to-noise ratio and/or a limited amount of information.

- Improve the efficiency of the alignment and reconstruction, such that real-time 3D information will become accessible during the tomography experiment. Such information will aid steering in-situ experiments in the electron microscope, where one is interested in the fast dynamical behavior of nanoparticles under external stimuli.

Reaching these objectives, will allow:

- Performing high-throughput electron tomography experiments with a time resolution far shorter than those reachable by conventional electron tomography. Such experiments will yield statistical relevant information concerning the nanoparticles their functionalities or structural properties.

- 3D investigations which benefit from the reduction in electron dose and are not possible by conventional means.

- Conducting quasi real-time 3D imaging experiments which improve the efficiency of the 3D studies and enable real-time in-situ experiments. Such studies will be essential to understand the morphological changes of nanosystems as function of e.g. temperature.

PART II: ACCELERATED ACQUISITION

5. Experimental Evaluation of Undersampling Schemes

One of the emerging challenges in the field of three-dimensional characterization of nanoparticles by electron tomography is to avoid degradation and deformation of the samples during the acquisition of a tilt series. In this chapter, we compare different approaches which lower the electron dose and therefore minimize beam induced sample degradation.

This chapter is based on:

Vanrompay, H., Béché, A., Verbeeck, J., & Bals, S. (2019). Experimental Evaluation of Undersampling Schemes for Electron Tomography of Nanoparticles. *Particle and Particle Systems Characterization*, *36*(7), 1900096. https://doi.org/10.1002/ppsc.201900096

The synthesis of the Au nanorod sample was carried out at the Bionanoplasmonics Laboratory, CIC biomaGUNE in Spain. The TEM characterization was carried out at the research group for electron microscopy of materials science (EMAT) at the University of Antwerp. The experimental data were acquired by A. Béché. I was responsible for all preprocessing, reconstructions and phantom studies.

5.1 Introduction

During a tomography experiment, a series of 2D projection images is collected over different tilt angles to cover an angular range that is as large as possible. Next, the tilt series serves as an input to a mathematical algorithm, which reconstructs the 3D structure. To obtain a reliable 3D reconstruction using conventional reconstruction algorithms such as FBP(Dudgeon & Mersereau, 1985) or SIRT(Gilbert, 1972), tilt series are typically acquired over a range of ± 75˚ with an increment of 1˚–3˚. Consequently, it is highly challenging or even impossible to perform a 3D investigation of radiation sensitive nanomaterials since their structure tends to alter during the acquisition of the tilt series. Various approaches have been proposed to overcome this limitation such as lowering the amount of necessary projection images, referred to as tilt-undersampling (T-US). Another suggested approach is image-undersampling (I-US), in which e.g. the electron dose is reduced during the tomography experiment.

During T-US, a smaller number of projection images with a larger tilt increment is acquired, while keeping the angular range as large as possible, as illustrated in **Figure 5.1a**. Batenburg et al. showed that even for T-US tomographic projection series with a rather large tilt increment, accurate reconstructions can be retrieved, provided that prior knowledge of the composition of the specimen is included.(Batenburg et al., 2009; Batenburg & Sijbers, 2011) In addition, it was proposed that including prior knowledge on the sparsity or compressibility of the reconstructed object in a known domain, can be beneficial during the reconstruction of extremely limited data sets.(Goris, Van den Broek, et al., 2012; Leary et al., 2013b)

I-US has been used when acquiring 2D high resolution images of beam sensitive materials.(Buban et al., 2010) Various approaches exist to lower the electron dose during an experiment ranging from increasing the pixel size while maintaining the frame size for each projection image, leading to an irreversible loss in resolution, to decreasing the beam current during the acquisition (**Figure 5.1b**). An alternative approach of I-US consists of reducing the amount of acquired pixels in a given projection image (**Figure 5.1c**).

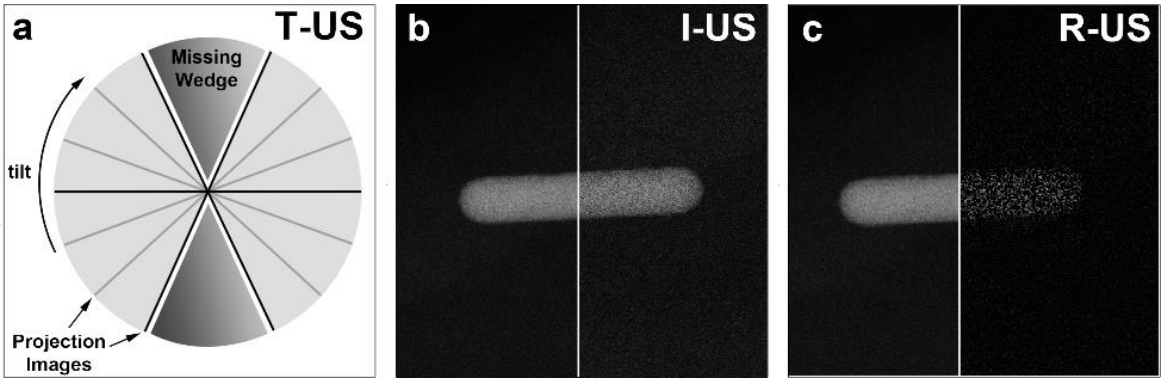

***Figure 5.1**: (a) illustration of T-US where less projection images are acquired (black lines) than in a conventional tomography experiment (gray lines). (b) Compositional illustration of a projection image acquired at full dose and at 50% of the dose by I-US. (c) Compositional illustration of a projection image acquired at full dose and at 50% of the dose by scanning only a select amount of pixels.*

Recently, it was demonstrated that by exploiting the principles of compressed sensing (CS) it is possible to restore the original image even though not all pixels in the image are scanned.(Béché et al., 2016; Stevens et al., 2018) Indeed, CS states that an image can be retrieved from a limited selection of its pixels, provided that the selection of these pixels is incoherent, and if the image is sparse in a predefined domain. The incoherence guarantees that artefacts resulting from the sparse sampling appear in a noise like manner in the predefined domain, thereby limiting their influence on the retrieved image. As a result, the amount of measurements needed to faithfully recover a sparse signal is primarily determined by the measure of incoherence between the measurement domain and the predefined sparse domain.(Candès & Romberg, 2007) Common choices for the predefined domain in which 2D HAADF-STEM images are sparse or at least compressible, are the discrete cosine domain, the discrete wavelet domain and the gradient domain.(Béché et al., 2016; Goris, Van den Broek, et al., 2012; Leary et al., 2013b, 2013a; Song et al., 2012; Sorzano et al., 2006; Stoschek & Hegerl, 1997; Vonesch et al., 2011).

Lustig et al. demonstrated, within the context of magnetic resonance imaging, that radial sampling of the Fourier space of the object, results into sufficient incoherence to apply CS.(Lustig et al., 2007, 2008) This analysis was extended towards electron tomography for a specific type of I-US for which subsets of pixels are measured in a random manner.(Donati et al., 2017) They validated that measuring randomly selected pixels is sufficiently

incoherent to the Haar wavelet, and therefore discrete gradient domain(Kamilov et al., 2012) to fulfil the incoherence criterion. In the remainder of this work, we will refer to this specific I-US approach as random-undersampling (R-US).

Donati et al. theoretically demonstrated the idea of performing tomographic reconstructions of R-US tilt series by exploiting the principles of CS. The superiority of R-US over T-US approaches for electron tomography reconstructions was proclaimed, albeit using simulated data.(Donati et al., 2017) On the other hand, Van den Broek et al. evidenced that when using the same dose, CS restoration of 2D R-US images does not outperform de-noising I-US images under counting noise conditions.(Van den Broek et al., 2019) The latter is in agreement with earlier work, which stated that the presence of counting noise enforces a bound to the accuracy which can be reached when restoring TEM images using CS.(Raginsky et al., 2010) Consequently, one may wonder about the role of CS during electron microscopy experiments. So far, it remains unclear which of the three main electron dose reducing techniques (T-US, I-US and R-US) is preferred for HAADF-STEM electron tomography experiments. The three approaches have not been directly compared to each other and a thorough empirical evaluation (based on experimental data) is lacking.

In this chapter, I will therefore compare the influence of these three dose limiting techniques on the quality of tomographic reconstructions based on experimental HAADF-STEM tilt series.(Béché et al., 2016) The outline of this chapter is as follows. First, we introduce the different acquisition procedures and discuss the reconstruction algorithm used here. We demonstrate the importance of incorporating the so-called acquisition mask during the reconstruction procedure and test the reliability of this approach. Finally, we compare the reconstruction accuracy of T-US, I-US and R-US for different electron doses.

5.2 From Acquisition to Reconstruction

In the following sections we will discuss the acquisition, processing and reconstruction of the undersampled tilt series. In addition, we provide simulation studies to support our R-US methodology.

5.2.1 Acquisition

A gold nanorod (Au NR) sample was imaged using an aberration-corrected cubed Thermo Fisher Scientific Titan electron microscope operating in HAADF-STEM mode at 300 kV. The Au NR forms an ideal test sample since it is stable under the electron beam and its morphology does not alter during a tomography experiment. In total, 7 tilt series were obtained of the same nanoparticle. The relevant acquisition parameters of the different dose limiting techniques are summarized in **Table 5.1**. To minimize the potential influence of electron beam damage, all images at a given tilt angle were acquired using the various imaging conditions, prior to tilting the stage to the next angle. First, a reference series was acquired over an angular range of -73° to 74° with a tilt increment of 3° of a NR for which its primary axis was aligned along the experimental tilt axis. All pixels were scanned with a 50 pA probe current (**Figure 5.2a**). Based on the reference series, 2 T-US series were created, one with a tilt increment of 6° and one with an increment of 15°, by removing images from the reference tilt series. Next, two series were collected of the same NR in which the total electron dose was lowered by 50% either by I-US or R-US (I-US; **Figure 5.2b** and R-US; **Figure 5.2d**). Finally, two additional series were acquired using an electron dose of only 20% of the dose used for the reference series (I-US; **Figure 5.2c** and R-US; **Figure 5.2e**).

Name	*Probe current*	*Tilt range and increment*	*Scanned pixels*	*Frame time (s)*	*Total dose (# electrons)*
Reference	50 pA	[-73°:3°: 74°]	100%	2.62	4.09×10^{16}
50% I-US	25 pA	[-73°:3°: 74°]	100%	2.62	2.05×10^{16}
20% I-US	10 pA	[-73°:3°: 74°]	100%	2.62	8.18×10^{15}
50% T-US	50 pA	[-73°:6°: 74°]	100%	2.62	2.05×10^{16}
20% T-US	50 pA	[-73°:15°: 74°]	100%	2.62	8.18×10^{15}
50% R-US	50 pA	[-73°:3°: 74°]	50%	1.31	2.05×10^{16}
20% R-US	50 pA	[-73°:3°: 74°]	20%	0.52	8.18×10^{15}

***Table 5.1**: Abbreviations of the dose limiting techniques, relevant acquisition parameters and the amount of electrons used for the acquisition of the tilt series.*

During the I-US acquisition, the probe current was respectively lowered to 25 pA (50%) or 10 pA (20%) and all pixels were scanned. At high doses the probe current was determined by measuring the total electron current intercepted on the viewing screen with a calibrated pico-ampere meter. However, the pico-ampere meter has a limited precision at low doses. In order to overcome this limitation, a relation between the probe current and the amount of detected counts, which are accurate in the low dose regime, was established for high doses and interpolated towards the low dose regime. The amount of detected counts was determined by imaging the rochigram and calculating its total signal. For the R-US acquisition, the total electron dose was equally lowered, by selectively scanning 50% or 20% of the pixels in a random manner with a 50 pA probe current. The R-US datasets were experimentally acquired using a fast electromagnetic beam blanker placed in the condenser system or the electron microscope. Using a pseudo random generator, it is possible to blank the beam in a random manner, thereby acquiring images yielding a limited amount of scanned pixels.(Béché et al., 2016)

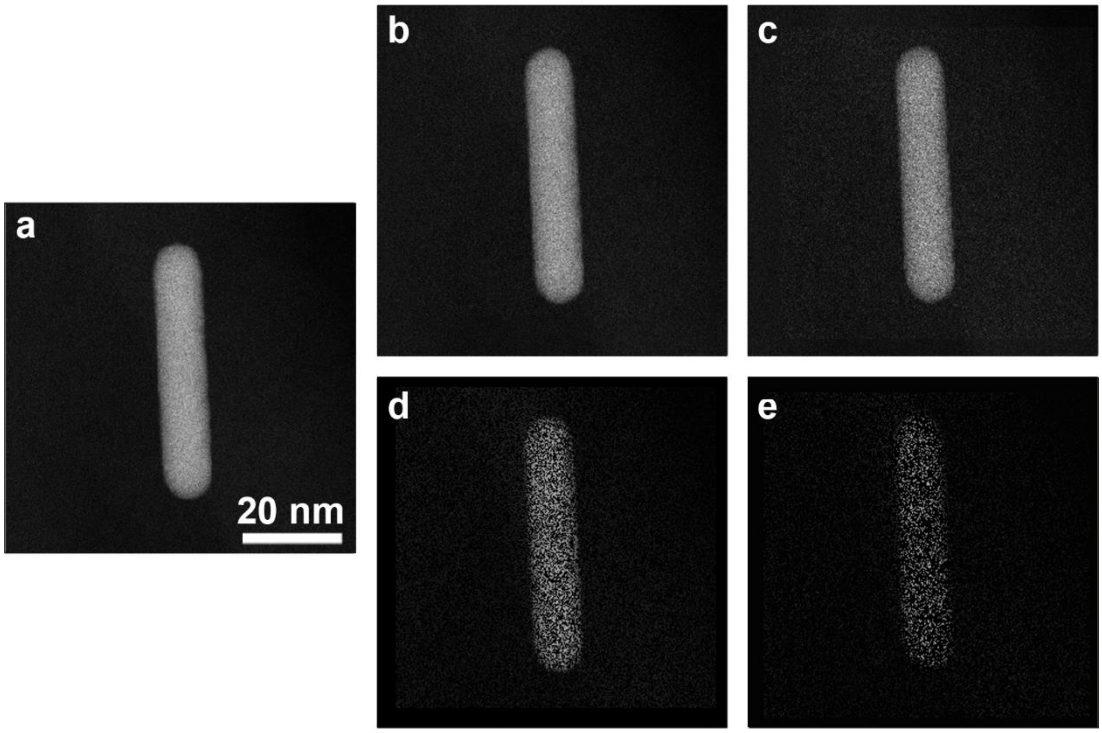

Figure 5.2*: (a-c) HAADF-STEM projections acquired with respectively a probe current of 50, 25 or 10 pA. (d-e) HAADF-STEM projections acquired using a probe current of 50 pA but with only scanning respectively 50% or 20% of the pixels.*

5.2.2 Alignment

After acquisition, the tilt series were aligned with respect to each other using a cross-correlation strategy(Foroosh et al., 2002; Nagashima et al., 2007; Takita et al., 2003; Yan & Liu, 2008). However, since every R-US projection image was acquired with a different, random, acquisition mask, the outcome of the alignment is far from optimal. In **Figure 5.3c** the cross-correlation, convolved by a Gaussian, is displayed of two consecutive R-US projection images (**Figure 5.3a-b**). The correlation is broad, making a maximum retrieval challenging. Therefore, the images in the R-US tilt series were first restored using an ASTRA-Toolbox(Bleichrodt et al., 2016; Palenstijn et al., 2016; van Aarle et al., 2015; Van Den Berg et al., 2009) implementation of total variation (TV) and the Chambolle-Pock minimization strategy(Chambolle & Pock, 2011; Sidky et al., 2012), as will be discussed in **Section 5.2.3**, prior to estimating the alignment parameters (**Figure 5.3d-f**). The distribution in the cross-correlation narrows down and the position of the maximum changes, ensuring a far more accurate estimation of the translational parameters, and therefore positively influencing the reconstruction quality. Next, these parameters where applied to the non-restored R-US projection images.

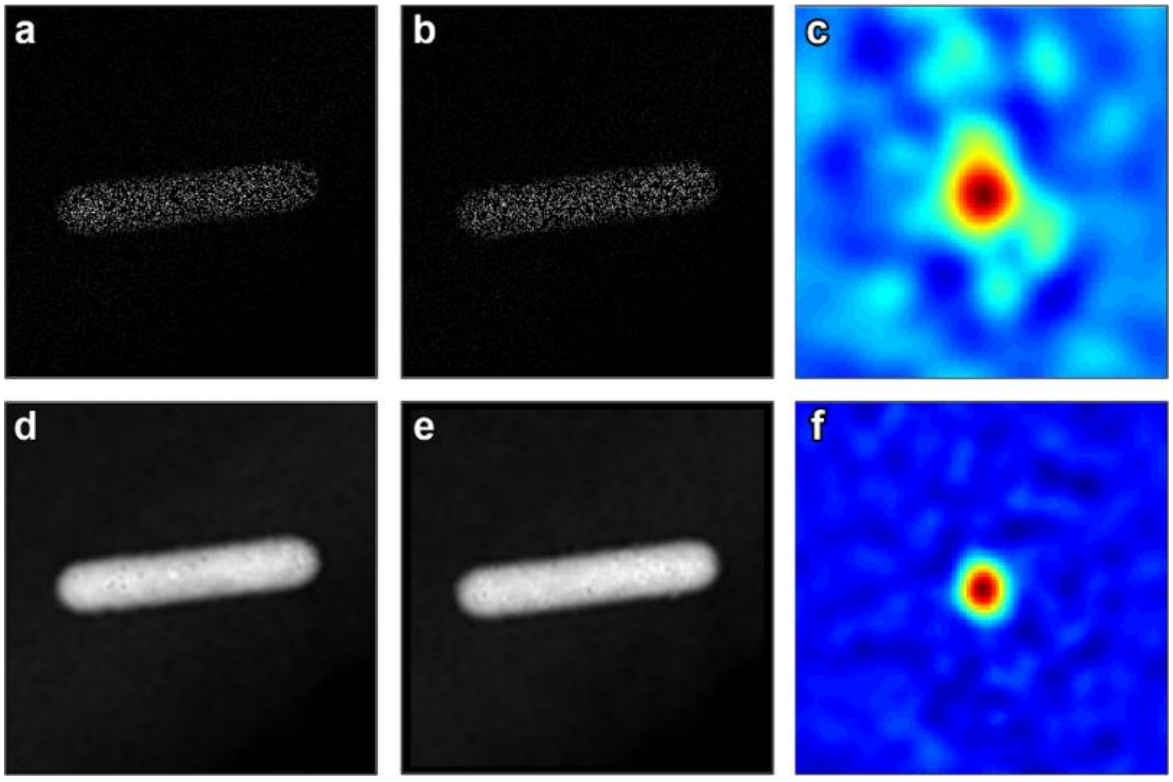

***Figure 5.3**: (a-c) Two sequential R-US HAADF-STEM projection images and the correlation between both. (d-f) The projection images after restoring and the correlation between both.*

5.2.3 Reconstruction

After alignment, the tilt series were used as input for a tomographic reconstruction, during which we exploit prior knowledge on the acquisition mask as well as on the idea that the object has a compressible representation in the gradient domain. Hereby, the following set of equations is solved utilizing the ASTRA-Toolbox implementation of the 3D TV and the Chambolle-Pock minimization strategy:

$$\hat{x} = argmin_x \|MWx - p\|_{l_2} + \mu \|TV(x)\|_{l_1}, \qquad [5.1]$$

where $\hat{x}$ represents the estimated reconstruction of the unknown object x and the measured HAADF-STEM projection images are defined as p. W corresponds to the projection matrix. M indicates a mask operator, based on the acquisition mask. In case all pixels are scanned, such as for the I-US and T-US projection images, the mask operator equals the identity operator. $TV(x)$ determines the discrete gradient of the reconstructed object x and μ is a hyper parameter that regulates the relative importance of the sparsity in the transform domain and the data fidelity in the reconstruction domain. Restricting the l_1 norm of the discrete gradient, imposes a constraint on the amount of gray level variations within the reconstructed object. This type of minimization is therefore most suited for objects that consist out of homogeneous regions separated be sharp boundaries, referred to as piecewise constant regions, relevant for many nanoparticle systems. Even when the object under consideration is not strictly sparse in the discrete gradient domain, its piecewise constant approximation may still contain valuable information concerning boundaries within the nanoparticle systems.(Leary et al., 2013b; Lustig et al., 2007) It should be noted that the mask operator M directly works on the projection matrix W during the reconstruction. In this manner, the minimization process tries to find a solution where the simulated masked projection images of the unknown object match the experimental ones.

It was empirically found that setting μ to 1, hence putting equal weight on the data fidelity and sparsity term, leads to reconstructions that best resemble the homogeneous Au NR. In **Figure 5.4** we show identical central slices through the NR, obtained from reconstructing the reference data series for various values of μ. It is evident that a small value of μ leads to a noisy reconstruction, whereas an overestimation of μ results in a loss of high frequency information. From these 2D results, it was determined that setting μ equal to 1,

serves as a good starting point for the 3D reconstruction. Although reconstructing single 2D slices provides a computationally efficient way of evaluating the optimal value for μ, the reconstructions displayed throughout this work were all performed in 3D. Hence, the discrete gradient of the reconstructed object was minimized in three dimensions instead of two. This additional constraint during the reconstruction leads to significantly less intensity variations than those obtained when reconstructing single 2D slices.

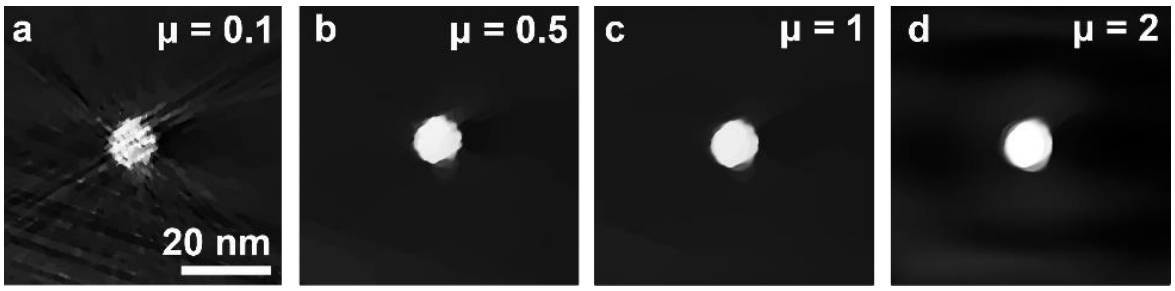

***Figure 5.4**: (a-d) 2D reconstructed central slices through the NR for various values of μ, obtained from the reference series.*

5.2.4 Verification Studies

Donati et al. used simulated R-US projection images to show that the incorporated approach, defined by **Equation [5.1]**, leads to more accurate reconstructions in comparison to previous work wherein the R-US projection data were first restored by CS and afterwards used as input for reconstruction.(Donati et al., 2017; Saghi et al., 2015) Here, we will verify these findings based on experimental data. In **Figure 5.5**, we compare the outcome of a 3D reconstruction of the reference series (**a**) with the 3D reconstruction of a R-US tilt series without the use of prior information (**b**), a 3D reconstruction in which the input images have been restored prior to the reconstruction (**c**) and a 3D reconstruction in which the acquisition mask was incorporated during the CS reconstruction (**d**). This comparison was performed for the 20% R-US tomography series since it corresponds to a heavily underdetermined reconstruction problem and therefore is the most challenging case to reconstruct. When the prior knowledge of the acquisition mask was neglected during the reconstruction, the outcome is obviously very noisy (**Figure 5.5b**). In the case where the projection images were restored prior to the 3D reconstruction, gray level variations in the final results are present and the reconstruction appears smoother (**Figure 5.5c**). Such variations are not expected for a homogeneous Au NR. However, by incorporating the acquisition mask during the CS reconstruction, the gray level throughout the reconstruction is almost constant (**Figure 5.5d**). Hence, for the remainder of this work we will include the acquisition mask during the

tomographic reconstruction procedure to investigate experimentally the influence I-US, T-US and R-US acquisition procedures on the final reconstruction quality.

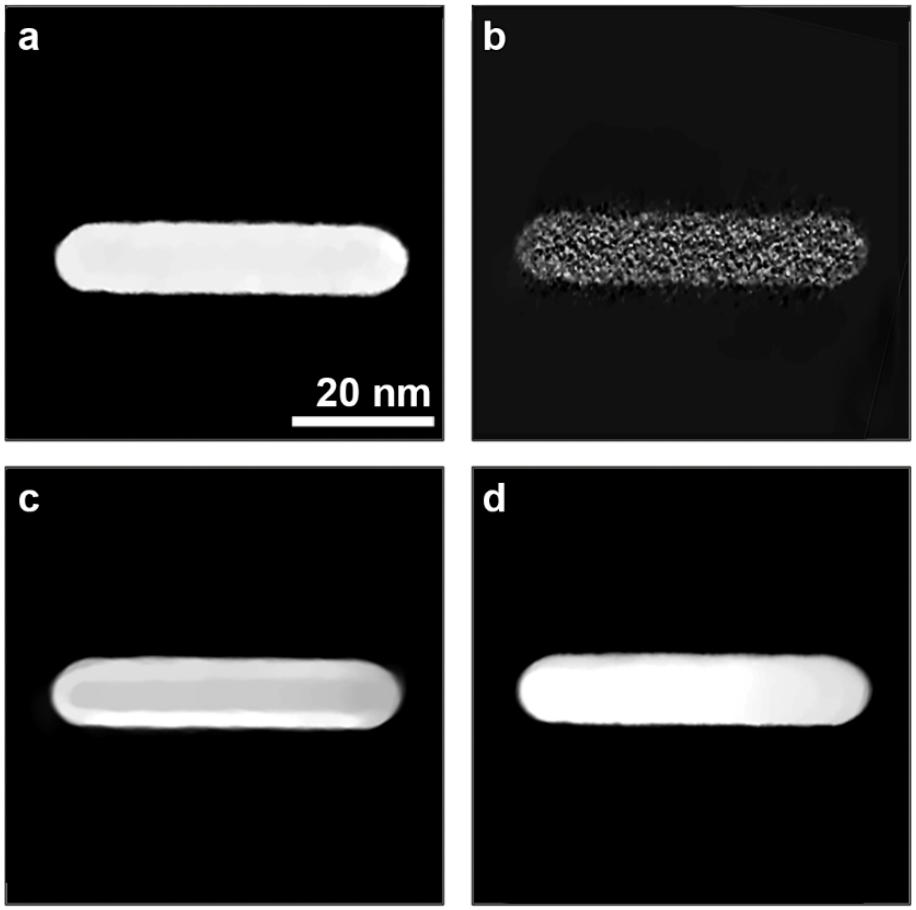

Figure 5.5*: Identical central orthoslices through 3D reconstructions of (a) the reference series, and the 20% R-US tilt series where (b) no prior information of the acquisition mask was included during the regularized reconstruction, (c) the prior knowledge of the mask was used to restore the projection images before serving as input to the reconstruction or (d) the prior knowledge of the acquisition mask was incorporated during the CS reconstruction.*

To investigate the reliability of the experimental R-US acquisition methodology and to rule out any imperfections, we created virtual R-US tilt series by multiplying the reference dataset with a random binary acquisition mask. The masks were simulated by thresholding uniformly distributed random matrices such that 20% of the pixels were set to 1 and the remaining pixels to 0. We will refer to this series as the virtual R-US series (VR-US). Both the experimental R-US as VR-US were used to recover the 3D structure of the Au NR using **Equation [5.1]**. The first column of **Figure 5.6** shows 3D renderings of the reconstructions corresponding to the 20% R-US series (**a**) and 20% VR-US series (**d**). The second and third

column illustrate non-central XY and XZ orthoslices through the respective reconstructions. Little to no difference is found between the reconstruction of the R-US and VR-US tilt series. We can therefore conclude that the experimental implementation of the CS-acquisition is reliable.

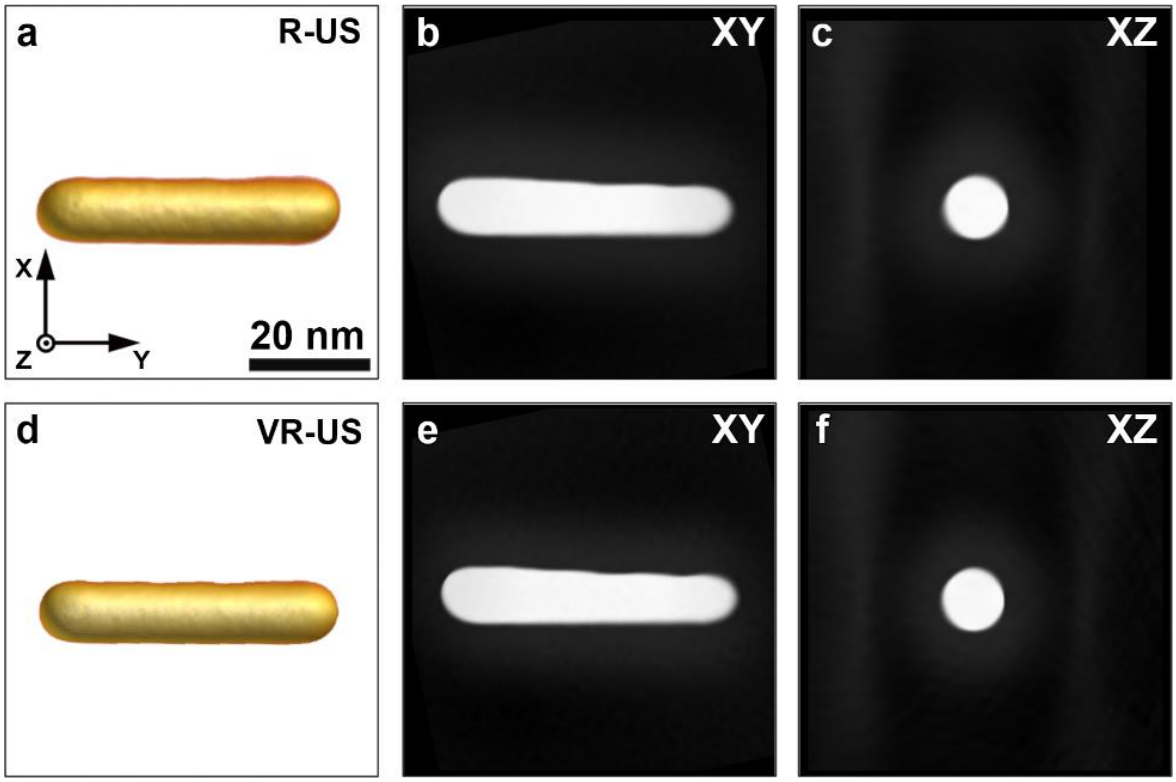

***Figure 5.6**: (a-c) 3D rendering and non-central orthogonal slices through the reconstructions of the 20% R-US tilt series. (d-f) 3D rendering and identical orthogonal slices through the 20% VR-US reconstruction.*

5.2.5 Importance of Incoherence

To stress the importance of the random sampling during R-US, structured undersampling (S-US) was examined through simulation. As opposed to randomly scanning a subset of pixels, the scanning step was here increased such that for every 5 pixels only 1 was scanned. The scanning direction was chosen perpendicular to the principal axis of the NR, similar as during the experimental acquisition. The simulated S-US projection images are shown in **Figure 5.7**.

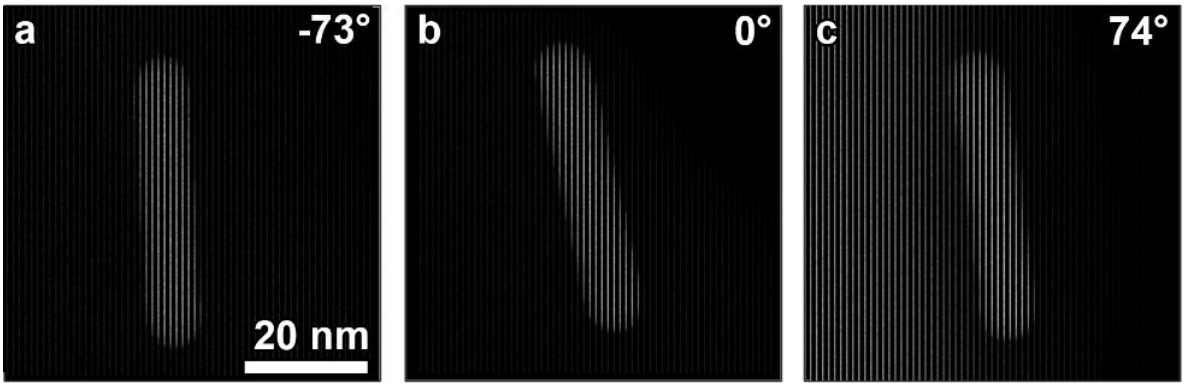

***Figure 5.7**: (a-c) Simulated S-US projection images at different tilt angles.*

A central orthoslice through the reconstruction of the S-US series is compared to those obtained from the reconstructed reference and 20% R-US series (**Figure 5.8**). As indicated by the white arrows, S-US causes ripples along the NR's surface, which are not present in the reference nor in the 20% R-US reconstruction. This validates that it is indeed essential to select the pixels in a random manner, as S-US causes aliasing artefacts when sampling below the Nyquist frequency due to the decrease in incoherence.(Donati et al., 2017)

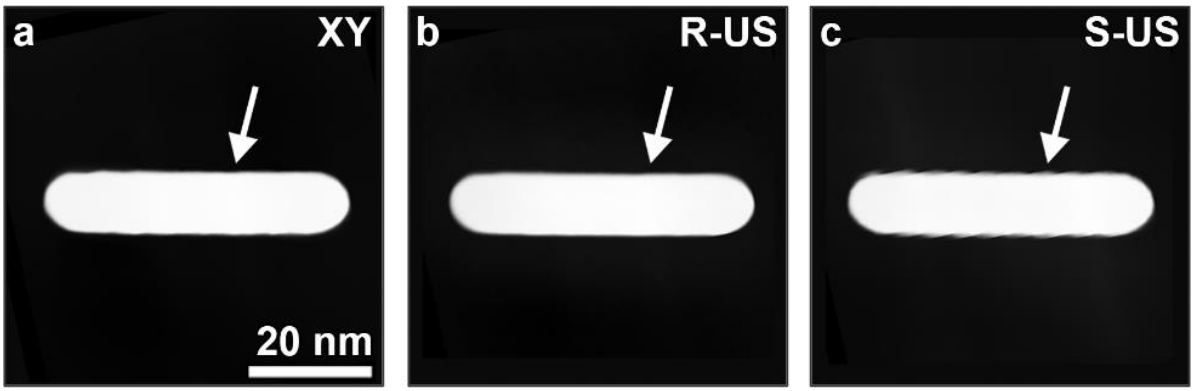

***Figure 5.8**: (a-c) Central XY orthoslices through the reconstructions of respectively the reference series, the 20% R-US series and the 20% virtual S-US series.*

5.3 Results and Discussion

Here, we will investigate the effect of various experimental dose limiting techniques (I-US, T-US and R-US) on the reconstruction quality. In order to compare the outcome of 3D reconstructions resulting from I-US, T-US and R-US in a reliable manner, we used the following approach: all reconstructions were performed following **Equation [5.1]**, with the acquisition mask set to 1 for scanned pixels. The top row of **Figure 5.9** displays 3D renderings of the reconstructions calculated from the reference series (**a**), the 50% I-US series (**b**), the 50% T-US series (**c**) and the 50% R-US (**d**). In the second and third row, non-central orthoslices along the XY and XZ plane through the reconstructions are visualized, which respectively show the presence of indentations and a facet along the NR's surface.

For all dose limiting techniques, reconstructions with little to no gray level variation in the orthoslices are obtained, in agreement with the expected homogeneity of a Au NR. Furthermore, the surface structure is recovered relatively well. To illustrate the good agreement between the various reconstructions, they were all segmented and the absolute difference to the binary reference reconstruction was calculated (**Figure 5.9m,q**). Hence, voxels which are labelled differently in the segmentations of the undersampled data, in comparison to the binary reference reconstruction, are highlighted. The threshold was determined by Otsu's method(Otsu, 1979) for each reconstruction separately. The results are displayed in the last two rows of **Figure 5.9** for the XY and XZ orthoslices. For all methods, the differences are found to be very sparse and confirm the qualitative interpretation.

When the dose is lowered to 20% (**Figure 5.10**), it can be seen that the surface characteristics of the NR become more difficult to distinguish. From the XY orthoslices (**Figure 5.10,** second row) features corresponding to surface roughness have almost disappeared, except for the I-US case (**Figure 5.10f**) where some details remain visible. Similar observations can be made from the XZ orthoslices (**Figure 5.10,** third row). Both the T-US as the R-US reconstruction (**k-l**) yield a more cylindrical shape of the NR, whereas in the I-US reconstruction (**j**) the surface facet remains pronounced. In the two bottom rows of **Figure 5.10**, the misclassified voxels with respect to the reference data sets are presented. Whereas the dissimilarity for the I-US reconstruction (**n,r**) remains restricted, the difference for both the T-US (**o,s**) and R-US (**p,t**) is more significant.

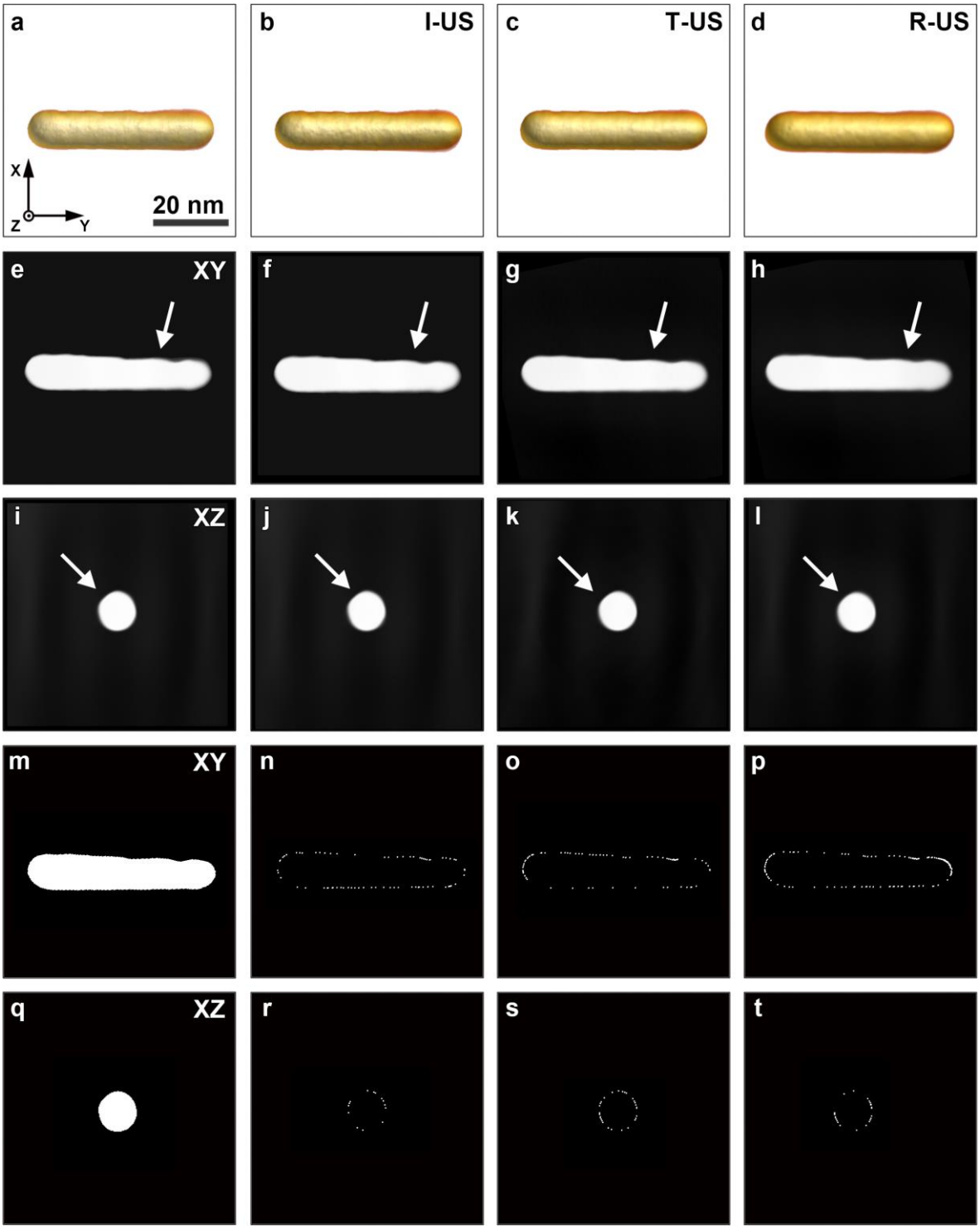

***Figure 5.9**: (a-l) 3D renderings and related orthoslices of the reconstructions from the reference and 50% undersampled tilt series. (m-t) orthoslices through the segmented reference reconstruction and the associated absolute differences with the segmented reconstructions of the 50% undersampled tilt series.*

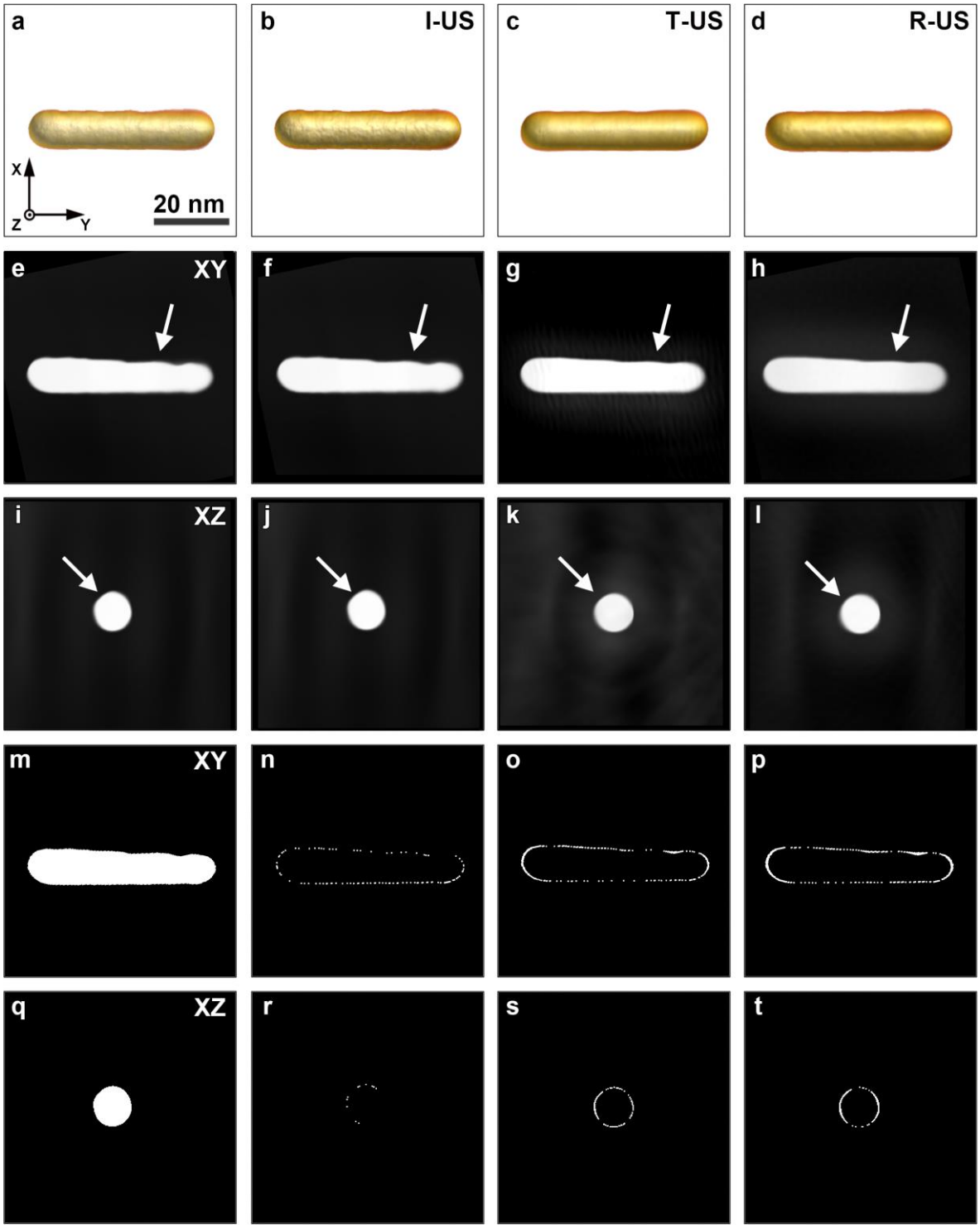

***Figure 5.10**: (a-l) 3D renderings and related orthoslices of the reconstructions from the reference and 20% undersampled tilt series. (m-t) othoslices through the segmented reference reconstruction and the associated absolute differences with the segmented reconstructions of the 20% undersampled tilt series.*

To investigate the differences in a quantitative manner, the shape error E_s was calculated as a weighted sum over absolute differences for each reconstruction with respect to the reference as follows:

$$E_s = \frac{\sum \left| Rec_{us}^{seg} - Rec_{ref}^{seg} \right|}{\sum Rec_{ref}^{seg}} * 100 \qquad [5.2]$$

Rec_{ref}^{seg} and Rec_{us}^{seg} refer to the segmented 3D reconstructions of the reference and undersampled series respectively. The sum over Rec_{ref}^{seg} defines the volume of the reference reconstruction. Before calculating the absolute difference, both reconstructions were optimally aligned using a MATLAB implementation of intensity-based rigid registration. Through gradient descent optimization, this operation minimizes the MSE between the two volumes by translating and rotating one of both volumes.

In this manner, the shape error E_s determines the relative amount of difference in shape between the reconstructions based on the reference and undersampled series, as a percentage of the total amount of misclassified voxels. E_s has the advantage over other quantitative measures such as the absolute difference or the mean squared error, that it is less influenced by background variations or small differences in gray level within the reconstructed object. The threshold for segmentation was determined by Otsu's method(Otsu, 1979) for each reconstruction separately. The outcome of this quantitative assessment is summarized in **Table 5.2.**

Since TV based CS reconstruction algorithms suppresses gray level variety within the reconstructed object, segmentation through binarization algorithms such as Otsu's method become straightforward. Hence the detrimental factor for the accuracy of the shape error, is the alignment between the undersampled and reference reconstruction. As explained before, this alignment is optimized using a MATLAB implementation of intensity-based image registration. To investigate the accuracy of this method, a simulation study was performed for which the reference reconstruction was randomly translated along three dimensions. Afterwards, the translated reference reconstruction was aligned back to the non-translated reference reconstruction, utilizing the proposed image registration technique, and the shape error was calculated. This procedure was repeated in total 300 times. If the alignment would be perfect one would expect to find for every repetition a shape error equal

to 0%, since the shape error was calculated between identical objects. Yet on average a shape error of 0.01% was found, providing the measure for the error on the derived shape error.

	I-US	*T-US*	*R-US*
E_s *50% undersampling*	**0.91** ± 0.01 %	1.81 ± 0.01 %	2.22 ± 0.01 %
E_s *20% undersampling*	**0.95** ± 0.01 %	6.00 ± 0.01 %	7.86 ± 0.01 %

Table 5.2*: The shape error (E_S) calculated for the reconstruction following from the I-US, T-US and R-US series, in case of 50% and 20% undersampling*

In agreement with the visual interpretation of our results, the shape errors indicate that the difference between the reconstructions remains small for 50% undersampling, independent of the used approach. Even for 50% T-US where the tilt increment was increased to 6°, which is higher than the typical tilt increment used for most electron tomography experiments (1-3°), the shape error is still limited to 2%. This error is similar to the error observed for 50% undersampling using R-US. These results are of keen interest for the development of strategies to decrease the duration of conventional tomography experiments, which is of importance to realize high-throughput electron tomography. However, recording a smaller amount of projection images is likely to be more advantageous than lowering the number of scanned pixels in each projection image. Indeed, in the former case less pre-acquisition steps, such as refocusing and repositioning at every tilt angle, are required. These additional actions will increase the total electron dose that is required, especially as often no beam shutter is used. Consequently, the illumination is present for the whole recording time, not just the exposure time of the actual images. T-US may therefore be considered beneficial in comparison to I-US and R-US, since the reduced amount of pre-acquisition steps results in a lower total accumulated dose. Moreover, both the refocusing and repositioning steps are more challenging for R-US, because of the low amount of scanned pixels. On the other hand, for large tilt increments, the necessary alignment of the tilt series becomes more complex. Consequently, a combinational approach between T-US and I-US is likely most optimal, but will also depend on the type of material being investigated.

For 20% undersampling, both the T-US as the R-US reconstructions become increasingly less accurate, while the shape error corresponding to the I-US reconstruction remains below 1%. This is in agreement with the visual comparison that was made in **Figure**

5.10. Based on these experimental results, we therefore conclude that I-US yields superior results in comparison to T-US and R-US, especially for the low dose case (20%). Furthermore, the quality of the reconstructions based on T-US and R-US is comparable. Our results indicate that for an electron tomography experiment, random sampling provides no benefit over spreading the same electron dose over all pixels. As presented earlier in literature, the inevitable presence of Poisson noise in every projection image severely bounds the performance of CS on R-US data.(Raginsky et al., 2010; Van den Broek et al., 2019) These earlier statements are here directly confirmed by our experimental results. As the theoretical constraint on CS in the presence of predominantly counting noise is general, and not limited to a specific sparsity transform, we expect these findings to be relevant even for other nanoparticle systems which are sparse in bases other than the gradient domain. Hence for a fixed electron budget, it is preferential to spread the total amount of electrons across as many pixels as possible.

Earlier theoretical predictions on the capacity of R-US to outperform T-US(Donati et al., 2017), were not found to be in accordance to the experimental findings. For a similar angular range and increment, no large difference in performance was found between R-US and T-US. One possible explanation could be related to the lack of a realistic noise model incorporated in the theoretical studies. Indeed, counting noise severely bounds the accuracy which can be reached when restoring R-US data by CS. When this essential aspect is neglected, it may result into optimistic prospects for R-US in comparison to experimental results were counting noise is predominant and unavoidable.

5.4 Conclusion

In this chapter, we evaluated three different dose limiting techniques for electron tomography of nanoparticles: lowering the number of two-dimensional projection images, reducing the probe current during the acquisition and scanning a smaller number of pixels in the 2D projection images, while keeping the total electron dose constant in all three cases. This comparison was made using experimentally acquired tilt series of a gold NR. In agreement with earlier theoretical work performed for 2D images, we conclude that for an electron tomography experiment, random- or tilt undersampling provide no benefit over spreading the same electron dose over all pixels.

5.5 Outlook

It is well known that besides the total electron dose, the dose rate plays an important role in sample degradation.(Jones et al., 2018; Thong et al., 2001) R-US is an effective strategy to lower the dose rate during the image acquisition. Since R-US does not necessarily provide a benefit over I-US, one could think of a synergistic approach between R-US an I-US instead. In contrast to scanning across the region of interest in the typical "sawtooth" manner, from left-to-right and top-to-bottom, an alternative scanning pattern could be devised for which all pixels are scanned in a completely random manner but with a decreased probe current. For sawtooth scanning, every illuminated area potentially overlaps with the previously excited region. Such dose accumulation may very well damage the sample. The random scan mode, on the other hand, would not only reduce the total electron dose, but the damage accumulation as well.(Zobelli et al., 2019) By ensuring that the illuminated area is sufficiently far from the previously exposed region, the accumulation of dose is minimized. In this manner, the scanned region has time to transition back to its ground state through, for instance, diffusion.

Nevertheless, fully random scanning suffers from the slow response time of deflection coils in the TEM. Therefore, the usage of alternative scanning patterns has been explored. A variation to fully random scanning consists out of scanning patterns wherefore the region of interest is scanned in a sequential pattern but only a fraction of pixels are acquired per pass(Thong et al., 2001). Other alternatives include line hopping(Kovarik et al., 2016), wherein each line is fully scanned but a predefined amount of lines is skipped per pass or the usage of Hilbert patterns(Biswas, 2000; Velazco et al., 2020). However, at best, these techniques are able to acquire images as fast as by conventional, sawtooth means. They do not necessarily decrease the duration of an electron tomography experiments and therefore do not improve its throughput. However, we demonstrated that I-US consistently outperforms R-US and T-US in terms of reconstruction accuracy. This information can be used to develop new, fast, acquisition methodologies. In the next chapter, we therefore propose a fast tomographic approach during which the projection images are acquired in a short amount of time (I-US) in order to improve the throughput of electron tomography experiments.

PART II: ACCELERATED ACQUISITION

6. Fast HAADF-STEM for High-Throughput Electron Tomography

A major drawback of electron tomography is the time required to perform a complete acquisition. This severely limits the throughput and statistical relevance of electron tomography experiments. In this chapter, we introduce a fast acquisition scheme for HAADF-STEM tomography, capable of reducing the total acquisition time by a factor of 10.

This chapter is based on:

Vanrompay, H., Bladt, E., Albrecht, W., Béché, A., Zakhozheva, M., Sánchez-Iglesias, A., Liz-Marzán, L. M., & Bals, S. (2018). 3D characterization of heat-induced morphological changes of Au nanostars by fast: In situ electron tomography. *Nanoscale*, *10*(48), 22792–22801. https://doi.org/10.1039/c8nr08376b

Vanrompay, H., Skorikov, A., Bladt, E., Béché, A., Freitag B., Verbeeck, J., & Bals, S. (2020). Fast versus conventional HAADF-STEM tomography: advantages and challenges. *In preparation.*

The synthesis of all nanoparticles was carried out at the Bionanoplasmonics Laboratory, CIC biomaGUNE in Spain. Together with A. Béché and E. Bladt, I was responsible for the development of the fast acquisition strategies. The acquisition of the all TEM data was performed in collaboration with E. Bladt. I performed all data processing and quantification.

6.1 Introduction

Electron tomography is currently a standard technique to visualize the morphology and internal structure of a wide variety of nanostructures in 3D. A major drawback of the technique is the time required to acquire a full tomographic tilt series, which hinders collecting enough data to obtain statistically relevant results. Moreover, the long lasting acquisition hampers the investigation of dynamic processes in 3D and may cause undesired changes within the nanoparticles. Therefore, one of the emerging challenges in the field of electron tomography is to improve the speed of tomography experiments, while preserving the quality of the 3D reconstructions. Overcoming such challenge will enable 3D TEM experiments which are not easily performed using conventional electron tomography due to possible beam-induced changes or simply due to time limitations. Recently, first attempts were made to accelerate the acquisition process of electron tomography tilt series(Migunov et al., 2015; Roiban et al., 2018) in TEM mode. In this chapter, we expand upon this research and introduce fast HAADF-STEM tomography. First, we discuss the developed acquisition strategy and all processing required to obtain a reconstruction from such "fast" datasets. Next, the proposed technique is qualitatively and quantitatively compared to conventional tomography. Finally, we introduce computational and hardware solutions to further improve upon the fast acquisition strategy.

6.2 Continuous HAADF-STEM tomography

A conventional electron tomography experiment is composed out of several consecutive steps (**Figure 6.1**, top). To retrieve the 3D structure of a nanoparticle, typically a tilt series of images is recorded from -75˚ to +75˚, with a tilt increment of 3˚. Such angular sampling provides a good compromise between the required acquisition time and the accuracy of the obtained reconstruction, when using standard reconstruction algorithms such as SIRT. At each tilt angle, the sample has to be shifted back in the field of view and the image has to be refocused before the next acquisition. Even when selecting a low frame time, the necessity of performing these steps in succession, attributes to a lengthy acquisition of approximately 1 hour.

Here, we propose to acquire the full tilt series in a continuous manner, meaning that the holder is rotating uninterruptedly and intermediate refocusing and repositioning is performed manually at the same time (**Figure 6.1**, bottom). In this manner, we avoid the

individual repositioning and refocus steps and are able to reduce the total acquisition time for a tilt series by at least a factor of 10.

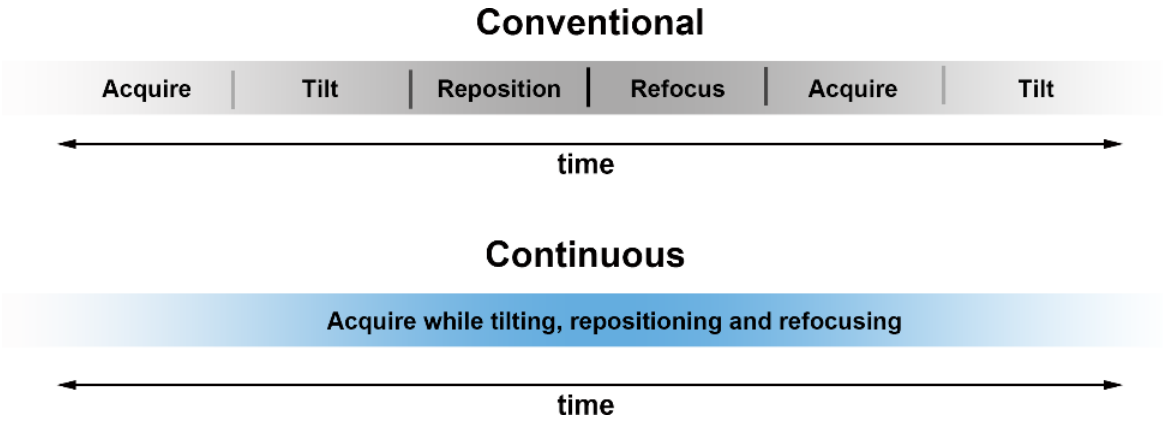

***Figure 6.1**: Graphic illustration of the difference between conventional and the proposed continuous tomography*

6.2.1 Acquisition

When acquiring in a continuous manner, the holder is tilted uninterruptedly while continuously acquiring projection images. Rather than a set of projection images, as is the case for conventional tomography, a projection "movie" is recorded instead. Because of the continuous tilt, the nanoparticle will also perform a slight tilt rotation while acquiring a single HAADF-STEM "frame". It is essential to keep the tilt angle per frame small enough to treat the frames as static projection images. If not, blurring effects might appear and deteriorate the reconstruction.(Baek & Pelc, 2011; Roiban et al., 2018) Such rotational blurring can be minimized by limiting the sample tilt per frame, either by increasing the acquisition speed, or by reducing the tilting speed.(Kalender, 2006; Kalender et al., 1990; Kerl et al., 2011; Marshall & Bosmans, 2012) Clearly, a compromise has to be made between tilt speed, frame time and signal-to-noise ratio during the acquisition.

In this chapter, we selected a frame time of 1 s and a tilt speed such that the sample was tilted from -75˚ to 75˚ in 5 minutes of time. This corresponds to a tilt increment of 0.5° per image, which is sufficiently small to treat the continuous projection movie as being built up out of static projection images. When using longer frame times at a similar tilting speed, it becomes impossible to track the nanoparticle and motion artefacts are observed, which deteriorated the quality of the continuous acquisition. Much shorter frame times, on the other hand, lower signal-to-noise ratio of the recorded images which might impede the manual

tracking and refocusing of the particle. Therefore, a frame time of 1 s and tilt increment of 0.5° per image were chosen as a good compromise between these factors. An example of a raw continuous tilt series is provided in the **Supplementary Movie 1** (see QR-code below)**.** In order to use the continuous projection image for electron tomography, an angle needs to be assigned to each projection. Given our static projection approximation, we gave a constant angle to each projection image, equal to the average tilt angle of the pixels in that image, as illustrated in **Figure 6.2**.

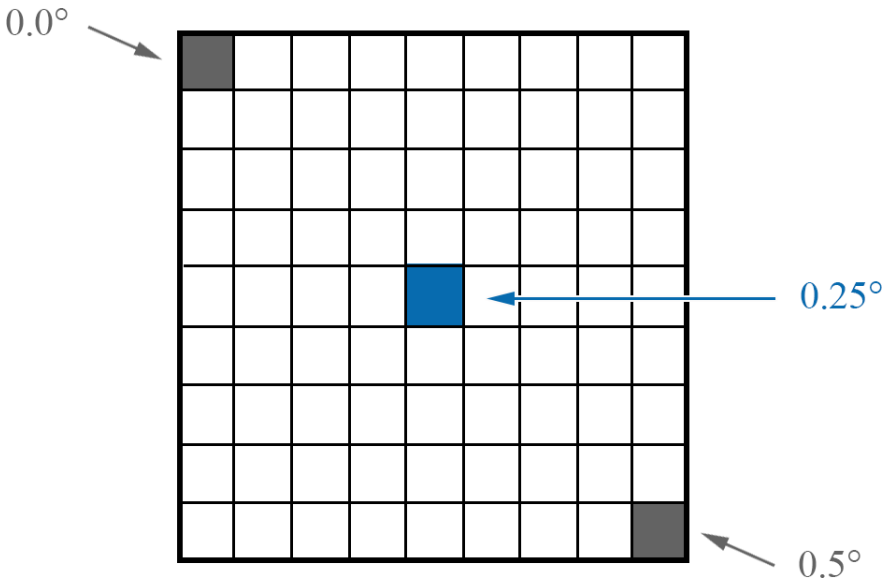

Figure 6.2*: For the static approximation, each projection frame was assigned its average tilt angle.*

6.2.2 Noise Correction

In **Figure 6.3a,** a continuous HAADF-STEM projection image of a Au decahedron is presented. Jitter along the scanning direction, can be observed due to mechanical instabilities during the continuous acquisition. Because of their directionality, these artefacts appear as a band of frequencies in Fourier space (**Figure 6.3b,** white arrow). The first step of the processing of the continuous data consists out of correcting for these artefacts by applying a directed low pass filter within Fourier space (**Figure 6.3c**), resulting in an improved image quality (**Figure 6.3d**). The width, orientation, inner radius and outer radius of this dedicated filter are manually tuned. Increasing, for instance, the width of the filter, improves the de-noising, but introduces additional directional blurring as well. It is clear that a compromise has to be made.

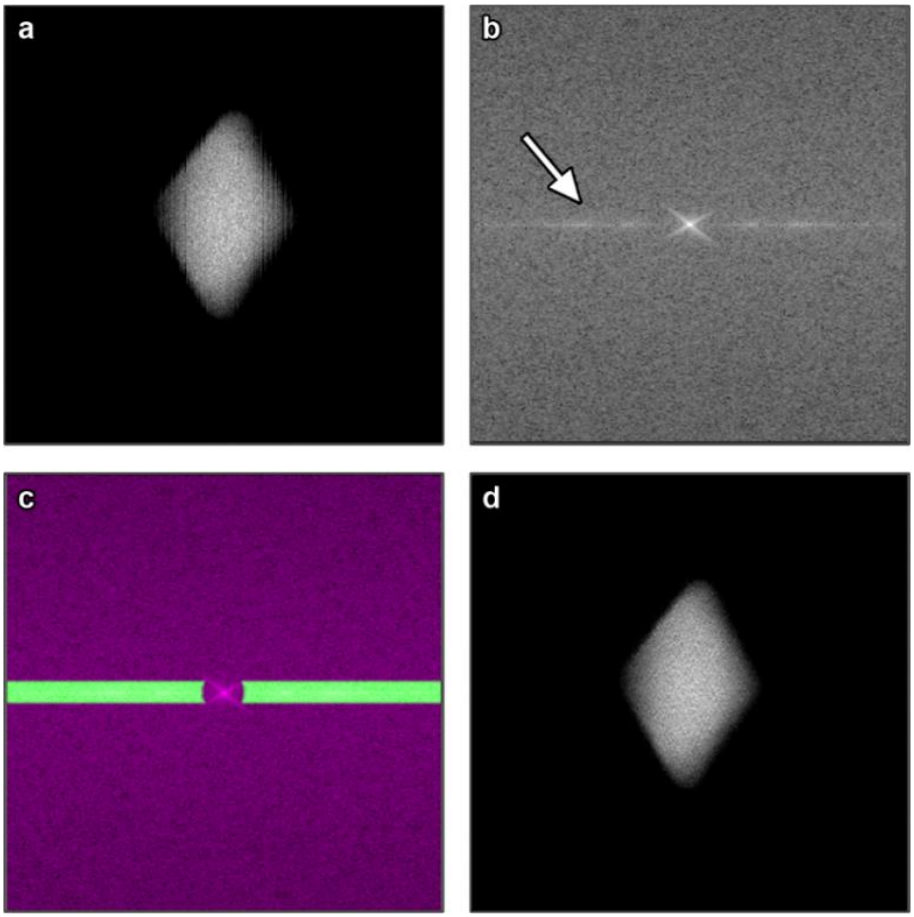

Figure 6.3*: (a) HAADF-STEM image obtained during the fast* continuous *acquisition of a single nanoparticle, revealing noise in the direction of scanning. (b) The amplitude of the Fourier transform of (a). (c) The dedicated low pass filter used to remove these frequencies and restore the projection image (d).*

6.2.3 Alignment

After correcting for the scanning jitter, the images are aligned using a cross-correlation approach. Since an imperfect setting of the eucentric height during the continuous acquisition causes considerable drift, the sample may partially move out of the field of view or movement artefacts may occur. In such cases the standard cross-correlation approach, where each image is aligned to the previous one, performs sub optimally. Therefore, we align all projection images to the average of a user selected number of previous projection images (typically 5 to 10). This considerably improves the stability of the alignment procedure. Furthermore, it reduces the negative influence of defocused and/or deformed images, caused by the manual tracking and focusing during the continuous acquisition. In **Figure 6.4,** we compare the average of the tilt series after it was aligned based on (**a**) only the previous

projection image or (**b**) the average of the 5 previous projection images. It can be seen that no precise alignment is obtained when the alignment is based on only the previous projection image. As expected, major improvements are found when aligning the projection images to an average of a subset of previous projection images. After performing the image alignment, tilt axis alignment is carried out as described in **Chapter 3**.

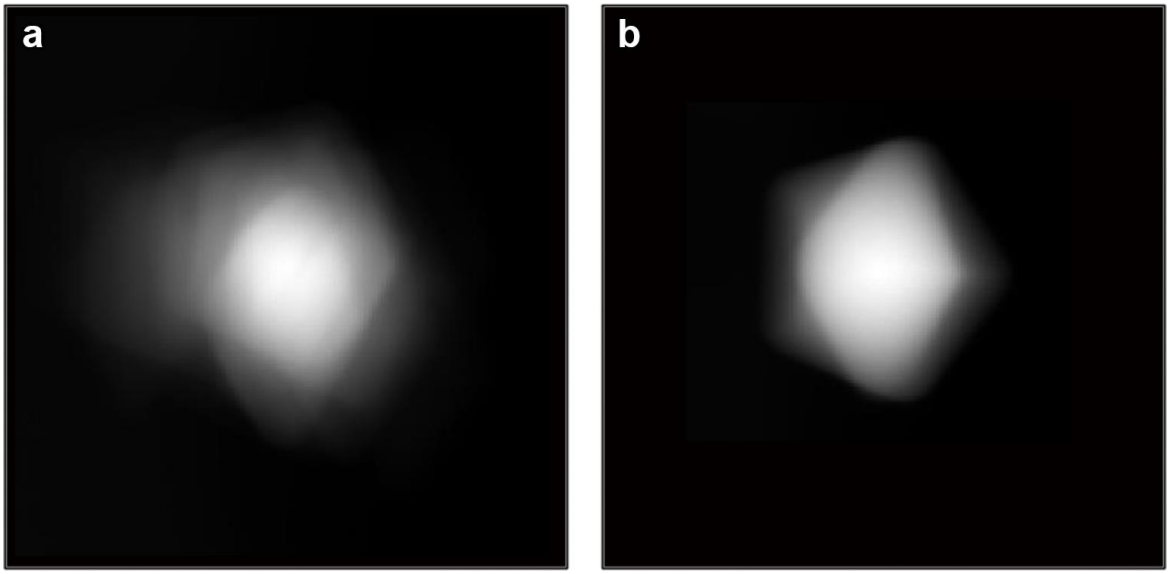

Figure 6.3*: Comparison of the average of the aligned tilt serues for which the alignment was performed using (a) only the previous projection image or (b) the average of the 5 previous projection images.*

6.2.4 Image Selection and Reconstruction

Distorted projection images do not only hamper the alignment; they will also negatively influence the reconstruction accuracy. Since the focus is manually tuned during the acquisition, defocused images can be present in the projection stack (**Figure 6.4a**)**.** In addition**,** an imperfect setting of the eucentric height and the associated necessity of manual tracking the nanoparticle during the acquisition, can induce motion artefacts. In **Figure 6.4b**, two subsequent projection images are superimposed, one in magenta and the other in green. Although that the tilt increment between both is small (0.5°), considerable differences are found which can be attributed to particle movement rather than the small tilt.

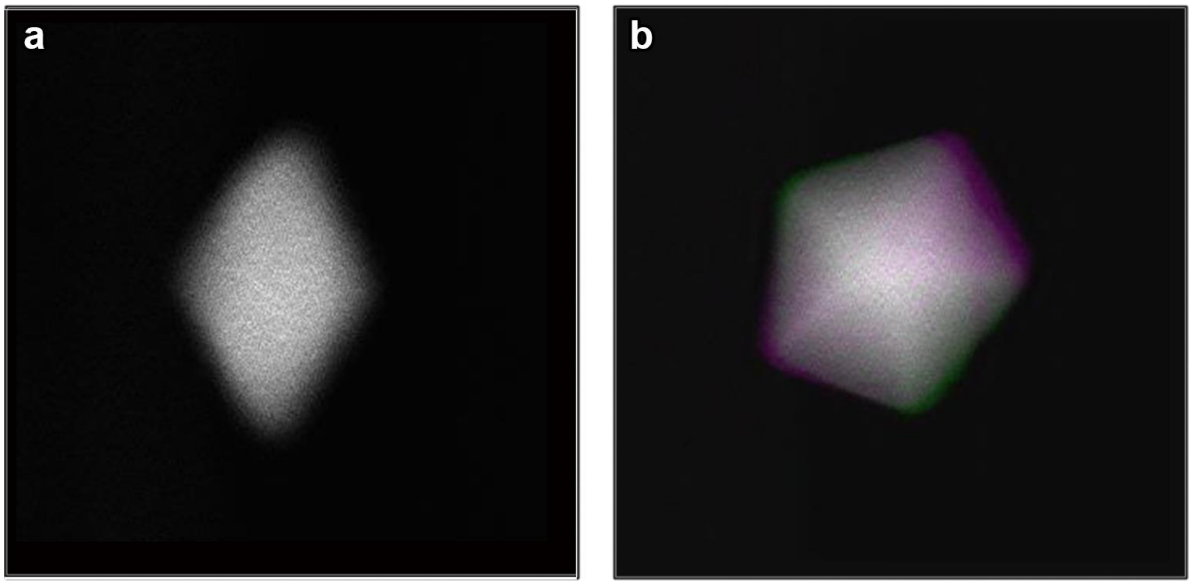

***Figure 6.4**: Example of the two of the most common remaining distortions related to (a) defocus and (b) movement artefacts. In (b) an overlay image is shown of two subsequent projection images. One is visualized in green and the other in magenta.*

After the initial alignment, deteriorated projection images are therefore removed from the tilt series in an automated manner (**Figure 6.5**). First, an initial reconstruction is calculated, from which forward projections are calculated for all angles present in the continuous series. Comparison between the forward projected and experimentally acquired projection images, allows to determine which projection images are of the least quality (e.g. **Figure 6.4**). Hereby, we evaluate the absolute deviation around the median of the normalized root mean square error (RMSE) between both images(Fienup, 1997), to assess which images predominantly deteriorate the reconstruction accuracy. The absolute deviation of the median provides a measure for the relative difference of the RMSE of a single projection image to the median of the RMSE of all projection images. It therefore provides an efficient method to detect outliers (i.e. the most deteriorated projection images) within the dataset.

The RMSE between each experimentally acquired projection image and their forward projected counterpart is calculated as follows:

$$RMSE_i = \sqrt{\sum_j^N \left(p_j^{exp,i} - p_j^{sim,i}\right)^2 / N}. \qquad [6.1]$$

The experimental continuous projection images and their forward projected counterparts are respectively defined as $p^{exp}$and p^{sim}. N stands for the amount of pixels in the projection

images. Once the error measure is obtained for each projection image, the absolute deviation around the median, is calculated as follows:

$$RMSE_i' = \frac{|RMSE_i - median(RMSE)|}{median(RMSE)}. \quad [6.2]$$

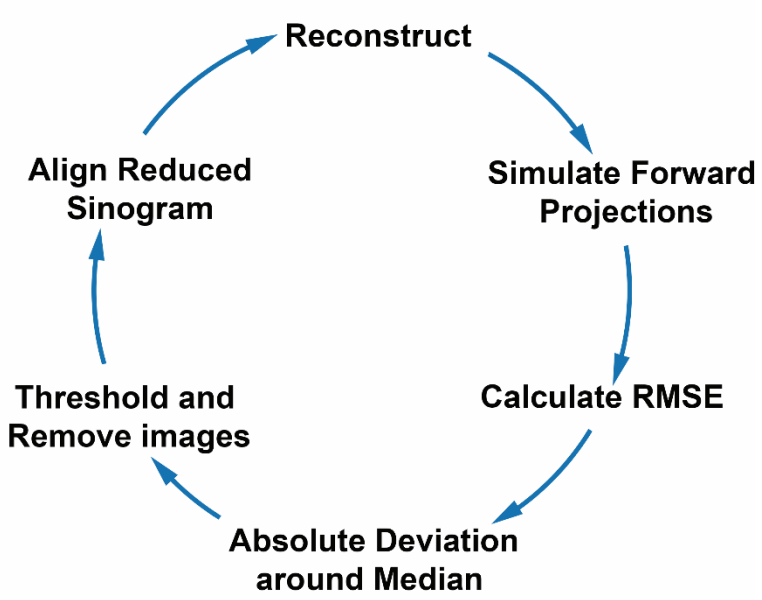

***Figure 6.5**: Illustration of the iterative scheme, used to remove deteriorated projection images.*

As stated before, this difference thus provides an indication for the relative distance of the RMSE of a certain projection image, to the median of the RMSEs of the entire projection series. However, images acquired at high tilt are generally shadowed by the holder and/or grid and therefore intrinsically differ more from their forward projected counterparts. Therefore, a low order polynomial was first fitted and subtracted from the absolute deviation signal. In **Figure 6.7a,** the absolute deviation around the median of the RMSE is plotted (blue line). By manually thresholding (red line) the absolute deviation, the most distorted images can be detected and consequently removed from the tilt series. **Figure 6.7 b-c** respectively depict one of the removed projection images alongside their forward projected counterpart. Finally, the reduced projection stack is realigned, as was discussed above, and this procedure is iteratively repeated until the values for the absolute deviations are below the preset threshold. Given the oversampling of projection images compared to a conventional series, removal of these images from the tilt series will not lower the quality of

the reconstruction. Finally, the 3D reconstruction is calculated by using the reduced tilt series as input to the EM reconstruction algorithm for 20 iterations.

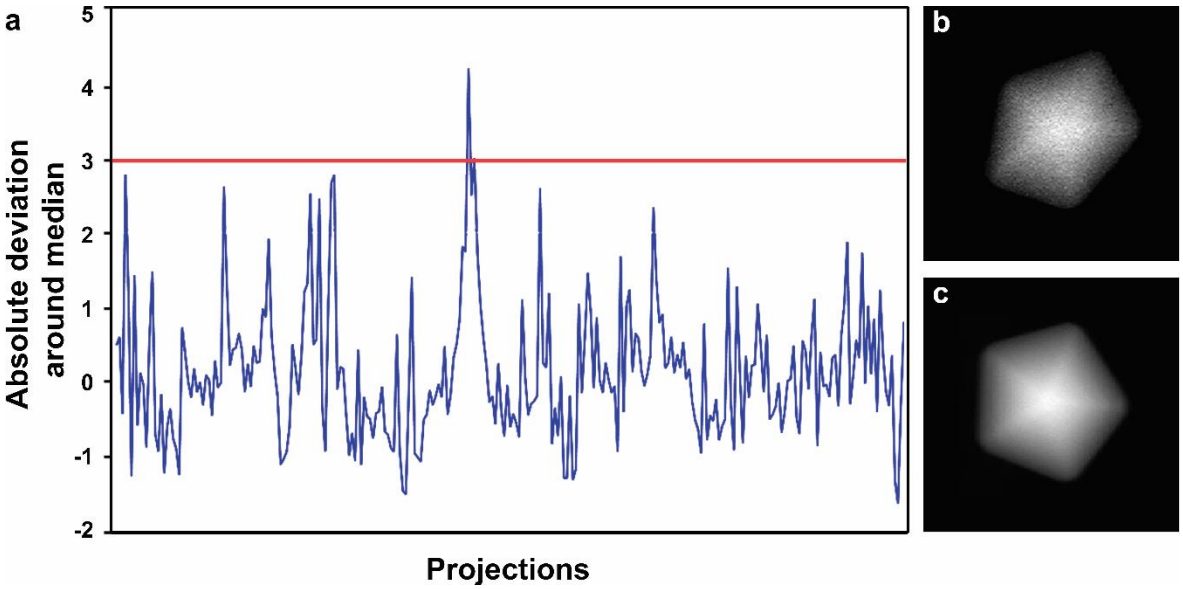

***Figure 6.7**: (a) Plot of the absolute deviation around the median of the normalized root mean square error (RMSE) between each (b) experimental projection and (c) its simulated counterpart.*

6.3 Qualitative and Quantitative Comparison

To validate the accuracy of the continuous acquisition approach, conventional and continuous tomographic series were obtained for the same nanoparticles. Each conventional series consisted out of 51 projection images which were acquired over an angular range of ± 75° with a tilt increment of 3°, at either the Thermo Fisher Scientific Titan TEM operated at 300 kV or Thermo Fisher Scientific Tecnai Osiris TEM operated at 200 kV. For every conventional projection image, a frame time of 6 s was used. Additional focus and repositioning steps lead to a total acquisition time of approximately 1 hour per conventional series. Next, fast continuous tilt series were collected from the same nanoparticles, using the same microscopes, with identical magnification and angular range. Details on the experimental parameters of the continuous series are listed in **Table 6.1**.

	Sample description	*Frame size (px)*	*Frame time (s)*	*Pixel size (pm)*	*Dwell time (µs)*	*Microscope*
Sample 1	Au decahedron	1024 x 1024	1	386	1	Titan (300 kV)
Sample 2	Au pentahedron	1024 x 1024	1	386	1	Titan (300 kV)
Sample 3	Au nanosphere	1024 x 1024	1	386	1	Titan (300 kV)
Sample 4	Au bipyramid	512 x 512	1	597	3	Osiris (200 kV)
Sample 5	Au nanostar	1024 x 1024	0.5	386	0.5	Titan (300 kV)
Sample 6	Au nanostar	1024 x 1024	0.5	386	0.5	Titan (300 kV)

***Table 6.1**: Experimental details of the continuous series acquired for both the qualitative and quantitative comparison.*

In **Figures 6.8-6.13,** a qualitative comparison is made between both acquisition techniques for the different nanoparticles. In each top row of the figures, a 3D rendering of the conventional reconstruction, together with two central orthoslices through the reconstruction are presented. The orientation of the orthoslices is indicated in the top right corner. In the second row, similar results are provided for the reconstruction obtained from a continuous tilt series. The bottom row displays the absolute difference between the segmented reconstructions. The threshold for the segmentation was determined based on the Otsu method for each reconstruction separately.(Otsu, 1979) In this manner, the absolute difference displays those voxels which are misclassified in the segmented reconstruction of the continuous acquisition in comparison to the segmented reconstruction of the conventional acquisition. To ensure that the observed differences are not related to misalignment between both reconstructions, the reconstructions were aligned to each other using intensity based image rigid registration prior to the segmentation, as previously explained in **Chapter 5**.

The overall shape of the morphologies based on continuous tilting show a good qualitative agreement to the conventional ones. Especially the isotropic nanoparticles (**Figures 6.8-6.11**) are well represented by the reconstruction of the continuous acquisition. In these cases, we can easily identify the edges or facets of the nanoparticles in the orthoslices through the reconstruction of the continuous acquisition. For the isotropic nanoparticles, the orthoslices through the absolute differences reveal only a thin layer of misclassified voxels for every investigated nanoparticle. This indicates that the continuous approach causes a slight blurring which can result from the application of the low pass filter, the fast acquisition, or the remaining deformed and/or defocused projection images still present in the tilt series. For the anisotropic nanostars (NSs) (**Figures 6.12-6.13**) the amount of blurring becomes more substantial and conceals small features present in the reconstruction. Nevertheless, the general shape of the reconstruction remains well represented. Once more, a thin layer of misclassified voxels is found at the surface of the nanoparticles, caused by blurring of the reconstruction.

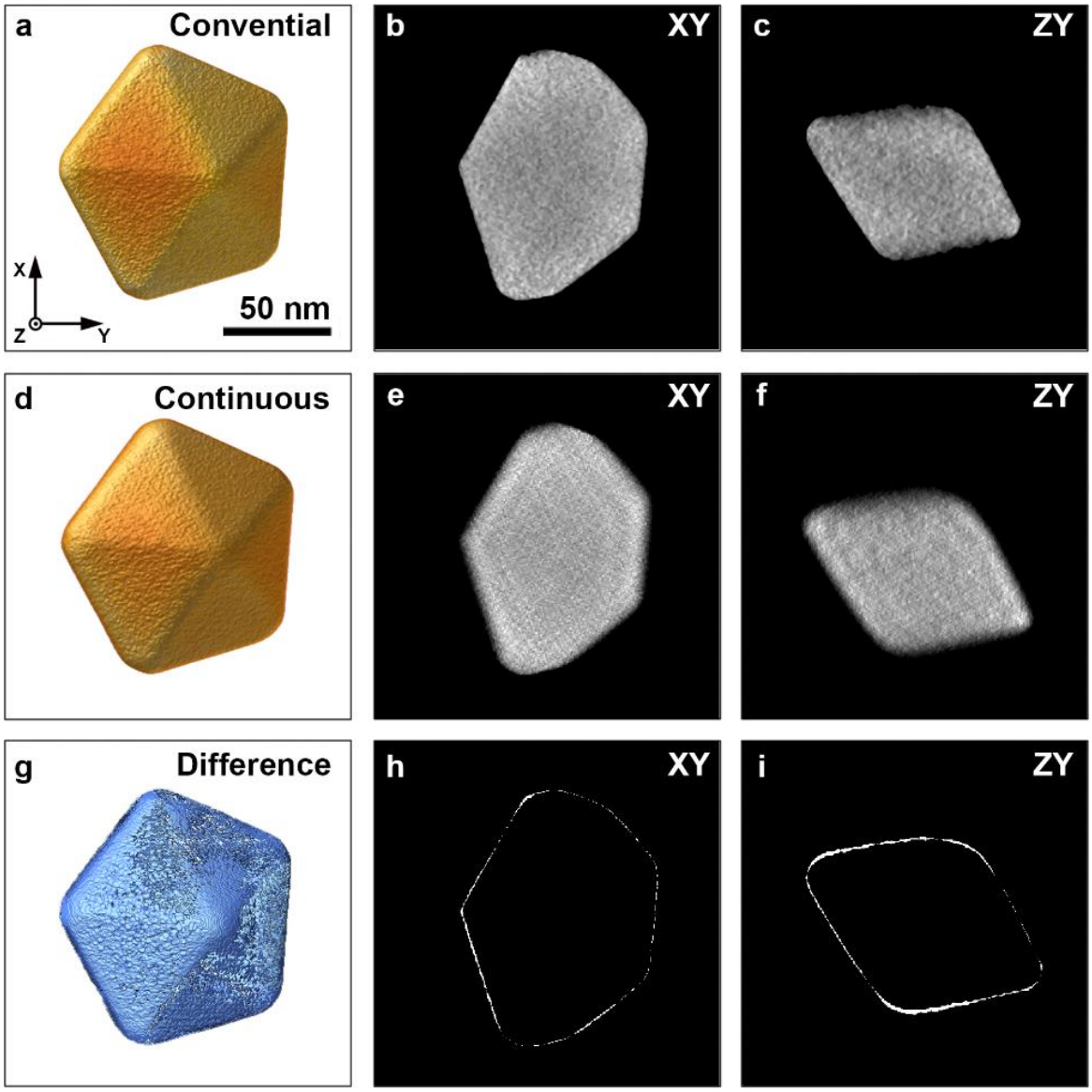

***Figure 6.8**: (a-c) 3D rendering of the reconstruction of the conventionally acquired tilt series of a Au decahedron, paired by 2 central orthoslices through it. (d-f) 3D rendering of the reconstruction of the continuously acquired tilt series, paired by 2 central orthoslices through it. (g-i) 3D rendering of the absolute difference, paired by 2 central orthoslices through it.*

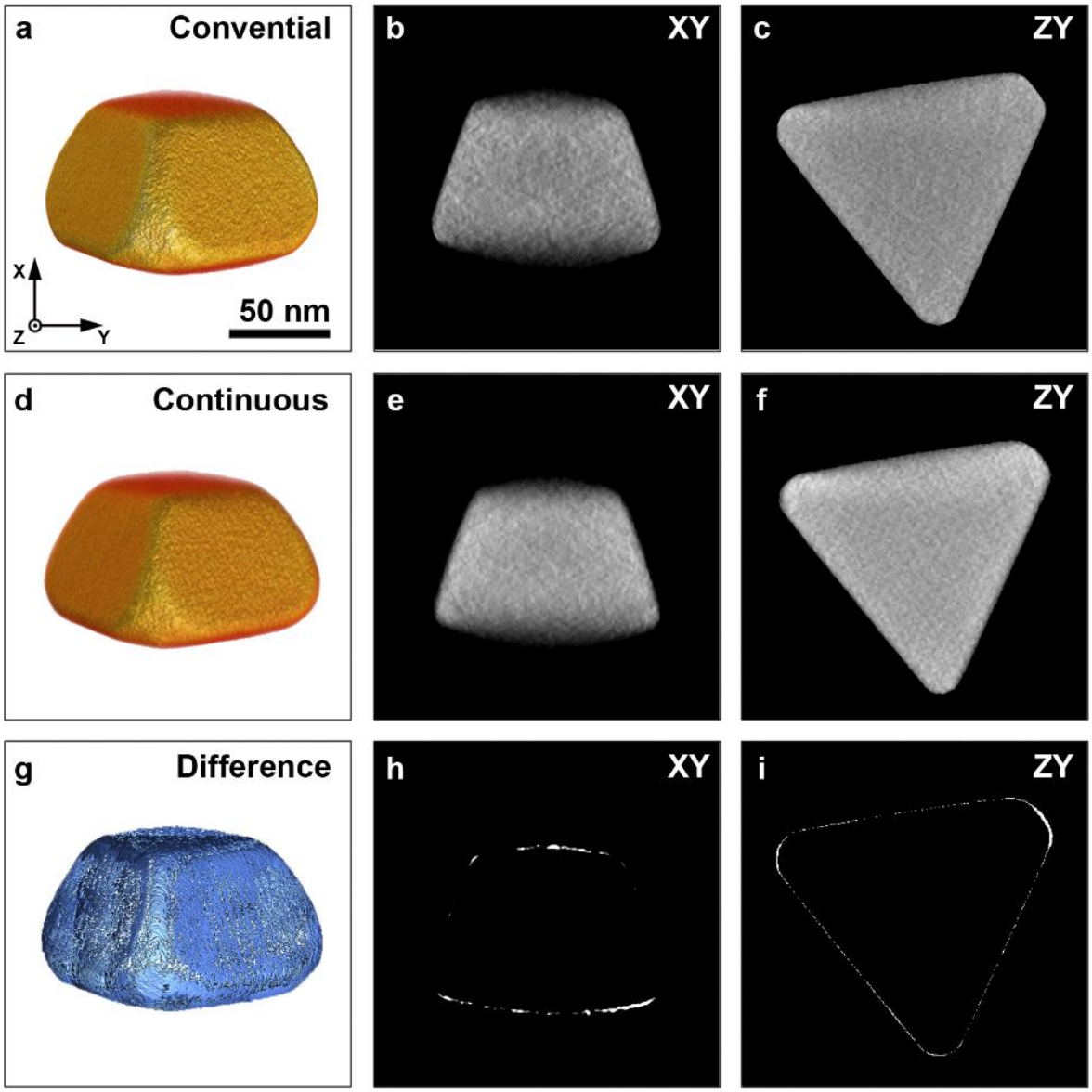

***Figure 6.9**: (a-c) 3D rendering of the reconstruction of the conventionally acquired tilt series of a Au pentahedron, paired by 2 central orthoslices through it. (d-f) 3D rendering of the reconstruction of the continuously acquired tilt series, paired by 2 central orthoslices through it. (g-i) 3D rendering of the absolute difference, paired by 2 central orthoslices through it.*

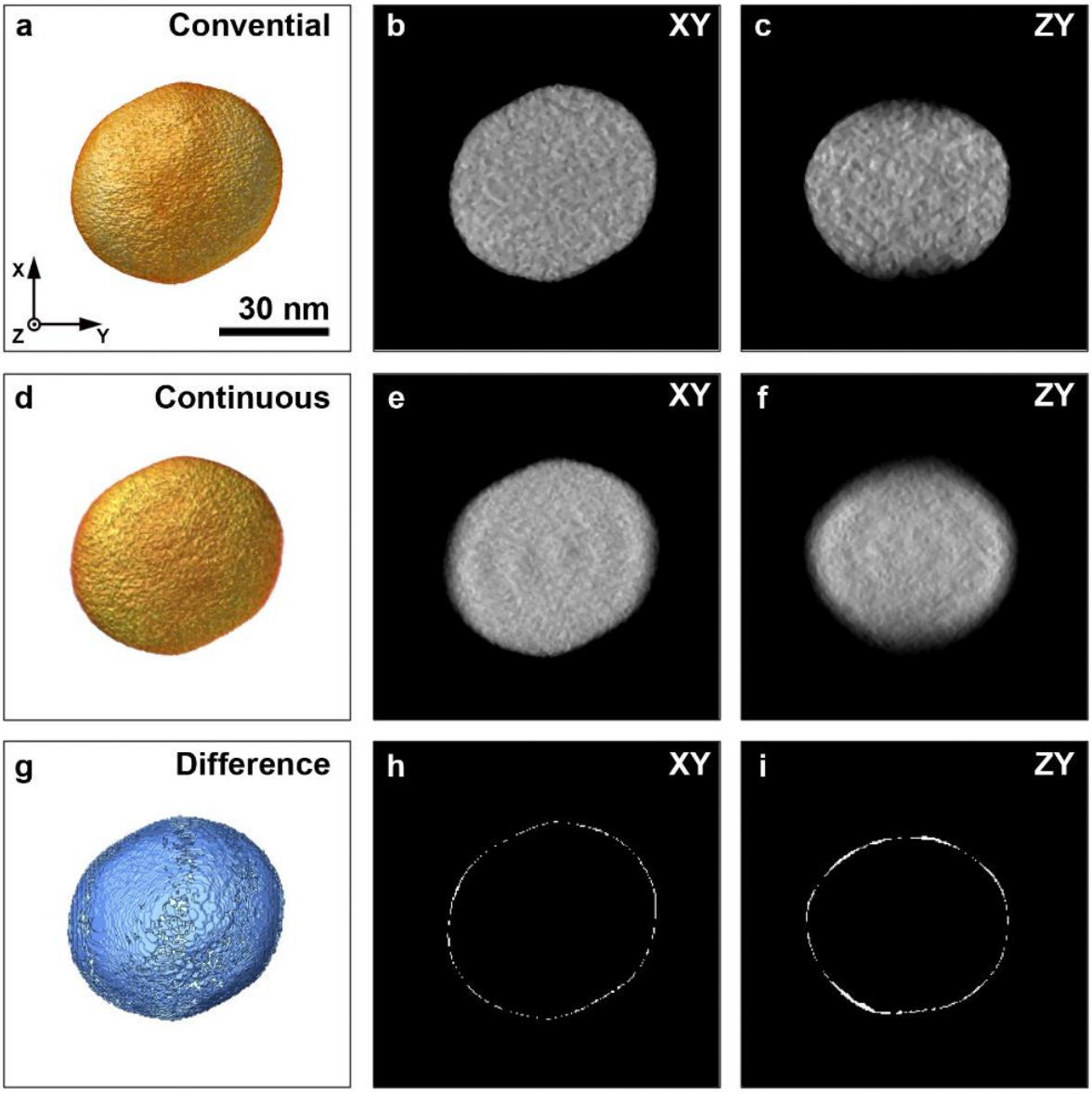

***Figure 6.10**: (a-c) 3D rendering of the reconstruction of the conventionally acquired tilt series of a Au nanosphere, paired by 2 central orthoslices through it. (d-f) 3D rendering of the reconstruction of the continuously acquired tilt series, paired by 2 central orthoslices through it. (g-i) 3D rendering of the absolute difference, paired by 2 central orthoslices through it.*

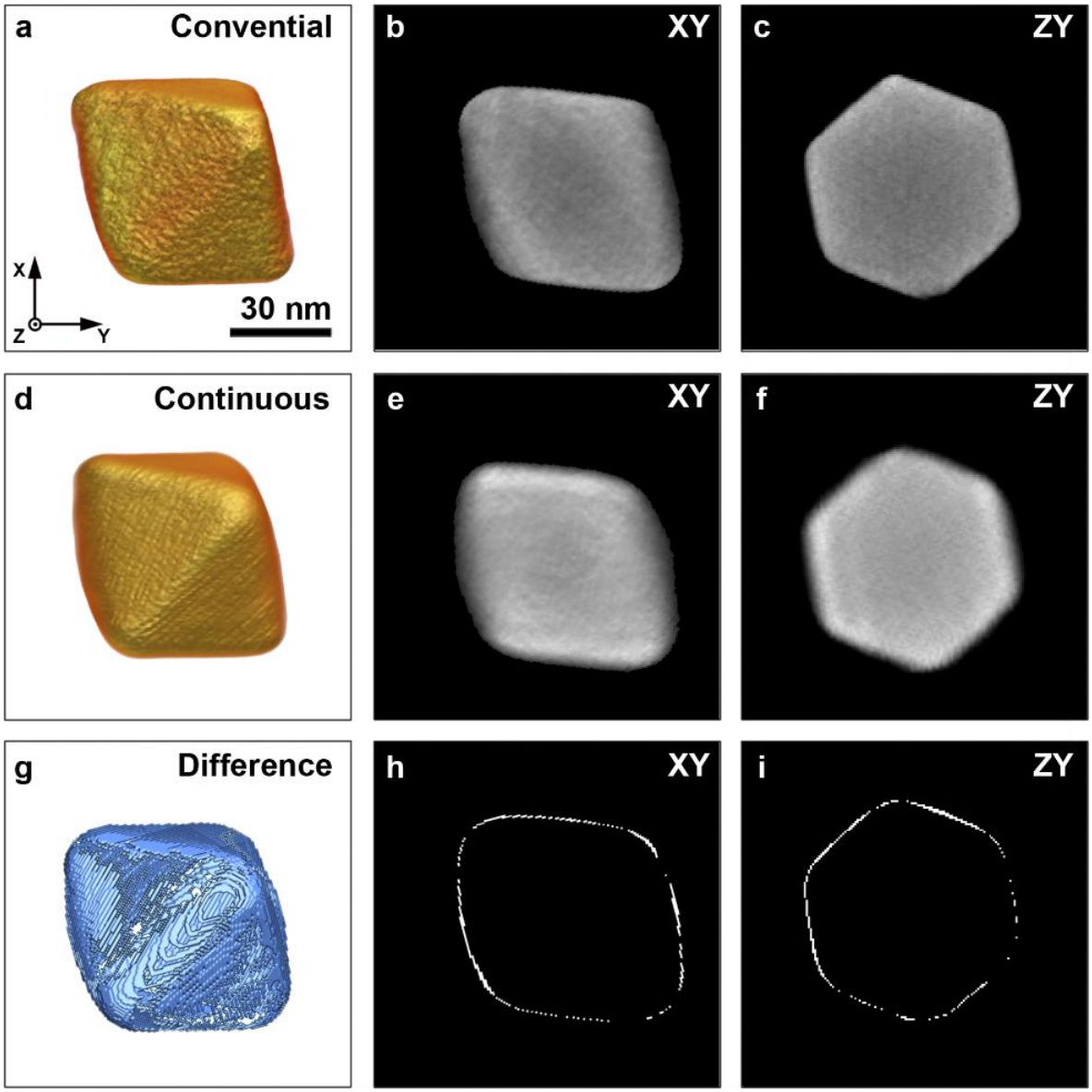

***Figure 6.11**: (a-c) 3D rendering of the reconstruction of the conventionally acquired tilt series of a Au bipyramid, paired by 2 central orthoslices through it. (d-f) 3D rendering of the reconstruction of the continuously acquired tilt series, paired by 2 central orthoslices through it. (g-i) 3D rendering of the absolute difference, paired by 2 central orthoslices through it.*

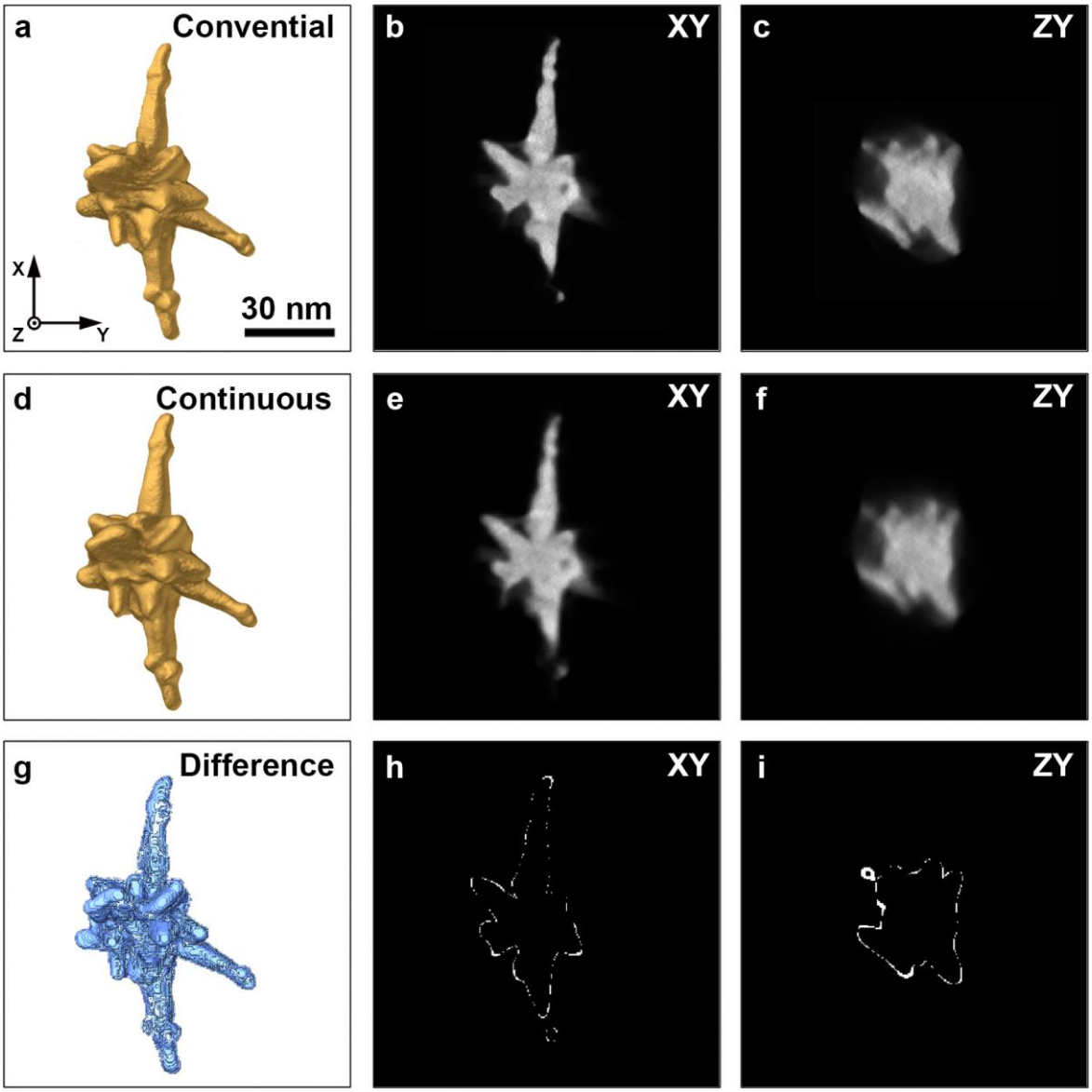

***Figure 6.12**: (a-c) 3D rendering of the reconstruction of the conventionally acquired tilt series of a Au NS, paired by 2 central orthoslices through it. (d-f) 3D rendering of the reconstruction of the continuously acquired tilt series, paired by 2 central orthoslices through it. (g-i) 3D rendering of the absolute difference, paired by 2 central orthoslices through it.*

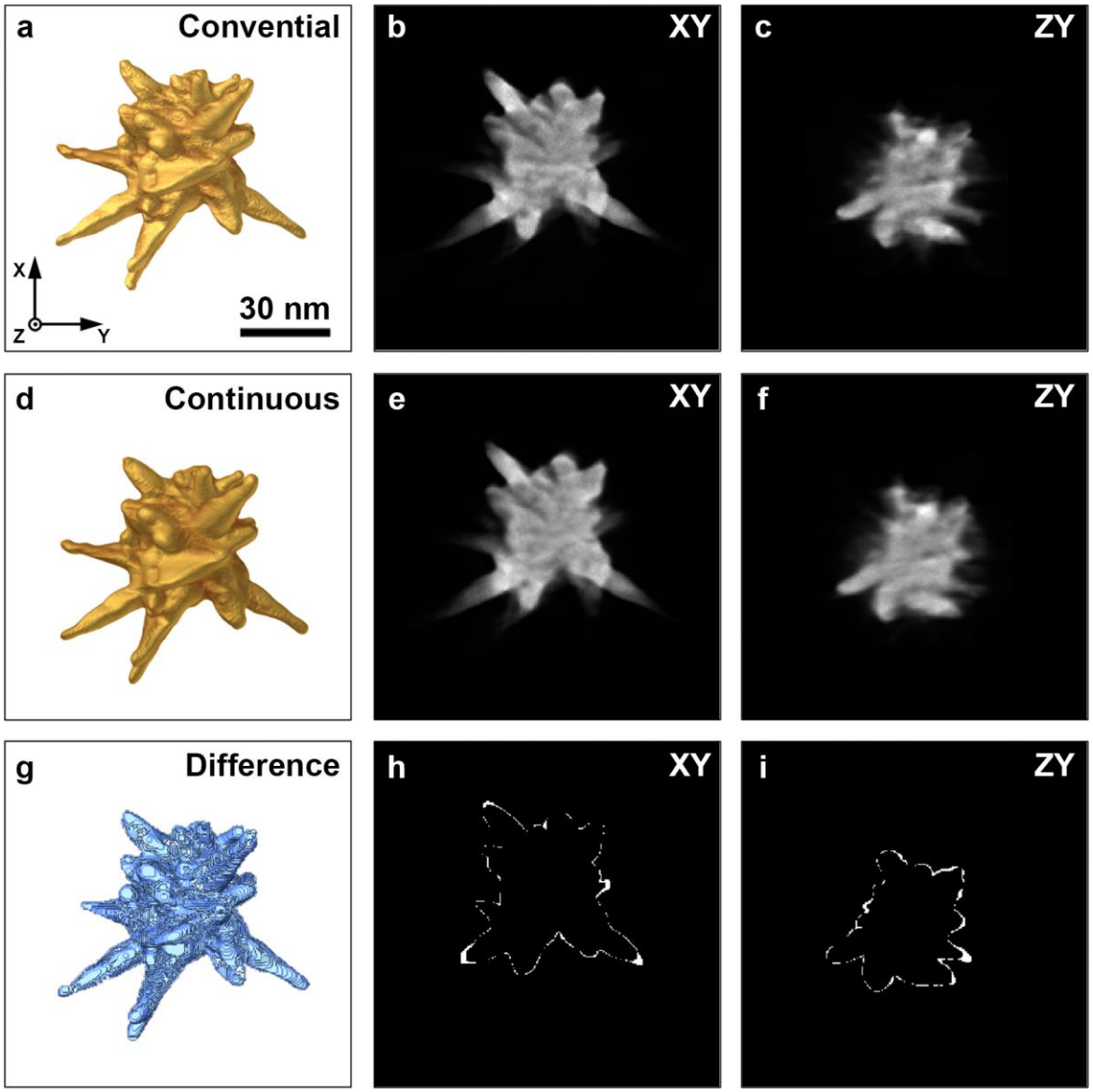

***Figure 6.13**: (a-c) 3D rendering of the reconstruction of the conventionally acquired tilt series of a Au NS, paired by 2 central orthoslices through it. (d-f) 3D rendering of the reconstruction of the continuously acquired tilt series, paired by 2 central orthoslices through it. (g-i) 3D rendering of the absolute difference, paired by 2 central orthoslices through it.*

To quantify the number of misclassified voxels, the shape error (E_s) was calculated using **Equation [5.2]**. In addition, the volume error (E_V), which corresponds to the relative volume difference between the conventional and continuous reconstructions, was determined. The obtained values are listed in **Table 6.2**.

	Sample 1	*Sample 2*	*Sample 3*	*Sample 4*	*Sample 5*	*Sample 6*
	Au decahedron	Au pentahedron	Au nanosphere	Au bipyramid	Au nanostar	Au nanostar
E_s	5.43 ± 0.01 %	5.48 ± 0.01 %	5.26 ± 0.01 %	7.93 ± 0.01 %	13.32 ± 0.01 %	10.98 ± 0.01 %
E_V	4.91 ± 0.01 %	2.40 ± 0.01 %	4.51 ± 0.01 %	2.27 ± 0.01 %	7.61 ± 0.01 %	2.65 ± 0.01 %

***Table 6.2**: The shape and volume errors calculated between the reconstructions obtained from the conventional and continuous acquisition strategies for the different nanoparticles.*

From **Table 6.2** it can be seen that, the volume error remains restricted, independent of the sample. For the simplest 3D geometries (sample 1-3), the shape error is far lower than those obtained for the anisotropic NSs (sample 5-6). This is likely attributed to the increased complexity of morphology of the NSs and their smaller features. We expect that the remaining artefacts present in the projection images have less influence on the reconstruction of simple geometries, than on the reconstructions of nanostructures with a more complex 3D shape. It should be noted that despite the simple geometry of the Au bipyramid (sample 4, **Figure 6.11**), a higher shape error was found than for samples 1-3. This can be attributed to the lower stability of the goniometer stage of the Tecnai Osiris TEM. Hereby, an increase in jitter and movement artefacts is observed when acquiring a continuous tomographic series, which negatively influences the reconstruction quality.

Nevertheless, we can conclude that for all samples the general morphology of the 3D reconstruction is conserved quite well. We can therefore still obtain valuable information on the nanoparticles investigated with the continuous tomography approach. Even more so, such results can be obtained in only a fraction of the time necessary to perform a conventional experiment.

6.4 Conclusions

We implemented a methodology to perform fast electron tomography in HAADF-STEM mode, which allows us to greatly reduce the total acquisition time of a tomographic experiment. We show that by using dedicated processing there is limited difference in reconstruction accuracy for isotropic nanoparticles. For anisotropic nanoparticles with a more complex shape, the discrepancy increases but the overall 3D shape remains comparable. In the next chapter we will apply continuous HAADF-STEM tomography to investigate the thermal stability of branched Au nanoparticles. The increased speed of the continuous approach, will allow us to examine the thermal reshaping with a shorter temporal resolution than possible with conventional tomography.

PART II: ACCELERATED ACQUISITION

7. Fast In-Situ Electron Tomography of Branched Au Nanoparticles

In this chapter, we combine fast tomography with a tomographic heating holder to monitor temperature-induced morphological changes of branched Au nanoparticles. Such investigation is essential since a thorough understanding of the thermal stability and potential reshaping of anisotropic nanoparticles is required for various applications.

This chapter is based on:

Vanrompay, H., Bladt, E., Albrecht, W., Béché, A., Zakhozheva, M., Sánchez-Iglesias, A., Liz-Marzán, L. M., & Bals, S. (2018). 3D characterization of heat-induced morphological changes of Au nanostars by fast: In situ electron tomography. *Nanoscale*, *10*(48), 22792–22801. https://doi.org/10.1039/c8nr08376b

The Au nanostars were synthesized at the Bionanoplasmonics Laboratory, CIC biomaGUNE in Spain. Together with E. Bladt, I was responsible for the acquisition of all the TEM data. I performed all data processing and quantification. The BEM simulations were carried out in association with W. Albrecht.

7.1 Introduction

Gold nanoparticles have shown enormous potential for applications in various fields, ranging from biology and medicine to chemistry and physics. Next to their catalytic activity, high chemical stability and bio-compatibility, Au NPs exhibit intriguing optical properties due to their well-defined localized surface plasmon resonances (LSPRs).(Chakraborty et al., 2014; Kelly et al., 2003) Such LSPRs lead to strong absorption and scattering of light, which causes a significant enhancement of incoming electromagnetic fields at the nanoparticles' surface.(Bohren & Huffman, 1998; Pelton et al., 2008) In addition, the plasmonic properties of Au nanoparticles can be tuned by varying their morphology, surface charge or dielectric environment.(Baffou & Quidant, 2013; Chakraborty et al., 2014; Kelly et al., 2003) As compared to spherical Au nanoparticles, branched nanoparticles show superior plasmonic properties, with electromagnetic field enhancements that are orders of magnitude larger.(N. Li et al., 2014; Pérez-Juste et al., 2005)

As a result, anisotropic Au NSs have gained great interest because of their superior plasmonic properties.(Espinosa et al., 2016; Guerrero-Martínez et al., 2011; Kumar et al., 2008) The electromagnetic field enhancement at their sharp tips(N. Li et al., 2014; Pérez-Juste et al., 2005), makes them ideal substrates for e.g. surface-enhanced Raman scattering (SERS),(Hao et al., 2007; Reguera et al., 2017) or generation of hot electrons.(Brongersma et al., 2015; Manjavacas et al., 2014; Mukherjee et al., 2013; Reguera et al., 2017) Moreover, by tailoring the NS morphology, the corresponding plasmon resonances can be conveniently tuned and shifted into the near infrared (NIR) wavelength range, thereby enabling applications in biological environments.(Guerrero-Martínez et al., 2011; Kumar et al., 2008) In fact, due to their efficient light-to-heat conversion, Au NSs have been employed for both in-vitro and in-vivo studies of photothermal cancer therapy.(Espinosa et al., 2016) The conversion efficiency strongly depends on the spectral position and intensity of the plasmon resonance. Therefore, it is essential to preserve the morphology of Au NSs, and thus their LSPR response upon laser excitation.(Inasawa et al., 2005; Taylor et al., 2014) Unfortunately, previous studies have shown that anisotropic Au nanoparticles readily deform into more rounded morphologies, upon heating or laser excitation.(Inasawa et al., 2005; Link et al., 2000; Taylor et al., 2014) For example, Au NRs reshape at temperatures that are hundreds of degrees below the bulk melting point of gold.(Petrova et al., 2006)

Obviously, such heat-induced deformations will affect the optical properties of the Au nanoparticles and consequently limit those applications where the morphology needs to be preserved. However, we do not possess sufficient information yet on the heat-induced morphological evolution of branched Au nanoparticles and the correlated change of their optical properties. Up to date, most studies have focused on understanding the (photo)thermal stability of large ensembles of Au nanoparticles, e.g. monitoring the extinction spectrum as a function of temperature.(Liu et al., 2009; Petrova et al., 2006; Tollan et al., 2009) On the other hand, in-situ heating experiments in a TEM may enable the direct observation of temperature-induced changes in single particles. However, so far, these studies have been consistently based on conventional, 2D images, which inherently limit such investigations to simple geometries such as rods or spheres.(Khalavka et al., 2007; Petrova et al., 2006; Whitney et al., 2007) To monitor the deformation of more complicated (branched) structures, 2D projection images are insufficient.

Electron tomography is currently a standard technique to visualize the morphology and internal structure of a wide variety of nanostructures in 3D. Exciting new developments in the field of TEM holder fabrication have recently resulted in heating holders that reach the tilt range required for electron tomography, thereby allowing for novel in-situ 3D heating studies. However, to perform elaborate in-situ heating experiments in 3D, several important limitations need to be overcome. A major drawback of electron tomography is the time needed to acquire a full tomographic tilt series, which will hamper the investigation of fast processes in 3D.(Roiban et al., 2018) In the previous chapter, we introduced a fast acquisition strategy, capable of acquiring a tomographic series 10 times faster than conventionally. Here we will use this approach to study heat induced chances of Au NSs, in 3D. Such experiments cannot be easily performed using conventional electron tomography due to possible beam-induced changes or simply due to time limitations. Using continuous acquisition approach, however, we are able to study the 3D morphological evolution of single Au NS as a function of both heating time and temperature.

7.2 Qualitative Analysis

Experiments were performed at 200 °C, 300 °C and 400 °C for a total heating time of 20 minutes, in order to decouple the effect of temperature and total amount of delivered heat on the morphological changes. All HAADF-STEM tilt series were acquired using a Thermo Fisher Scientific Titan electron microscope operated at 300 kV and a DENSsolutions tomography heating holder with MEMS-based heating chips.(van Omme et al., 2018) In **Figure 7.1**, HAADF-STEM projection images of the NS sample are presented. From projection images, it is clear that the NSs exhibit an anisotropic shape with several branches, apparently in random orientations.

The drastic reduction in acquisition time of the continuous approach enables the investigation of the morphology of such nanomaterials in 3D while heating, with a higher sampling rate compared to conventional tomography. Such experiments have been performed in 2D, but 3D results were unattainable so far. Fast continuous acquisition has the additional advantage that the electron dose and dose rate can be reduced. Dose and dose rate reduction is crucial, since it was recently shown that even apparently beam-insensitive nanomaterials such as Au NRs exhibit an altered thermal stability upon in-situ heating, compared to ex-situ experiments.(Albrecht et al., 2018) Here, we make use of this novel technique to study the heat-induced 3D morphological changes of highly anisotropic Au NSs.

Aided by the drastic reduction in acquisition time of the continuous tomography experiment, gradual changes can be examined, in contrast to earlier ex-situ work in which electron tomography series could only be obtained before and after heating.(Goris, Van Huis, et al., 2012) Monitoring the heat-induced changes on the same NS will not only give us insight into the thermal stability of these NSs but also reveal local structural differences and their influence on the observed reshaping. The latter cannot be achieved by indirect techniques such as optical ensemble measurements. Yet, such information is crucial to understand the NSs instability and reshaping behavior at elevated temperatures.

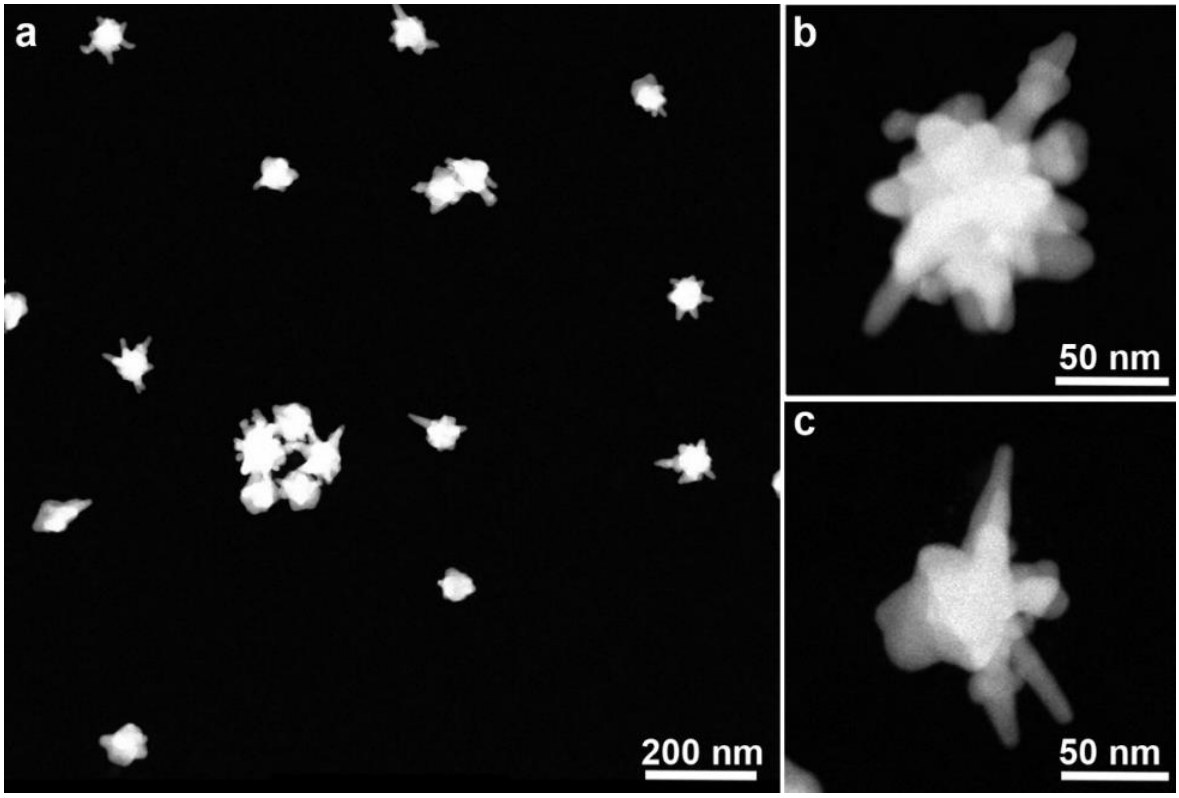

***Figure 7.1**: (a) Overview HAADF-STEM image of multiple Au NSs before heating. (b,c) HAADF-STEM images of single NSs.*

Based on previous studies(Baffou et al., 2009; Cao et al., 2007; Petrova et al., 2006; Taylor et al., 2014), we chose heating temperatures of 200 °C, 300 °C and 400 °C, and a total heating time of 20 min for each temperature. Below 200 °C, morphological changes occur slowly, on the order of hours, whereas above 400 °C reshaping of Au nanoparticles is almost instantaneous(Baffou et al., 2009; Petrova et al., 2006; Taylor et al., 2014). To determine the 3D morphological evolution as a function of time, continuous tilt series were acquired at intermediate time steps of 30 s, 60 s, 90 s, 120 s, 180 s, 300 s, 600 s and 1200 s for each temperature. Hence, the particle was heated for the given time and subsequently cooled down to room temperature, so as to quench further heat-induced morphological transformations. After quenching, a continuous tomographic series was acquired (**Figure 7.2**). This procedure was repeated for the various selected time steps. In this manner, the sampling of the morphological evolution is only limited by the number of acquired tilt series, which is greatly enhanced with our continuous acquisition approach. All data acquisition, processing and reconstruction was performed as introduced in **Section 6.2**.

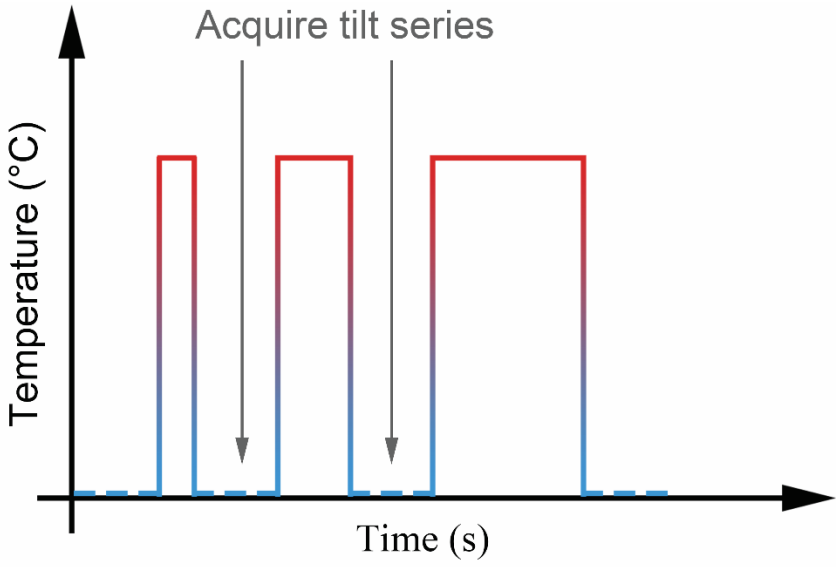

***Figure 7.2**: Schematic visualization of the fast in-situ tomography experiments.*

A complete time series of the morphological evolution of a Au NS for the temperature of 200 °C is shown in **Figure 7.3**. It is clear that all branches of the Au NS deform upon heating. Indeed, as indicated by the black arrows, a transformation is observed from relatively long and thin branches into short but broader branches, similar to the thermally induced deformation observed in 2D TEM images for other Au nanoparticles with symmetric geometries.(Inasawa et al., 2005; Petrova et al., 2006; Taylor et al., 2014) Most of the reshaping occurs during the first time steps of 30 s and 60 s (**Figures 7.3b-c**). After 60 s (**Figures 7.3d-i**), only minor additional morphological changes are observed. Based on these qualitative findings and the fact that reshaping gets enhanced at higher temperatures, we assume faster reshaping at 400 °C. Therefore, we acquired additional time series at 10 s and 20 s for 400 °C. The 3D visualizations of the complete time series for 300 °C and 400 °C are presented in **Figures 7.4** and **7.5**, respectively. At the higher temperatures, a similar morphological evolution, as discussed above, is noticed. For all temperatures, most of the deformation takes place within the first 30 s, after which the deformation slows down. However, the amount of total reshaping increases at higher temperatures and the observed final shape after heating for 1200 s strongly depends on the applied temperature. Whereas blunt tips can still be observed after heating 1200 s at 200 °C (**Figure 7.3**), no tip-like features can be observed at 400 °C, even after 30 s of heat treatment (**Figure 7.5**). Therefore, we conclude that in the time range presently investigated, the heating temperature has a more dominant influence than the duration of heating, which is in agreement with indirect optical bulk measurements.(Petrova et al., 2006)

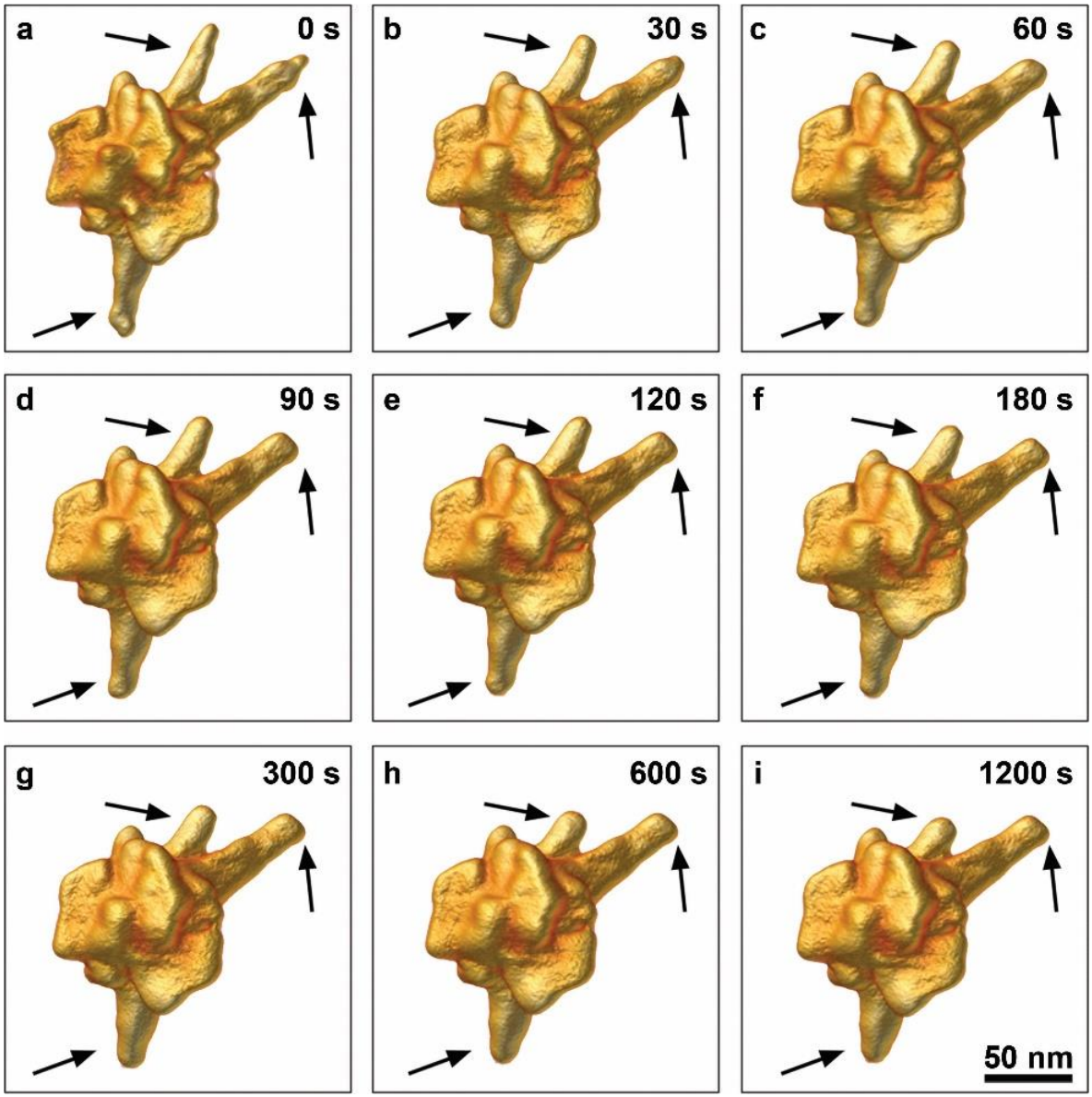

***Figure 7.3**: 3D visualizations of the same Au NS after different heating times at 200 °C. The duration of heating is indicated in the top right corner. The black arrows point towards the regions where morphological changes can be clearly seen.*

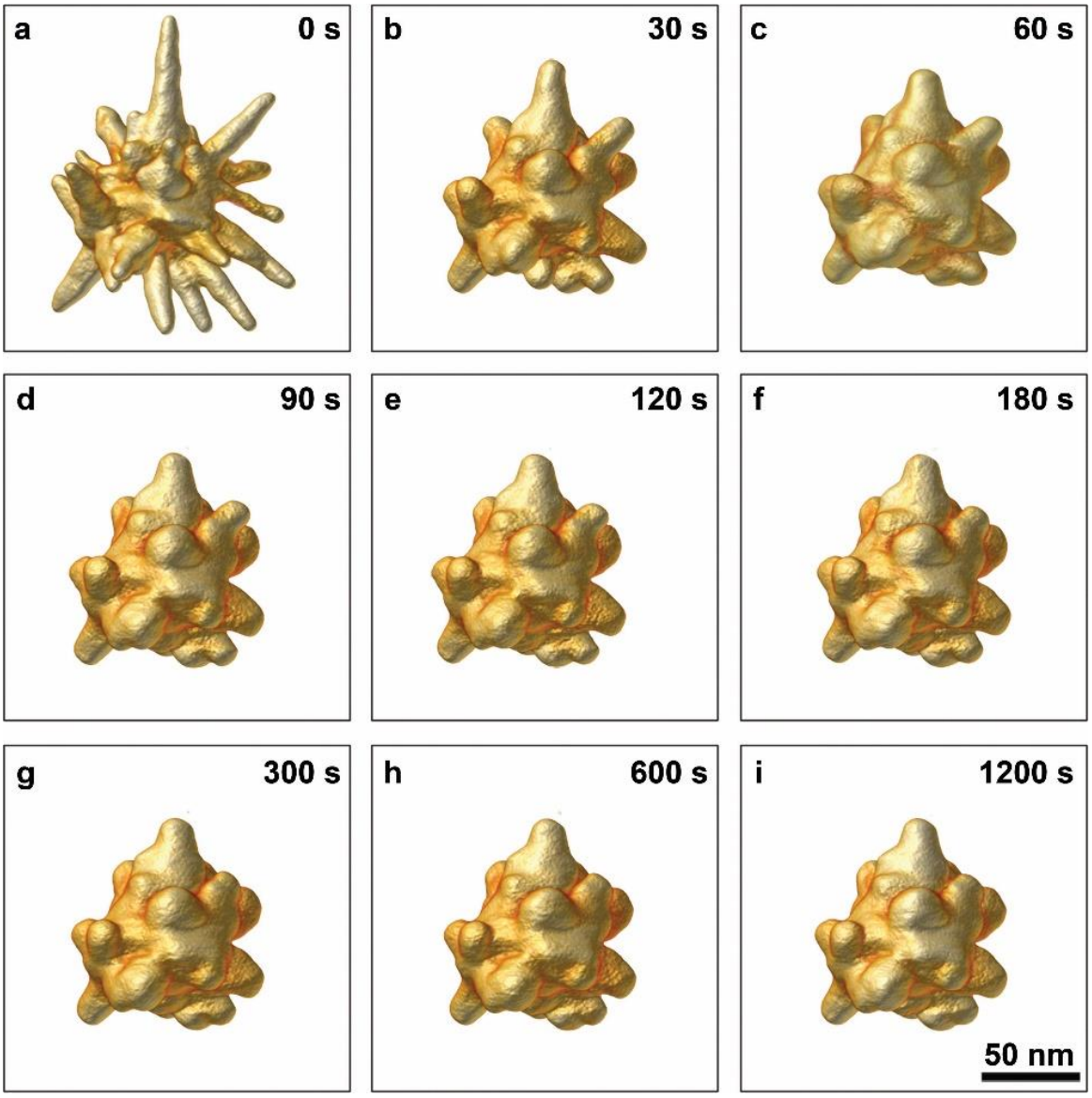

***Figure 7.4**: 3D visualizations of the same Au NS after different heating times at 300 °C. The duration of heating is indicated in the top right corner.*

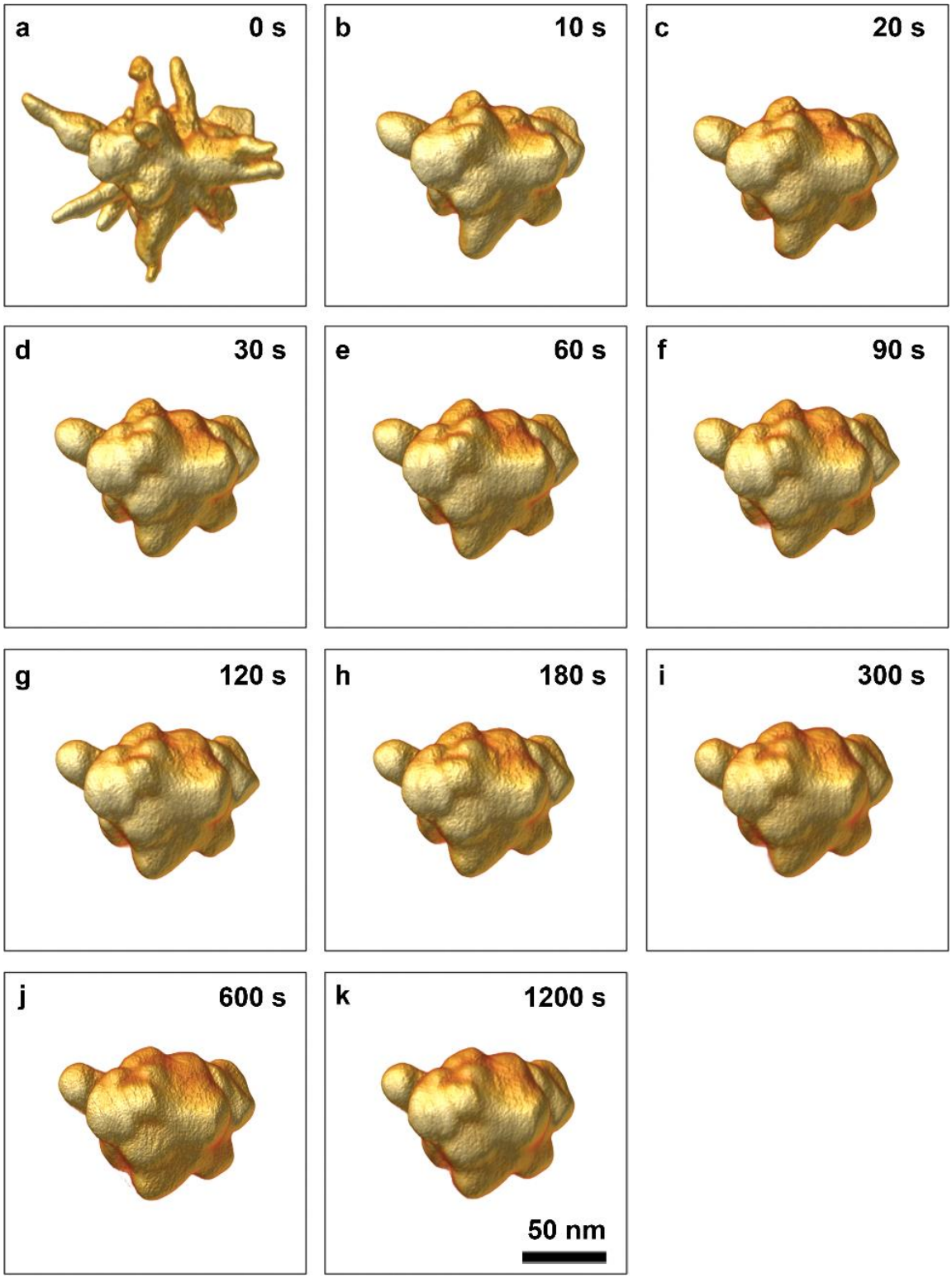

***Figure 7.5**: 3D visualizations of the same Au NS after different heating times at 400 °C. The duration of heating is indicated in the top right corner.*

7.3 Quantitative Analysis

To quantitatively analyze the morphological evolution as a function of local structural features, we calculated the differences between successive reconstructions. This 3D difference was determined by subtracting the segmented reconstructions in successive order (**Figures 7.3-7.5**). The segmentation threshold of the reconstruction prior to heating was determined through Otsu's method(Otsu, 1979). The subsequent thresholds were chosen such that the relative difference in volume to the initial state remained below 0.5%. Since all reconstructions were aligned with respect to each other, prior to the difference calculation, remaining discrepancies are directly related to morphological changes occurring during the heating. The range of possible threshold values to achieve a volume difference below 0.5% was used to determine the accuracy of the quantitative results. By calculating the amount of redistributed volume at the limits of this range, the accuracy on the results was determined as 1%.

Figure 7.6 displays the local volume redistribution for the first two heating steps and the last heating step, for each temperature. Local volume increments and reductions are presented as green and red regions, respectively. It is immediately obvious that in regions with a higher curvature, and thus predominantly at the tips of the branches, the local volume decreases whereas local volume increments are identified at low curvature areas. Furthermore, as hypothesized above, we show that volume redistributions slow down for longer heating times. Additionally, a clear distinction can be seen for the different temperatures, as discussed above. The higher the temperature, the further the atoms can diffuse. After 30 s at 200 °C, only the tips of the nanobranches disappear (red areas in **Figure 7.6a**), the atoms getting redistributed on the sides of the same branches (green areas in **Figure 7.6a**). At 300 °C, a large part of each branch is found to diffuse toward the body of the NS, and at 400 °C atoms from the branches completely redistribute toward the body of the NS.

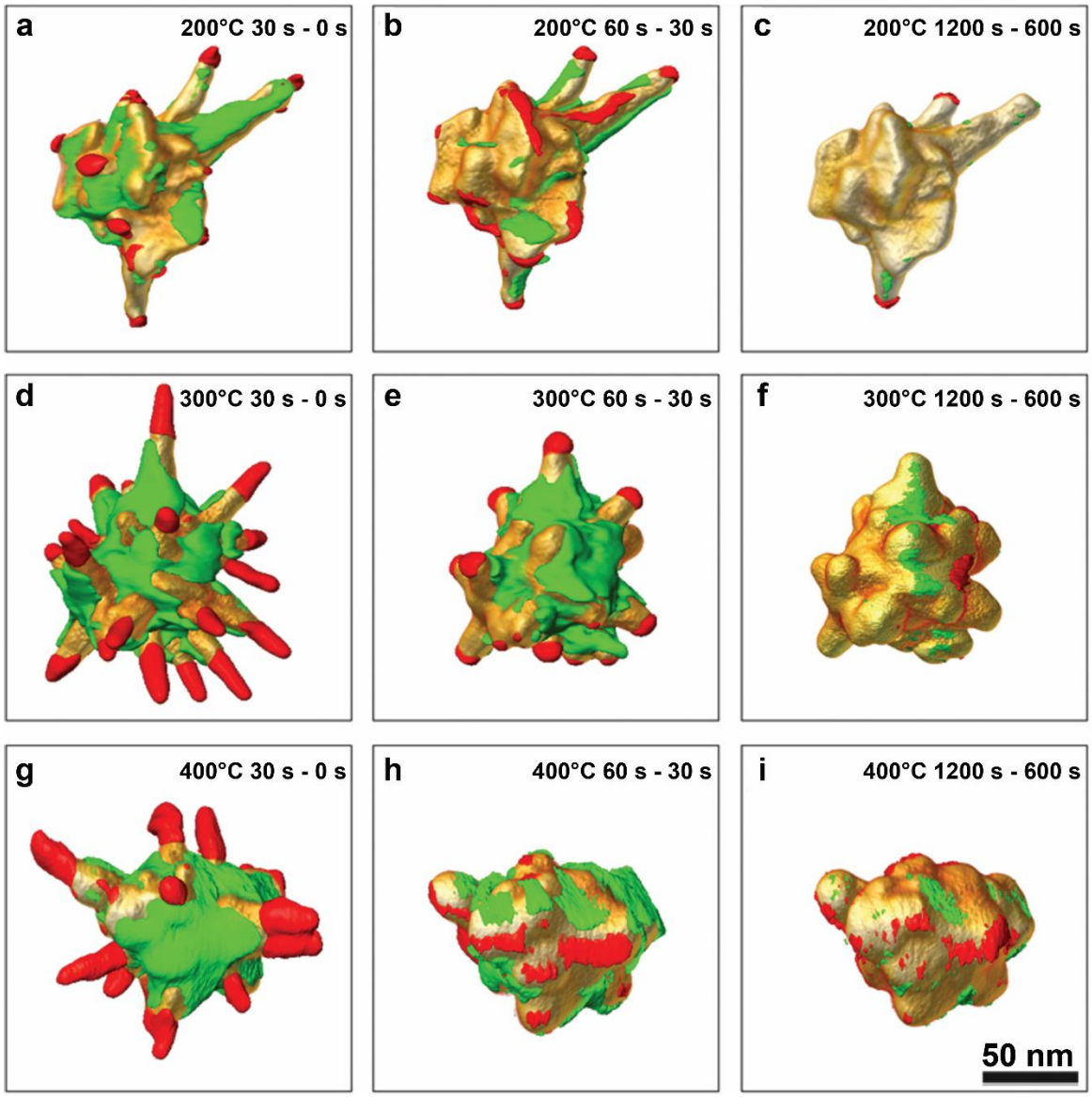

***Figure 7.6**: (a-i) Visualizations of the morphological changes during two successive heating steps, where volume increments and volume reductions are depicted in green and red, respectively. The order of subtraction is indicated in each panel, together with the temperature of heating.*

It is clear that the anisotropic NSs deform considerably at elevated temperatures. In thermal equilibrium, it is expected according to the Wulff theorem that Au nanocrystals of at least 200 atoms, form truncated octahedrons which expose (100) and (111) facets.(Wulff, 2014) Thus, from a thermodynamic point of view the Au NSs are indeed unstable. However, ligands present on the surface of the NSs, kinetically stabilize their shape at room temperature. However, at elevated temperatures this kinetic barrier can be overcome and the NSs deform toward thermodynamic more stable quasi-spheres, which possess a lower surface energy. The driving force behind the deformation is the minimization of the total amount of surface area, which is closely related to the particle curvature. Such behavior can be explained by the reduction of the number of undercoordinated surface atoms which attribute to high surface energies. A competing factor, influencing the morphological evolution, is the surface energy contribution from individual crystal facets. During the deformation the NS will therefore evolve to a structure with a maximal number of low surface energy facets and a minimal curvature.(Cho et al., 2020) Here, we demonstrate that for the Au NSs atoms diffuse from the sharpest parts of the nanobranches, or the NS tips, toward areas of lower curvature, a process that gets accelerated by increasing temperature, confirming a previous study on simple geometries which was based on 2D projections(Cho et al., 2020; Taylor et al., 2014). In summary, by taking advantage of the high temporal resolution of continuous tomography in combination with in-situ TEM, we were able to capture the dynamics of the thermally influenced morphological evolution of the Au NSs. It was demonstrated that their reshaping is predominately governed by surface curvature.

In order to quantitatively compare the effect of temperature and heating duration on the reshaping, the total amount of redistributed volume at each heating step was calculated for each temperature. Since the total redistributed volume is directly related to the relative volume initially present in the branches of the NS, and a different NS was studied at each temperature, the amount of redistributed volume was normalized by the total volume of the branches of the initial NS. The initial volume of the branches was determined by segmenting the 3D reconstruction of the NS and separating the core from the branches. The resulting total amount of redistributed volume as a function of heating time is plotted in **Figure 7.7a** (black: 200 °C, blue: 300 °C and magenta: 400 °C). The error (1%) on these measurements are determined by the accuracy of the required segmentation step, as earlier discussed. The results confirm that most of the heat-induced morphological changes occur within the first minute of heating, regardless of temperature. The plot in **Figure 7.7b** illustrates in more

detail the volume redistribution occurring during the first few minutes, indicating that most of the morphological changes has already taken place after 30 s. When heating the NSs further, the particles converge to a more stable configuration and less extensive heat-induced morphological changes are observed.

The amount of redistributed volume as function of heating duration was fitted by a two term exponential model:

$$a\, e^{bx} + c\, e^{dx} \qquad [7.1]$$

with *x* the duration of heating and *a*, *b*, *c* and *d* fitting parameters. Their derived values, alongside the R^2 value of the fit are listed in **Table 7.1**. While *a* and *c* regulate the height of the reached plateau value, *b* and *d* respectively control the slope of the plateau and sharpness of the initial rise.

	a	*b*	*c*	*d*	R^2
200 °C	18.75	43.53×10^{-5}	-18.75	-1.10	0.984
300 °C	61.17	4.81×10^{-5}	-61.04	-0.05	0.996
400 °C	86.66	-3.47×10^{-5}	-88.56	-0.10	0.960

***Table 7.1**: Derived parameters for fitting the thermal reshaping behavior of the Au NSs as function of heating duration by a two term exponential model.*

As the temperature increases, the height of the reached plateau (parameters *a* and *c*) is elevated as well. This demonstrates quantitatively that the magnitude of the morphological changes is predominantly determined by the heating temperature. At 200 °C, only 19 ± 1 % of the volume is redistributed after 30 s of heating. However, for 300 °C and 400 °C, the total redistributed volume after 30 s equals 49 ± 1 % and 87 ± 1 %, respectively. At the end of the heating time of 1200 s, the total redistributed volumes were 31 ± 1 %, 64 ± 1 % and 85 ± 1 %, for 200 °C, 300 °C and 400 °C, respectively. Thus, reshaping continues, though at a slower rate, after 30 s for 200 °C and 300 °C but does not progress further for 400 °C. At 300 °C and 400 °C the derived values for *b* remain relatively low, verifying that indeed a steady state was reached. For 200 °C however, *b* is approximately 10 times higher in absolute value, demonstrating that the morphological transformation was still ongoing. Thus, the NS converges faster to its final morphology when a higher heating temperature is introduced. More specifically, at 400 °C no volume redistribution was observed after 20 s of heating, at which a plateau value was reached. Although most of the redistribution was completed

within 30 s for 300 °C and 200 °C, reshaping continued up to about 300 s for 300 °C and for the total heating time of 1200 s for 200 °C. Finally, the sharpest onset of the morphological evolution (parameter *d*) was found at 200 °C.

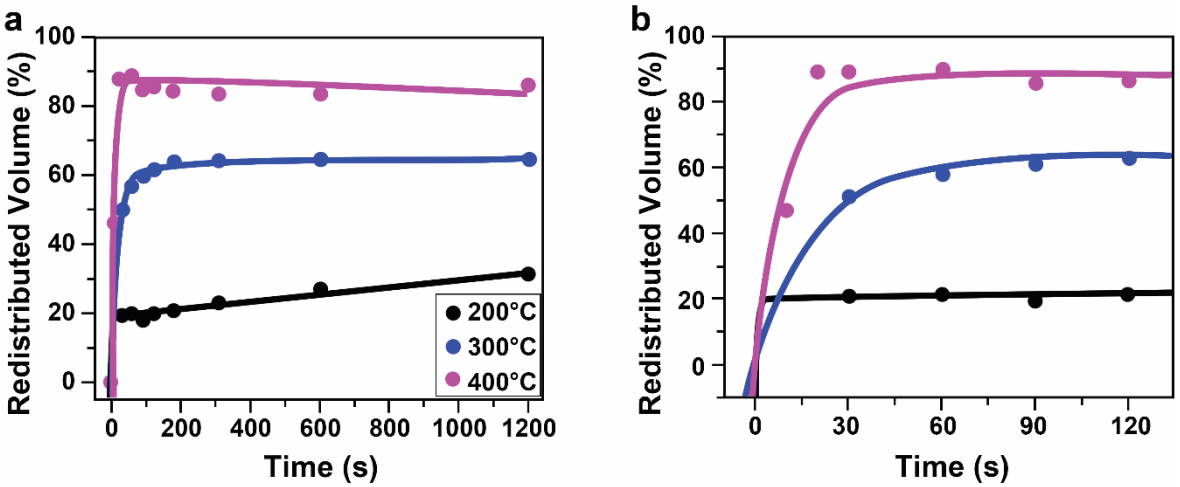

***Figure 7.7**: (a) Total amount of redistributed volume normalized to the relative volume of the branches of the initial NS, as a function of time for 200 °C (black dots), 300 °C (blue dots) and 400 °C (magenta dots). (b) Detailed view of the volume redistribution occurring during the first two minutes. The redistributed volume as function of heating duration was fitted by a two term exponential model (solid lines).*

Earlier thermal stability studies also found a clear dependence of the deformation of Au nanoparticles on temperature.(Baffou et al., 2009; Petrova et al., 2006; Taylor et al., 2014) For example, Petrova et al. compared the reshaping of Au NRs at 100 °C, 150 °C, 200 °C and 250 °C, over the course of 1200 min, by optical ensemble extinction spectroscopy and scanning electron microscopy.(Petrova et al., 2006) At 250 °C they observed complete reshaping of the Au NRs into a spherical shape, within about 20 min. For lower temperatures the final aspect ratio of 1 was not reached even after 1200 min, but intermediate aspect ratios were observed. The authors raised the question whether these were real intermediate states or whether sample changes were then evolving very slowly. It should be mentioned that optical ensemble measurements can only give an average image due to sample polydispersity. We are fully aware of the difference between heating in air or vacuum, nevertheless the results obtained here are of high interest to answer such questions, since they enable us to directly quantify heat-induced changes for an individual nanoparticle in 3D. The results presented in **Figures 7.3-7.7** show that the amount of redistributed volume saturates over time, revealing that these are real intermediate states that do not change upon

further heating at the same temperature. To fully comprehend the influence of the environment, these experiments will have to be extended to environmental TEM.

It is important to note that ligands surrounding the nanoparticles (CTAB) can be transformed into a protective amorphous carbon layer by the electron beam, which has been shown to prevent deformation of Au NRs upon in-situ heating, even for heating at 400 °C for one hour.(Albrecht et al., 2018) This again stresses the need for a fast acquisition procedure to perform such in-situ experiments in 3D. Over the course of time of one conventional tomography experiment, we were able to perform ten fast tomographic acquisitions. By continuously rotating while acquiring, we did not only lower the acquisition time, but the electron dose rate was reduced as well. Consequently, the undesirable build-up of a surrounding carbon layer was slowed down during the initial acquisition and such a protective effect was minimized. However, we still observe a remaining influence of a protective carbon layer, with respect to NSs that were out of the field of view during the experiment. For the case of heating at 400 °C for 1200 s, non-irradiated NSs exhibited a more rounded morphology in comparison to the irradiated NSs (**Figure 7.8**). Unfortunately, it is difficult to quantify the difference in deformation, as the specific initial morphology of NSs that were out of the field of view remains unknown.

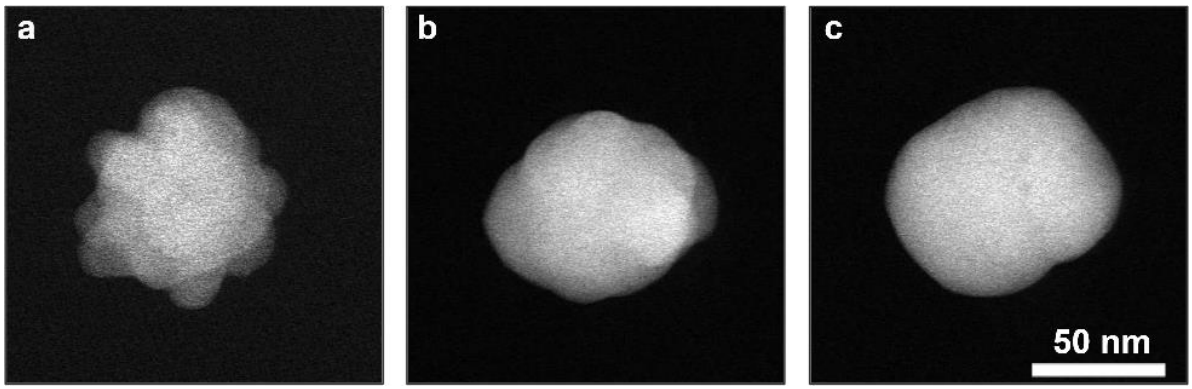

***Figure 7.8**: HAADF-STEM images of Au NSs after heating at 400 °C for 1200 s. The NS in (a) was investigated using our fast acquisition approach. The NSs in (b) and (c) were not investigated during heating and only an image after the total heating time was acquired. It can be observed that the NSs in (b) and (c) have a more rounded end morphology.*

7.4 Optical Properties

It has been reported that the presence of sharp tips in both Pt NSs and Au NSs leads to a strong enhancement of the SERS activity.(Guerrero-Martínez et al., 2011; Kumar et al., 2008; Tian et al., 2006) The reshaping of sharp tips will therefore heavily influence the desired optical and electronic properties of NSs. Kumar et al. demonstrated that the strong field enhancement of Au NSs was predominately directed by the angle and the sharpness of the tips(Kumar et al., 2008). In order to quantify the sharpness of the Au NS tips during the morphological evolution, the Gaussian curvature of the surface was calculated for every 3D reconstruction.(Rusinkiewicz, 2004) We demonstrate this calculation for the experiment performed at 300 °C, as the selected NS exhibited many branches.

The distributions of positive values of the tip curvature after 0 s, 30 s and 1200 s of heating at 300 °C are plotted in **Figure 7.9a**. With elongated heating duration, an overall increase in the relative occurrence of low curvature values, along with a decrease of high curvature values can be observed. Specifically, the initial shoulder around 0.01 nm^{-2} (black histogram), indicated by the black arrow in the inset of **Figure 7.9a** and attributed to the sharp tips, completely vanishes after heating for 30 s (green histogram). Accordingly, the relative frequencies around 0.005 nm^{-2} increase after 30 s, indicating the deformation toward blunter tips, i.e. more extended areas of lower curvature. After 1200 s (magenta histogram), no shoulders can be observed anymore, while the contributions around 0 nm^{-2} increases, due to the complete deformation of the tips.

To visualize the curvature in 3D, **Figures 7.9b-d** display the corresponding volume renderings for the Au NS before and after heating for 30 s and 1200 s at 300 °C, superimposed with a color map illustrating the measured Gaussian curvature for every nanobranch. The color scales linearly between -0.02 (blue) and 0.02 nm^{-2} (red). Overall, the curvature of the whole nanoparticle is distributed around 0 nm^{-2} (green), with contributions of high curvatures from the tips (red) and minimal contributions (blue) due to negative curvature where the tips grow out of the body of the nanoparticle. These visualizations confirm again the significant change in curvature of the nanobranches upon heating. As discussed earlier, during the NS deformation the total amount of surface area, which is related to the particle curvature, decreases. Once the NS has lost its most prominent features, the sharp tips of its branches, the morphological evolution slows down. This provides direct in-situ 3D evidence for the dependence between the rate of heat-induced reshaping and the

curvature of the branches of highly anisotropic NSs, which confirms the recently proposed curvature-induced surface diffusion mechanism for reshaping of Au nanoparticles below the melting point.(Taylor et al., 2014)

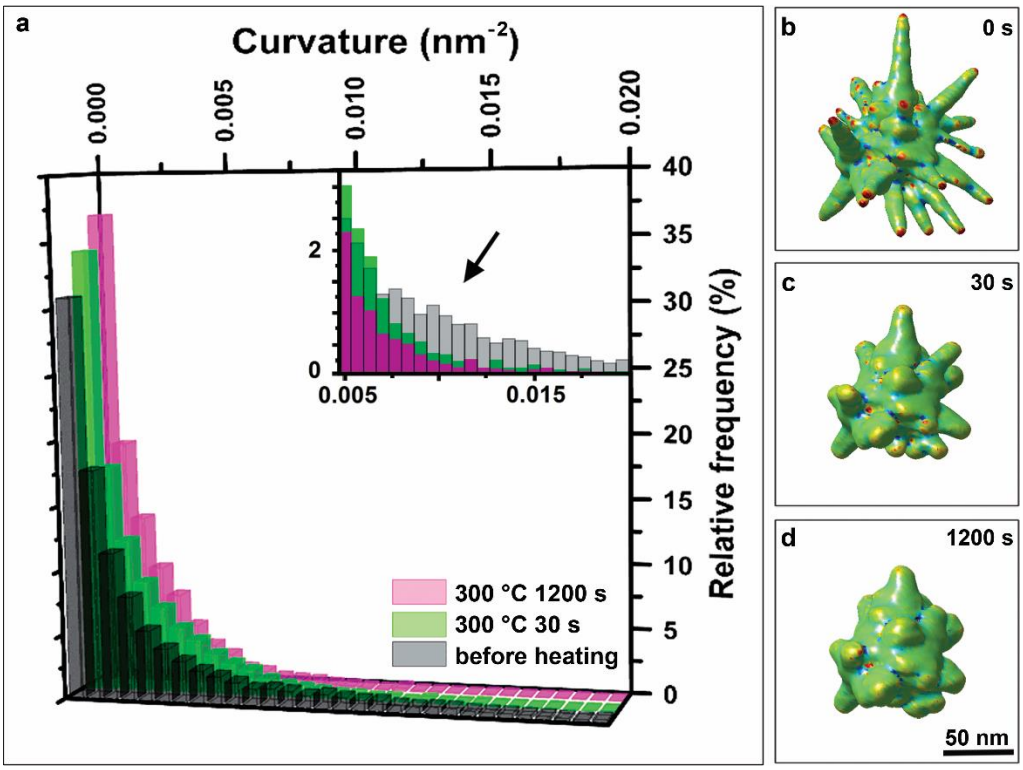

***Figure 7.9**: (a) Histograms illustrating the measured curvature after different durations of heating at 300 °C. In every case, 30 bins were used to calculate the distribution. The inset illustrates a magnified 2D view of the histograms ranging from 0.005 nm^{-2} to 0.02 nm^{-2}, in which the black arrow highlights the loss of high curvature as function of temperature. Visualization of the curvature of the Au NS before heating (b), after 30 s of heating (c) and after 1200 s of heating (d). The color scale is directly related to the measured curvature values, red and blue representing high positive and high negative curvatures, respectively.*

The decrease in curvature strongly alters the optical properties of the Au NS, which hampers applications where heating is involved. In order to evaluate the influence of the thermally induced morphological changes on the plasmonic properties of the Au NS, we performed Boundary Element Method (BEM) simulations using the MNPBEM toolbox.(Hohenester & Trügler, 2012) By using the reconstructed 3D shape as an input for BEM simulations, we can investigate the connection between the 3D shape transformations and the consequent changes of the optical properties at elevated temperatures. This information is highly valuable toward understanding Au NSs performance in practical

applications. The quasi-static approximation was used and the localized surface plasmon resonances were monitored at 150 points in a wavelength range from 500 nm to 1000 nm. A surrounding dielectric constant of 1, corresponding to vacuum, was used. The reconstructed NSs were discretized in 6000 vertices using Amira 5.4.0 and used as an input for the BEM simulations. The amount of vertices was chosen high enough to obtain a realistic depiction of the NS's structure, while staying sufficiently low for computational considerations.

Figure 7.10a displays the extinction spectra calculated for the unheated and heated NS at 300 °C for 30 s and 1200 s. The polarization direction was chosen along the x-axis and the particle was rotated in order to align one tip in that direction. Due to the complex structure of the NS, the spectra contain several peaks which was also observed in previous studies.(Nehl et al., 2006; Tsoulos et al., 2017) For the extinction spectrum of the unheated NS (black curve) the peak at 805 nm is attributed to the tip aligned with the x-axis (**see Figure 7.13**). Upon heating, it is obvious that the longitudinal LSPR peak drastically blue-shifts due to the loss of sharpness of the tip and decrease in aspect ratio. Specifically, after 1200 s of heating at 300 °C, the maximum of the extinction cross section dropped by a factor of 10 and the resonance peak, connected to the tip aligned along the x-axis, shifts from 800 nm to 600 nm. The deformation of the tip also has a direct influence on the electric field amplification and in turn on the SERS enhancement. Therefore, we calculated the average electric field enhancement under illumination wavelength ranging from 500 nm to 1000 nm.

The results for 300 °C are shown in **Figure 7.10b-d**. As expected from the extinction cross sections, the electric field enhancement drops significantly upon heating. Specifically, the enhancement drops by 73% upon heating the NS for 30 s at 300 °C and continues to decrease by 82% of the original enhancement after heating for 1200 s. The extinction cross sections and the induced electric fields for the NSs heated at 200 °C and 400 °C are presented in **Figures 7.11** and **7.12**. Due to the less severe deformation of the NS heated at 200 °C, the changes in the extinction spectrum in field enhancement are not as drastic as for 300 °C. Even so, the field enhancement decreases by 44% after heating for 30 s (**Figure 7.11b-d**). At 400 °C, almost all interesting plasmonic features are lost due to the strong deformation to a quasi-spherical shape (**Figure 7.12b-d**). As a result, for applications where elevated or even moderate temperatures are required, e.g. certain photocatalytic reactions, the observed decrease in field enhancement will influence their efficiency. Therefore, the information that can be provided by our experiments is of crucial importance when incorporating these materials in future applications.

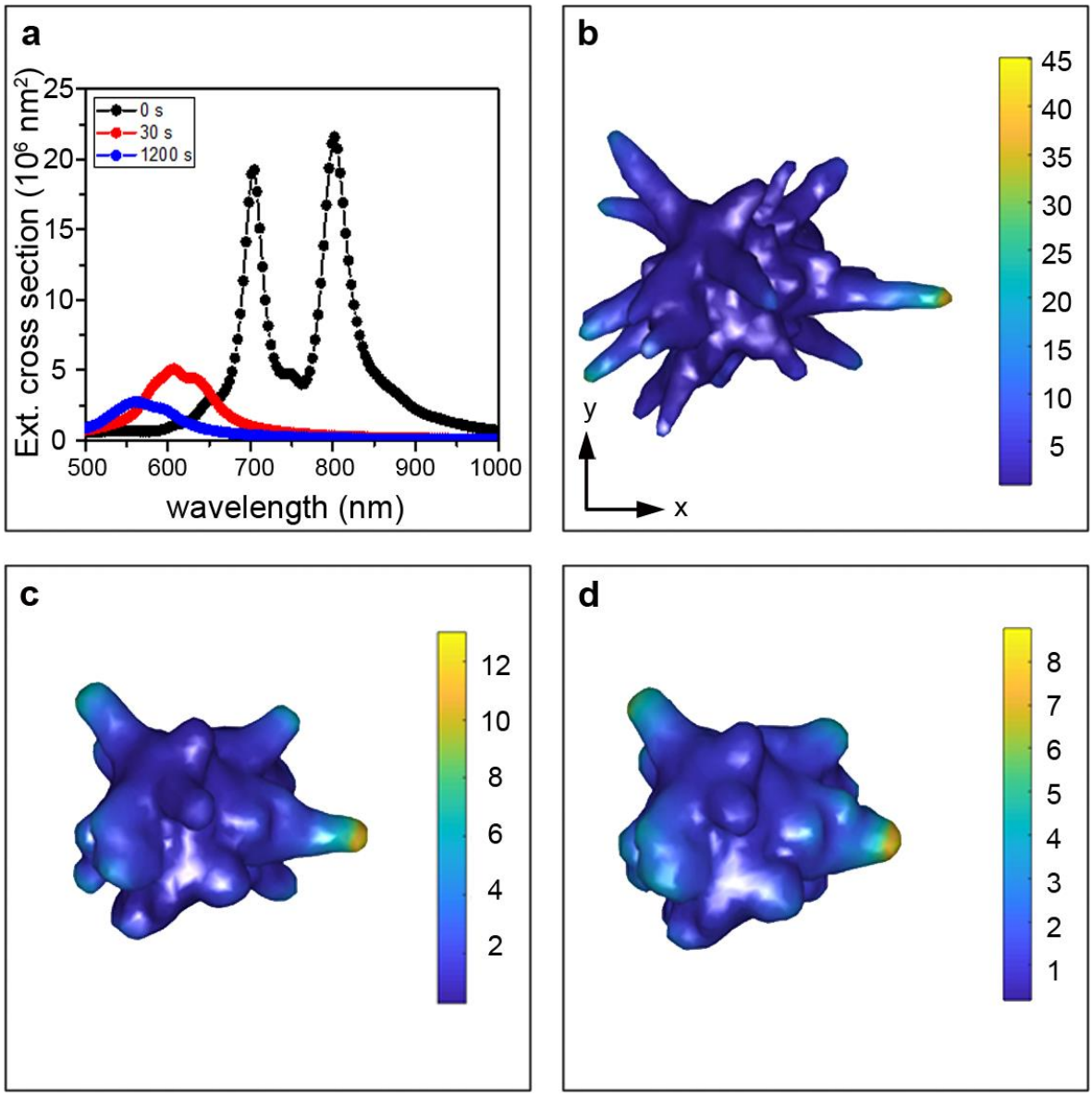

***Figure 7.10**: BEM simulations of the Au NS heated at 300 °C, performed on a simplified surface deduced from the corresponding 3D tomographic reconstructions. (a) Extinction cross sections for the unheated and heated NS, after 30 s and 1200 s of heating at 300°C. The calculated average induced electric field is shown for (b) the unheated NS, (c) after heating for 30 s at 300 °C and (d) after heating for 1200 s at 300 °C.*

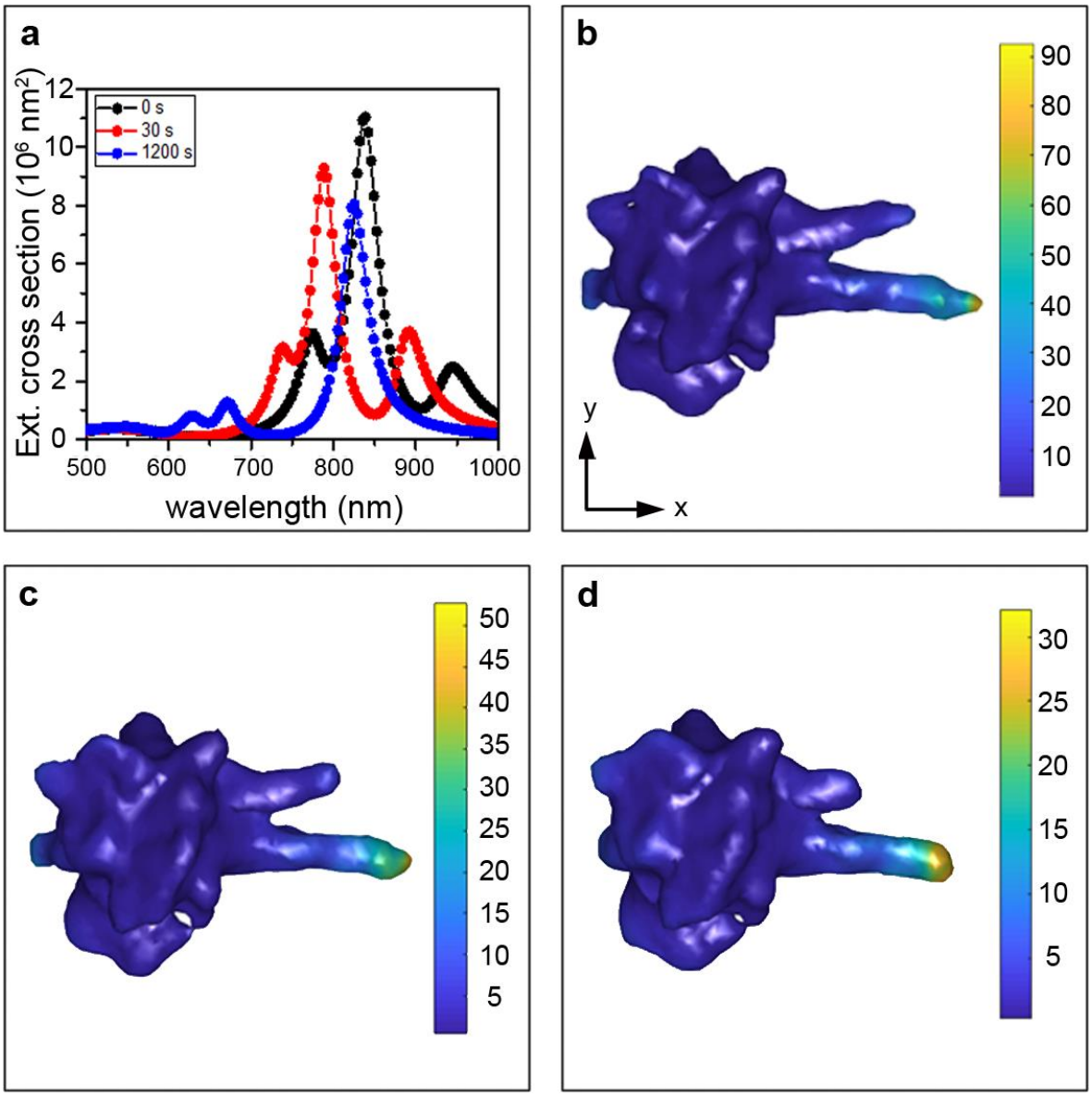

***Figure 7.11**: BEM simulations of the Au NS heated at 200 °C, performed on a simplified surface deduced from the corresponding 3D tomographic reconstructions. (a) Extinction cross sections for the unheated and heated NS, after 30 s and 1200 s of heating at 200°C. The calculated average induced electric field is shown for (b) the unheated NS, (c) after heating for 30 s at 200 °C and (d) after heating for 1200 s at 200 °C.*

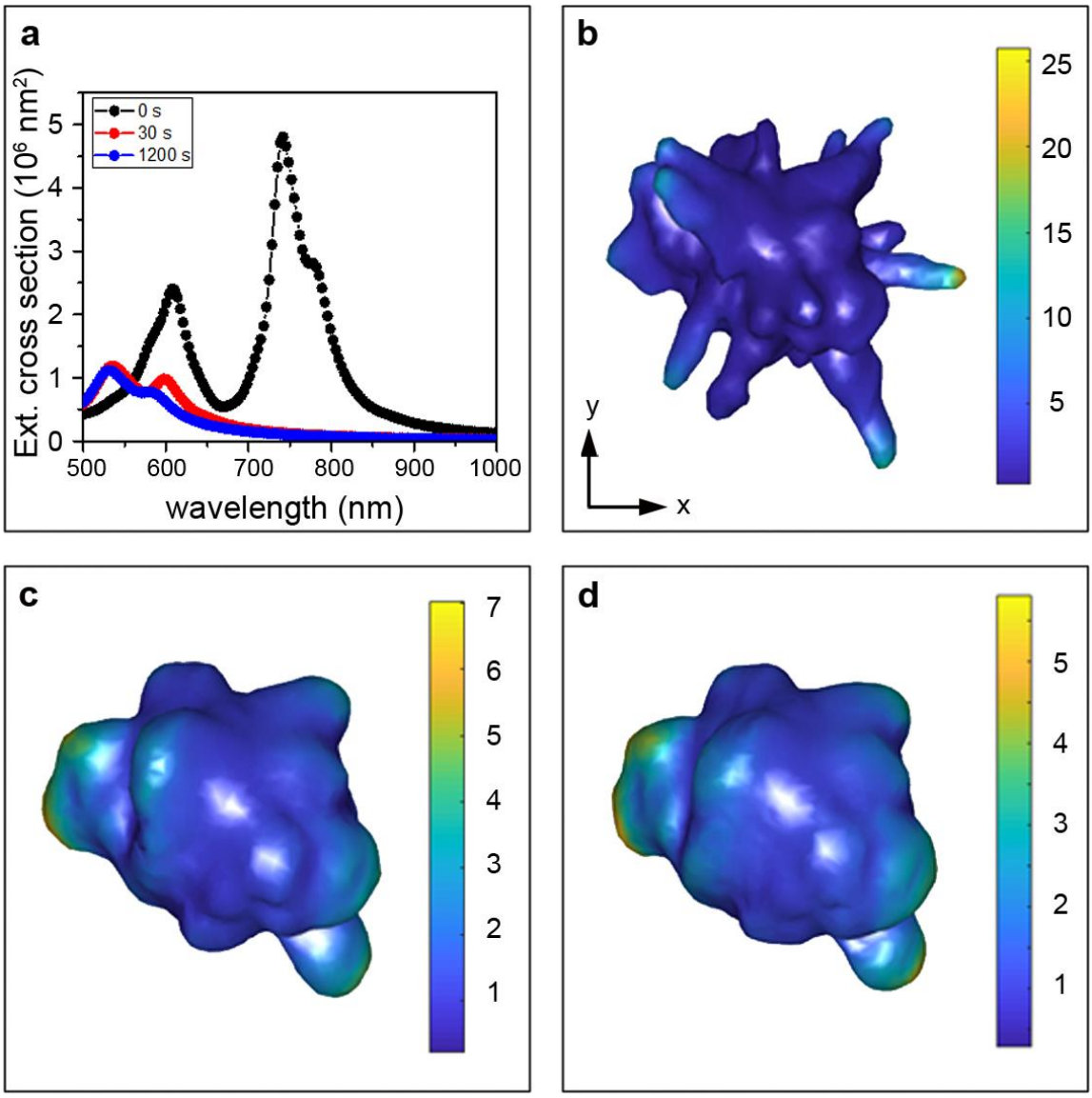

***Figure 7.12**: BEM simulations of the Au NS heated at 400 °C, performed on a simplified surface deduced from the corresponding 3D tomographic reconstructions. (a) Extinction cross sections for the unheated and heated NS, after 30 s and 1200 s of heating at 400°C. The calculated average induced electric field is shown for (b) the unheated NS, (c) after heating for 30 s at 400 °C and (d) after heating for 1200 s at 400 °C.*

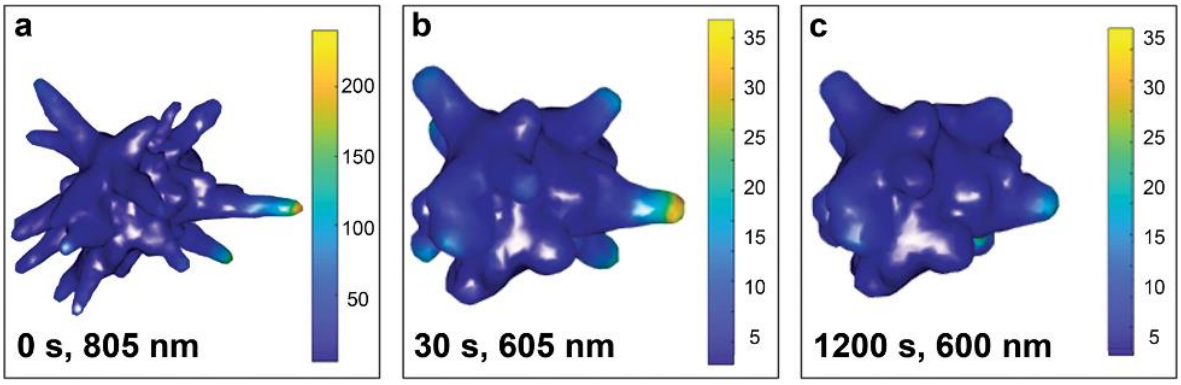

***Figure 7.13**: Illustration of electric field enhancement maps at different times during the heating process. The electric field enhancement was plotted for specific wavelengths. Both the time as the chosen wavelength are specified in the bottom left corner of the subfigure. The polarization direction was chosen similar as before, along the axis of the "highlighted" nanobranch.*

7.5 Conclusions

The continuous electron tomography methodology allowed us to observe the morphological evolution of a Au NS heated at 200 °C, 300 °C and 400 °C, at different time steps up to 1200 s. Due to the highly reduced acquisition time of the tilt series, gradual changes at distinct time steps during heating were investigated, which allowed us to record the 3D morphological changes as a function of heating time and temperature. We were thereby able to quantify local volume reductions and increments, as well as determine the local curvatures of the NSs during heating. At elevated temperatures, the sharp tips at the end of the nanobranches were observed to reshape into shorter and blunter tips. While it has been previously postulated by indirect methods that curvature-induced surface diffusion is the driving mechanism of such reshaping, our experiments directly confirm this hypothesis. We additionally showed that the major part of the morphological evolution occurs within the first minute of heating, regardless of temperature. The shape transition subsequently slows down and a stable final morphology is reached. The amount of total reshaping was found to increase for higher temperatures and the final morphology of the NSs to depend on the heating temperature, which thus has a more significant influence than the heating time. From BEM simulations we additionally discovered that reshaping leads to a drastic decrease in electric field enhancement, which must be taken into account for applications where heating of NSs is unavoidable.

7.6 Outlook

In this chapter we beneficially applied the continuous tomography technique to investigate the thermal reshaping of Au NSs. The technique introduced in **Chapter 6** and applied here is general and is therefore not restricted to specific nanoparticles or experiments. We therefore foresee that fast tomography can be applied for a wide range of different in-situ experiments where the time resolution is restricted by the amount of tomography series that can be acquired within a single experiment. For instance, the investigation of the physics underlying alloying of nanoparticles(Skorikov et al., 2019) or the formation of twins may benefit as well from the proposed acquisition strategy. Furthermore, we firmly believe that fast tomography might evolve into a standard acquisition strategy, given its many advantages. In the duration that a single nanoparticle can be investigated by conventional means, 10 fast tomographic series of different nanoparticles can be acquired, thereby improving the statistic relevance of the obtained results. Nevertheless, to become a standard acquisition approach, the reconstruction accuracy has to further improve. In the next chapter, we discuss computational and hardware solutions to further enhance the quality of the fast tomographic acquisition.

PART II: ACCELERATED ACQUISITION

8. Improving the Accuracy of Fast HAADF-STEM Tomography

Continuous HAADF-STEM tomography is able to obtain tomographic series in only a fraction of time necessary to perform a conventional acquisition. However, discrepancies between reconstructions obtained from continuous and conventional tilt series were found. In this chapter we present two strategies, to reduce these deviations.

This chapter is based on:

Vanrompay, H., Skorikov, A., Bladt, E., Béché, A., Freitag B., Verbeeck, J., & Bals, S. (2020). Fast versus conventional HAADF-STEM tomography: advantages and challenges. *In preparation*

The Au octopods were synthesized at the Skrabalak group at Indiana University in the United States. The branched Au nanoparticles were synthesized at the Odom group at Northwestern University in the United States. The synthesis of the Au@Ag nanoparticles was carried out at the Bionanoplasmonics Laboratory, CIC biomaGUNE in Spain. Together with A. Skorikov, I was responsible for the development of the fast acquisition strategies. The acquisition of the all TEM data was performed in collaboration and A. Skorikov. I performed all data processing and quantification.

8.1 Neural Network Assisted Image Enhancement

As introduced in **Section 6.2.2**, a dedicated low-pass filter is used to remove the jitter caused by the continuous tilt in the projection images. However, this approach aims to de-noise the projection images without any knowledge about the investigated nanostructures, potentially causing a loss in structural information. A promising approach to overcome this limitation is the use of deep learning methods to enhance the quality of the continuous projection images. In recent years, the application of deep learning for image processing has significantly grown in popularity owing to the widespread availability of accessible software (e.g. Tensorflow(Abadi et al., 2016) and PyTorch(Paszke et al., 2017)) , which facilitates the training and employment of deep networks. Convolutional Neural Networks (CNNs) in particular, have been widely used in the field of tomography for image de-noising(Wang et al., 2015; Xie et al., 2012; X. Yang et al., 2018; You et al., 2018), enhancing the quality of tomographic reconstruction(H. Chen et al., 2017; Hendriksen et al., 2019; Ledig et al., 2017) or even improving the reconstruction algorithm itself (Bladt et al., 2015; Hendriksen et al., 2020; Janssens et al., 2015; Pelt et al., 2018).

In principle, CNNs successively convolve images with learned convolutional filters and store the intermediate results in layers. The layers can contain multiple images, each resulting from the convolution with a different filter. As the filter slides, or convolves, across the input image, it multiplies its values to those of the image. These multiplications are added up to produce a single output value (**Figure 8.1a**). The corresponding value of the next layer is found by adding a scalar bias and applying a non-linear activation function. This process is often referred to as feature mapping since each convolutional filter is trained to find different features in an image. In general the j^{th} image of the i^{th} layer (x_i^j) in a CNN is computed as follows:

$$x_i^j = \sigma\left(\sum_{k=0}^{N_{i-1}} C_{f_{ijk}}\, x_{i-1}^k + b_{ij}\right). \qquad [8.1]$$

The number of images in the previous layer is represented by N_{i-1}. $C_{f_{ijk}}$ is the 2D convolution with the learned filter f_{ijk}. b_{ij} is an additional learned bias and σ the non-linear activation function such as ReLU(Nair & Hinton, 2010).

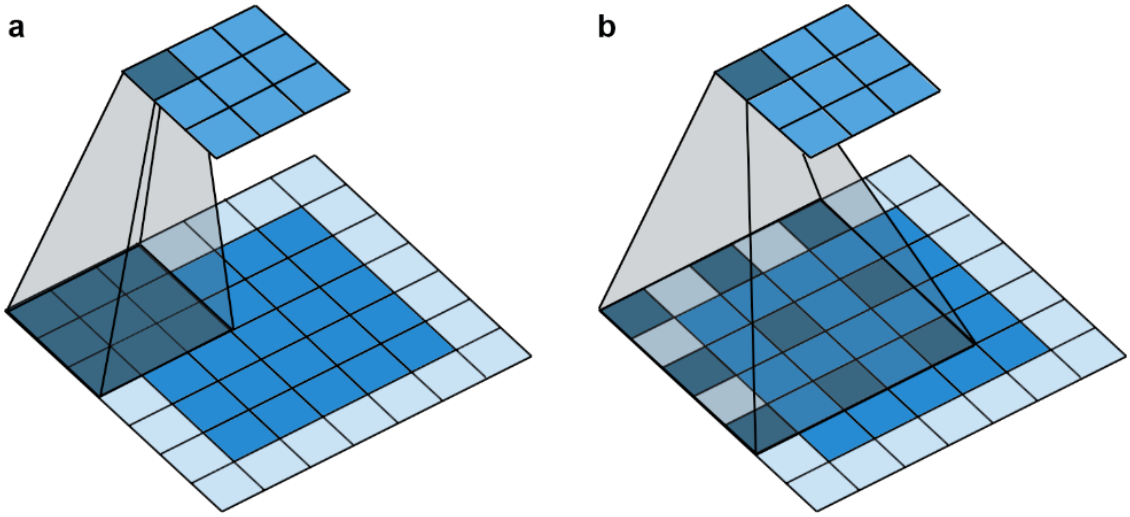

***Figure 8.1**: Illustration of the principle of a convolution (a) and a dilated convolution (b) with padding equal to 1 and the stride set to 2.*

An example of a two layer CNN is illustrated in **Figure 8.2a.** Each arrow represents the execution of the feature mapping. In supervised learning, the trainable parameters (f_{ijk} and b_{ij}) are learned by presenting the network with a large amount of input and target images. In this manner, the CNN attempts to retrieve the most optimal parameters, by iteratively passing the input images through the network and adapting its parameters to minimize the difference between the output of the network and the target images.

Commonly used CNN architectures for improving tomographic images are encoder-decoder networks, such as U-net (**Figure 8.2b**).(Ronneberger et al., 2015) These networks include down- and upscaling operations such that the trainable filters (f_{ijk}) can capture information at different scales. The skip connections (dashed lines) ensure that the information obtained at all scales contributes to the output. Although encoder-decoder networks are often able to produce accurate results, they generally include large amounts of intermediate images and trainable parameters (e.g. millions or more).(Ronneberger et al., 2015) The extensive size and complicated structure of such CNNs impose significant challenges. The large number of trainable parameters demands for a large amount of training data. In addition, the multitude of intermediate images, results in high computer memory requirements when presented with large input image sizes, as is common in TEM imaging. Finally, the structure, initialization and choice of hyper parameters of the neural network itself has a detrimental influence on the final accuracy.(Pelt & Sethian, 2017) All together, this leads to highly problem specific and computationally demanding neural networks which

require a tedious trial-and-error set up. Recently, the Mixed-Scale Dense (MS-D) neural network architecture was proposed, designed to alleviate the limitations of current CNN architectures (**Figure 8.2c**). The MS-D network is densely connected to promote the transmission of information. Furthermore, dilated convolutions are used for capturing image features at various scales, discarding the need for scaling operations (**Figure 8.1**).(Pelt et al., 2018; Pelt & Sethian, 2017) As a result, the MS-D architecture lowers the amount of necessary intermediate layers, thus trainable parameters. This reduces the need for a large amount of training images which in turn enables training on larger images. Furthermore, MS-D networks are more stable with respect to the hyper parameter selection, making them widely applicable to various problems. (Pelt et al., 2018; Pelt & Sethian, 2017)

Here, we will train a MS-D network for pre-processing continuously acquired projection data, in an attempt to improve the quality of the reconstruction. Collecting a sufficiently large training dataset for training a neural network is often one of the key limitations of supervised learning. Our strategy is as follows: conventional and continuous tomographic series were acquired for 6 different nanoparticles at various microscope settings (**Table 6.1**). For each of these nanoparticles, a reconstruction based on the conventional series was obtained using the EM reconstruction algorithm. Afterwards, simulated, forward projections were calculated along all "continuous" projection angles. Projection images from the experimental tilt series which were previously deemed overtly deteriorated (**Section 6.2.4**), were removed from both the experimental as well as the forward projected tilt series and are not included in the training data set. In this manner, a large number of input-target images was generated per nanoparticle (~ 250). Prior to training, all projection images were cropped to an image size of 512 x 512 pixels, when necessary. The neural network was set up using a PyCUDA implementation of the MS-D network.(Klöckner et al., 2012; Pelt et al., 2018; Pelt & Sethian, 2017) The network was 100 layers deep with the dilation for each layer evenly spread between 1 and 10, as proposed in previous work.(Hendriksen et al., 2019; Pelt et al., 2018) The network was trained using the ADAM algorithm(Kingma & Ba, 2015) with a mini-batch size of a single 2D image.

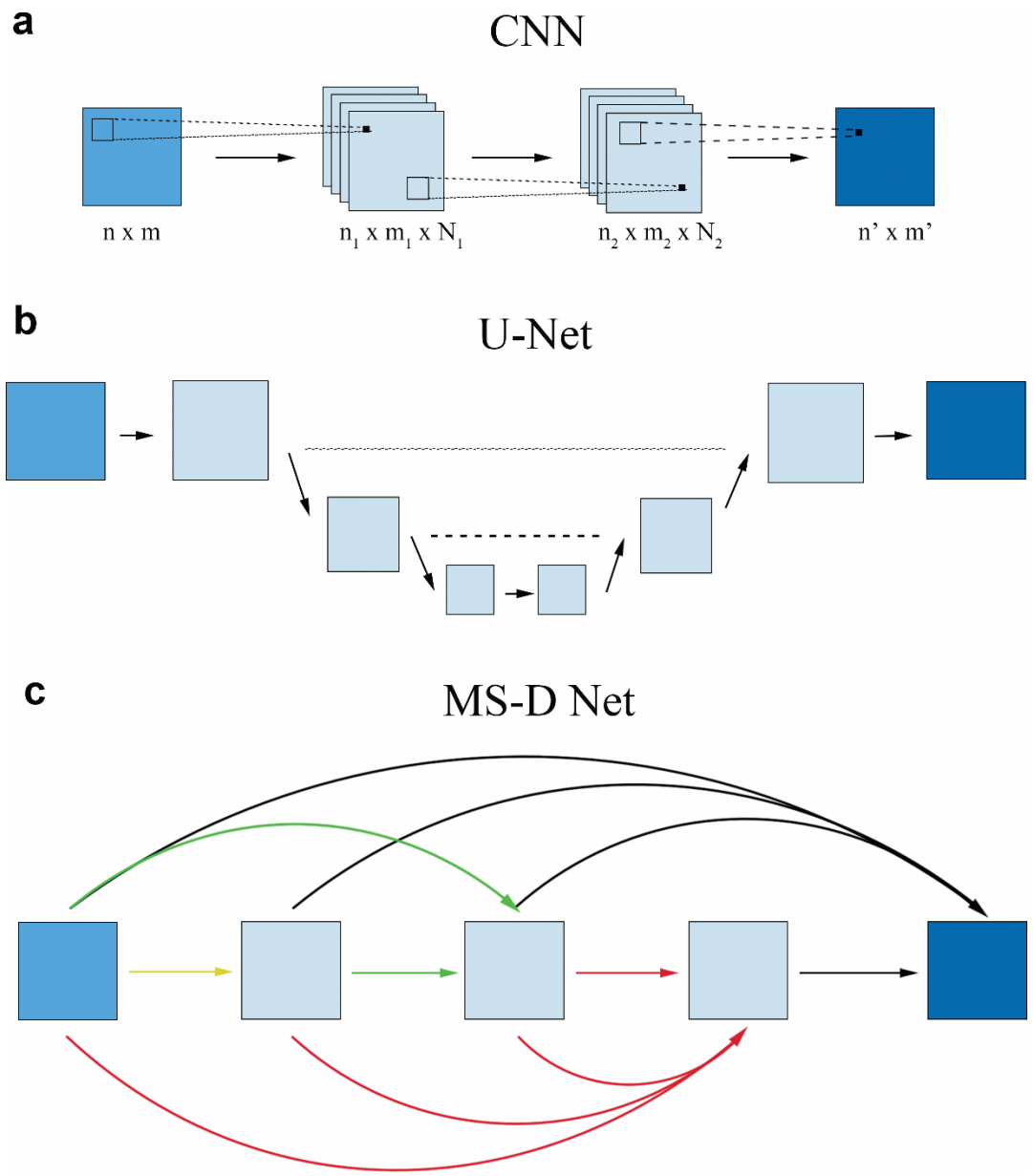

***Figure 8.2**: Schematic representations of: (a) a two layer CNN, the arrows represent the convolutions with nonlinear activation. (b) A U-net architecture which includes down- and upscaling of the images. The dashed lines represent skip connections. (c) A MS-D network. The arrows represent dilated convolutions, each color representing a different dilation.*

During training, the network convolves its learned filters with the provided input images and compares its output to the provided target image. The filters are adjusted to minimize the MSE between the network output and the target image. To evaluate the progress of training, an independent validation set was constructed. The validation set was composed out of input-target image pairs unknown to the neural network. The MSE of the validation set is calculated after every 250 gradient steps and the training is stopped when no

notable improvement in validation error is found after 25000 gradient steps. The network, yielding the lowest validation error is then used to filter all continuous projection data. All computations were performed on a workstation containing a single NVIDIA GTX 1060 GPU with 6 GB of global memory.

In **Figure 8.3** an example is shown of (**a**) an input and (**b**) corresponding target image of the Au decahedron (**Table 6.1**, sample 1), included in the validation set. **Figure 8.3c** displays the output of the trained network, when presented with the input image, depicted in **Figure 8.3a.** It is clear that the MS-D network efficiently removes the jitter without introducing any blurring. The network output is in very good agreement with the provided target image (**Figure 8.3b**). A comparison to **Figure 8.3d,** where the jitter is removed using the previously proposed low pass filter, shows that the MS-D net results in sharper images with a higher signal-to-noise ratio.

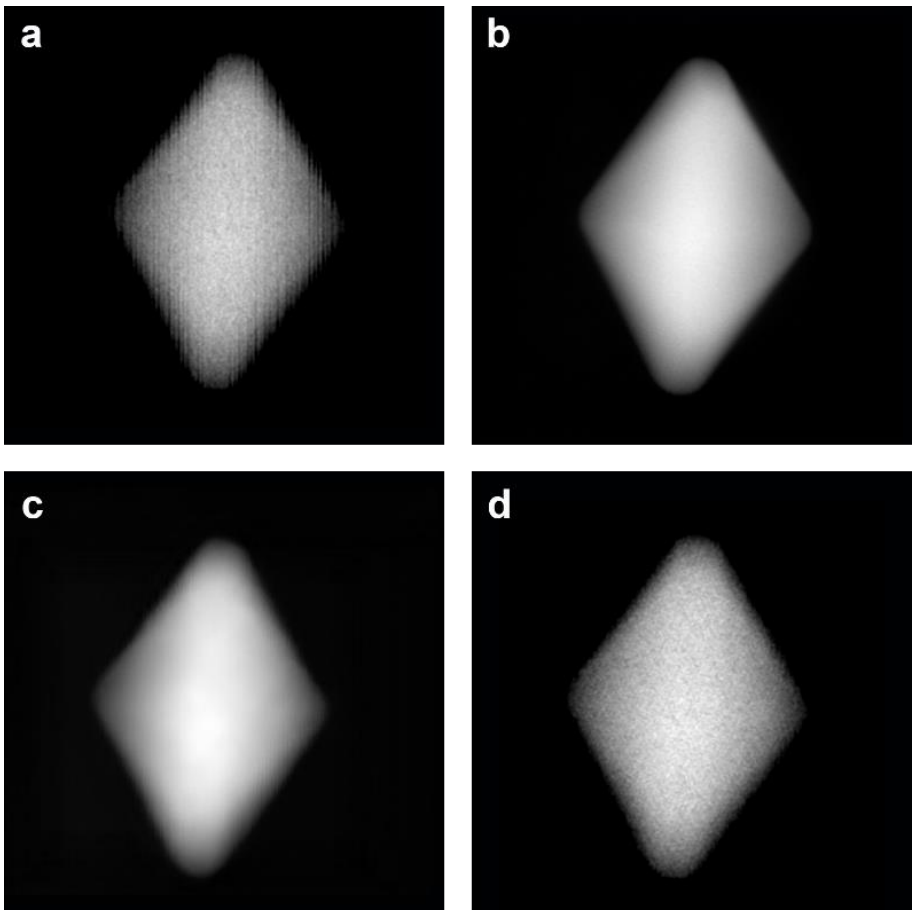

***Figure 8.3**: (a-b) Input and target image taken from the validation data set. (c) The input image after applying the trained filter from the MS-D network. (d) The input image after applying directional low pass filter.*

To evaluate the benefit of processing the continuous projection images with the trained MS-D filter, instead of the simple directed low-pass filter, the MS-D network was used to remove the scanning jitter present in each continuous projection image of the samples listed in **Table 6.1**. In **Figures 8.4-8.9,** the 3D reconstructions and associated central orthoslices obtained from the conventional series (top row), the continuous series using the directed low pass filter (middle row) and the continuous series using the MS-D filter (bottom row) are shown. Except for the application of the MS-D filter instead of the directed low pass filter, all processing was performed as described in **Section 6.2**.

Clearly, pre-processing the continuous projection images with the MS-D network, efficiently reduces all noise present in the orthoslices. The reconstructions contain almost no artefacts and have more homogeneous gray level distributions than the reconstructions obtained from the conventionally acquired series. Such homogeneity expresses the noise reducing capabilities of neural networks and facilitates further quantification where segmentation is involved. However, for the Au nanosphere (**Figure 8.6**), remaining streaks can be observed within the orthoslices, indicating that the scanning jitter was not completely removed from the experimental data. Similar observations can be made in **Figure 8.7i** for the Au bipyramid. This might indicate that the observed jitter is too specific for the used experimental conditions (e.g. magnification or dwell time) to be able train a generally well performing network, with a confined depth. Little change is observed in the NS reconstructions when applying the MS-D network (**Figures 8.8-8.9**). It is likely that the shape of the NSs diverges too far from the other nanoparticles within the training dataset (**Table 6.1**), leading to suboptimal performance for the NS sample.

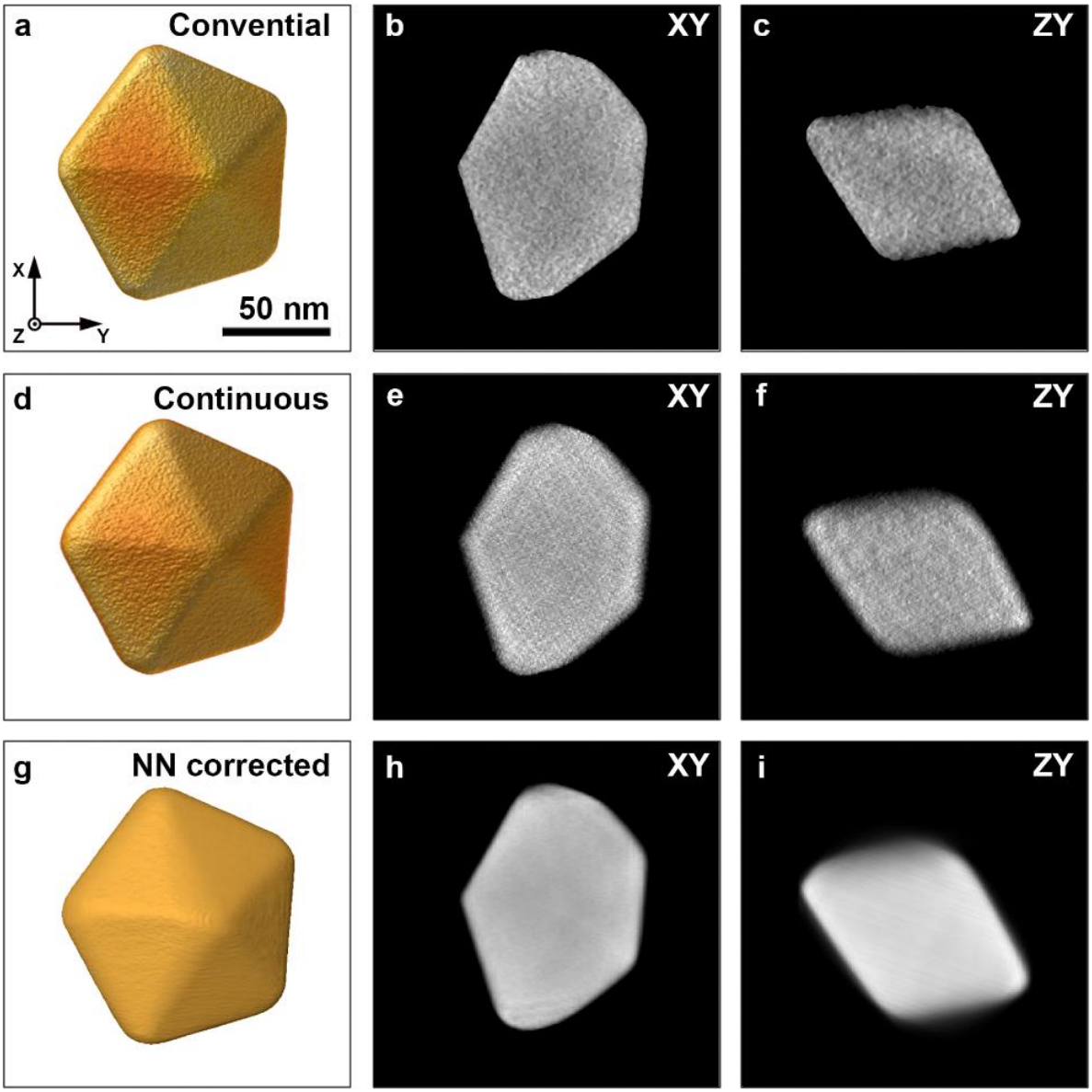

***Figure 8.4**: (a-c) 3D rendering of the reconstruction of the conventionally acquired tilt series of a Au decahedron, paired by two central orthoslices through it. (d-f) 3D rendering of the reconstruction of the continuously acquired tilt series, paired by 2 central orthoslices through it, using the directed low-pass filter for pre-processing. (g-i) 3D rendering of the reconstruction of the continuously acquired tilt series, paired by 2 central orthoslices through it, using the trained MS-D net for pre-processing.*

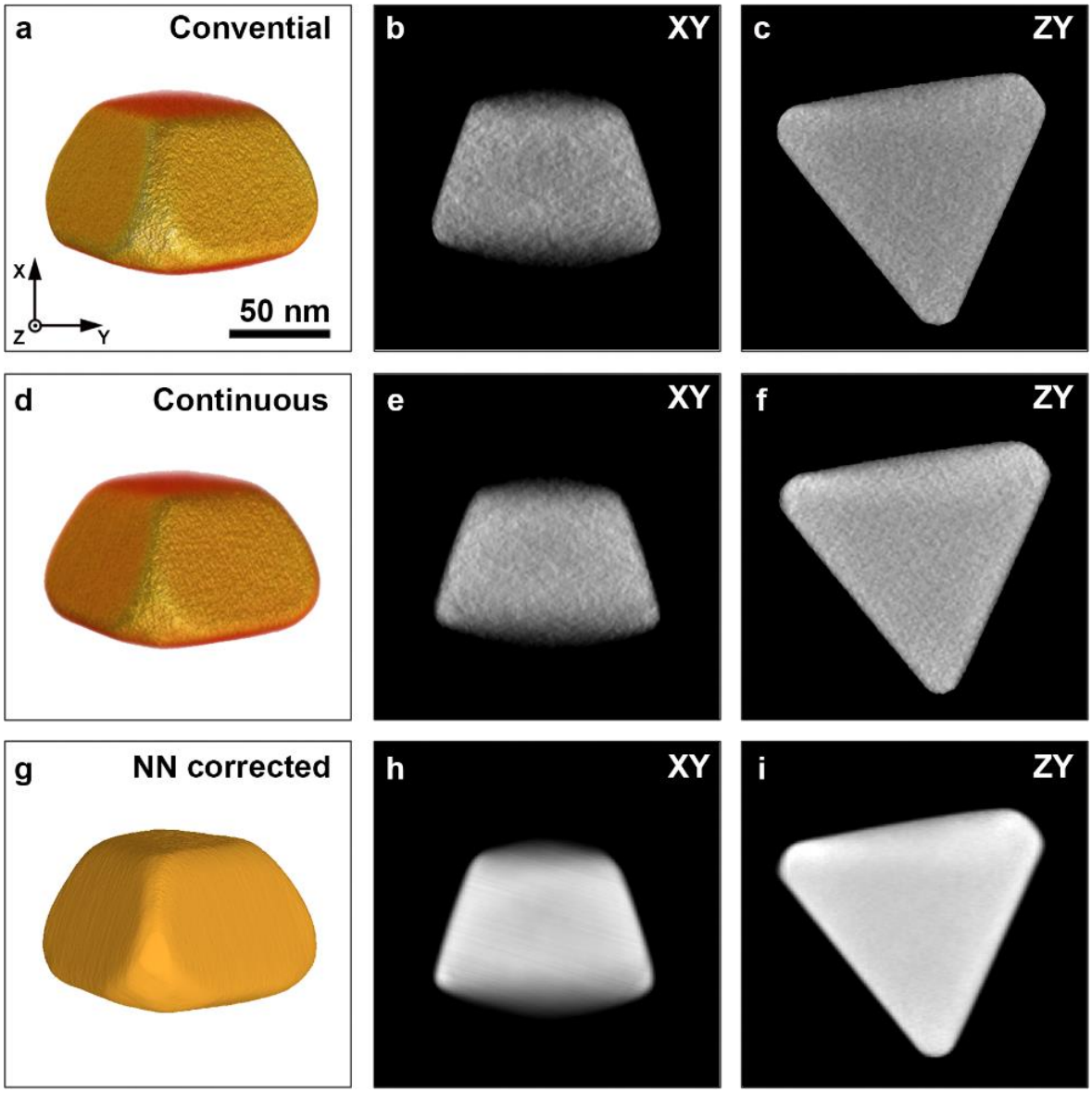

***Figure 8.5**: (a-c) 3D rendering of the reconstruction of the conventionally acquired tilt series of a Au pentahedron, paired by two central orthoslices through it. (d-f) 3D rendering of the reconstruction of the continuously acquired tilt series, paired by 2 central orthoslices through it, using the directed low-pass filter for pre-processing. (g-i) 3D rendering of the reconstruction of the continuously acquired tilt series, paired by 2 central orthoslices through it, using the trained MS-D net for pre-processing.*

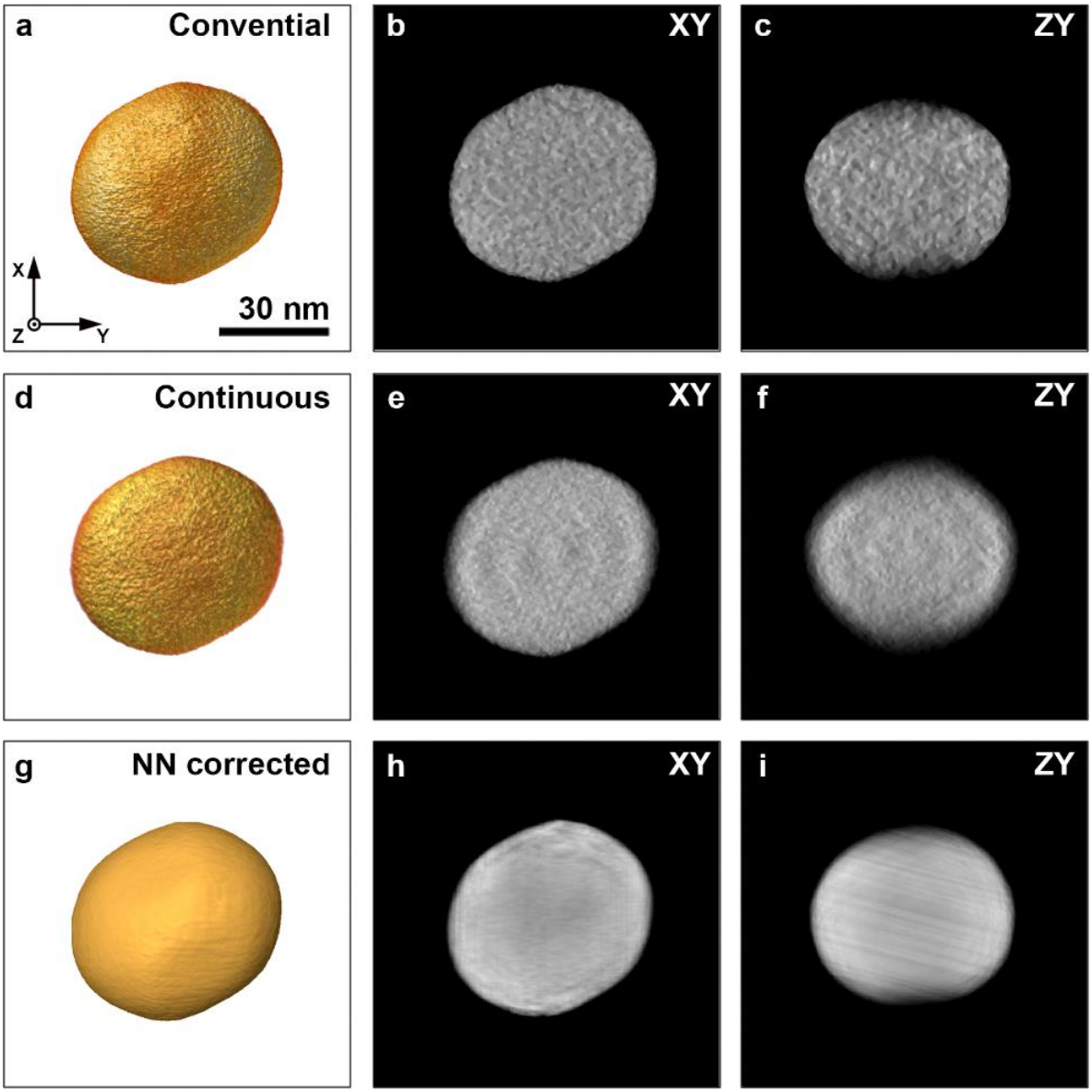

Figure 8.6: *(a-c) 3D rendering of the reconstruction of the conventionally acquired tilt series of a Au nanosphere, paired by two central orthoslices through it. (d-f) 3D rendering of the reconstruction of the continuously acquired tilt series, paired by 2 central orthoslices through it, using the directed low-pass filter for pre-processing. (g-i) 3D rendering of the reconstruction of the continuously acquired tilt series, paired by 2 central orthoslices through it, using the trained MS-D net for pre-processing.*

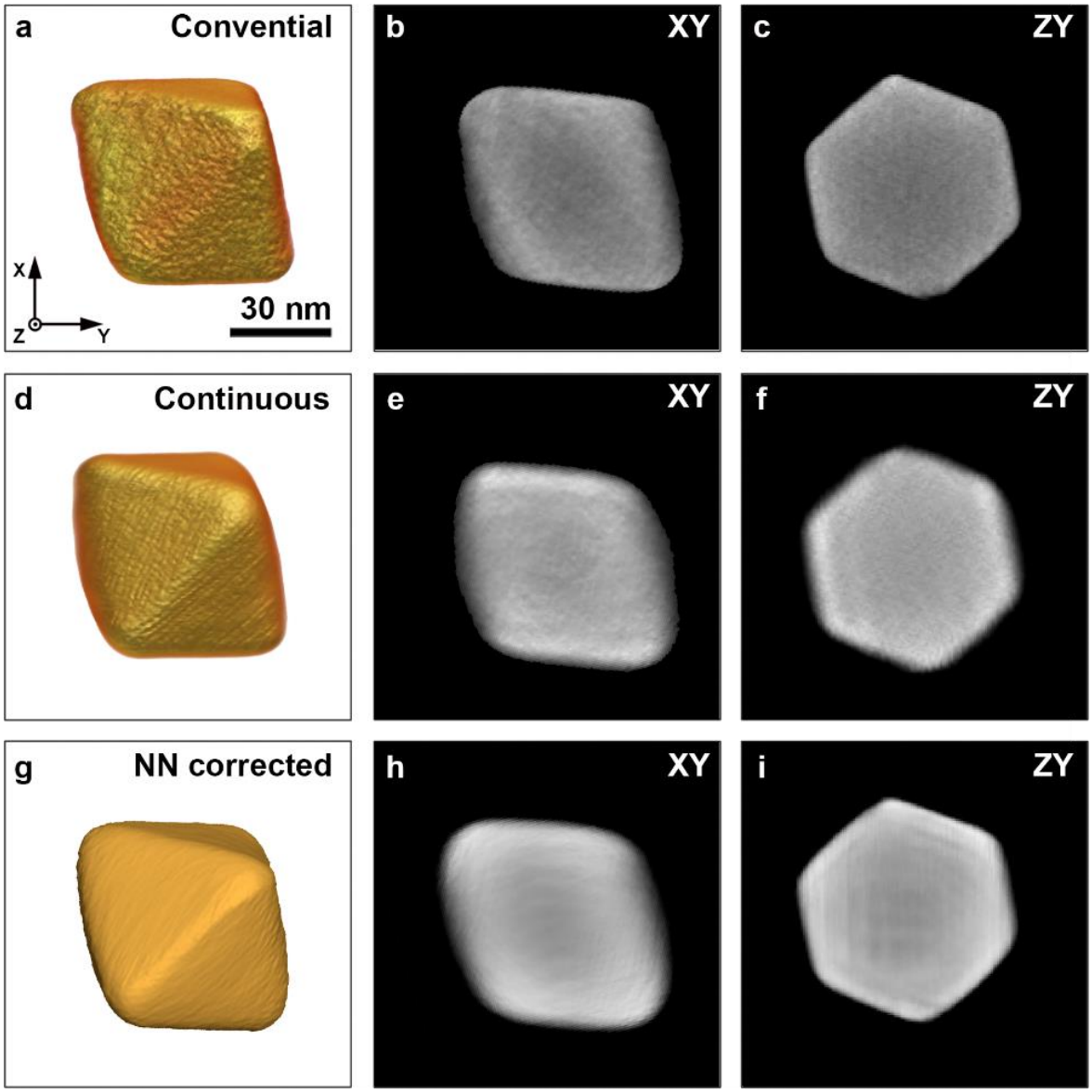

***Figure 8.7**: (a-c) 3D rendering of the reconstruction of the conventionally acquired tilt series of a Au bipyramid, paired by two central orthoslices through it. (d-f) 3D rendering of the reconstruction of the continuously acquired projection images, paired by 2 central orthoslices through it, using the directed low-pass filter for pre-processing. (g-i) 3D rendering of the reconstruction of the continuously acquired tilt series, paired by 2 central orthoslices through it, using the trained MS-D net for pre-processing.*

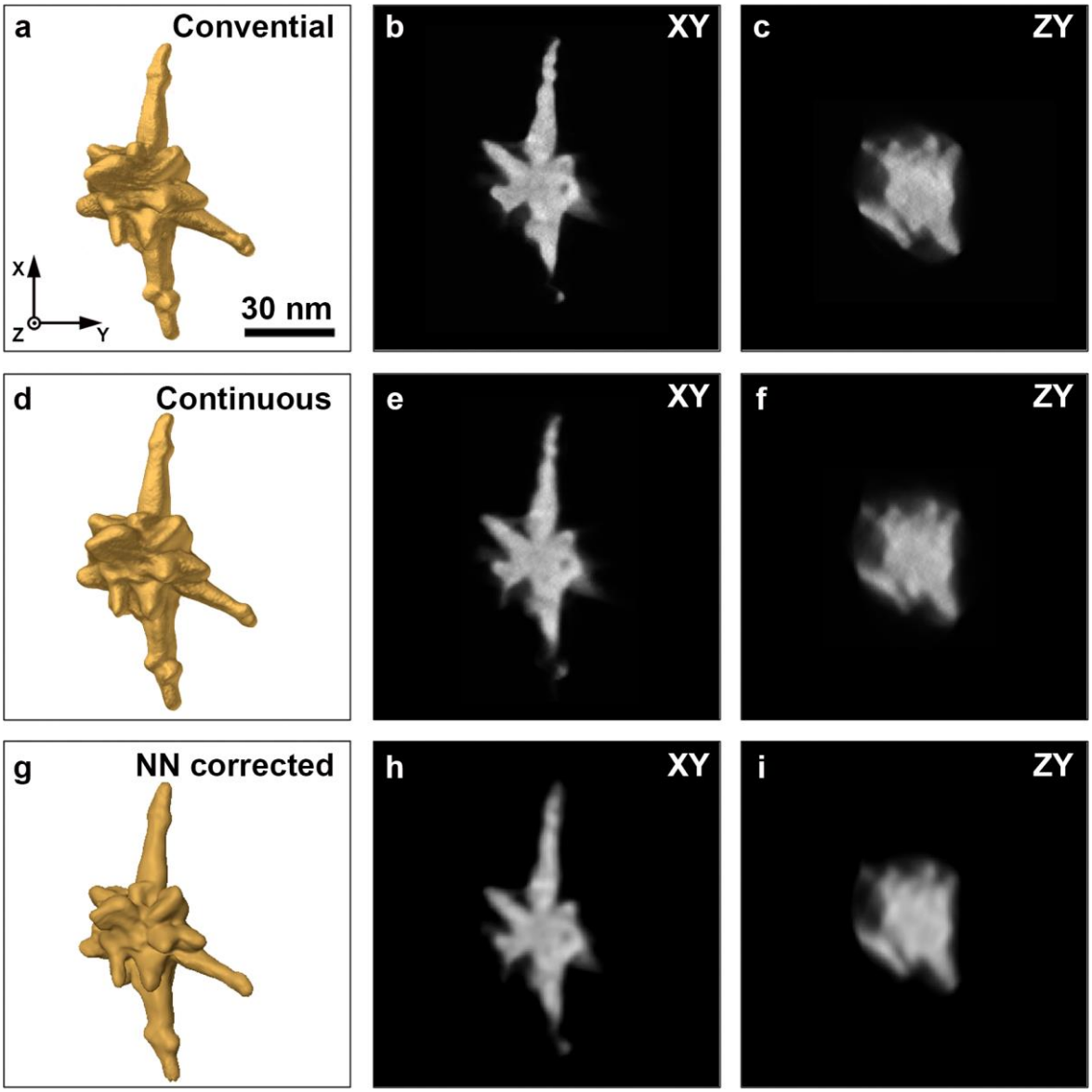

***Figure 8.8**: (a-c) 3D rendering of the reconstruction of the conventionally acquired tilt series of a Au NS, paired by two central orthoslices through it. (d-f) 3D rendering of the reconstruction of the continuously tilt series, paired by 2 central orthoslices through it, using the directed low-pass filter for pre-processing. (g-i) 3D rendering of the reconstruction of the continuously acquired tilt series, paired by 2 central orthoslices through it, using the trained MS-D net for pre-processing.*

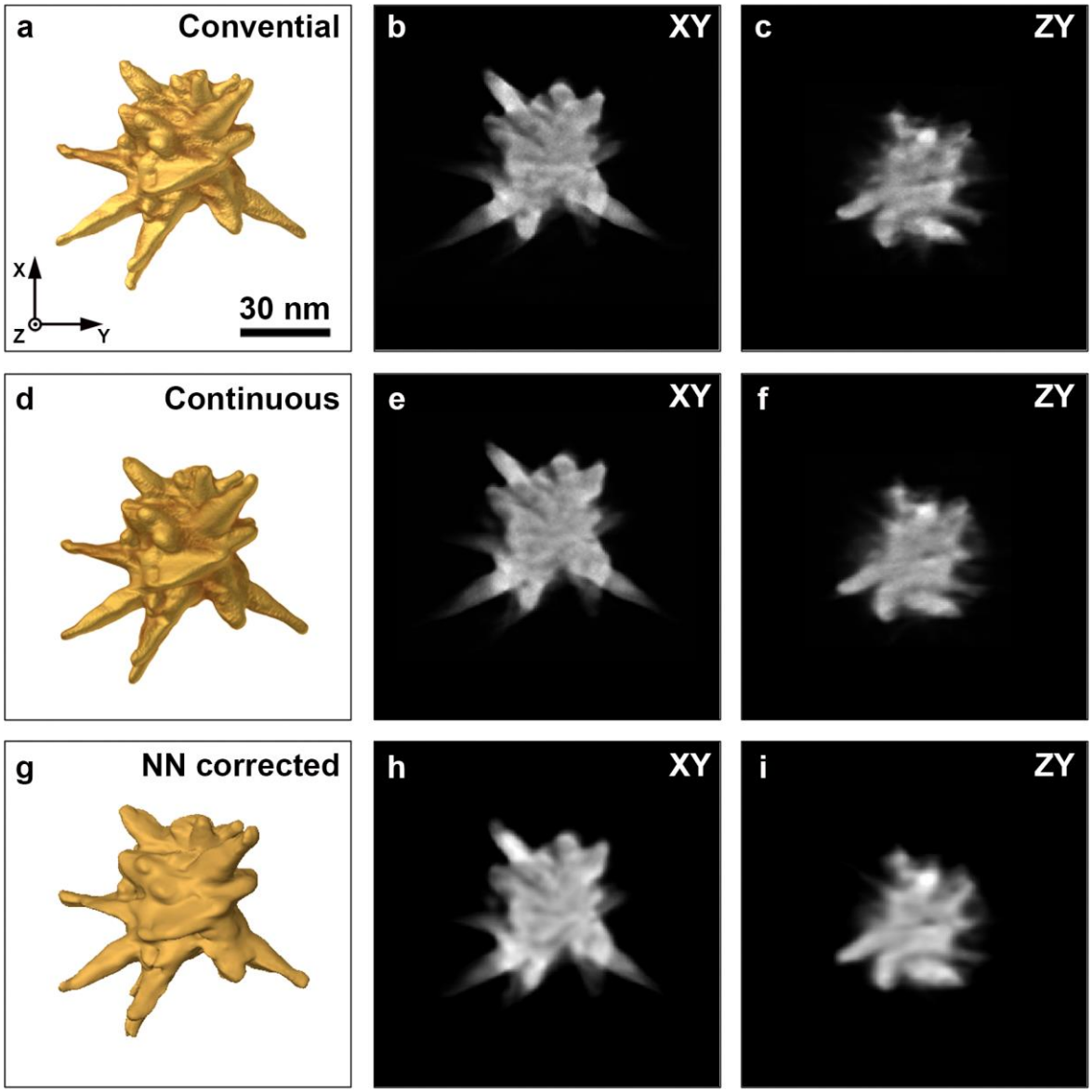

***Figure 8.9**: (a-c) 3D rendering of the reconstruction of the conventionally acquired tilt series of a Au NS, paired by two central orthoslices through it. (d-f) 3D rendering of the reconstruction of the continuously acquired tilt series, paired by 2 central orthoslices through it, using the directed low-pass filter for pre-processing. (g-i) 3D rendering of the reconstruction of the continuously acquired tilt series, paired by 2 central orthoslices through it, using the trained MS-D net for pre-processing.*

To quantify the observed differences, the shape and volume errors were calculated for the reconstructions obtained from the continuous tilt series after processing by the trained MS-D network. The conventional reconstructions served as ground truth. The calculated values are listed in **Table 8.1**. For comparison, we included the values previously obtained when using the directed low-pass filter for the jitter removal.

		E_s	E_s *MS-D*	E_V	E_V *MS-D*
Sample 1	Au decahedron	5.43 ± 0.01 %	**3.29 ±** 0.01 %	4.91 ± 0.01 %	**0.76** ± 0.01 %
Sample 2	Au pentahedron	5.48 ± 0.01 %	**4.88 ±** 0.01 %	2.40 ± 0.01 %	**2.00** ± 0.01 %
Sample 3	Au nanosphere	5.26 ± 0.01 %	**3.97 ±** 0.01 %	4.51 ± 0.01 %	**3.30** ± 0.01 %
Sample 4	Au bipyramid	7.93 ± 0.01 %	**4.04 ±** 0.01 %	**2.27** ± 0.01 %	2.39 ± 0.01 %
Sample 5	Au nanostar	13.32 ± 0.01 %	**12.97** ± 0.01 %	7.61 **±** 0.01 %	**2.84** ± 0.01 %
Sample 6	Au nanostar	**10.98** ± 0.01 %	18.00 **±** 0.01 %	**2.65** ± 0.01 %	9.39 ± 0.01 %

Table 8.1*: The shape and volume errors calculated between the reconstructions obtained from the conventional and continuous acquisition strategies using the different pre-processing methodologies.*

Table 8.1 demonstrates that the use of the MS-D network considerably reduces both the shape as volume error for the specimens with a simple 3D geometry (sample 1-4). For the shape error, improvements of up to ~50% are found. However, for more complex morphologies, such as the NSs, the MS-D network at most achieves a comparable accuracy as obtained when processing the data with the directed low-pass filter. For the second NS (sample 6) the MS-D network even performs considerably worse. We believe this may result from an underrepresentation of projection images yielding anisotropic shapes in the training dataset. Nevertheless, altogether the neural network approach shows great promise for handling and improving the continuous projection images. We believe that by expanding the training data set or with more complex approaches where for instance multiple consecutive projection images are used as input-target pairs(Hendriksen et al., 2019), or where a network

is trained to improve the reconstruction itself(Bladt et al., 2015), even more adequate results may be obtained.

8.2 Fast Incremental Tomography

Although supervised learning can improve the reconstruction accuracy, they require a large and diverse training set in order to learn generally applicable filters. This is the reason to consider hardware solutions as well. Whereas the influence of the jitter can be minimised through complicated post-processing methods, it is preferential to avoid such noise altogether. Therefore, we propose a hybrid acquisition strategy that combines the advantages of the conventional and continuous acquisition method, referred to as the fast incremental acquisition strategy (**Figure 8.10**). When applying this incremental approach, the specimen is rapidly tilted between predefined angles. At each angle, a certain relaxation time is imposed which can be used to reposition and refocus the sample manually. Although projection images are continuously acquired, the tilting is performed in an incremental manner, similar as during the conventional method. Therefore, projection images are also obtained while the goniometer is stable, efficiently removing the source of the perceived jitter. In this manner, the incremental approach provides a compromise between the potential speed of a continuous acquisition, and the image quality of a conventional acquisition. An example of a raw incremental tilt series is provided in the **Supplementary Movie 2** (see QR-code below). This incremental approach was implemented through a combination of Python and TEM scripting, effectively interacting with each other through COM objects.

To evaluate the difference in reconstruction quality between the continuous and incremental approach, we acquired conventional, continuous and incremental tilt series for five sample morphologies. However, the particles are different than those used in **Chapter 6** and in **Section 8.1**. Each conventional series consisted out of 51 projection images, acquired over an angular range of ± 75° with a tilt increment of 3°.

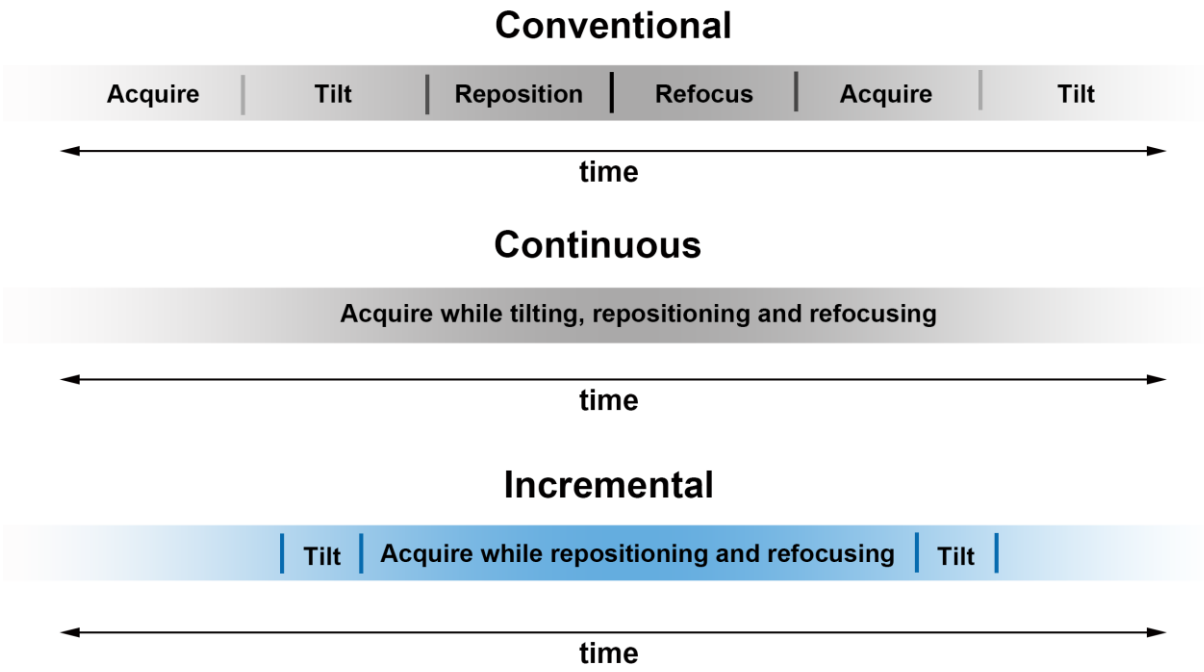

***Figure 8.10**: Graphic illustration of conventional, continuous and incremental tomography.*

	Sample description	*Frame size (px)*	*Frame time (s)*	*Pixel size (pm)*	*Dwell time (µs)*	*Microscope*
Sample 7	Au octopod	512 x 512	1	1086	3	Titan (300 kV)
Sample 8	Au octopod	512 x 512	1	1193	3	Osiris (200 kV)
Sample 9	Au@Ag rod	512 x 512	1	771	3	Titan (300 kV)
Sample 10	Au@Ag nanoparticle	512 x 512	1	597	3	Osiris (200 kV)
Sample 11	branched Au nanoparticle	512 x 512	1	388	3	Titan (300 kV)

***Table 8.2**: Experimental details of the tilt series acquired for evaluating the different acquisition methodologies.*

To qualitatively compare the continuous and incremental acquisition approaches, reconstructions were calculated for both and compared to the reconstruction obtained from the conventional tilt series. Both the continuous and incremental series were processed according to **Section 6.2**, with exception to not applying the low-pass filter for the incremental series. Such filtering was no longer required since the jitter was already experimentally removed. In **Figures 8.11-8.15**, 3D renderings of the reconstructions of respectively the conventional, continuous and incremental series are shown together with central orthoslices.

For the Au octopods (sample 7-8), shown in **Figures 8.11-8.12**, little difference is found between the reconstructions obtained from the conventional, continuous and incremental acquisition. Since these nanostructures are relatively large, the acquisitions could be performed at moderate magnification. The vibrations caused by the mechanical instabilities occur at such a small scale that for such moderate magnifications their effect is almost negligible. It should be noted that as a side effect of the large size of the nanoparticles, absorption artefacts (i.e. the underestimated intensity in the interior) can be seen in both reconstructions.

In **Figures 8.13-8.14,** reconstructions of Au@Ag nanoparticles (sample 9-10) are shown. To accurately investigate the interface between the Au and Ag phases, a higher experimental magnification was required. The blurring induced by the continuous acquisition prevents observing an accurate separation between both phases. However, the incremental reconstruction reduces the amount of blurring considerably, enabling an accurate investigation of the Au-Ag interface and their potential intermixture.(Skorikov et al., 2019) Similar effects are observed for the branched Au nanoparticle (sample 11, **Figure 8.15**), where the incremental acquisition reduces the mechanical instabilities and consequently the blurring artefacts.

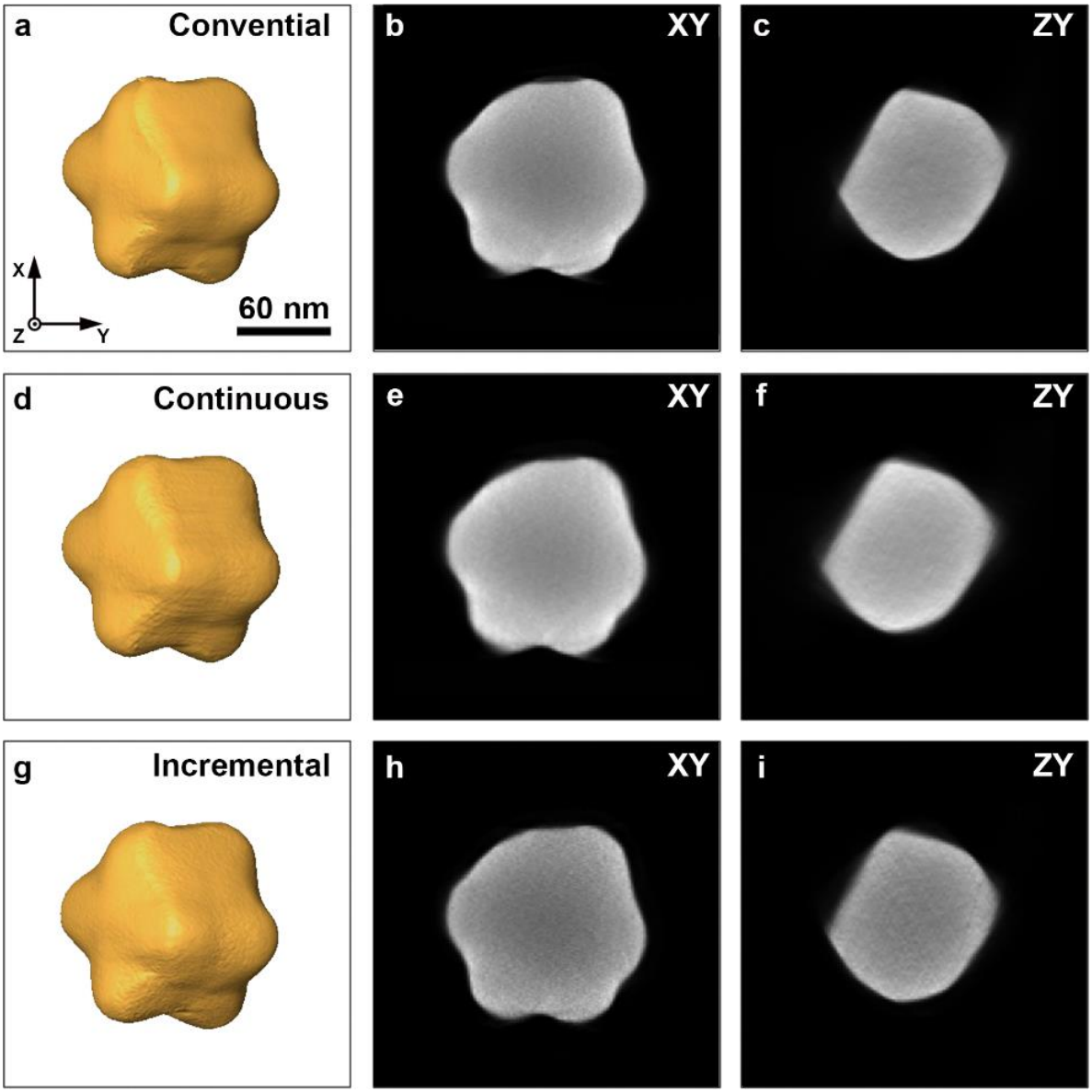

***Figure 8.11**: (a-c) 3D rendering of the reconstruction of the conventionally acquired tilt series of a Au octopod, paired by two central orthoslices through it. (d-f) 3D rendering of the reconstruction of the continuously acquired tilt series, paired by 2 central orthoslices through it. (g-i) 3D rendering of the reconstruction of the incremental acquired tilt series, paired by 2 central orthoslices through it.*

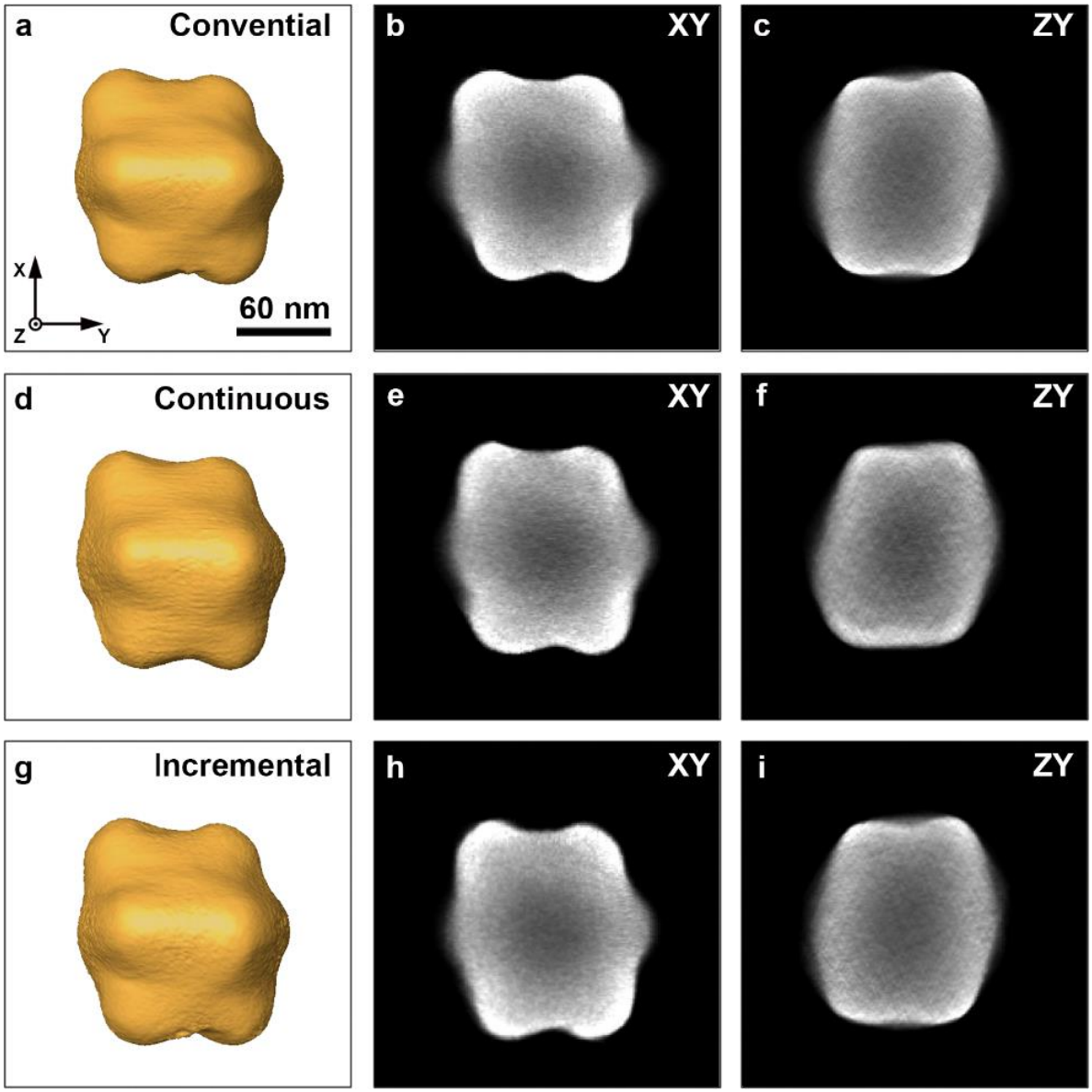

***Figure 8.12**: (a-c) 3D rendering of the reconstruction of the conventionally acquired tilt series of a Au octopod, paired by two central orthoslices through it. (d-f) 3D rendering of the reconstruction of the continuously acquired tilt series, paired by 2 central orthoslices through it. (g-i) 3D rendering of the reconstruction of the incremental acquired tilt series, paired by 2 central orthoslices through it.*

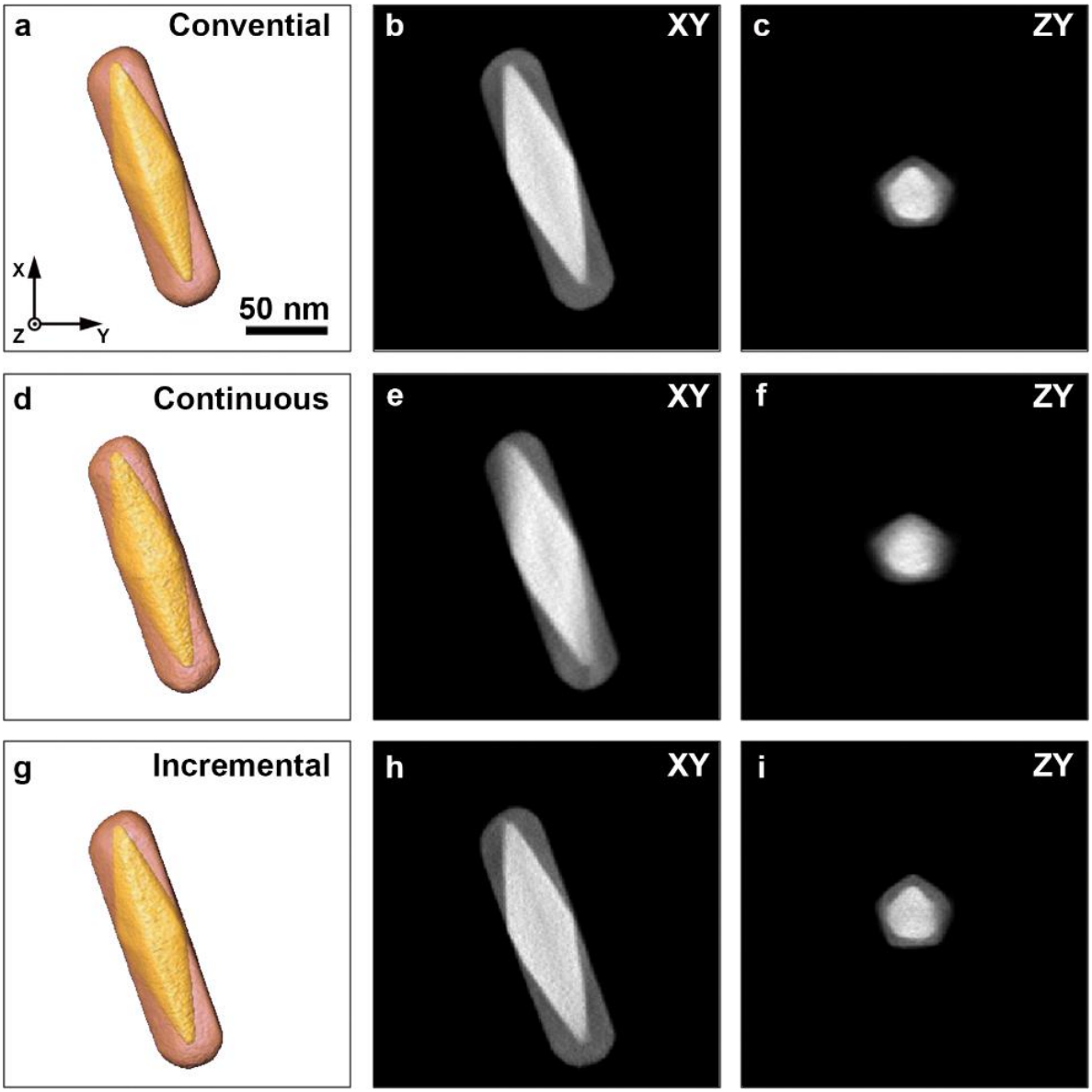

***Figure 8.13**: (a-c) 3D rendering of the reconstruction of the conventionally acquired tilt series of a Au@Ag NR, paired by two central orthoslices through it. (d-f) 3D rendering of the reconstruction of the continuously acquired tilt series, paired by 2 central orthoslices through it. (g-i) 3D rendering of the reconstruction of the incremental acquired tilt series, paired by 2 central orthoslices through it.*

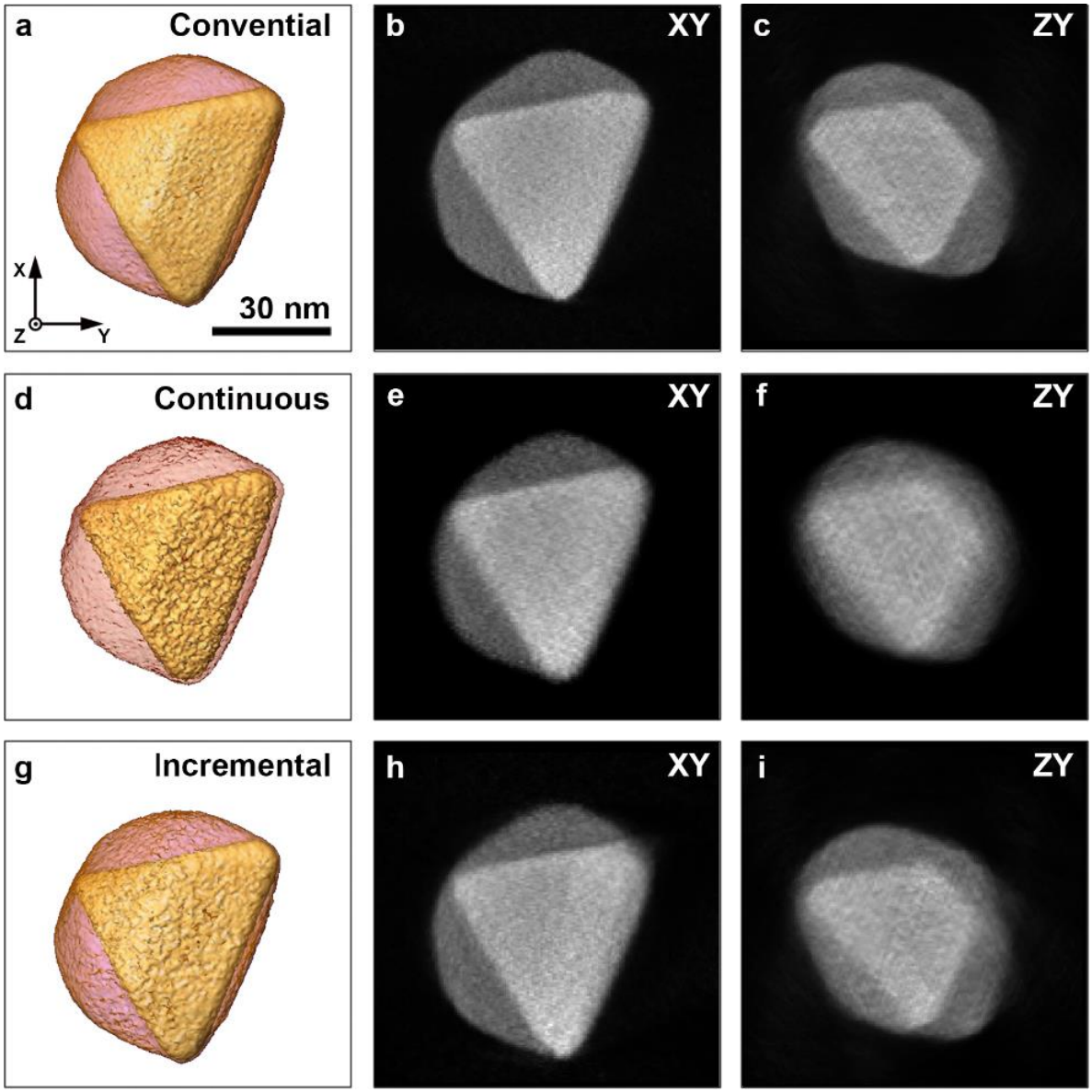

***Figure 8.14**: (a-c) 3D rendering of the reconstruction of the conventionally acquired tilt series of a Au@Ag nanoparticle, paired by two central orthoslices through it. (d-f) 3D rendering of the reconstruction of the continuously acquired tilt series, paired by 2 central orthoslices through it. (g-i) 3D rendering of the reconstruction of the incremental acquired tilt series, paired by 2 central orthoslices through it.*

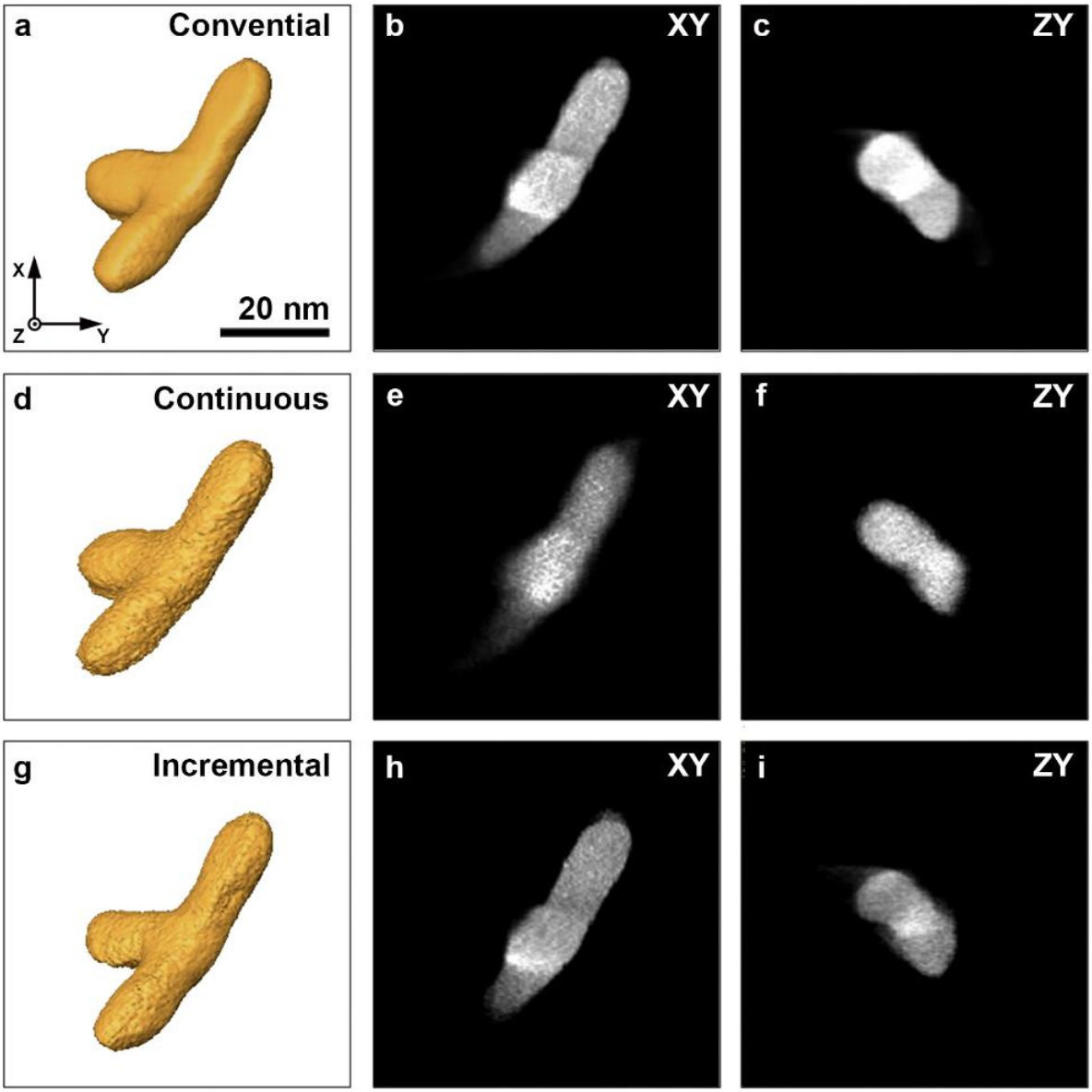

***Figure 8.15**: (a-c) 3D rendering of the reconstruction of the conventionally acquired tilt series of a branched Au nanoparticle, paired by two central orthoslices through it. (d-f) 3D rendering of the reconstruction of the continuously acquired tilt series, paired by 2 central orthoslices through it. (g-i) 3D rendering of the reconstruction of the incremental acquired tilt series, paired by 2 central orthoslices through it.*

To analyze the differences quantitatively, both the shape and volume errors were calculated. For the Au@Ag nanoparticles, an error measure was defined for each separate phase. In all cases, the threshold(s) for the segmentation were determined through Otsu's method(Otsu, 1979). In **Table 8.3** the calculated errors are summarised. The reconstructions calculated from the conventional tilt series where used as ground truth.

		E_S *continuous*	E_S *incremental*	E_V *continuous*	E_V *incremental*
Sample 7	Au octopod (Titan)	2.95 ± 0.01 %	**2.26 ± 0.01 %**	2.05 ± 0.01 %	**1.69 ± 0.01 %**
Sample 8	Au octopod (Osiris)	6.24 ± 0.01 %	**4.70 ± 0.01 %**	5.25 ± 0.01 %	**2.74 ± 0.01 %**
Sample 9, Au	Au@Ag rod (Titan)	8.09 ± 0.01 %	**3.77 ± 0.01 %**	5.61 ± 0.01 %	**0.25 ± 0.01 %**
Sample 9, Ag		14.96 ± 0.01 %	**8.34 ± 0.01 %**	4.08 ± 0.01 %	**0.42 ± 0.01 %**
Sample 10, Au	Au@Ag nanoparticle (Osiris)	9.15 ± 0.01 %	**8.81 ± 0.01 %**	**1.37 ± 0.01 %**	1.78 ± 0.01 %
Sample 10, Ag		24.00 ± 0.01 %	**16.24 ± 0.01 %**	16.85 ± 0.01 %	**4.68 ± 0.01 %**
Sample 11	branched Au nanoparticle (Titan)	16.30 ± 0.01 %	**12.90 ± 0.01 %**	5.88 ± 0.01 %	**1.23 ± 0.01 %**

Table 8.3*: The shape and volume errors calculated between the reconstructions obtained from the continuous and incremental acquisition strategies for the different nanoparticles.*

From **Table 8.3** it can be seen that the incremental approach improves the reconstruction accuracy considerably. Especially for the Au@Ag nanoparticles a substantial reduction in both errors is found. Noteworthy, the shape error for the Au octopod investigated in Titan TEM (sample 7) is lower that of the shape error for the near identical octopod investigated in the Osiris TEM (sample 8), independent of the used the acquisition approach. This expresses that the microscope itself strongly influences the accuracy which can be achieved by the fast acquisition methodologies. This observed difference in error relates to the improved stability of the goniometric stage of the Titan TEM in comparison to the

Tecnai Osiris TEM. As the stability of the goniometer stage improves, the fast approaches will produce more accurate results.

Previously we discussed that the magnification plays a vital role as well. Indeed, for the Au octopod (sample 7) investigated at the Titan TEM with a pixel size of 1086 pm, a shape error of 2.95 ± 0.01 % was found for the continuous acquisition. The branched nanoparticle (sample 11) which was also investigated in the Titan TEM albeit using a much smaller pixel size (338 pm), resulted in a far higher shape error, equal to 16.30 ± 0.01 %. This clearly shows that indeed at such small scales, the vibrations induced by the mechanical instabilities play a more detrimental role on the reconstruction accuracy.

To conclude, a hybrid approach for fast tomography was presented that involves incremental tilting during a continuous acquisition. The total run time of the incremental acquisition depends on the selected tilt increment and relaxation time imposed at each tilt. It was demonstrated that this hybrid acquisition methodology considerably increases the reconstruction accuracy, especially for heterogeneous nanoparticles. A downside of the incremental approach is that during the tilt it is impossible to manually track the nanoparticles. As a consequence, the particle more easily drifts out of the field of view during the acquisition. In addition, the maximal achievable speed is limited by the chosen tilt increment and relaxation time. Large tilt increments and short relaxation periods will speed up the acquisition, but complicate the tracking of the particle. It is clear that for each fast tomography experiment care has to be taken in choice of microscope, experimental settings and acquisition strategy. Although the presented acquisition methods can drastically reduce the run time of the acquisition of a tilt series, one key limitation remains the duration of the post-processing and reconstruction. These are typically performed after the experiment has been completed. Therefore, no 3D information is available to steer the tomographic acquisition while it is ongoing. In **Chapter 9** we will provide a solution for this restriction.

PART III: ACCELERATED RECONSTRUCTION

9. Reconstruction of Arbitrary Slices for Real-Time Tomography

3D investigations typically comprise multiple steps, including acquisition, reconstruction, and analysis/quantification. Usually, the latter two steps are performed offline, at a dedicated workstation. This sequential workflow prevents on-the-fly control of experimental parameters to improve the quality of the 3D reconstruction, to select a relevant nanoparticle for further characterization or to steer an in-situ tomography experiment. Here, we present an efficient approach to overcome these limitations, based on the real-time reconstruction of arbitrary 2D reconstructed slices through a 3D object.

This chapter is based on:

Vanrompay, H., Buurlage, J. W., Pelt, D. M., Kumar, V., Xiaolu Z., Liz-Marzán L.M., Bals, S., & Batenburg, K. J. (2020). Real-time reconstruction of arbitrary slices for quantitative and in-situ three-dimensional characterization of nanoparticles. *Particle and Particle Systems Characterization*. https://doi.org/10.1002/ppsc.202000073

The synthesis of the samples was carried out at the Bionanoplasmonics Laboratory, CIC biomaGUNE in Spain. The RECAST3D software was developed at the CWI in the Netherlands. All TEM acquisition was carried out at the research group for electron microscopy of materials science (EMAT) at the University of Antwerp. I was responsible for the acquisition, analysis and reconstruction of all datasets. Together with J. W. Buurlage and D. M. Pelt, I designed the novel procedures for reading the projection images, their alignment, reconstruction, and analysis in the RECAST3D software.

9.1 Introduction

During a typical electron tomography experiment, a series of 2D projection images are collected along various tilt angles, to cover an angular range that is as large as possible. After alignment of the tilt series, they serve as the input to a mathematical algorithm that reconstructs the 3D structure of the object. Although the acquisition of a tilt series can be automated, it can take (many) hours to obtain all images, depending on the complexity of the experiment. In addition, both the alignment and the reconstruction of the acquired projection images are carried out through offline post-processing procedures, performed at a dedicated workstation. These steps are computationally demanding, leading to a total data processing time of at least 1 hour. To dramatically accelerate the acquisition of tilt series, fast tomography was introduced.

As was shown in **Chapter 7**, fast HAADF-STEM tomography enables a new range of experiments, during which the dynamic behavior of nanoparticles can be probed in 3D. These experiments are at the state of the art with respect to acquisition time. However, since the alignment and reconstruction are performed offline, after the tilt series has been acquired, it is difficult or even impossible to identify potential problems concerning the acquisition parameters or the sample conditions during the TEM experiment. Consequently, efficient optimization of the experimental settings of a 3D in-situ experiment remains far from straightforward. Moreover, when studying nanoparticles by electron microscopy, it is of key importance to investigate those structures that are representative of the entire sample. On the other hand, sometimes very specific structures need to be selected for further characterization by TEM. Especially when the 3D structure of the nanoparticles is of importance, evaluating the relevance of a given particle for further investigation is difficult based on conventional, 2D TEM imaging. The ability to extract information about the 3D structure of a nanoparticle during its TEM investigation would enable the operator to immediately perform additional, optimized or more detailed experiments of the same nanoparticle if necessary. One would be able to select e.g. particles with a specific 3D morphology prior to performing more advanced or detailed TEM experiments. Finally, to fully exploit the potential of in-situ holders and novel acquisition methodologies, direct 3D visual feedback will be of essence to adjust the experimental parameters on-the-fly, in response to the observed dynamics of the nanoparticles. Clearly, realizing real-time 3D feedback would make a crucial impact in the

field of 3D (in-situ) characterization of nanoparticles, and may even become as standard for conventional TEM.

Here we report on a real-time workflow for electron tomography applied to nanoparticles, where alignment, reconstruction and analysis are all carried out while acquiring the tilt series. This chapter is structured as follows. First, we describe the concept of real-time reconstruction of arbitrary slices and how its implementation in the RECAST3D software has already enabled real-time synchrotron X-ray tomography. We also discuss which specific challenges have prevented using similar ideas for electron tomography. Next, we propose the novel ingredients that we have used to extend the RECAST3D software for electron tomography. Afterwards, two case studies will be presented to illustrate that our approach enables a quantitative, real-time 3D characterization of the structure of complex nanoparticles. We also demonstrate the ability to quantitatively investigate their dynamic behavior in real-time during in-situ experiments. Finally, the conclusions are presented.

9.2 Real-time Reconstruction of Arbitrary Slices

Recent developments concerning detector sensitivity and acquisition strategies have reduced the time to perform an entire acquisition for electron tomography from hours to several minutes or even less. As a consequence, there is an emerging need to develop reconstruction methodologies which can operate on the same time scale, i.e. in real-time. Previous research has focused on accelerating electron tomography reconstructions by improving the reconstruction algorithms or enabling them to run in parallel on large computational clusters or on multiple GPUs.(Nikitin et al., 2017; Palenstijn et al., 2011; Xu et al., 2010) It has been reported that, when using a single NVIDIA GTX TITAN Z GPU, a 2048 x 2048 x 1024 FBP reconstruction can be obtained within approximately 10 minutes.(Buurlage et al., 2018) Such a short reconstruction time can be further reduced down to 2 minutes by making use of 4 GPUs. When more advanced iterative reconstruction algorithms such as SIRT(Gilbert, 1972) are applied, capable of handling noisy and limited data, significantly longer computation times are required, even when using multiple GPUs.(Buurlage et al., 2018; Buurlage, Bisseling, et al., 2019)

The computational load further increases when using state-of-the-art reconstruction algorithms, such as DART or TVM, which exploit prior knowledge about the reconstructed object. Although GPU implementations of reconstruction methods for 3D tomography do significantly accelerate the reconstruction process, the computational power of a single GPU is not enough to enable real-time 3D tomography, especially given the recent drive towards accelerated acquisition. Moreover, it has been demonstrated that, provided with dedicated post-processing, FBP-type of reconstruction algorithms can produce more accurate reconstructions in a significantly shorter time than iterative (regularized) methods.(Pelt et al., 2018)

One way to realize real-time reconstructions is to provide a dedicated GPU cluster for each electron microscope, which is complex and costly. The recently developed reconstruction software RECAST3D provides an alternative way to overcome this limitation.(Buurlage et al., 2018) RECAST3D is available as open-source software(Buurlage et al., 2020) under the GPL license and is based on the idea that inspecting a 3D reconstructed volume is typically carried out by slicing through the reconstructed volume in various suitable directions, effectively looking at a set of 2D slices. This approach requires a single workstation equipped with a powerful GPU, thereby avoiding the need for a complex and costly GPU-cluster setup. The software exploits the intrinsic speed of the FBP algorithm to reconstruct user-selected, arbitrarily oriented, 2D slices through the 3D structure in real time, without ever performing a full 3D volume reconstruction (**Figure 9.1**).

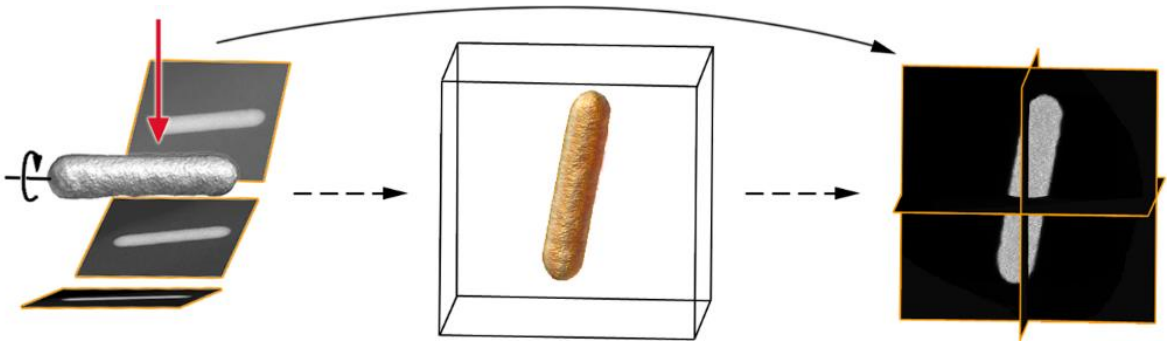

***Figure 9.1**: Illustration of the workflow of a conventional tomography experiment (dashed arrows). First, 2D projection images are acquired. The direction of the electron beam is indicated by the red arrow. Next, a complete 3D reconstruction is performed. Finally, orthogonal 2D slices through the 3D reconstruction are investigated. RECAST3D provides a new approach (solid line) in which user selected slices are reconstructed on demand.*

Although such slices are 2D images, they represent subsets of the 3D inner structure of the sample under investigation. A combination of different slices therefore yields quasi-3D information. Moreover, these slices can be computed at any arbitrary position and along any angle, enabling the TEM operator to dynamically highlight features of interest of the investigated object. Since reconstructing 2D slices is computationally far less expensive and significantly more data efficient than reconstructing the entire 3D structure, slices can be automatically updated on-the-fly during the acquisition of a tilt series. While the experiment is ongoing, the user can dynamically translate and rotate the selected slices through the reconstruction, guided by a low resolution 3D preview of the full reconstruction as demonstrated in Supplementary **Movie 3** (see QR-code below). Consequently, the quasi-3D tomographic view can be constructed in only a fraction of the time needed to acquire a regular 3D reconstruction of the entire structure, providing the groundwork for true real-time tomography.

The feasibility and usefulness of this approach has first been demonstrated for X-ray tomography at the TOMCAT beamline at the Swiss Light Source (PSI), where dynamic phenomena could be observed during imaging.(Buurlage, Marone, et al., 2019) Unfortunately, this concept cannot be translated to electron tomography in a straightforward manner because of several key differences between X-ray and electron tomography. Indeed, in X-ray tomography a large number of projection images is typically acquired over a complete angular range, resulting in an almost ideal sampling of the projection data space. Such data sets correspond exactly to the scenario where FBP provides accurate reconstructions. In contrast, in electron tomography, the risk of sample degradation or deformation during an electron tomography experiment makes it either impossible or undesirable to acquire a high amount of noise-free projection images. Therefore, the projection data are typically incomplete since the tilt increment is much larger (at least by a factor of 10) and the tilt range smaller (due to the missing wedge), as compared to X-ray tomography. In the case of imperfect projection data, either because of noise present in the projection images or when only a few projection images are available, FBP tends to result in imaging artefacts that hamper a quantitative interpretation of the reconstruction. In the field of electron tomography, FBP is therefore typically outperformed by algebraic reconstruction methods such as the SIRT(Gilbert, 1972) (**Figure 2.8**), which however are much slower than FBP and are not

suitable for reconstructing arbitrarily oriented slices.(D. Chen et al., 2014; Pontana, Duhamel, et al., 2011; Pontana, Pagniez, et al., 2011)

Another key difference between electron tomography and X-ray tomography is the need for aligning the individual TEM projection images after their acquisition. Although several standard software packages are currently available for the alignment of electron tomography tilt series, none of them are able to perform the alignment in real-time.

9.3 Real-time Reconstruction of Arbitrary Slices for Electron Tomography

We introduce herein new computational ingredients that overcome all of these limitations and enable real-time reconstruction of arbitrary slices for electron tomography. These new components have been added to the open-source RECAST3D software, thereby making them available to the entire electron microscopy community. Next, we discuss the dedicated features that were incorporated into the RECAST3D reconstruction framework, specialized for electron tomography.

9.3.1 Tilt Series Alignment

When a new projection is acquired, it is aligned in real-time with respect to previous projections by first performing a center-of-mass correction based on the segmented projection image, using Otsu's thresholding method(Otsu, 1979), followed by a conventional cross-correlation method. This image alignment protocol is well-suited for aligning images of single nanoparticles. The center-of-mass correction shifts the center-of-mass of each projection image to the middle of that image and serves to provide a good starting point for the refined cross-correlation alignment. The cross-correlation between the subsequent projection images is computed as described in **Section 3.5.3**.

9.3.2 Tilt Axis Alignment

It is well known that a misaligned tilt axis of the projection images can lead to smearing artefacts in the reconstruction (**Figure 3.7**), which are typically corrected offline.(Hayashida et al., 2018) Therefore, support was added for on-the-fly adjustment of the tilt axis alignment parameters. These adjustments are applied retroactively to the full set

of projections. In this manner, the operator can manually translate and rotate the computational tilt axis and directly observe its effect on the reconstructed slices in order to optimally match it to the experimental tilt axis (see **Section 3.5.4**). These adjustments are applied to the modeled data geometry and leave the projection data untouched.

9.3.3 Reconstruction

RECAST3D relies on the computational efficiency of the FBP algorithm, which provides reliable 3D reconstructions given that a sufficient number of high signal-to-noise projection images are available. For this discussion, let us assume we acquire *P* projection images consisting of *N x N* pixels. The FBP algorithm for reconstructing a 3D volume of size *N x N x N* comprises two steps. First, the data are filtered in Fourier space which requires $O(P \times N^2 \times \log N)$ operations. Next, the filtered data are back projected onto the 3D volume. This back projection step requires $O(P \times N^3)$ operations, and therefore dominates the computational complexity of the FBP algorithm. The voxel intensity f_{FBP} at position (x,y,z) can therefore be retrieved as:

$$f_{FBP}(x,y,z) = \int_0^{\pi} g_{filtered}(\theta, x\cos\theta + y\sin\theta, z)\, d\theta \qquad [8.1]$$

with $g_{filtered}$ being the data after a 1D filter has been applied. This implies that, after filtering the projection data, the voxel intensity at any position (x, y, z) can be computed directly from the filtered projections, independently of the rest of the 3D volume. This local property of FBP enables one to efficiently reconstruct any subset of the 3D volume directly from the filtered projection data.

In particular, back projecting onto an arbitrarily oriented 2D slice consisting of *N x N* voxels can be performed in only $O(P \times N^2)$ operations. Since *N* is typically in the range of 10^3, this is significantly more efficient than a full 3D back projection. The back projections onto slices are therefore performed in the RECAST3D implementation as follows. Instead of back projecting onto the whole 3D volume, a slab of size *N x N x 1* is defined which coincides with the central axial slice of the acquisition geometry. To reconstruct a newly requested arbitrarily oriented slice, we modify the vectors associated to the acquisition geometry (the direction of the rays, as well as the detector position and orientation) so that the requested slice is the central slice of the modified geometry. We then run a standard back projection algorithm with the modified geometry and obtain the reconstruction for the requested slice. Modifying the geometry can be done efficiently, without ever changing the

pre-filtered projection data. Using this method, any slice can be reconstructed from the filtered data with minimal overhead compared to a reconstruction of the central slice.

Moreover, the filtering step can be performed in real time while acquiring projection images, and does not impact the reconstruction time for the chosen set of 2D slices, or when a new set of slices is selected for reconstruction. Although we focus on single-axis tomography in this work, it is worth mentioning that the method discussed here can be applied for any acquisition geometry for which a method is available that has the same computational structure as FBP: a relatively inexpensive filtering step followed by a back projection step. Such an FBP-like algorithm exists as well for instance for dual-axis tomography(Mastronarde, 1997) and laminography(Myagotin et al., 2013).

Reconstruction results of a range of linear algebraic reconstruction methods can be accurately approximated by computing a so-called algebraic filter and using this computed filter within the FBP algorithm, instead of the conventional filters displayed in **Figure 2.4**.(Pelt & Batenburg, 2015) The filter calculation itself is computationally intensive, but once determined, the resulting filter can be used with the same computational efficiency as FBP. To overcome the limitations of the classical FBP algorithm for electron tomography, support for algebraic filter methods was added to RECAST3D. By computing algebraic filters based on the SIRT algorithm and using these filters in FBP, arbitrary slices can now be reconstructed that are in close agreement with the output of SIRT. Other than the precomputation of the filters, which can be performed prior to the experiment, the reconstruction time is identical to standard FBP when this method is used. For the remainder of this work we will refer to this type of reconstruction as SIRT–FBP. Adding these new computational components to the RECAST3D software, enables real-time electron tomography which will drastically optimize the efficiency of 3D characterization of nanomaterials, but more importantly will enable a new range of experiments such as real-time (in-situ) electron tomography. As a proof of concept, we describe in what follows two different examples of electron tomography experiments wherein the benefits of this novel technique will be highlighted.

9.4 Results and Discussion

To achieve real-time visualization during electron tomography experiments, a workstation was coupled to the electron microscope, to function as a reconstruction server. This server received the tomographic projection images while being acquired at the electron microscope, via a 1Gbps network connection and comprised an Intel Core i9-9900K CPU, 32 GB RAM, and a NVIDIA GeForce GTX 1070 GPU with 8 GB global memory. All results presented in this work were calculated on this workstation. The reconstruction workflow consists of two asynchronous operations: a preprocessing operation, and a reconstruction operation, both performed multiple times during the experiment. The first operation refers to the pre-processing of the projection images. This operation is performed immediately after a projection image is acquired, and is done completely independently from the reconstruction operation. The computationally most demanding part of this operation is to apply the algebraic filter, and to align the projection images. Using our implementation, the total time to perform this pre-processing operation is orders of magnitude shorter than the time required for the operator to acquire a projection image. Therefore, this operation is not a bottleneck for our real-time methodology. The second, reconstruction, operation is performed each time a new slice is chosen for visualization. Using the workstation described above, and for a dataset consisting of 51 projection images of 1024 x 1024 pixels, the total time elapsed from the moment a user selects a new slice, until the reconstruction shows in RECAST3D is approximately 60 milliseconds.

9.4.1 Explorative Quasi-3D Imaging

As a first case study we investigate Au@Ag NRs. Although Au NRs have been widely studied as excellent anisotropic plasmonic nanomaterials, Ag is known to be a more efficient plasmonic metal. However, the lower chemical stability of Ag compared to Au, leads to more complicated and less controlled nanoparticle synthesis methods. Therefore, efforts have been focused toward using pre-formed Au nanoparticles, such as penta-twinned bipyramids, as templates for the seeded growth of Ag NRs. However, the specific 3D shape, chemical composition and distribution of the different elements strongly affect the properties of the resulting core-shell nanoparticles.(Albrecht et al., 2017; Guisbiers et al., 2016; Joo et al., 2009; M. Shao et al., 2016) In particular, the plasmon resonances of core-shell nanoparticles depend sensitively on both edge and corner truncations present in the 3D structure, as well as on the core-shell geometry. Moreover, potential alloying between the

constituent metals would also strongly influence the plasmonic response.(Cortie & McDonagh, 2011; Jing et al., 2014) 3D investigations of the structure and composition are therefore of critical importance to understand the properties of these nanoparticles.

To investigate the 3D distribution of Au and Ag in the core-shell nanoparticle, conventional HAADF-STEM tomography is applied. The first step in such an electron tomography experiment is the selection of a representative nanoparticle with a suitable position and orientation on the grid. Typically, one can only decide if the investigated nanoparticle and its location are indeed suitable, once the 3D reconstruction has been completed offline. This, obviously, strongly reduces the efficiency of the experiment and leads to suboptimal use of microscopy time. Furthermore, the lack of real-time 3D feedback prevents the dynamic tuning of acquisition parameters during data collection, e.g. to obtain a sufficient signal-to-noise ratio and/or resolution in the final reconstruction. Providing a fast quasi-3D image of the structure under investigation overcomes these limitations and enables a much more effective use of the TEM.

A HAADF-STEM projection image of one Au@Ag nanoparticle is presented in **Figure 9.2a**. A tilt series was acquired over an angular range of ± 72° with a 9° interval, using a Thermo Fisher Scientific Osiris electron microscope operated at 200 kV. Regions with different intensities can be clearly observed and an apparent rod-like shape of the nanoparticle is readily recognized. While the acquisition of the tilt series is ongoing, the projection images are instantly aligned and pre-filtered. Simultaneously, arbitrarily oriented slices are reconstructed using the SIRT–FBP algorithm for which the filter was pre-computed to resemble 100 iterations of SIRT. **Figure 9.2b** highlights the selected slices within the RECAST3D software. Shown in **Figure 9.2c** is an enlarged quasi-3D visualization of the investigated structure, obtained after only acquiring 17 projection images only. The background of the arbitrary oriented slices was set to transparent to enhance the 3D interpretation. The process described above, along with the selection of the slices is demonstrated in **Supplementary Movie 3** (see QR-code below).

Based on the real-time quasi-3D reconstruction one can immediately decide whether the selected particle is representative, e.g. in this case whether the shape corresponds to a rod with pentagonal symmetry, and whether the missing wedge effect is within reasonable limits. Whereas it is impossible to determine the precise structure of the rod from a single projection image (**Figure 9.2a**), sharp facets, indicated by the green arrows, can be identified in the quasi-3D reconstruction. Furthermore, one can alter the acquisition parameters such as tilt interval, magnification, image size, beam current, to name a few, and immediately observe their influence on the reconstruction quality. For example, in **Figure 9.2d** an identical quasi-3D view is shown after decreasing the tilt interval from 9° to 3°. Clearly this improves the contrast of the reconstruction, enabling a better qualitative interpretation of both the morphology and composition of the bimetallic nanoparticle. In this manner, one can determine from a limited number of projection images whether the particle under investigation is of interest, and if so decide how to optimize the acquisition parameters.

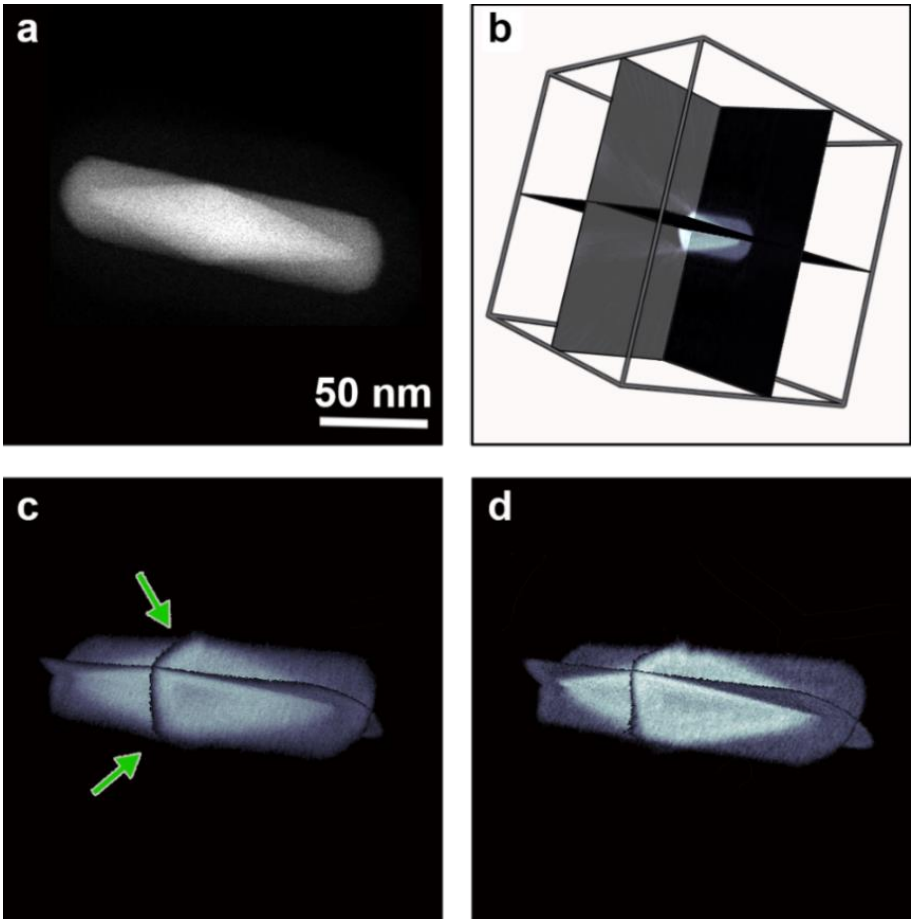

***Figure 9.2**: (a) 2D HAADF-STEM image of a Au@Ag NR. (b) Illustration of the selected slices. (c-d) Quasi-3D depiction of the SIRT–FBP reconstruction, based on a tomographic series with tilt intervals of 9° and 3°.*

In addition to qualitative information, real-time quantitative information can be obtained as well. The RECAST3D software has support for user-written Python plugins, which can be used to perform real-time analysis of specific features in the reconstructed 2D slices. For our example, we designed a plugin to evaluate the histogram and a line profile from a selected slice. **Figure 9.3a** illustrates the selected slice obtained from the SIRT–FBP reconstruction. The histogram of the selected slice and a line profile through the slice are respectively shown in **Figures 9.3b-c**. The histogram bins (**Figure 9.3b)** corresponding to the background, Ag and Au signals, are respectively displayed in gray, red and blue. The line across which the line profile is calculated, is indicated in red in **Figure 9.3a.**

It is possible to gain quantitative insight on the mixture of the Au and Ag phase by assessing the histogram and a line profile. Indeed, the histogram of the reconstructed intensities in **Figure 9.3b** shows a clear segregation between the Au and Ag phase. This is confirmed by the sharp edges, indicated by black arrows, in the recorded line profile (**Figure 9.3c**). In addition, such line profiles reveal the shell thickness. Given that the distribution of the constituent metals and the size ratio between the core and shell strongly influence the plasmon response of the nanoparticles, the acquired knowledge is of great importance. Hence, on-the-fly access to arbitrary reconstructed slices opens the way to performing online quantitative data analysis. Moreover, in this case study, it would also enable the operator to select e.g. particles with a specific shell thickness for further TEM investigation of the plasmonic properties.

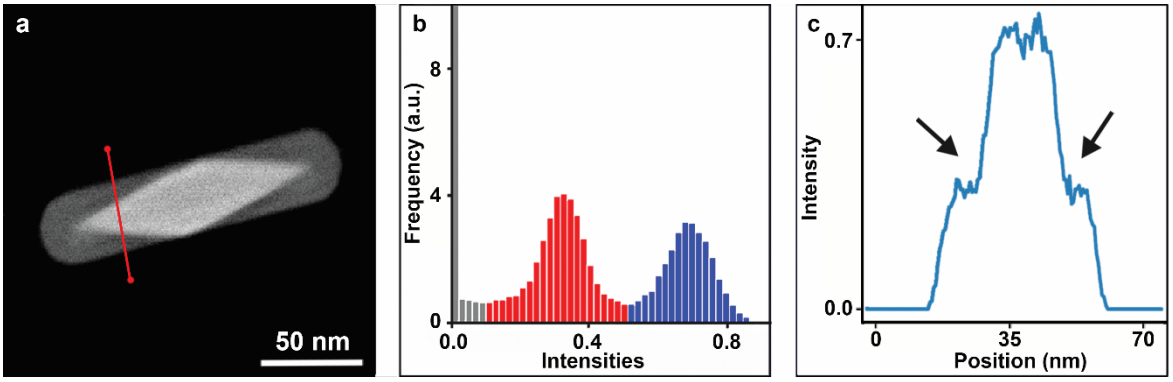

***Figure 9.3**: (a) a central slice, reconstructed by SIRT–FBP for which the filter was pre-computed to resemble 100 iterations of SIRT. The line profile is calculated along the line shown in red. (b) Histogram of the central slice indicating the intensities corresponding to the background (gray), Ag (red) and Au (blue). (c) Line profile through the slice. The sharp transition between Au and Ag is indicated by the black arrows.*

9.4.2 Real-Time In-Situ Tomography

In addition to the advantages discussed above, the ability to visualize and analyze arbitrary slices in real time is ideal toward performing in-situ 3D characterization by TEM. As an example of such an experiment, we present a 3D study of anisotropic Au NSs. Because of their anisotropic shape and strong field enhancements at their tips, these NSs are ideal substrates for plasmonics and SERS.(Guerrero-Martínez et al., 2011; Hao et al., 2007; Kong et al., 2017; Yuan et al., 2012) A representative 2D HAADF-STEM image of a Ns is shown in **Figure 9.4a**. As presented in **Chapter 7**, a well-known problem of such anisotropic nanostructures is their tendency to reshape at moderately high temperature, including photothermal effects related to intense laser irradiation.(Baffou et al., 2009; Baffou & Quidant, 2013; Baffou & Rigneault, 2011; Cao et al., 2007) It is thus important to understand the deformation under these conditions, and to ultimately optimize their stability, which requires an accurate investigation of changes of the 3D structure during heating.

In **Chapter 7** the morphological evolution of Au NSs at elevated temperature was investigated by combining continuous electron tomography with in-situ heating.[25] Although these experiments provided important information toward understanding the reshaping process, they were carried out in a rather inefficient manner. The main reason for this is that 2D HAADF-STEM projection images of such anisotropic nanoparticles are not sufficient to determine whether a specific nanostructure has the desired 3D morphology (e.g. a given number of branches), prior to starting the 3D in-situ experiment. More importantly, if the 3D reconstruction is performed offline, it is nearly impossible to monitor how the structure changes as a function of the external conditions (e.g. temperature, heating time etc.) while the experiment is ongoing, especially for highly anisotropic nanoparticles. Since the RECAST3D methodology yields real-time and quasi-3D information on the investigated structure, these limitations can be overcome.

The experiments were performed using a DENSsolutions wildfire heating holder and a Thermo Fisher Scientific Osiris electron microscope operated at 200 kV. A conventional tomography series was acquired at room temperature, over a tilt range of ± 75° with a 3° increment. **Figure 9.4b** shows the orientation of the chosen slices. Each slice was reconstructed using the SIRT–FBP algorithm, for which the filter was pre-computed to resemble 100 iterations of SIRT. As mentioned above, the position and orientation of the slices can be adapted on-the-fly to investigate features of the nanoparticle that are of

particular interest. By exploring the 3D structure of the nanoparticle in this manner, 8 sharp branches were identified, 7 of which can be seen in the single quasi-3D view presented in **Figure 9.4c**. The selection of the slices and the identification of the different branches is demonstrated in the **Supplementary Movie 4** (see QR-code below). Since it is expected that the most apparent morphological changes will occur at sharp branches,(Inasawa et al., 2005; Link et al., 2000; Taylor et al., 2014) we propose that this particular NS is an ideal candidate for the in-situ experiment. This is not always obvious from a single HAADF-STEM projection, since it is only a 2D projection of the true 3D structure, which can be very misleading.

To initiate the morphological transition, the NS was heated at 300 °C in different steps for the duration of 2, 6, and 18 minutes. The first heating step was chosen to last for 2 minutes only, as we previously demonstrated that most heat-induced deformation occurs within the first few minutes. We decided on the duration of subsequent heating steps by using the immediate feedback provided by RECAST3D. After each heating step, the nanoparticle was quenched to room temperature to temporarily interrupt the morphological evolution and to acquire a HAADF-STEM tomographic series using the settings described above. Visual inspection of the quasi-3D image in **Figure 9.4d** tells us that after only 2 minutes of heating, the NS has already deformed. We observe that several of the branches underwent a transformation, in agreement with the observations made in **Chapter 7**, from a long sharp morphology to a broad and shorter shape with a more rounded tip. The lower right branch at the back of the NS, indicated by a red arrow, almost completely disappears after 2 minutes of heating. Direct contact of this tip with the support during the experiment might explain this behavior, as was observed as well in earlier studies.(Albrecht et al., 2019) However, the fast feedback provided by the set of slices indicates that the change of all other branches remains relatively limited. Therefore, we decided to increase the duration of the heat treatment to 6 minutes during the next heating step. From **Figure 9.4e,** it can be seen that subsequent heating results in further shrinkage of the branches, during which the volume redistributes along their surface. We do observe that the deformation slows down, which can be attributed to the interaction between the electron beam and the ligands surrounding the NS, forming a protective carbon shell.(Albrecht et al., 2018) Based on these immediate results, we decided to heat the nanoparticle once more for 18 minutes. From **Figure 9.4f,** it is clear that reshaping has stagnated

and that except for the shrinkage of the foremost branch (indicated by the green arrow), only minor additional changes can be appreciated.

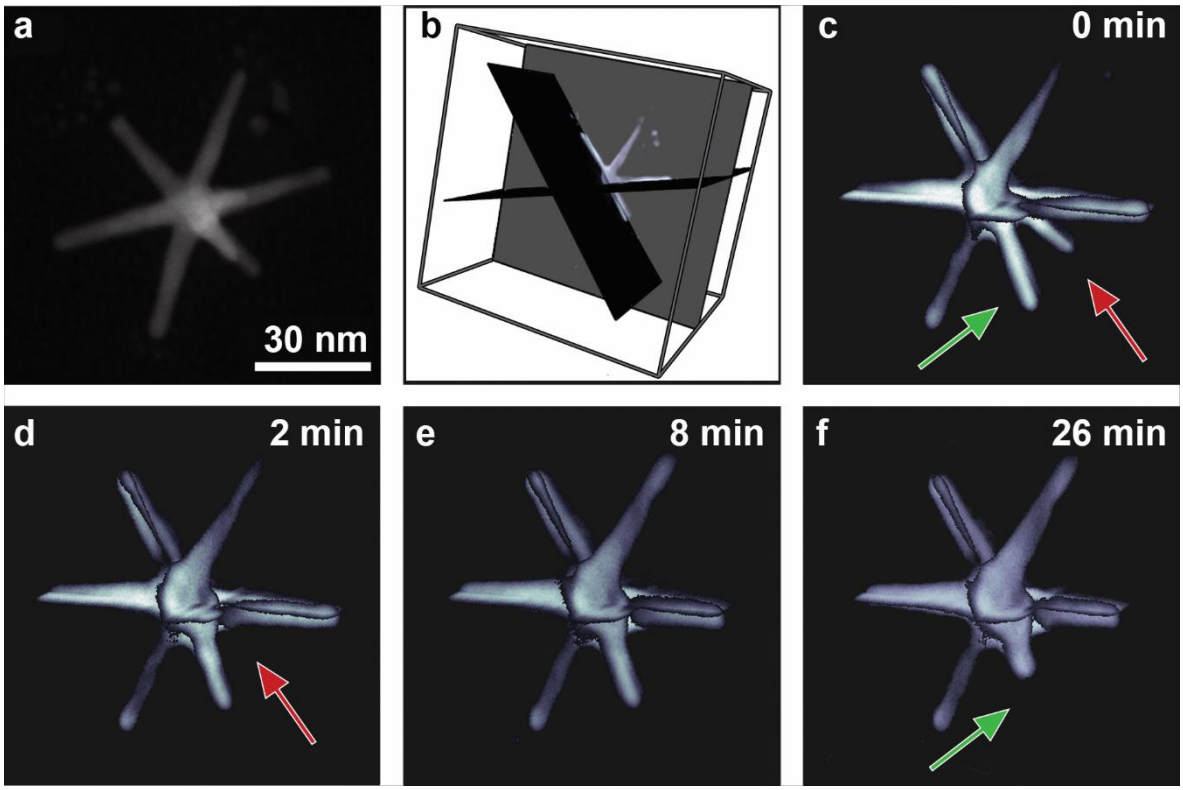

***Figure 9.4**: (a) 2D HAADF-STEM image of a Au NS. (b) 3D depiction of the selected slices reconstructed by SIRT–FBP, for which the filter was pre-computed to resemble 100 iterations of SIRT. (c-f) Quasi-3D view of the SIRT–FBP reconstruction of the NS after respectively 0, 2, 8, and 26 minutes of accumulated heating at 300 °C.*

RECAST3D can also be used to extract quantitative information in real time. For the branches of NS, we anticipate that the curvature would decrease as a function of heating time. By monitoring curvature changes, we can quantify how much the NS reshapes over time and consequently evaluate the pace of the morphological evolution and whether it has been completed or not. Therefore, a Python plug-in was developed to monitor the curvature of the NS. Our approach is as follows: a user-selected slice, e.g. **Figure 9.5a**, is first segmented based on Otsu's thresholding method(Otsu, 1979), as illustrated in **Figure 9.5b**. From the segmented slice, the perimeter of the largest binary component is determined using a marching squares algorithm.(Lorensen & Cline, 1987) Next, the perimeter is downsampled by a user-selected factor, resulting in a small collection of points along the edge of the NS (**Figure 9.5c**). In this manner, the curvature can be calculated along longer sections of the

segmented circumference of the slice, making the procedure less prone to noise. A circle is fitted to every 3 consecutive points along the downsampled perimeter. The inverse of the radius of the fitted circle provides a measure for the curvature. Finally, the measured curvature is assigned a positive or a negative sign, depending on whether the center of the fitted circle lies respectively inside or outside the perimeter. The calculated curvature, interpolated along the perimeter of the NS and superimposed on the segmented slice reconstruction, is plotted in **Figure 9.5d**. The combination of the RECAST3D software with the calculation of curvature enables us to interpret the obtained TEM results, in a fast and quantitative manner. **Figure 9.6** shows curvature maps for every heating step, calculated for comparable slices through the reconstructed NS. The total duration of heating is indicated at the top right corner. As expected, the sharpest parts of the branches vanish first during heating.

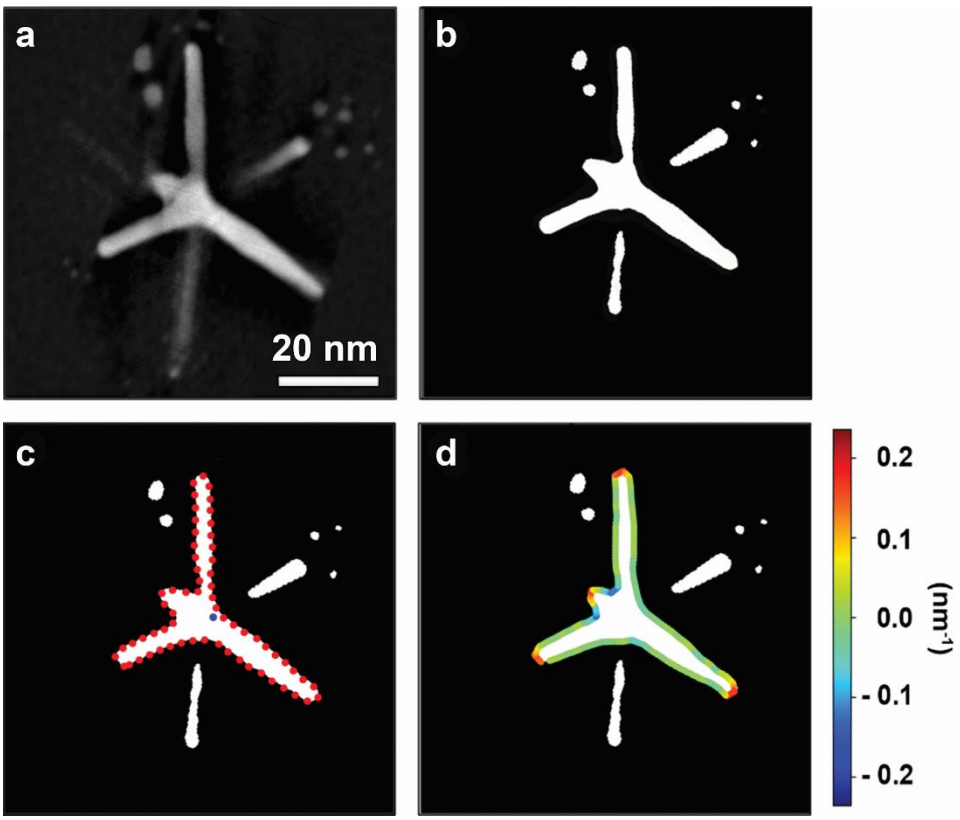

Figure 9.5*: (a) Slice reconstructed using the SIRT–FBP reconstruction, for which the filter was pre-computed to resemble 100 iterations of SIRT. (b) Thresholded reconstruction. (c) From the binary reconstructed slices, both the centroid (blue dot) and the perimeter (red dots) are determined. The perimeter was downsampled by a factor 20. (d) Calculated curvature, interpolated along the edge of the binary object.*

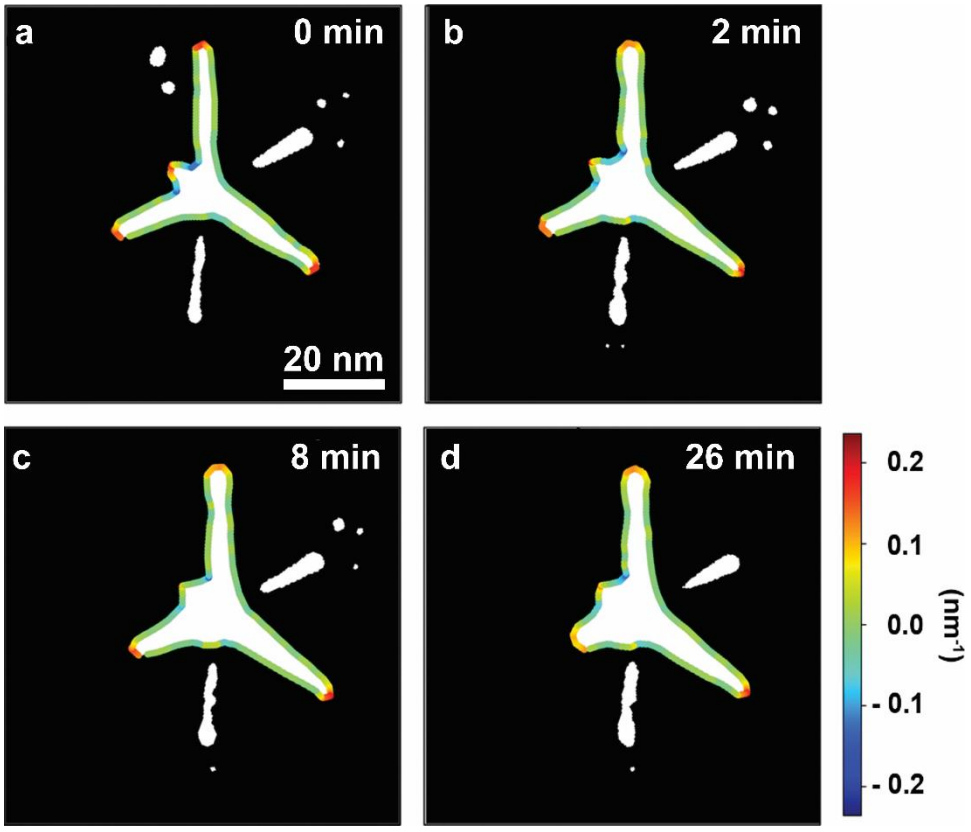

Figure 9.6*: (a-d) Calculated curvature superimposed on the segmented slice reconstruction after each heating step.*

In **Figure 9.7a,** histograms of the calculated positive curvature values are presented. The analysis was performed on a specifically chosen slice, away from contact with the heating chip. From the histograms, which can be extracted in real time during the in-situ experiment, it is possible to discern a shift from the high curvature values to lower values over the course of heating. **Figure 9.7b** displays the maximal curvature as a function of the accumulated duration of heating. It is apparent that the morphological evolution can be directly monitored from the change in maximal curvature. Most of the transition occurs at the first heating steps, during which the long thin branches lose their sharp tips and become blunt. After the first 8 minutes of heating, the decline in maximal curvature slows down, indicating that the amount of morphological evolution decreases. After 26 minutes of heating, the volume redistribution has almost stopped. Such an active feedback is crucial to adaptively control the parameters of an in-situ investigation. This example shows that quasi-3D reconstructions can be used to provide real-time qualitative and quantitative information. In this manner, all experimental parameters can be efficiently tuned while the experiment is

ongoing. Consequently, the operator is able to investigate a higher number of nanoparticles during a given microscopy session, leading to more statistically significant information.

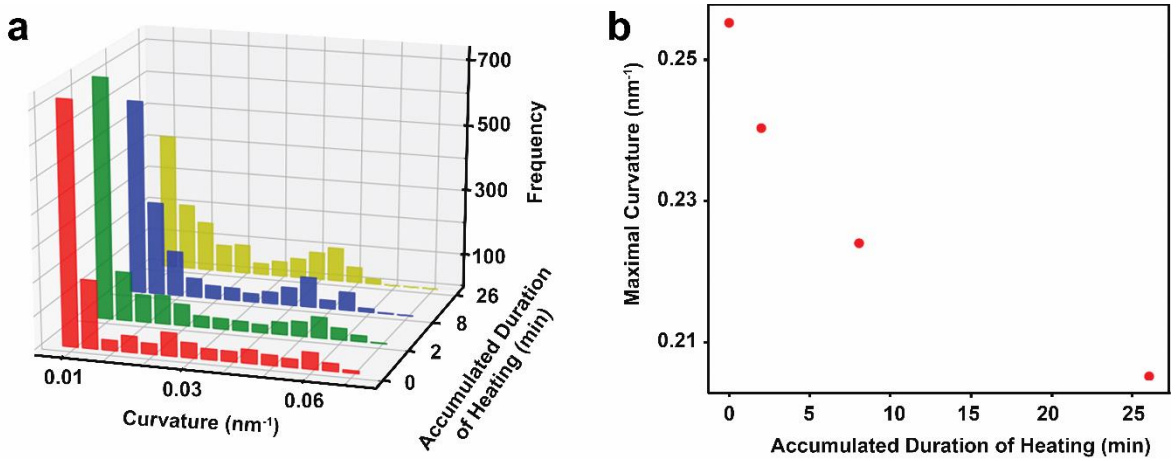

***Figure 9.7**: (a) Histograms of the obtained curvature values from RECAST3D. (b) The maximal curvature of one slice plotted as a function of the duration of heat treatment.*

9.5 Conclusion

We propose a new approach to compute high quality 2D slices through nanoparticles in real time, based on electron tomography tilt series. This technique is of great importance to improve the efficiency of 3D characterization of nanomaterials by TEM. It enables explorative imaging and provides valuable information to dynamically adjust the acquisition parameters during an electron tomography experiment. Moreover, quantification of specific features of nanoparticles becomes possible in real time, even while performing in-situ experiments. We therefore consider the ability to gain real-time quasi-3D visualizations as the next (r)evolution in the field of 3D characterization of nanomaterials.

General Conclusions

As stated at the end of **Chapter 4** the main objectives of my thesis were:

- To develop acquisition strategies that enable the recording of tomographic series in a few minutes. The reduction of the acquisition time will be accompanied by a decrease in electron dose, allowing new 3D experiments to be conducted.

- To propose new computational methods capable of processing the tilt series acquired using fast acquisition schemes. Such developments are necessary since the fast tilt series will typically yield a lower signal-to-noise ratio and/or a limited amount of information.

- To improve the efficiency of the alignment and reconstruction, such that real-time 3D information will become accessible during the tomography experiment. Such information will aid steering in-situ experiments in the electron microscope, where one is interested in the fast dynamical behavior of nanoparticles under external stimuli.

In order to obtain my first goal, I followed different strategies. In **Chapter 5,** I evaluated three different undersampling methods which:

- Reduce the scanning time per pixel yielding a lower signal-to-noise ratio in the projection images (I-US).
- Reduce the number of projection images in the tilt series (T-US).
- Reduce the number of scanned pixels in each projection image (R-US).

Each of these methods shows potential to reduce the acquisition duration, the electron dose or the dose rate. It was revealed that for obtaining an optimum reconstruction quality it is preferential to spread the electron budget over as many pixels as possible. Although the electron dose is similarly reduced for all undersampling techniques, R-US decreases the electron dose rate more strongly. We therefore envisage that this kind of acquisition scheme will lead to major breakthroughs in the investigation of samples that were so far too sensitive to the electron beam to be investigated in 3D, such as zeolites or metalorganic frameworks.

Based on the performance of the I-US acquisition, I proposed a continuous acquisition methodology for HAADF-STEM tomography in **Chapter 6**, which effectively lowers the duration of the acquisition by a factor of 10. Since the number of projection images that is acquired in a continuous tilt series is much higher and each projection image has a limited signal-to-noise ratio, the continuous tilt series pose a computational challenge. Dedicated pre-processing was developed to align and de-noise the continuous tilt series. It was demonstrated that such dedicated pre-possessing leads to sufficiently accurate reconstructions to obtain reliable quantitative results. I therefore foresee that continuous tomography will be instrumental in future experiments for obtaining statistical relevant 3D results concerning parameters such as particle size and surface morphology. Furthermore, the reduced dose rate of continuous tomography may enable the investigation of beam sensitive samples as well.

As explained in the introduction, fast tomography will enable a broad range of novel experiments, including the combination of electron tomography and in-situ experiments. An application of the approach I developed was presented in **Chapter 7.** Here the reduced experimental time of continuous tomography was exploited to investigate the thermal stability of Au nanostars with a high temporal resolution. The ability to directly monitor the heat induced changes at the nanometer scale, in combination with BEM simulations, improved the understanding of the thermal reshaping behaviour of the nanostars. Such studies are of crucial importance to incorporate such nanostructures in functional nanodevices or to use them in real-life applications.

In **Chapter 8**, I proposed several methods to further enhance the accuracy of fast tomography. Convolutional Neural Networks were applied to refine the pre-processing of continuous tomography series. Shape error improvements of up to approximately 50% were reported on. Provided that sufficient training data are available, CNNs can augment the continuous tomography capabilities. Although the training of such networks may be time intensive, once trained they can process the continuous projection images almost instantaneously. In addition, a hybrid acquisition strategy, referred to as the incremental tomography, was presented. By continuously acquiring projection images while the stage tilted in increments, the shape error could be strongly reduced as well. A drawback of this hybrid tilting scheme, is the increased complexity of tracking and focusing the projection images while being acquired, therefore increasing the risk of losing the particle during the acquisition.

As a general guideline, continuous tomography is to be used when uninterrupted feedback is required for tracking the nanoparticle during the acquisition. If sufficient training data are available or can be collected, the accuracy of the continuous approach can be drastically improved by using neural network based pre-processing. However, when there is little sample drift during the tilt and/or insufficient training data can be collected (e.g. in case of radiation sensitive samples), incremental tomography is preferential.

In **Chapter 9**, I presented a new workflow for electron tomography experiments which provides quasi real-time 3D information. In this manner, the efficiency of 3D studies was improved and I was able to flexibly steer in-situ investigations. I envisage that RECAST3D will become a new standardised tool to provide direct 3D feedback during electron tomography experiments. With the incorporation of RECAST3D during TEM experiments, the throughput of the TEM experiment remains limited by the speed of acquisition. Until now, RECAST3D was combined with conventional electron tomography. In this manner, the impressive computational power of the RECAST3D methodology was not yet fully exploited.

Outlook

In the next stage of my research I aim to explore the combination of fast tomography acquisition approaches with RECAST3D. Ultimately, this will lead to a total experimental time of only a few minutes, which is far lower than those for conventional tomography experiments (2 hours at minimum). The use of RECAST3D during fast tomography will require more efficient pre-processing methods as those introduced in **Chapter 6**, where iterative methodologies were applied to improve the quality of the tilt series. I foresee to overcome this challenge by exploiting the similarity of projection images acquired at closely related angles or through the application of dedicated machine learning strategies to efficiently remove or optimize deteriorated projection images.

In addition, by designing automated focus and repositioning protocols, manual tuning will no longer be required. Such protocols may benefit from the incorporation of laser interferometry to obtain the position and orientation of the holder at any time. In this manner, the location of the nanoparticle of interest would be known throughout the experiment, without the necessity of using additional electrons to attain such information. Altogether this will increase the achievable speed of the accelerated acquisition in a dose efficient manner.

The combination of fast acquisition methodologies with RECAST3D will only further improve the efficiency and throughput of electron tomography. This might even prompt the application of dynamical tomography(Bonnet et al., 2003; Münch, 2011; Van Eyndhoven et al., 2015) for in-situ (S)TEM experiments wherein the morphological evolution no longer needs to be quenched, but projection images can be acquired while the nanostructure is changing instead. This will be crucial to enhance the physical relevance of such state-of-the-art experiments.

Furthermore, I envisage to expand the fast (in-situ) acquisition methodology to different imaging modalities. This will broaden both the type of nanoscale information which can be obtained in a fast and efficient manner, as well as expand the types of nanomaterials which can be investigated with increased statistical relevance. Fast (in-situ) multimode tomography, for instance, can help understanding the influence of structural defects on the thermal stability of nanoparticles or aid in comprehending the role of structural defects on

the growing mechanisms of nanoparticles. In **Part II** different STEM strategies were presented, capable of reducing the electron dose and/or dose rate. However, these methods might not suffice for extremely beam sensitive materials such as polymeric or composite materials. Since soft matter becomes increasingly important in current and future nanotechnology, novel TEM approaches should be considered as well. Recently, first attempts were made to accelerate the acquisition process in TEM mode using a direct electron detection camera to record a tomographic tilt series in only 3.5s but with a missing wedge of 80°.(Migunov et al., 2015) By lowering the speed of the rotation and implementing automatic procedures to keep the particle in field of view and focus, it will be possible to reduce the size of the missing wedge. In this manner, the accuracy of fast TEM will drastically improve, allowing accurate 3D quantification of soft matter.

Further advances in (S)TEM hardware (e.g. detector sensitivity) and the development of improved processing methodologies (e.g. by using dedicated CNNs), will continue to improve the accuracy of fast tomography. In combination with the aforementioned automated focus and repositioning protocols, for example through the use of laser interferometry, this could open the way to perform fast tomographic acquisitions at higher magnifications. In this manner, the high-resolution capabilities of the electron microscope could be fully exploited. Ultimately this may enable one to retrieve 3D quantitative information at the atomic scale in a statistical relevant manner.

Scientific Contributions

Journal Articles:

- Geboes, B., Ustarroz, J., Sentosun, K., Vanrompay, H., Hubin, A., Bals, S., & Breugelmans, T. (2016). Electrochemical Behavior of Electrodeposited Nanoporous Pt Catalysts for the Oxygen Reduction Reaction. *ACS Catalysis*, *6*(9), 5856–5864. https://doi.org/10.1021/acscatal.6b00668

- Mernissi Cherigui, E. A., Sentosun, K., Bouckenooge, P., Vanrompay, H., Bals, S., Terryn, H., & Ustarroz, J. (2017). Comprehensive Study of the Electrodeposition of Nickel Nanostructures from Deep Eutectic Solvents: Self-Limiting Growth by Electrolysis of Residual Water. *Journal of Physical Chemistry C*, *121*(17), 9337–9347. https://doi.org/10.1021/acs.jpcc.7b01104

- Ustarroz, J., Geboes, B., Vanrompay, H., Sentosun, K., Bals, S., Breugelmans, T., & Hubin, A. (2017b). Electrodeposition of Highly Porous Pt Nanoparticles Studied by Quantitative 3D Electron Tomography: Influence of Growth Mechanisms and Potential Cycling on the Active Surface Area. *ACS Applied Materials and Interfaces*, *9*(19), 16168–16177. https://doi.org/10.1021/acsami.7b01619

- Loreto, S., Vanrompay, H., Mertens, M., Bals, S., & Meynen, V. (2018). The Influence of Acids on Tuning the Pore Size of Mesoporous TiO2 Templated by Non-Ionic Block Copolymers. *European Journal of Inorganic Chemistry*, *2018*(1), 62–65. https://doi.org/10.1002/ejic.201701266

- Van Der Burgt, J. S., Geuchies, J. J., Van Der Meer, B., Vanrompay, H., Zanaga, D., Zhang, Y., Albrecht, W., Petukhov, A. V., Filion, L., Bals, S., Swart, I., & Vanmaekelbergh, D. (2018). Cuboidal Supraparticles Self-Assembled from Cubic CsPbBr3 Perovskite Nanocrystals. *Journal of Physical Chemistry C*, *122*(27), 15706–15712. https://doi.org/10.1021/acs.jpcc.8b02699

- Vanrompay, H., Bladt, E., Albrecht, W., Béché, A., Zakhozheva, M., Sánchez-Iglesias, A., Liz-Marzán, L. M., & Bals, S. (2018). 3D characterization of heat-induced morphological changes of Au nanostars by fast: In situ electron tomography. *Nanoscale*, *10*(48), 22792–22801. https://doi.org/10.1039/c8nr08376b

- Queraltó, A., Graf, D., Frohnhoven, R., Fischer, T., Vanrompay, H., Bals, S., Bartasyte, A., & Mathur, S. (2019). LaFeO3 Nanofibers for High Detection of Sulfur-Containing Gases. *ACS Sustainable Chemistry and Engineering*, *7*(6), 6023–6032. https://doi.org/10.1021/acssuschemeng.8b06132

- Blommaerts, N., Vanrompay, H., Nuti, S., Lenaerts, S., Bals, S., & Verbruggen, S. W. (2019). Unraveling Structural Information of Turkevich Synthesized Plasmonic Gold–Silver Bimetallic Nanoparticles. *Small*, *15*(42), 1902791. https://doi.org/10.1002/smll.201902791

- Vanrompay, H., Béché, A., Verbeeck, J., & Bals, S. (2019). Experimental Evaluation of Undersampling Schemes for Electron Tomography of Nanoparticles. *Particle and Particle Systems Characterization*, *36*(7), 1900096. https://doi.org/10.1002/ppsc.201900096

- Albrecht, W., Bladt, E., Vanrompay, H., Smith, J. D., Skrabalak, S. E., & Bals, S. (2019). Thermal Stability of Gold/Palladium Octopods Studied in Situ in 3D: Understanding Design Rules for Thermally Stable Metal Nanoparticles. *ACS Nano*, *13*(6), 6522–6530. https://doi.org/10.1021/acsnano.9b00108

- Vanrompay, H., Buurlage, J. W., Pelt, D. M., Kumar, V., Xiaolu Z., Liz-Marzán L.M., Bals, S., & Batenburg, K. J. (2020). Real-time reconstruction of arbitrary slices for quantitative and in-situ three-dimensional characterization of nanoparticles. *Particle and Particle Systems Characterization*. https://doi.org/10.1002/ppsc.202000073

- Vanrompay, H., Skorikov, A., Bladt, E., Béché, A., Freitag B., Verbeeck, J., & Bals, S. (2020). Fast versus conventional HAADF-STEM tomography: advantages and challenges. *In preparation*

Poster Presentations:

- Quantitative Structural Characterization of Porous Nanomaterials by Advanced Electron Tomography, Golden Jubilee Meeting of the Royal Belgian Society for Microscopy (RBSM2016), Brussel – Belgium, 8-9 September 2016.

- Quantitative Structural Characterization of Porous Nanomaterials by Advanced Electron Tomography, European Microscopy Congress (EMC2016), Lausanne – Switzerland, 21-25 Augustus 2017.

- 3D investigation of heat-induced morphological changes of Au nanostars using a fast HAADF-STEM tomography, International Conference on In Situ and Correlative Electron Microscopy (CISCEM2018), Saarbrücken – Germany, 10-12 October 2018.

- Experimental Evaluation of Undersampling Schemes for Electron Tomography of Nanoparticles, FWO - Image Reconstruction Workshop 2019, Ghent – Belgium, 20 September 2019.

References

Abadi, M., Barham, P., Chen, J., Chen, Z., Davis, A., Dean, J., Devin, M., Ghemawat, S., Irving, G., Isard, M., Kudlur, M., Levenberg, J., Monga, R., Moore, S., Murray, D. G., Steiner, B., Tucker, P., Vasudevan, V., Warden, P., … Zheng, X. (2016). TensorFlow: A system for large-scale machine learning. *Proceedings of the 12th USENIX Symposium on Operating Systems Design and Implementation, OSDI 2016*, 265–283.

Albrecht, W., Bladt, E., Vanrompay, H., Smith, J. D., Skrabalak, S. E., & Bals, S. (2019). Thermal Stability of Gold/Palladium Octopods Studied in Situ in 3D: Understanding Design Rules for Thermally Stable Metal Nanoparticles. *ACS Nano*, *13*(6), 6522–6530. https://doi.org/10.1021/acsnano.9b00108

Albrecht, W., van de Glind, A., Yoshida, H., Isozaki, Y., Imhof, A., van Blaaderen, A., de Jongh, P. E., de Jong, K. P., Zečević, J., & Takeda, S. (2018). Impact of the electron beam on the thermal stability of gold nanorods studied by environmental transmission electron microscopy. *Ultramicroscopy*, *193*, 97–103. https://doi.org/10.1016/j.ultramic.2018.05.006

Albrecht, W., Van Der Hoeven, J. E. S., Deng, T. S., De Jongh, P. E., & Van Blaaderen, A. (2017). Fully alloyed metal nanorods with highly tunable properties. *Nanoscale*, *9*(8), 2845–2851. https://doi.org/10.1039/c6nr08484b

Arslan, I., Tong, J. R., & Midgley, P. A. (2006). Reducing the missing wedge: High-resolution dual axis tomography of inorganic materials. *Ultramicroscopy*, *106*(11–12), 994–1000. https://doi.org/10.1016/j.ultramic.2006.05.010

Baek, J., & Pelc, N. J. (2011). Effect of detector lag on CT noise power spectra. *Medical Physics*, *38*(6), 2995–3005. https://doi.org/10.1118/1.3589135

Baffou, G., & Quidant, R. (2013). Thermo-plasmonics: Using metallic nanostructures as nano-sources of heat. *Laser and Photonics Reviews*, *7*(2), 171–187. https://doi.org/10.1002/lpor.201200003

Baffou, G., Quidant, R., & Girard, C. (2009). Heat generation in plasmonic nanostructures: Influence of morphology. *Applied Physics Letters*, *94*(15), 153109. https://doi.org/10.1063/1.3116645

Baffou, G., & Rigneault, H. (2011). Femtosecond-pulsed optical heating of gold nanoparticles. *Physical Review B - Condensed Matter and Materials Physics*, *84*(3), 035415. https://doi.org/10.1103/PhysRevB.84.035415

Bai, S., Shi, B., Ma, L., Yang, P., Liu, Z., Li, D., & Chen, A. (2009). Synthesis of LaFeO3 catalytic materials and their sensing properties. *Science in China, Series B: Chemistry*, *52*(12), 2106–2113. https://doi.org/10.1007/s11426-009-0289-3

Bals, S., Goris, B., De Backer, A., Van Aert, S., & Van Tendeloo, G. (2016). Atomic resolution electron tomography. *MRS Bulletin*, *41*(7), 525–530. https://doi.org/10.1557/mrs.2016.138

Bals, S., Goris, B., Liz-Marzán, L. M., & Van Tendeloo, G. (2014). Three-dimensional characterization of noble-metal nanoparticles and their assemblies by electron tomography. *Angewandte Chemie - International Edition*, *53*(40), 10600–10610. https://doi.org/10.1002/anie.201401059

Bals, S., Goris, B., & Van Tendeloo, G. (2012). Adding New Dimension to Electron Tomography: Measuring Atomic Structures and Properties in 3D. *Microscopy and Microanalysis*, *18*(S2), 524–525. https://doi.org/10.1017/S1431927612004473

Bari, M. A., Curran, R. L. T., & Kindzierski, W. B. (2015). Field performance evaluation of Maxxam passive samplers for regional monitoring of ambient SO2, NO2 and O3 concentrations in Alberta, Canada. *Atmospheric Environment*, *114*, 39–47. https://doi.org/10.1016/j.atmosenv.2015.05.031

Batenburg, K. J., Bals, S., Sijbers, J., Kübel, C., Midgley, P. A., Hernandez, J. C., Kaiser, U., Encina, E. R., Coronado, E. A., & Van Tendeloo, G. (2009). 3D imaging of nanomaterials by discrete tomography. *Ultramicroscopy*, *109*(6), 730–740. https://doi.org/10.1016/j.ultramic.2009.01.009

Batenburg, K. J., & Sijbers, J. (2011). DART: a practical reconstruction algorithm for discrete tomography. *IEEE Transactions on Image Processing : A Publication of the IEEE Signal Processing Society*, *20*(9), 2542–2553. https://doi.org/10.1109/TIP.2011.2131661

Bayes, T., & Price, R. (1763). An Essay towards Solving a Problem in the Doctrine of Chances. By the Late Rev. Mr. Bayes, F. R. S. Communicated by Mr. Price, in a Letter to John Canton, A. M. F. R. S. *Philosophical Transactions of the Royal Society of London*, *53*, 370–418.

Béché, A., Goris, B., Freitag, B., & Verbeeck, J. (2016). Development of a fast electromagnetic beam blanker for compressed sensing in scanning transmission electron microscopy. *Applied Physics Letters*, *108*(9), 093103. https://doi.org/10.1063/1.4943086

Bialuschewski, D., Hoppius, J. S., Frohnhoven, R., Deo, M., Gönüllü, Y., Fischer, T., Gurevich, E. L., & Mathur, S. (2018). Laser-Textured Metal Substrates as Photoanodes for Enhanced PEC Water Splitting Reactions. *Advanced Engineering Materials*, *20*(9). https://doi.org/10.1002/adem.201800167

Biswas, S. (2000). Hilbert scan and image compression. *Proceedings - International Conference on Pattern Recognition*, *3*, 207–210. https://doi.org/10.1109/icpr.2000.903522

Bladt, E., Pelt, D. M., Bals, S., & Batenburg, K. J. (2015). Electron tomography based on highly limited data using a neural network reconstruction technique. *Ultramicroscopy*, *158*, 81–88. https://doi.org/10.1016/j.ultramic.2015.07.001

Bleichrodt, F., van Leeuwen, T., Palenstijn, W. J., van Aarle, W., Sijbers, J., & Batenburg, K. J. (2016). Easy implementation of advanced tomography algorithms using the ASTRA toolbox with Spot operators. *Numerical Algorithms*, *71*, 673–697. https://doi.org/10.1007/s11075-015-0016-4

Blommaerts, N., Vanrompay, H., Nuti, S., Lenaerts, S., Bals, S., & Verbruggen, S. W. (2019). Unraveling Structural Information of Turkevich Synthesized Plasmonic Gold–Silver Bimetallic Nanoparticles. *Small*, *15*(42), 1902791. https://doi.org/10.1002/smll.201902791

Bohren, C. F., & Huffman, D. R. (1998). Absorption and Scattering of Light by Small Particles. In *Absorption and Scattering of Light by Small Particles* (Vol. 98). https://doi.org/10.1002/9783527618156

Bonnet, S., Koenig, A., Roux, S., Hugonnard, P., Guillemaud, R., & Grangeat, P. (2003). Dynamic X-ray computed tomography. *Proceedings of the IEEE*, *91*(10), 1574–1587. https://doi.org/10.1109/JPROC.2003.817868

Borries, B. v., & Ruska, E. (1933). Die Abbildung durchstrahlter Folien im Elektronenmikroskop. *Zeitschrift Für Physik*, *83*(3–4), 187–193. https://doi.org/10.1007/BF01331139

Bracewell, R. (1956). Strip Integration in Radio Astronomy. *Australian Journal of Physics*, *9*(2), 198. https://doi.org/10.1071/ph560198

Brongersma, M. L., Halas, N. J., & Nordlander, P. (2015). Plasmon-induced hot carrier science and technology. In *Nature Nanotechnology* (Vol. 10, Issue 1, pp. 25–34). https://doi.org/10.1038/nnano.2014.311

Buban, J. P., Ramasse, Q., Gipson, B., Browning, N. D., & Stahlberg, H. (2010). High-resolution low-dose scanning transmission electron microscopy. *Journal of Electron Microscopy*, *59*(2), 103–112. https://doi.org/10.1093/jmicro/dfp052

Burdet, P., Saghi, Z., Filippin, A. N., Borrás, A., & Midgley, P. A. (2016). A novel 3D absorption correction method for quantitative EDX-STEM tomography. *Ultramicroscopy*, *160*, 118–129. https://doi.org/10.1016/j.ultramic.2015.09.012

Busch, H. (1926). Berechnung der Bahn von Kathodenstrahlen im axialsymmetrischen elektromagnetischen Felde. *Annalen Der Physik*, *386*(25), 974–993. https://doi.org/10.1002/andp.19263862507

Buurlage, J. W., Bisseling, R. H., & Batenburg, K. J. (2019). A geometric partitioning method for distributed tomographic reconstruction. *Parallel Computing*, *81*, 104–121. https://doi.org/10.1016/j.parco.2018.12.007

Buurlage, J. W., Kohr, H., Palenstijn, W. J., & Batenburg, K. J. (2018). Real-time quasi-3D tomographic reconstruction. *Measurement Science and Technology*, *29*(6), 064005. https://doi.org/10.1088/1361-6501/aab754

Buurlage, J. W., Marone, F., Pelt, D. M., Palenstijn, W. J., Stampanoni, M., Batenburg, K. J., & Schlepütz, C. M. (2019). Real-time reconstruction and visualisation towards dynamic feedback control during time-resolved tomography experiments at TOMCAT. *Scientific Reports*, *9*(1), 18379. https://doi.org/10.1038/s41598-019-54647-4

Buurlage, J. W., Palenstijn, W. J., Hendriksen, A., Pelt, D. M., Graas, A., & Kohr, H. (2020). *RECAST3D*. https://doi.org/10.5281/ZENODO.3773540

Candès, E., & Romberg, J. (2007). Sparsity and incoherence in compressive sampling. *Inverse Problems*, *23*(3), 969–985. https://doi.org/10.1088/0266-5611/23/3/008

Cao, L., Barsic, D. N., Guichard, A. R., & Brongersma, M. L. (2007). Plasmon-assisted local temperature control to pattern individual semiconductor nanowires and carbon nanotubes. *Nano Letters*, *7*(11), 3523–3527. https://doi.org/10.1021/nl0722370

Carn, S. A., Clarisse, L., & Prata, A. J. (2016). Multi-decadal satellite measurements of global volcanic degassing. *Journal of Volcanology and Geothermal Research*, *311*, 99–134. https://doi.org/10.1016/j.jvolgeores.2016.01.002

Carn, S. A., Fioletov, V. E., Mclinden, C. A., Li, C., & Krotkov, N. A. (2017). A decade of global volcanic SO2 emissions measured from space. *Scientific Reports*, *7*, 44095. https://doi.org/10.1038/srep44095

Carpenter, M. A., Mathur, S., & Kolmakov, A. (2013). Metal oxide nanomaterials for chemical sensors. In *Metal Oxide Nanomaterials for Chemical Sensors*. https://doi.org/10.1007/978-1-4614-5395-6

Chakraborty, A., Ghosh, S., Mukhopadhyay, P., Dinara, S. M., Bag, A., Mahata, M. K., Kumar, R., Das, S., Sanjay, J., Majumdar, S., & Biswas, D. (2014). Trapping effect analysis of AlGaN/InGaN/GaN Heterostructure by conductance frequency measurement. *MRS Proceedings*, *2*, 81–87. https://doi.org/10.1007/s13398-014-0173-7.2

Chambolle, A., & Pock, T. (2011). A first-order primal-dual algorithm for convex problems with applications to imaging. *Journal of Mathematical Imaging and Vision*, *40*(1), 120–145. https://doi.org/10.1007/s10851-010-0251-1

Chen, D., Goris, B., Bleichrodt, F., Mezerji, H. H., Bals, S., Batenburg, K. J., de With, G., & Friedrich, H. (2014). The properties of SIRT, TVM, and DART for 3D imaging of tubular domains in nanocomposite thin-films and sections. *Ultramicroscopy*, *147*, 137–148. https://doi.org/10.1016/j.ultramic.2014.08.005

Chen, H., Zhang, Y., Kalra, M. K., Lin, F., Chen, Y., Liao, P., Zhou, J., & Wang, G. (2017). Low-Dose CT with a residual encoder-decoder convolutional neural network. *IEEE Transactions on Medical Imaging*, *36*(12), 2524–2535. https://doi.org/10.1109/TMI.2017.2715284

Cho, H., Shin, J. W., & Ryoo, R. (2020). Atomic Scale Mechanisms Underlying Thermal Reshaping of Anisotropic Gold Nanocrystals Revealed by in Situ Electron Microscopy. *The Journal of Physical Chemistry C*. https://doi.org/10.1021/acs.jpcc.0c04281

Choi, S. H., Choi, S. J., Min, B. K., Lee, W. Y., Park, J. S., & Kim, I. D. (2013). Facile Synthesis of p-type Perovskite SrTi0.65Fe 0.35O3-δ Nanofibers Prepared by Electrospinning and Their Oxygen-Sensing Properties. *Macromolecular Materials and Engineering*, *9*, 38271–38279. https://doi.org/10.1002/mame.201200375

Colomban, P. (2009). The use of metal nanoparticles to produce yellow, red and iridescent colour, from bronze age to present times in lustre pottery and glass: Solid state chemistry, spectroscopy and nanostructure. *Journal of Nano Research*, *8*, 109–132. https://doi.org/10.4028/www.scientific.net/JNanoR.8.109

Cormack, A. M. (1963). Representation of a function by its line integrals, with some radiological applications. *Journal of Applied Physics*, *34*(9), 2722–2727. https://doi.org/10.1063/1.1729798

Cortie, M. B., & McDonagh, A. M. (2011). Synthesis and optical properties of hybrid and alloy plasmonic nanoparticles. In *Chemical Reviews* (Vol. 111, Issue 6, pp. 3713–3735). https://doi.org/10.1021/cr1002529

Crewe, A. V., Wall, J., & Lanomore, J. (1970). Visibility of single atoms. *Science*, *168*(3937), 1338–1340. https://doi.org/10.1126/science.168.3937.1338

De Broglie, L. (1925). Recherches sur la théorie des Quanta. *Annales de Physique*, *10*(3), 22–128. https://doi.org/10.1051/anphys/192510030022

De Broglie, L. (1929). The wave nature of the electron. *Nobel Lectures, Physics 1922-1941*, 244–256. http://www.nobelprize.org/nobel_prizes/physics/laureates/1929/

De Rosier, D. J., & Klug, A. (1968). Reconstruction of three dimensional structures from electron micrographs. *Nature*, *217*(5124), 130–134. https://doi.org/10.1038/217130a0

Ding, B., & Si, Y. (2011). *Electrospun nanofibers for energy and environmental applications*. Springer-Verlag. https://doi.org/10.1016/j.egypro.2019.01.016

Ding, B., Wang, M., Wang, X., Yu, J., & Sun, G. (2010). Electrospun nanomaterials for ultrasensitive sensors. *Materials Today*, *13*(11), 16–27. https://doi.org/10.1016/S1369-7021(10)70200-5

Donati, L., Nilchian, M., Trépout, S., Messaoudi, C., Marco, S., & Unser, M. (2017). Compressed sensing for STEM tomography. *Ultramicroscopy*, *179*, 47–56. https://doi.org/10.1016/j.ultramic.2017.04.003

Donoho, D. L. (2006). Compressed sensing. *IEEE Transactions on Information Theory*, *52*(4), 1289–1306. https://doi.org/10.1109/TIT.2006.871582

Dudgeon, D. E., & Mersereau, R. M. (1985). Multidimensional Digital Signal Processing. In *IEEE Communications Magazine* (Vol. 23, Issue 1, p. 63). https://doi.org/10.1109/MCOM.1985.1092416

Egerton, R. F., Li, P., & Malac, M. (2004). Radiation damage in the TEM and SEM. *Micron*, *35*(6), 399–409.

Ernst, A. (1874). A contribution to the Theory of the Microscope, and the nature of Microscopic Vision. In *Proceedings of the Bristal Naturalists's Society* (Vol. 1, pp. 200–261).

Espinosa, A., Silva, A. K. A., Sánchez-Iglesias, A., Grzelczak, M., Péchoux, C., Desboeufs, K., Liz-Marzán, L. M., & Wilhelm, C. (2016). Cancer Cell Internalization of Gold Nanostars Impacts Their Photothermal Efficiency In Vitro and In Vivo: Toward a Plasmonic Thermal Fingerprint in Tumoral Environment. *Advanced Healthcare Materials*, *5*(9), 1040–1048. https://doi.org/10.1002/adhm.201501035

Fan, H. T., Xu, X. J., Ma, X. K., & Zhang, T. (2011). Preparation of LaFeO3 nanofibers by electrospinning for gas sensors with fast response and recovery. *Nanotechnology*, *22*(11), 115502. https://doi.org/10.1088/0957-4484/22/11/115502

Fienup, J. R. (1997). Invariant error metrics for image reconstruction. *Applied Optics*, *36*(32), 8352–8357. https://doi.org/10.1364/ao.36.008352

Fioletov, V. E., McLinden, C. A., Krotkov, N., Li, C., Joiner, J., Theys, N., Carn, S., & Moran, M. D. (2016). A global catalogue of large SO2 sources and emissions derived from the Ozone Monitoring Instrument. *Atmospheric Chemistry and Physics*, *16*, 11497–11519. https://doi.org/10.5194/acp-16-11497-2016

Fitchard, E. E., Aldridge, J. S., Reckwerdt, P. J., & Mackie, T. R. (1998). Registration of synthetic tomographic projection data sets using cross- correlation. *Physics in Medicine and Biology*, *43*(6), 1645–1657. https://doi.org/10.1088/0031-9155/43/6/020

Foroosh, H., Zerubia, J. B., & Berthod, M. (2002). Extension of phase correlation to subpixel registration. *IEEE Transactions on Image Processing*, *11*(3), 188–199. https://doi.org/10.1109/83.988953

Freestone, I., Meeks, N., Sax, M., & Higgitt, C. (2008). The Lycurgus Cup - A Roman nanotechnology. *Gold Bulletin*, *40*(4), 270–277. https://doi.org/10.1007/BF03215599

Gad, A. E., Hoffmann, M. W. G., Hernandez-Ramirez, F., Prades, J. D., Shen, H., & Mathur, S. (2012). Coaxial p-Si/n-ZnO nanowire heterostructures for energy and sensing applications. *Materials Chemistry and Physics*, *135*(2–3), 618–622. https://doi.org/10.1016/j.matchemphys.2012.05.034

Giebelhaus, I., Varechkina, E., Fischer, T., Rumyantseva, M., Ivanov, V., Gaskov, A., Morante, J. R., Arbiol, J., Tyrra, W., & Mathur, S. (2013). One-dimensional CuO-SnO2 p-n heterojunctions for enhanced detection of H2S. *Journal of Materials Chemistry A*, *1*, 11261–11268. https://doi.org/10.1039/c3ta11867c

Gilbert, P. (1972). Iterative methods for the three-dimensional reconstruction of an object from projections. *Journal of Theoretical Biology*, *36*(1), 105–117. https://doi.org/10.1016/0022-5193(72)90180-4

Gonzalez, C. M., Liu, Y., & Scaiano, J. C. (2009). Photochemical Strategies for the Facile Synthesis of Gold− Silver Alloy and Core− Shell Bimetallic Nanoparticles†. *The Journal of Physical Chemistry C*, *113*(27), 11861–11867. https://doi.org/10.1021/jp902061v

Gordon, R., Bender, R., & Herman, G. T. (1970). Algebraic Reconstruction Techniques (ART) for three-dimensional electron microscopy and X-ray photography. *Journal of Theoretical Biology*, *29*(3), 471–476. https://doi.org/10.1016/0022-5193(70)90109-8

Goris, B., Bals, S., Van Den Broek, W., Carbó-Argibay, E., Gómez-Graña, S., Liz-Marzán, L. M., & Van Tendeloo, G. (2012). Atomic-scale determination of surface facets in gold nanorods. *Nature Materials*, *11*(11), 930–935. https://doi.org/10.1038/nmat3462

Goris, B., De Beenhouwer, J., De Backer, A., Zanaga, D., Batenburg, K. J., Sánchez-Iglesias, A., Liz-Marzán, L. M., Van Aert, S., Bals, S., Sijbers, J., & Van Tendeloo, G. (2015). Measuring Lattice Strain in Three Dimensions through Electron Microscopy. *Nano Letters*, *15*(10), 6996–7001. https://doi.org/10.1021/acs.nanolett.5b03008

Goris, B., Freitag, B., Zanaga, D., Bladt, E., Altantzis, T., Ringnalda, J., & Bals, S. (2014). Towards quantitative EDX results in 3 dimensions. *Microscopy and Microanalysis*, *20*(SR), 766–767. https://doi.org/10.1017/S1431927614005558

Goris, B., Van den Broek, W., Batenburg, K. J., Heidari Mezerji, H., & Bals, S. (2012). Electron tomography based on a total variation minimization reconstruction technique. *Ultramicroscopy*, *113*, 120–130. https://doi.org/10.1016/j.ultramic.2011.11.004

Goris, B., Van Huis, M. A., Bals, S., Zandbergen, H. W., Manna, L., & Van Tendeloo, G. (2012). Thermally induced structural and morphological changes of CdSe/CdS octapods. *Small*, *8*(6), 937–942. https://doi.org/10.1002/smll.201101897

Guerrero-Martínez, A., Barbosa, S., Pastoriza-Santos, I., & Liz-Marzán, L. M. (2011). Nanostars shine bright for you. Colloidal synthesis, properties and applications of branched metallic nanoparticles. In *Current Opinion in Colloid and Interface Science* (Vol. 16, Issue 2, pp. 118–127). https://doi.org/10.1016/j.cocis.2010.12.007

Guisbiers, G., Mendoza-Cruz, R., Bazán-Díaz, L., Velázquez-Salazar, J. J., Mendoza-Perez, R., Robledo-Torres, J. A., Rodriguez-Lopez, J. L., Montejano-Carrizales, J. M., Whetten, R. L., & José-Yacamán, M. (2016). Electrum, the gold-silver alloy, from the bulk scale to the nanoscale: Synthesis, properties, and segregation rules. *ACS Nano*, *10*(1), 188–198. https://doi.org/10.1021/acsnano.5b05755

Haberfehlner, G., Orthacker, A., Albu, M., Li, J., & Kothleitner, G. (2014). Nanoscale voxel spectroscopy by simultaneous EELS and EDS tomography. *Nanoscale*, *6*, 14563–14569. https://doi.org/10.1039/c4nr04553j

Hackner, A., Beer, S., Müller, G., Fischer, T., & Mathur, S. (2011). Fast responding ephedrine detection with miniaturized surface ionization gas sensors. *Procedia Engineering*, *25*, 1325–1328. https://doi.org/10.1016/j.proeng.2011.12.327

Haider, M., Rose, H., Uhlemann, S., Schwan, E., Kabius, B., & Urban, K. (1998). A spherical-aberration-corrected 200 kV transmission electron microscope. *Ultramicroscopy*, *75*(1), 53–60. https://doi.org/10.1016/S0304-3991(98)00048-5

Hansell, A., & Oppenheimer, C. (2004). Health Hazards from Volcanic Gases: A Systematic Literature Review. *Archives of Environmental Health*, *59*(12), 628–639. https://doi.org/10.1080/00039890409602947

Hao, F., Nehl, C. L., Hafner, J. H., & Nordlander, P. (2007). Plasmon resonances of a gold nanostar. *Nano Letters*, *7*(3), 729–732. https://doi.org/10.1021/nl062969c

Hart, R. G. (1968). Electron microscopy of unstained biological material: The polytropic montage. *Science*, *159*(3822), 1464–1467. https://doi.org/10.1126/science.159.3822.1464

Hayashida, M., Ogawa, S., & Malac, M. (2018). Evaluation of electron tomography reconstruction methods for interface roughness measurement. *Microscopy Research and Technique*, *81*(5), 515–519. https://doi.org/10.1002/jemt.23006

Heidari Mezerji, H., Van den Broek, W., & Bals, S. (2011). A practical method to determine the effective resolution in incoherent experimental electron tomography. *Ultramicroscopy*, *111*(5), 330–336. https://doi.org/10.1016/j.ultramic.2011.01.021

Hendriksen, A. A., Pelt, D. M., & Batenburg, K. J. (2020). *Noise2Inverse: Self-supervised deep convolutional denoising for linear inverse problems in imaging*. https://doi.org/arXiv:2001.11801

Hendriksen, A. A., Pelt, D. M., Palenstijn, W. J., Coban, S. B., & Batenburg, K. J. (2019). On-the-fly machine learning for improving image resolution in tomography. *Applied Sciences (Switzerland)*, *9*(12), 2445. https://doi.org/10.3390/app9122445

Hernandez-Ramirez, F., Prades, J. D., Hackner, A., Fischer, T., Mueller, G., Mathur, S., & Morante, J. R. (2011). Miniaturized ionization gas sensors from single metal oxide nanowires. *Nanoscale*, *3*, 630–634. https://doi.org/10.1039/c0nr00528b

Hernandez-Ramirez, F., Prades, J. D., Jimenez-Diaz, R., Fischer, T., Romano-Rodriguez, A., Mathur, S., & Morante, J. R. (2009). On the role of individual metal oxide nanowires in the scaling down of chemical sensors. *Physical Chemistry Chemical Physics*, *11*(33), 7105–7110. https://doi.org/10.1039/b905234h

Hohenester, U., & Trügler, A. (2012). MNPBEM - A Matlab toolbox for the simulation of plasmonic nanoparticles. *Computer Physics Communications*, *183*(2), 370–381. https://doi.org/10.1016/j.cpc.2011.09.009

Hoppe, W., Langer, R., Knesch, G., & Poppe, C. (1968). Protein-Kristallstrukturanalyse mit Elektronenstrahlen. *Die Naturwissenschaften*, *55*(7), 333–336. https://doi.org/10.1007/BF00600449

Houben, L., & Bar Sadan, M. (2011). Refinement procedure for the image alignment in high-resolution electron tomography. *Ultramicroscopy*, *111*(9–10), 1512–1520. https://doi.org/10.1016/j.ultramic.2011.06.001

Hounsfield, G. N. (1973). Computerized transverse axial scanning (tomography): I. Description of system. *British Journal of Radiology*, *46*(552), 1016–1022. https://doi.org/10.1259/0007-1285-46-552-1016

Huber, F., Riegert, S., Madel, M., & Thonke, K. (2017). H2S sensing in the ppb regime with zinc oxide nanowires. *Sensors and Actuators, B: Chemical*, *239*, 358–363. https://doi.org/10.1016/j.snb.2016.08.023

Hwang, D. K., Kim, S., Lee, J. H., Hwang, I. S., & Kim, I. D. (2011). Phase evolution of perovskite LaNiO3 nanofibers for supercapacitor application and p-type gas sensing properties of LaOCl-NiO composite nanofibers. *Journal of Materials Chemistry*, *21*(6), 1959–1965. https://doi.org/10.1039/c0jm02256j

Inasawa, S., Sugiyama, M., & Yamaguchi, Y. (2005). Laser-induced shape transformation of gold nanoparticles below the melting point: The effect of surface melting. *Journal of Physical Chemistry B*, *109*(8), 3104–3111. https://doi.org/10.1021/jp045167j

Janssens, E., De Beenhouwer, J., Van Dael, M., Verboven, P., Nicolaï, B., & Sijbers, J. (2015). Neural netwok based X-ray tomography for fast inspection of apples on a conveyor belt system. *Proceedings - International Conference on Image Processing, ICIP*, 917–921. https://doi.org/10.1109/ICIP.2015.7350933

Jing, H., Zhang, Q., Large, N., Yu, C., Blom, D. A., Nordlander, P., & Wang, H. (2014). Tunable plasmonic nanoparticles with catalytically active high-index facets. *Nano Letters*, *14*(6), 3674–3682. https://doi.org/10.1021/nl5015734

Jones, L., Varambhia, A., Beanland, R., Kepaptsoglou, D., Griffiths, I., Ishizuka, A., Azough, F., Freer, R., Ishizuka, K., Cherns, D., Ramasse, Q. M., Lozano-Perez, S., & Nellist, P. D. (2018). Managing dose-, damage- and data-rates in multi-frame spectrum-imaging. *Microscopy*, *67*, 98–113. https://doi.org/10.1093/jmicro/dfx125

Joo, S. H., Park, J. Y., Tsung, C. K., Yamada, Y., Yang, P., & Somorjai, G. A. (2009). Thermally stable Pt/mesoporous silica core-shell nanocatalysts for high-temperature reactions. *Nature Materials*, *8*(2), 126–131. https://doi.org/10.1038/nmat2329

Kaczmarz, S. (1937a). Angenäherte Auflösung von Systemen linearer Gleichungen. *Bulletin International de l'Académie Polonaise Des Sciences et Des Lettres. Classe Des Sciences Mathématiques et Naturelles. Série A, Sciences Mathématiques*, *35*, 355–357.

Kaczmarz, S. (1937b). Angenäherte Auflösung von Systemen linearer Gleichungen. *Bulletin International de l'Académie Polonaise Des Sciences et Des Lettres. Classe Des Sciences Mathématiques et Naturelles. Série A, Sciences Mathématiques*, *35*, 355.

Kaczmarz, S. (1993). Approximate solution of systems of linear equations†. *International Journal of Control*, *57*(6), 1269–1271. https://doi.org/10.1080/00207179308934446

Kalender, W. A. (2006). X-ray computed tomography. *Physics in Medicine and Biology*, *51*(13), R29-43. https://doi.org/10.1088/0031-9155/51/13/R03

Kalender, W. A., Seissler, W., Klotz, E., & Vock, P. (1990). Spiral volumetric CT with single-breath-hold technique, continuous transport, and continuous scanner rotation. *Radiology*, *176*(1), 181–183. https://doi.org/10.1148/radiology.176.1.2353088

Kamilov, U., Bostan, E., & Unser, M. (2012). Wavelet shrinkage with consistent cycle spinning generalizes total variation denoising. *IEEE Signal Processing Letters*, *19*(4), 187–190. https://doi.org/10.1109/LSP.2012.2185929

Kawai, S., Onishi, I., Ishikawa, T., Yagi, K., Iwama, T., Miyatake, K., Iwasawa, Y., Matsushita, M., Kaneyama, T., & Kondo, Y. (2014). A double silicon drift type detector system for EDS with ultrahigh efficiency and throughput for TEM. *Microscopy and Microanalysis*, *20*, 1150–1151. https://doi.org/10.1017/S143192761400748X

Ke, X., Bals, S., Cott, D., Hantschel, T., Bender, H., & Van Tendeloo, G. (2010). Three-dimensional analysis of carbon nanotube networks in interconnects by electron tomography without missing wedge artifacts. *Microscopy and Microanalysis*, *16*(2), 210–217. https://doi.org/10.1017/S1431927609991371

Kelly, K. L., Coronado, E., Zhao, L. L., & Schatz, G. C. (2003). The optical properties of metal nanoparticles: The influence of size, shape, and dielectric environment. *Journal of Physical Chemistry B*, *107*(3), 668–677. https://doi.org/10.1021/jp026731y

Kerl, H. U., Isaza, C. T., Boll, H., Schambach, S. J., Nolte, I. S., Groden, C., & Brockmann, M. A. (2011). Evaluation of a continuous-rotation, high-speed scanning protocol for micro-computed tomography. *Journal of Computer Assisted Tomography*, *35*(4), 517–523. https://doi.org/10.1097/RCT.0b013e31821c662b

Khalavka, Y., Ohm, C., Sun, L., Banhart, F., & Sönnichsen, C. (2007). Enhanced thermal stability of gold and silver nanorods by thin surface layers. *Journal of Physical Chemistry C*, *111*(35), 12886–12889. https://doi.org/10.1021/jp075230f

Kim, H. J., & Lee, J. H. (2014). Highly sensitive and selective gas sensors using p-type oxide semiconductors: Overview. *Sensors and Actuators, B: Chemical*, *192*, 607–627. https://doi.org/10.1016/j.snb.2013.11.005

Kim, K., Kim, K. L., Choi, J.-Y., Lee, H. B., & Shin, K. S. (2010). Surface Enrichment of Ag Atoms in Au/Ag Alloy Nanoparticles Revealed by Surface-Enhanced Raman Scattering of 2,6-Dimethylphenyl Isocyanide. *The Journal of Physical Chemistry C*, *114*(8), 3448–3453. https://doi.org/10.1021/jp9112624

Kim, S., Spenko, M., Trujillo, S., Heyneman, B., Santos, D., & Cutkoskly, M. R. (2008). Smooth vertical surface climbing with directional adhesion. *IEEE Transactions on Robotics*, *24*(1), 65–74. https://doi.org/10.1109/TRO.2007.909786

Kingma, D. P., & Ba, J. L. (2015). Adam: A method for stochastic optimization. *3rd International Conference on Learning Representations, ICLR 2015 - Conference Track Proceedings*.

Klöckner, A., Pinto, N., Lee, Y., Catanzaro, B., Ivanov, P., & Fasih, A. (2012). PyCUDA and PyOpenCL: A scripting-based approach to GPU run-time code generation. *Parallel Computing*, *38*(3), 157–174. https://doi.org/10.1016/j.parco.2011.09.001

Knoll, M., & Ruska, E. (1932). Das Elektronenmikroskop. In *Zeitschrift für Physik* (Vol. 79, Issues 9–10, p. 699). https://doi.org/10.1007/BF01330526

Kong, X. T., Wang, Z., & Govorov, A. O. (2017). Plasmonic Nanostars with Hot Spots for Efficient Generation of Hot Electrons under Solar Illumination. *Advanced Optical Materials*, *5*(15), 1600594. https://doi.org/10.1002/adom.201600594

Konstantynovski, K., Njio, G., Börner, F., Lepcha, A., Fischer, T., Holl, G., & Mathur, S. (2018). Bulk detection of explosives and development of customized metal oxide semiconductor gas sensors for the identification of energetic materials. *Sensors and Actuators, B: Chemical*, *258*, 1252–1266. https://doi.org/10.1016/j.snb.2017.11.116

Koster, A. J., Ziese, U., Verkleij, A. J., Janssen, A. H., & De Jong, K. P. (2000). Three-dimensional transmission electron microscopy: a novel imaging and characterization technique with nanometer scale resolution for materials science. *Journal of Physical Chemistry B*, *104*(40), 9368–9370. https://doi.org/10.1021/jp0015628

Kovarik, L., Stevens, A., Liyu, A., & Browning, N. D. (2016). Implementing an accurate and rapid sparse sampling approach for low-dose atomic resolution STEM imaging. *Applied Physics Letters*, *109*, 164102. https://doi.org/10.1063/1.4965720

Kumar, S., Pastoriza-Santos, I., Rodríguez-González, B., Javier García De Abajo, F., & Liz-Marzán, L. M. (2008). High-yield synthesis and optical response of gold nanostars. *Nanotechnology*, *19*(1), 015606. https://doi.org/10.1088/0957-4484/19/01/015606

Laplace, P.-S. (1812). Théorie analytique des probabilitiés. In *Reprinted in Oeuvres Complètes de Laplace.*

Lasagni, F. A., Lasagni, A. F., Huertas-Olivares, I., Holazapfel, C., & Mücklich, F. (2010). 3D Nano-characterisation of materials by FIB-SEI/EDS tomography. *IOP Conference Series: Materials Science and Engineering*, *7*, 012016. https://doi.org/10.1088/1757-899x/7/1/012016

Leary, R., Saghi, Z., Midgley, P. A., & Holland, D. J. (2013a). Compressed Sensing Electron Tomography: Theory and Applications. *Microscopy and Microanalysis*, *19*(S2), 546–547. https://doi.org/10.1017/s1431927613004728

Leary, R., Saghi, Z., Midgley, P. A., & Holland, D. J. (2013b). Compressed sensing electron tomography. *Ultramicroscopy*, *131*, 70–91. https://doi.org/10.1016/j.ultramic.2013.03.019

Ledig, C., Theis, L., Huszár, F., Caballero, J., Cunningham, A., Acosta, A., Aitken, A., Tejani, A., Totz, J., Wang, Z., & Shi, W. (2017). Photo-realistic single image super-resolution using a generative adversarial network. *Proceedings - 30th IEEE Conference on Computer Vision and Pattern Recognition, CVPR 2017*, 105–114. https://doi.org/10.1109/CVPR.2017.19

Lehnen, T., Valldor, M., Nižňanský, D., & Mathur, S. (2014). Hydrothermally grown porous FeVO4 nanorods and their integration as active material in gas-sensing devices. *Journal of Materials Chemistry A*, *2*, 1862–1868. https://doi.org/10.1039/c3ta12821k

Lepinay, K., Lorut, F., Pantel, R., & Epicier, T. (2013). Chemical 3D tomography of 28nm high K metal gate transistor: STEM XEDS experimental method and results. *Micron*, *47*, 43–49. https://doi.org/10.1016/j.micron.2013.01.004

Li, N., Zhao, P., & Astruc, D. (2014). Anisotropic gold nanoparticles: Synthesis, properties, applications, and toxicity. *Angewandte Chemie - International Edition*, *53*(7), 1756–1789. https://doi.org/10.1002/anie.201300441

Li, T., Albee, B., Alemayehu, M., Diaz, R., Ingham, L., Kamal, S., Rodriguez, M., & Whaley Bishnoi, S. (2010). Comparative toxicity study of Ag, Au, and Ag-Au bimetallic nanoparticles on Daphnia magna. *Analytical and Bioanalytical Chemistry*, *398*(2), 689–700. https://doi.org/10.1007/s00216-010-3915-1

Liao, T.-W., Yadav, A., Hu, K.-J., van der Tol, J., Cosentino, S., D'Acapito, F., Palmer, R. E., Lenardi, C., Ferrando, R., Grandjean, D., & Lievens, P. (2018). Unravelling the nucleation mechanism of bimetallic nanoparticles with composition-tunable core–shell arrangement. *Nanoscale*, *10*(14), 6684–6694. https://doi.org/10.1039/C8NR01481G

Link, S., Burda, C., Nikoobakht, B., & El-Sayed, M. A. (2000). Laser-induced shape changes of colloidal gold nanorods using femtosecond and nanosecond laser pulses. *Journal of Physical Chemistry B*, *104*(26), 6152–6163. https://doi.org/10.1021/jp000679t

Link, S., & Wang, Z. L. (1999). Alloy Formation of Gold - Silver Nanoparticles and the Dependence of the Plasmon Absorption on Their Composition. *Journal of Physical Chemistry B*, *103*, 3529–3533.

Lipson, S. G., Lipson, H., & Tannhauser, D. S. (1995). Optical Physics. In *Optical Physics*. https://doi.org/10.1017/cbo9781139170413

Liu, Y., Mills, E. N., & Composto, R. J. (2009). Tuning optical properties of gold nanorods in polymer films through thermal reshaping. *Journal of Materials Chemistry*, *19*(18), 2704–2709. https://doi.org/10.1039/b901782h

Liz-Marzán, L. M. (2006). Tailoring surface plasmons through the morphology and assembly of metal nanoparticles. *Langmuir*, *22*(1), 32–41. https://doi.org/10.1021/la0513353

Lorensen, W. E., & Cline, H. E. (1987). Marching cubes: A high resolution 3D surface construction algorithm. *Proceedings of the 14th Annual Conference on Computer Graphics and Interactive Techniques, SIGGRAPH 1987*, 163–169. https://doi.org/10.1145/37401.37422

Løvvik, O. M., & Opalka, S. M. (2008). Reversed surface segregation in palladium-silver alloys due to hydrogen adsorption. *Surface Science*, *602*(17), 2840–2844. https://doi.org/https://doi.org/10.1016/j.susc.2008.07.016

Lu, L., Burkey, G., Halaciuga, I., & Goia, D. V. (2013). Core–shell gold/silver nanoparticles: Synthesis and optical properties. *Journal of Colloid and Interface Science*, *392*, 90–95. https://doi.org/https://doi.org/10.1016/j.jcis.2012.09.057

Lustig, M., Donoho, D. L., & Pauly, J. M. (2007). Sparse MRI: The application of compressed sensing for rapid MR imaging. *Magnetic Resonance in Medicine*, *58*(6), 1182–1195. https://doi.org/10.1002/mrm.21391

Lustig, M., Donoho, D. L., Santos, J. M., & Pauly, J. M. (2008). Compressed sensing MRI: A look at how CS can improve on current imaging techniques. *IEEE Signal Processing Magazine*, *25*(2), 72–82. https://doi.org/10.1109/MSP.2007.914728

Mallin, M. P., & Murphy, C. J. (2002). Solution-Phase Synthesis of Sub-10 nm Au−Ag Alloy Nanoparticles. *Nano Letters*, *2*(11), 1235–1237. https://doi.org/10.1021/nl025774n

Manjavacas, A., Liu, J. G., Kulkarni, V., & Nordlander, P. (2014). Plasmon-induced hot carriers in metallic nanoparticles. *ACS Nano*, *8*(8), 7630–7638. https://doi.org/10.1021/nn502445f

Marone, F., & Stampanoni, M. (2012). Regridding reconstruction algorithm for real-time tomographic imaging. *Journal of Synchrotron Radiation*, *19*(6), 1029–1037. https://doi.org/10.1107/S0909049512032864

Marshall, N. W., & Bosmans, H. (2012). Measurements of system sharpness for two digital breast tomosynthesis systems. *Physics in Medicine and Biology*, *57*, 7629–7650. https://doi.org/10.1088/0031-9155/57/22/7629

Mastronarde, D. N. (1997). Dual-axis tomography: An approach with alignment methods that preserve resolution. *Journal of Structural Biology*, *120*(3), 343–352. https://doi.org/10.1006/jsbi.1997.3919

Mathur, S., Ganesan, R., Grobelsek, I., Shen, H., Ruegamer, T., & Barth, S. (2007). Plasma-assisted modulation of morphology and composition in tin oxide nanostructures for sensing applications. *Advanced Engineering Materials*, *9*(8), 658–663. https://doi.org/10.1002/adem.200700086

Maziarz, W., Kusior, A., & Trenczek-Zajac, A. (2016). Nanostructured TiO2-based gas sensors with enhancedsensitivity to reducing gases. *Beilstein Journal of Nanotechnology*, *7*, 1718–1726. https://doi.org/10.3762/BJNANO.7.164

McLinden, C. A., Fioletov, V., Shephard, M. W., Krotkov, N., Li, C., Martin, R. V., Moran, M. D., & Joiner, J. (2016). Space-based detection of missing sulfur dioxide sources of global air pollution. *Nature Geoscience*, *9*, 496–500. https://doi.org/10.1038/ngeo2724

Midgley, P. A., Ward, E. P. W., Hungría, A. B., & Thomas, J. M. (2007). Nanotomography in the chemical, biological and materials sciences. *Chemical Society Reviews*, *36*(9), 1477–1494. https://doi.org/10.1039/b701569k

Midgley, P. A., & Weyland, M. (2003). 3D electron microscopy in the physical sciences: The development of Z-contrast and EFTEM tomography. *Ultramicroscopy*, *96*(3–4), 413–431. https://doi.org/10.1016/S0304-3991(03)00105-0

Mie, G. (1908). Beiträge zur Optik trüber Medien, speziell kolloidaler Metallösungen. *Annalen Der Physik*, *330*(3), 377–445. https://doi.org/10.1002/andp.19083300302

Migunov, V., Ryll, H., Zhuge, X., Simson, M., Strüder, L., Batenburg, K. J., Houben, L., & Dunin-Borkowski, R. E. (2015). Rapid low dose electron tomography using a direct electron detection camera. *Scientific Reports*, *5*, 14516. https://doi.org/10.1038/srep14516

Moon, T. K. (1996). The expectation-maximization algorithm. *IEEE Signal Processing Magazine*, *13*(6), 47–60. https://doi.org/10.1109/79.543975

Mukherjee, S., Libisch, F., Large, N., Neumann, O., Brown, L. V., Cheng, J., Lassiter, J. B., Carter, E. A., Nordlander, P., & Halas, N. J. (2013). Hot electrons do the impossible: Plasmon-induced dissociation of H 2 on Au. *Nano Letters*, *13*(1), 240–247. https://doi.org/10.1021/nl303940z

Münch, B. (2011). Spatiotemporal computed tomography of dynamic processes. *Optical Engineering*, *50*(12), 3201. https://doi.org/10.1117/1.3660298

Myagotin, A., Voropaev, A., Helfen, L., Hänschke, D., & Baumbach, T. (2013). Efficient volume reconstruction for parallel-beam computed laminography by filtered backprojection on multi-core clusters. *IEEE Transactions on Image Processing*, *22*(12), 5348-61. https://doi.org/10.1109/TIP.2013.2285600

Nagashima, S., Ito, K., Aoki, T., Ishii, H., & Kobayashi, K. (2007). A high-accuracy rotation estimation algorithm based on ID phase-only correlation. *Lecture Notes in Computer Science (Including Subseries Lecture Notes in Artificial Intelligence and Lecture Notes in Bioinformatics), 4633 LNCS*, 210–221. https://doi.org/10.1007/978-3-540-74260-9_19

Nair, V., & Hinton, G. E. (2010). Rectified linear units improve Restricted Boltzmann machines. *ICML 2010 - Proceedings, 27th International Conference on Machine Learning*.

Nasrollahzadeh, M., Sajadi, S. M., Sajjadi, M., & Issaabadi, Z. (2019). Applications of Nanotechnology in Daily Life. *Interface Science and Technology*, 113–143. https://doi.org/10.1016/B978-0-12-813586-0.00004-3

Neethirajan, S., & Jayas, D. S. (2011). Nanotechnology for the Food and Bioprocessing Industries. In *Food and Bioprocess Technology* (Vol. 4, Issue 1, pp. 39–47). https://doi.org/10.1007/s11947-010-0328-2

Nehl, C. L., Liao, H., & Hafner, J. H. (2006). Optical properties of star-shaped gold nanoparticles. *Nano Letters*, *6*(4), 683–688. https://doi.org/10.1021/nl052409y

Niewiarowski, P. H., Stark, A. Y., & Dhinojwala, A. (2016). Sticking to the story: Outstanding challenges in gecko-inspired adhesives. *Journal of Experimental Biology*, *219*(7), 912–919. https://doi.org/10.1242/jeb.080085

Nikitin, V. V., Andersson, F., Carlsson, M., & Duchkov, A. A. (2017). Fast hyperbolic Radon transform represented as convolutions in log-polar coordinates. *Computers and Geosciences*, *105*, 21–33. https://doi.org/10.1016/j.cageo.2017.04.013

Obradors, X., Puig, T., Gibert, M., Queraltó, A., Zabaleta, J., & Mestres, N. (2014). Chemical solution route to self-assembled epitaxial oxide nanostructures. *Chemical Society Reviews*, *43*(7), 2200–2225. https://doi.org/10.1039/c3cs60365b

Otsu, N. (1979). Threshold Selection Method From Gray-Level Histograms. *IEEE Trans Syst Man Cybern*, *9*(1), 62–66. https://doi.org/10.1109/tsmc.1979.4310076

Palenstijn, W. J., Batenburg, K. J., & Sijbers, J. (2011). Performance improvements for iterative electron tomography reconstruction using graphics processing units (GPUs). *Journal of Structural Biology*, *176*(2), 250–253. https://doi.org/10.1016/j.jsb.2011.07.017

Palenstijn, W. J., Bédorf, J., Sijbers, J., & Batenburg, K. J. (2016). A distributed ASTRA toolbox. *Advanced Structural and Chemical Imaging*, *2*(1). https://doi.org/10.1186/s40679-016-0032-z

Pan, J., Ganesan, R., Shen, H., & Mathur, S. (2010). Plasma-modified SnO2 nanowires for enhanced gas sensing. *Journal of Physical Chemistry C*, *114*(18), 8245–8250. https://doi.org/10.1021/jp101072f

Paszke, A., Chanan, G., Lin, Z., Gross, S., Yang, E., Antiga, L., & Devito, Z. (2017). Automatic differentiation in PyTorch. *31st Conference on Neural Information Processing Systems*, 1. https://doi.org/10.1017/CBO9781107707221.009

Pelt, D. M., & Batenburg, K. J. (2015). Accurately approximating algebraic tomographic reconstruction by filtered backprojection. *International Meeting on Fully Three-Dimensional Image Reconstruction in Radiology and Nuclear Medicine.*, 158–161.

Pelt, D. M., Batenburg, K. J., & Sethian, J. A. (2018). Improving tomographic reconstruction from limited data using mixed-scale dense convolutional neural networks. *Journal of Imaging*, *4*(11), 128. https://doi.org/10.3390/jimaging4110128

Pelt, D. M., & Sethian, J. A. (2017). A mixed-scale dense convolutional neural network for image analysis. *Proceedings of the National Academy of Sciences of the United States of America*, *115*(2), 254–259. https://doi.org/10.1073/pnas.1715832114

Pelton, M., Aizpurua, J., & Bryant, G. (2008). Metal-nanoparticle plasmonics. In *Laser and Photonics Reviews* (Vol. 2, Issue 3, pp. 136–159). https://doi.org/10.1002/lpor.200810003

Pérez-Juste, J., Pastoriza-Santos, I., Liz-Marzán, L. M., & Mulvaney, P. (2005). Gold nanorods: Synthesis, characterization and applications. *Coordination Chemistry Reviews*, *249*(17-18 SPEC. ISS.), 1870–1901. https://doi.org/10.1016/j.ccr.2005.01.030

Petrova, H., Pérez-Juste, J., Pastoriza-Santos, I., Hartland, G. V., Liz-Marzán, L. M., & Mulvaney, P. (2006). On the temperature stability of gold nanorods: Comparison between thermal and ultrafast laser-induced heating. *Physical Chemistry Chemical Physics*, *8*(7), 814–821. https://doi.org/10.1039/b514644e

Pontana, F., Duhamel, A., Pagniez, J., Flohr, T., Faivre, J. B., Hachulla, A. L., Remy, J., & Remy-Jardin, M. (2011). Chest computed tomography using iterative reconstruction vs filtered back projection (Part 2): Image quality of low-dose CT examinations in 80 patients. *European Radiology*, *21*(3), 636–643. https://doi.org/10.1007/s00330-010-1991-4

Pontana, F., Pagniez, J., Flohr, T., Faivre, J. B., Duhamel, A., Remy, J., & Remy-Jardin, M. (2011). Chest computed tomography using iterative reconstruction vs filtered back projection (Part 1): Evaluation of image noise reduction in 32 patients. *European Radiology*, *21*(3), 627–635. https://doi.org/10.1007/s00330-010-1990-5

Popov, A. P., Lademann, J., Priezzhev, A. V., & Myllylä, R. (2005). Effect of size of TiO2 nanoparticles embedded into stratum corneum on ultraviolet-A and ultraviolet-B sun-blocking properties of the skin. *Journal of Biomedical Optics*, *10*(6), 064037. https://doi.org/10.1117/1.2138017

Pyeon, M., Ruoko, T. P., Leduc, J., Gönüllü, Y., Deo, M., Tkachenko, N. V., & Mathur, S. (2018). Critical role and modification of surface states in hematite films for enhancing oxygen evolution activity. *Journal of Materials Research*, *33*(4), 455–466. https://doi.org/10.1557/jmr.2017.465

Pyeon, M., Wang, M., Gönüllü, Y., Kaouk, A., Jäckle, S., Christiansen, S., Hwang, T., Moon, K. Il, & Mathur, S. (2016). Design of multi-layered TiO2-Fe2O3 photoanodes for photoelectrochemical water splitting: Patterning effects on photocurrent density. *MRS Communications*, *6*(4), 442–448. https://doi.org/10.1557/mrc.2016.54

Queraltó, A., Graf, D., Frohnhoven, R., Fischer, T., Vanrompay, H., Bals, S., Bartasyte, A., & Mathur, S. (2019). LaFeO3 Nanofibers for High Detection of Sulfur-Containing Gases. *ACS Sustainable Chemistry and Engineering*, *7*(6), 6023–6032. https://doi.org/10.1021/acssuschemeng.8b06132

Queraltó, A., Pérez Del Pino, Á., Ricart, S., Obradors, X., & Puig, T. (2013). Laser-induced metal organic decomposition for Ce0.9Zr 0.1O2-y epitaxial thin film growth. *Journal of Alloys and Compounds*, *574*, 246–254. https://doi.org/10.1016/j.jallcom.2013.04.171

Radon, J. (1917). Über die Bestimmung von Funktionen durch ihre Integralwerte längs gewisser Mannigfaltigkeiten. *Berichte Sachsische Akademie Der Wissenschaften Leipzig. Journal of Mathematical Physics*, *69*, 71–86. https://doi.org/10.1090/psapm/027/692055

Raginsky, M., Willett, R. M., Harmany, Z. T., & Marcia, R. F. (2010). Compressed sensing performance bounds under poisson noise. *IEEE Transactions on Signal Processing*, *58*(8), 3990–4002. https://doi.org/10.1109/TSP.2010.2049997

Reguera, J., Langer, J., Jiménez De Aberasturi, D., & Liz-Marzán, L. M. (2017). Anisotropic metal nanoparticles for surface enhanced Raman scattering. *Chemical Society Reviews*, *46*(13), 3866–3885. https://doi.org/10.1039/c7cs00158d

Richard P. Feynman. (1960). There's a Plenty of Room At the bottom. *Engineering and Science*, *23*, 22–36.

Righettoni, M., Amann, A., & Pratsinis, S. E. (2015). Breath analysis by nanostructured metal oxides as chemo-resistive gas sensors. *Materials Today*, *18*(3), 163–171. https://doi.org/10.1016/j.mattod.2014.08.017

Roiban, L., Li, S., Aouine, M., Tuel, A., Farrusseng, D., & Epicier, T. (2018). Fast 'Operando' electron nanotomography. *Journal of Microscopy*, *269*(2), 117–126. https://doi.org/10.1111/jmi.12557

Ronneberger, O., Fischer, P., & Brox, T. (2015). U-net: Convolutional networks for biomedical image segmentation. *Lecture Notes in Computer Science (Including Subseries Lecture Notes in Artificial Intelligence and Lecture Notes in Bioinformatics)*, 234–241. https://doi.org/10.1007/978-3-319-24574-4_28

Rose, H., & Wan, W. (2005). Aberration correction in electron microscopy. *Proceedings of the IEEE Particle Accelerator Conference*, *7*(12), 50–55. https://doi.org/10.1109/PAC.2005.1590354

Rumyantseva, M. N., Vladimirova, S. A., Vorobyeva, N. A., Giebelhaus, I., Mathur, S., Chizhov, A. S., Khmelevsky, N. O., Aksenenko, A. Y., Kozlovsky, V. F., Karakulina, O. M., Hadermann, J., Abakumov, A. M., & Gaskov, A. M. (2018). p-CoOx/n-SnO2 nanostructures: New highly selective materials for H2S detection. *Sensors and Actuators, B: Chemical*, *255*, 564–571. https://doi.org/10.1016/j.snb.2017.08.096

Rusinkiewicz, S. (2004). Estimating curvatures and their derivatives on triangle meshes. *Proceedings - 2nd International Symposium on 3D Data Processing, Visualization, and Transmission. 3DPVT 2004*, 486–493. https://doi.org/10.1109/TDPVT.2004.1335277

Saghi, Z., Benning, M., Leary, R., Macias-Montero, M., Borras, A., & Midgley, P. A. (2015). Reduced-dose and high-speed acquisition strategies for multi-dimensional electron microscopy. *Advanced Structural and Chemical Imaging*, *1*(1), 7. https://doi.org/10.1186/s40679-015-0007-5

Sánchez-Ramírez, J. F., Pal, U., Nolasco-Hernández, L., Mendoza-Álvarez, J., & Pescador-Rojas, J. A. (2008). Synthesis and optical properties of Au-Ag alloy nanoclusters with controlled composition. *Journal of Nanomaterials*, *2008*, 9. https://doi.org/10.1155/2008/620412

Scherzer, O. (1936). Über einige Fehler von Elektronenlinsen. *Zeitschrift Für Physik*, *101*, 593–603. https://doi.org/10.1007/BF01349606

Schlossmacher, P., Klenov, D. O., Freitag, B., & von Harrach, H. S. (2010). Enhanced Detection Sensitivity with a New Windowless XEDS System for AEM Based on Silicon Drift Detector Technology. *Microscopy Today*, *18*(4), 14–20. https://doi.org/10.1017/s1551929510000404

Schulz, J., Hohenberg, H., Pflücker, F., Gärtner, E., Will, T., Pfeiffer, S., Wepf, R., Wendel, V., Gers-Barlag, H., & Wittern, K. P. (2002). Distribution of sunscreens on skin. *Advanced Drug Delivery Reviews*, *54*(SUPPL.), S157–S163. https://doi.org/10.1016/S0169-409X(02)00120-5

Shao, F., Hoffmann, M. W. G., Prades, J. D., Zamani, R., Arbiol, J., Morante, J. R., Varechkina, E., Rumyantseva, M., Gaskov, A., Giebelhaus, I., Fischer, T., Mathur, S., & Hernández-Ramírez, F. (2013). Heterostructured p-CuO (nanoparticle)/n-SnO2 (nanowire) devices for selective H2S detection. *Sensors and Actuators, B: Chemical*, *181*, 130–135. https://doi.org/10.1016/j.snb.2013.01.067

Shao, M., Chang, Q., Dodelet, J. P., & Chenitz, R. (2016). Recent Advances in Electrocatalysts for Oxygen Reduction Reaction. *Chemical Reviews*, *116*(6), 3594–3657. https://doi.org/10.1021/acs.chemrev.5b00462

Shulaker, M. M., Hills, G., Park, R. S., Howe, R. T., Saraswat, K., Wong, H. S. P., & Mitra, S. (2017). Three-dimensional integration of nanotechnologies for computing and data storage on a single chip. *Nature*, *547*, 74–78. https://doi.org/10.1038/nature22994

Shulaker, M. M., Hills, G., Patil, N., Wei, H., Chen, H. Y., Wong, H. S. P., & Mitra, S. (2013). Carbon nanotube computer. *Nature*, *501*(7468), 526–530. https://doi.org/10.1038/nature12502

Sidky, E. Y., Jorgensen, J. H., & Pan, X. (2012). Convex optimization problem prototyping for image reconstruction in computed tomography with the ChambollePock algorithm. *Physics in Medicine and Biology*, *57*(10), 3065–3091. https://doi.org/10.1088/0031-9155/57/10/3065

Skorikov, A., Albrecht, W., Bladt, E., Xie, X., Van Der Hoeven, J. E. S., Van Blaaderen, A., Van Aert, S., & Bals, S. (2019). Quantitative 3D Characterization of Elemental Diffusion Dynamics in Individual Ag@Au Nanoparticles with Different Shapes. *ACS Nano*, *13*(11), 13421–13429. https://doi.org/10.1021/acsnano.9b06848

Slater, T. J. A., Camargo, P. H. C., Burke, M. G., Zaluzec, N. J., & Haigh, S. J. (2014). Understanding the limitations of the Super-X energy dispersive x-ray spectrometer as a function of specimen tilt angle for tomographic data acquisition in the S/TEM. *Journal of Physics: Conference Series*, *522*(1), 012025. https://doi.org/10.1088/1742-6596/522/1/012025

Slater, T. J. A., Janssen, A., Camargo, P. H. C., Burke, M. G., Zaluzec, N. J., & Haigh, S. J. (2016). STEM-EDX tomography of bimetallic nanoparticles: A methodological investigation. *Ultramicroscopy*, *162*, 61–73. https://doi.org/10.1016/j.ultramic.2015.10.007

Smith, P. R., Peters, T. M., & Bates, R. H. T. (1973). Image reconstruction from finite numbers of projections. *Journal of Physics A: General Physics*, *6*(3), 361. https://doi.org/10.1088/0305-4470/6/3/011

Song, K., Comolli, L. R., & Horowitz, M. (2012). Removing high contrast artifacts via digital inpainting in cryo-electron tomography: An application of compressed sensing. *Journal of Structural Biology*, *178*(2), 108–120. https://doi.org/10.1016/j.jsb.2012.01.003

Sorzano, C. O. S., Ortiz, E., López, M., & Rodrigo, J. (2006). Improved Bayesian image denoising based on wavelets with applications to electron microscopy. *Pattern Recognition*, *39*(6), 1205–1213. https://doi.org/10.1016/j.patcog.2005.12.009

Stevens, A., Luzi, L., Yang, H., Kovarik, L., Mehdi, B. L., Liyu, A., Gehm, M. E., & Browning, N. D. (2018). A sub-sampled approach to extremely low-dose STEM. *Applied Physics Letters*, *112*(4), 043104. https://doi.org/10.1063/1.5016192

Stoschek, A., & Hegerl, R. (1997). Denoising of electron tomographic reconstructions using multiscale transformations. *Journal of Structural Biology*, *120*(3), 257–265. https://doi.org/10.1006/jsbi.1997.3925

Takita, K., Aoki, T., Sasaki, Y., Higuchi, T., & Kobayashi, K. (2003). High-Accuracy Subpixel Image Registration Based on Phase-Only Correlation. *IEICE Transactions on Fundamentals of Electronics, Communications and Computer Sciences*, *E86-A*(8), 1925–1934.

Taylor, A. B., Siddiquee, A. M., & Chon, J. W. M. (2014). Below melting point photothermal reshaping of single gold nanorods driven by surface diffusion. *ACS Nano*, *8*(12), 12071–12079. https://doi.org/10.1021/nn5055283

Thong, J. T. L., Lee, K. W., & Wong, W. K. (2001). Reduction of charging effects using vector scanning in the scanning electron microscope. *Scanning*, *23*(6), 395–402. https://doi.org/10.1002/sca.4950230606

Tian, N., Zhou, Z. Y., Sun, S. G., Cui, L., Ren, B., & Tian, Z. Q. (2006). Electrochemical preparation of platinum nanothorn assemblies with high surface enhanced Raman scattering activity. *Chemical Communications*, *39*, 4090–4092. https://doi.org/10.1039/b609164d

Tikhonov, A. N. (1963). Solution of Incorrectly Formulated Problems and the Regularisation Method. *Soviet Mathematics Doklady*, *4*, 1035–1038.

Tollan, C. M., Marcilla, R., Pomposo, J. A., Rodriguez, J., Aizpurua, J., Molina, J., & Mecerreyes, D. (2009). Irreversible thermochromic behavior in gold and silver nanorod/polymeric ionic liquid nanocomposite films. *ACS Applied Materials and Interfaces*, *1*(2), 348–352. https://doi.org/10.1021/am800058x

Tsoulos, T. V., Han, L., Weir, J., Xin, H. L., & Fabris, L. (2017). A closer look at the physical and optical properties of gold nanostars: An experimental and computational study. *Nanoscale*, *9*(11), 3766–3773. https://doi.org/10.1039/c6nr09091e

Turkevich, J., Stevenson, P. C., & Hillier, J. (1953). The Formation of Colloidal Gold. *The Journal of Physical Chemistry*, *57*(7), 670–673. https://doi.org/10.1021/j150508a015

Uppal, M. A., Ewing, M. B., & Parkin, I. P. (2011). One-pot synthesis of core-shell silver-gold nanoparticle solutions and their interaction with methylene blue dye. *European Journal of Inorganic Chemistry*, *29*, 4534–4544. https://doi.org/10.1002/ejic.201100536

van Aarle, W., Palenstijn, W. J., De Beenhouwer, J., Altantzis, T., Bals, S., Batenburg, K. J., & Sijbers, J. (2015). The ASTRA Toolbox: A platform for advanced algorithm development in electron tomography. *Ultramicroscopy*, *157*, 35–47. https://doi.org/10.1016/j.ultramic.2015.05.002

Van Aert, S., Batenburg, K. J., Rossell, M. D., Erni, R., & Van Tendeloo, G. (2011). Three-dimensional atomic imaging of crystalline nanoparticles. *Nature*, *470*(7334), 374–377. https://doi.org/10.1038/nature09741

Van Den Berg, E., Friedlander, M. P., Hennenfent, G., Herrmann, F. J., Saab, R., & Yilmaz, Ö. (2009). Algorithm 890: Sparco: A testing framework for sparse reconstruction. *ACM Transactions on Mathematical Software*, *35*(4), 1–16. https://doi.org/10.1145/1462173.1462178

Van den Broek, W., Reed, B. W., Béché, A., Velazco, A., Verbeeck, J., & Koch, C. T. (2019). Various Compressed Sensing Setups Evaluated Against Shannon Sampling Under Constraint of Constant Illumination. *IEEE Transactions on Computational Imaging*, *5*(3), 502–514. https://doi.org/10.1109/tci.2019.2894950

Van Eyndhoven, G., Batenburg, K. J., Kazantsev, D., Van Nieuwenhove, V., Lee, P. D., Dobson, K. J., & Sijbers, J. (2015). An Iterative CT Reconstruction Algorithm for Fast Fluid Flow Imaging. *IEEE Transactions on Image Processing*, *24*(11), 4446–4458. https://doi.org/10.1109/TIP.2015.2466113

van Omme, J. T., Zakhozheva, M., Spruit, R. G., Sholkina, M., & Pérez Garza, H. H. (2018). Advanced microheater for in situ transmission electron microscopy; enabling unexplored analytical studies and extreme spatial stability. *Ultramicroscopy*, *192*, 14–20. https://doi.org/10.1016/j.ultramic.2018.05.005

Vanrompay, H., Bladt, E., Albrecht, W., Béché, A., Zakhozheva, M., Sánchez-Iglesias, A., Liz-Marzán, L. M., & Bals, S. (2018). 3D characterization of heat-induced morphological changes of Au nanostars by fast: In situ electron tomography. *Nanoscale*, *10*(48), 22792–22801. https://doi.org/10.1039/c8nr08376b

Velazco, A., Nord, M., Béché, A., & Verbeeck, J. (2020). *Evaluation of different rectangular scan strategies for STEM imaging*. https://doi.org/arXiv:2002.09370

Verbruggen, S. W., Keulemans, M., Filippousi, M., Flahaut, D., Van Tendeloo, G., Lacombe, S., Martens, J. A., & Lenaerts, S. (2014). Plasmonic gold-silver alloy on TiO2 photocatalysts with tunable visible light activity. *Applied Catalysis B: Environmental*, *156–157*, 116–121. https://doi.org/10.1016/j.apcatb.2014.03.027

Verbruggen, S. W., Keulemans, M., Goris, B., Blommaerts, N., Bals, S., Martens, J. A., & Lenaerts, S. (2016). Plasmonic “rainbow” photocatalyst with broadband solar light response for environmental applications. *Applied Catalysis B: Environmental*, *188*, 147–153. https://doi.org/10.1016/j.apcatb.2016.02.002

von Ardenne, M. (1938). Das Elektronen-Rastermikroskop - Theoretische Grundlagen. *Zeitschrift Für Physik*, *109*(9–10), 553–572. https://doi.org/10.1007/BF01341584

Von Hagen, R., Sneha, M., & Mathur, S. (2014). Ink-jet printing of hollow SnO 2 nanospheres for gas sensing applications. *Journal of the American Ceramic Society*, *97*(4), 1035–1040. https://doi.org/10.1111/jace.12832

Vonesch, C., Wang, L., Shkolnisky, Y., & Singer, A. (2011). Fast wavelet-based single-particle reconstruction in Cryo-EM. *Proceedings - International Symposium on Biomedical Imaging*, 1950–1953. https://doi.org/10.1109/ISBI.2011.5872791

Wang, X., Tao, Q., Wang, L., Li, D., & Zhang, M. (2015). Deep convolutional architecture for natural image denoising. *2015 International Conference on Wireless Communications and Signal Processing, WCSP 2015*, 1–4. https://doi.org/10.1109/WCSP.2015.7341021

Whitney, A. V., Elam, J. W., Stair, P. C., & Van Duyne, R. P. (2007). Toward a thermally robust operando surface-enhanced raman spectroscopy substrate. *Journal of Physical Chemistry C*, *111*(45), 16827–16832. https://doi.org/10.1021/jp074462b

Wulff, G. (2014). XXV. Zur Frage der Geschwindigkeit des Wachsthums und der Auflösung der Krystallflächen. *Zeitschrift Für Kristallographie - Crystalline Materials*. https://doi.org/10.1524/zkri.1901.34.1.449

Xie, J., Xu, L., & Chen, E. (2012). Image denoising and inpainting with deep neural networks. *Advances in Neural Information Processing Systems*, 1.

Xu, W., Xu, F., Jones, M., Keszthelyi, B., Sedat, J., Agard, D., & Mueller, K. (2010). High-performance iterative electron tomography reconstruction with long-object compensation using graphics processing units (GPUs). *Journal of Structural Biology*, *171*(2), 142–153. https://doi.org/10.1016/j.jsb.2010.03.018

Yan, H., & Liu, J. G. (2008). Robust phase correlation based motion estimation and its applications. *BMVC 2008 - Proceedings of the British Machine Vision Conference 2008*, 104.1-104.10. https://doi.org/10.5244/C.22.104

Yang, X., De Andrade, V., Scullin, W., Dyer, E. L., Kasthuri, N., De Carlo, F., & Gürsoy, D. (2018). Low-dose x-ray tomography through a deep convolutional neural network. *Scientific Reports*, *8*, 2575. https://doi.org/10.1038/s41598-018-19426-7

Yang, Y., Chen, C. C., Scott, M. C., Ophus, C., Xu, R., Pryor, A., Wu, L., Sun, F., Theis, W., Zhou, J., Eisenbach, M., Kent, P. R. C., Sabirianov, R. F., Zeng, H., Ercius, P., & Miao, J. (2017). Deciphering chemical order/disorder and material properties at the single-atom level. *Nature*, *542*, 75–79. https://doi.org/10.1038/nature21042

You, C., Yang, Q., Shan, H., Gjesteby, L., Li, G., Ju, S., Zhang, Z., Zhao, Z., Zhang, Y., Cong, W., & Wang, G. (2018). Structurally-sensitive multi-scale deep neural network for low-dose CT denoising. *IEEE Access*, *6*, 41839–41855. https://doi.org/10.1109/ACCESS.2018.2858196

Yuan, H., Khoury, C., Fales, A., Wilson, C., Grant, G., & Vo-Dinh, T. (2012). Plasmonic gold nanostars: A potential agent for molecular imaging and cancer therapy. *Biomedical Optics, BIOMED 2012*, BM2A.8. https://doi.org/10.1364/biomed.2012.bm2a.8

Zanaga, D., Altantzis, T., Polavarapu, L., Liz-Marzán, L. M., Freitag, B., & Bals, S. (2016). A New Method for Quantitative XEDS Tomography of Complex Heteronanostructures. *Particle and Particle Systems Characterization*, *33*(7), 396–403. https://doi.org/10.1002/ppsc.201600021

Zanaga, D., Altantzis, T., Sanctorum, J., Freitag, B., & Bals, S. (2016). An alternative approach for ζ-factor measurement using pure element nanoparticles. *Ultramicroscopy*, *164*, 11–16. https://doi.org/10.1016/j.ultramic.2016.03.002

Zanaga, D., Bleichrodt, F., Altantzis, T., Winckelmans, N., Palenstijn, W. J., Sijbers, J., De Nijs, B., Van Huis, M. A., Sánchez-Iglesias, A., Liz-Marzán, L. M., Van Blaaderen, A., Batenburg, K. J., Bals, S., & Van Tendeloo, G. (2016). Quantitative 3D analysis of huge nanoparticle assemblies. *Nanoscale*, *8*(1), 292–299. https://doi.org/10.1039/c5nr06962a

Zobelli, A., Woo, S. Y., Tararan, A., Tizei, L. H. G., Brun, N., Li, X., Stéphan, O., Kociak, M., & Tencé, M. (2019). Spatial and spectral dynamics in STEM hyperspectral imaging using random scan patterns. *Ultramicroscopy*, *212*, 112912. https://doi.org/10.1016/j.ultramic.2019.112912

Acknowledgments

When I was young, I always dreamed of being an astronaut. The ability of going beyond Earth and “touch” the stars, thrilled me. However, over the course of my studies I took a rather sharp turn. Instead of traversing through the vastness of space, I had the pleasure of exploring a completely different but equally fascinating dimension; the nanoscale world. Coincidentally, some of the nanoparticles I investigated during my PhD studies were star shaped, hence somewhat fulfilling my childhood dream. Perhaps my change of interest from the macroscopic- to atomic world was for the best, given that “touching” these nanoscale stars is considerable less deadly than “touching” any real stars. During my PhD studies I was able to grow as a person and as a scientist. However, PhD studies are not an individual experience, rather you strive together with colleagues to reach common goals in the best possible way. Therefore, I’d like to take the opportunity to thank all of them sincerely.

First of all, I wish to express my gratitude to my promotor, Prof. Dr. Sara Bals. Sara never tires of her passion for obtaining new insights into the properties of nanomaterials. She always patiently assisted me in conducting experiments, writing papers and preparing presentations. Over the course of my master and PhD studies, she learned me what it takes to be a self-critical, independent researcher.

I wish to thank the members of my doctoral committee; Prof. Dr. Floris Wuyts, Prof. Dr. Pierre Van Mechelen, Prof. Dr. Jo Verbeeck, Prof. Dr. Sammy Verbruggen, Prof. Dr. Joost Batenburg and Dr. Hugo Perez-Garza for taking the time to carefully read my thesis. I very much enjoyed the discussions during my pre-defense, and your feedback aided in shaping my thesis into its final form.

I also would like to thank, Prof. Dr. Jo Verbeeck, Prof. Dr. Sandra Van Aert, Prof. Dr. Thomas Altantzis, Prof. Dr. Tim Pennycoock, Prof. Dr. Joke Hadermann, Prof. Dr. Dirk Lamoen, Prof. Dr. Nick Schryvers and Prof. Dr. Staf Van Tendeloo for the inspiring discussions and providing the means for us, PhD students, to conduct scientific research.

Let me also thank Bart, Martin, Dr. Anton-Jan Bons, Dr. Erik Robert, Prof. Dr. Joost Batenburg, Lucian and Alexander for supporting my FWO-SB grant application and for their aid in bringing it to a successful conclusion.

Without nanomaterials there would be no nanoscience. I wish to thank Prof. Dr. Luis Liz-Marzán, Dr. Zhuo Xiaolu, Dr. Ana Sánchez Iglesias and Vished Kumar, for providing all sorts of nanoparticles. In addition, I would like to express my gratitude towards, Prof. Dr. Silvia Lenaerts, Prof. Dr. Sammy Verbruggen, Dr. Natan Blommaerts and Silvia Nuti, I really enjoyed the interesting collaboration on the alloyed Ag/Au nanoparticles. I wish to thank Prof. Dr. Ausrine Bartasyte, Prof. Dr. Sanjay Mathur, Dr. Albert Queraltó, David Graf, Robert Frohnhoven and Thomas Fischer for providing the fascinating porous nanofibers. I would like to express my appreciation to Prof. Dr. Teri Odom and Priscilla Choo for the provision of the Au branched nanoparticles. I also want to thank Prof. Dr. Sara Skrabalak and Joshua Smith for sharing the symmetric Au octopods with us. In general, a sincere thank you for all researchers that provided samples during my PhD.

A tremendous thank you to Prof. Dr. Joost Batenburg and his researchers. In special, Jan-Willem, Daan and Willem Jan, with whom I enjoyed working together and who were always there to help me during my research stays. Those research stays often felt more as holiday than work, while being very productive. I very much appreciated our close collaboration and I hope it will continue in the future.

I would also like to thank Dr. Hugo Perez-Garza and Dr. Marina Zakhozheva for the collaboration on the heating experiments and providing the holders and MEMS based chips that opened the pathway towards in-situ electron tomography at EMAT. I wish to thank Dr. Bert Freitag, Dr. Holger Kohr and Dr. Erik Franken for sharing the enthusiasm concerning fast electron tomography.

Without all the support, we would not be able to perform any science. I would like to thank Lydia and Miek for their administrative assistance, which made it easy for me to dedicate myself to research. Liesbet for the many laughs and your creative aid in designing posters, presentations and the cover of my thesis. Stijn and Tine for helping with sample preparation and their lab support, and Koen for the IT support. Ursula and Armand for always being there whenever I mistreated our microscopes and for all of our interesting discussions. I really appreciated all your help. I also want to thank all (past) colleagues of EMAT for their assistance during my PhD. In special; Eva, Wiebke, Nathalie, Magnus, Alexander and Saskia for always being there to answer my (many) questions, the fun collaboration concerning fast in-situ tomography or taking the time to read through my thesis. One colleague deserves some special acknowledgement; Mylène, thank you for all the joyful moments, relaxing walks and just being there.

Tenslotte wil ik mijn familie bedanken; Annelies, Machteld, Ivo, Marc, Lutgard, Naomi, Mark en Cindy. Bedankt om steeds in mij te geloven en altijd interesse te tonen in mijn werk, zelfs als het onduidelijk was wat ik nu eigenlijk net allemaal onderzocht. Bedankt aan mijn levenslange vrienden voor de leuke en ontspannende momenten waarop ik mijn gedachten kon verzetten. Ten slotte wil ik ontzettend graag mijn vrouw Anaïs bedanken. Jij was er steeds wanneer de wind woest waaide door mijn hoofd. Woorden kunnen niet uitdrukken wat jij voor mij betekent. Ik kan niet wachten om met jou nog zoveel meer mee te maken. Zij and zij kunnen we alles aan, wat er ook nog komt.